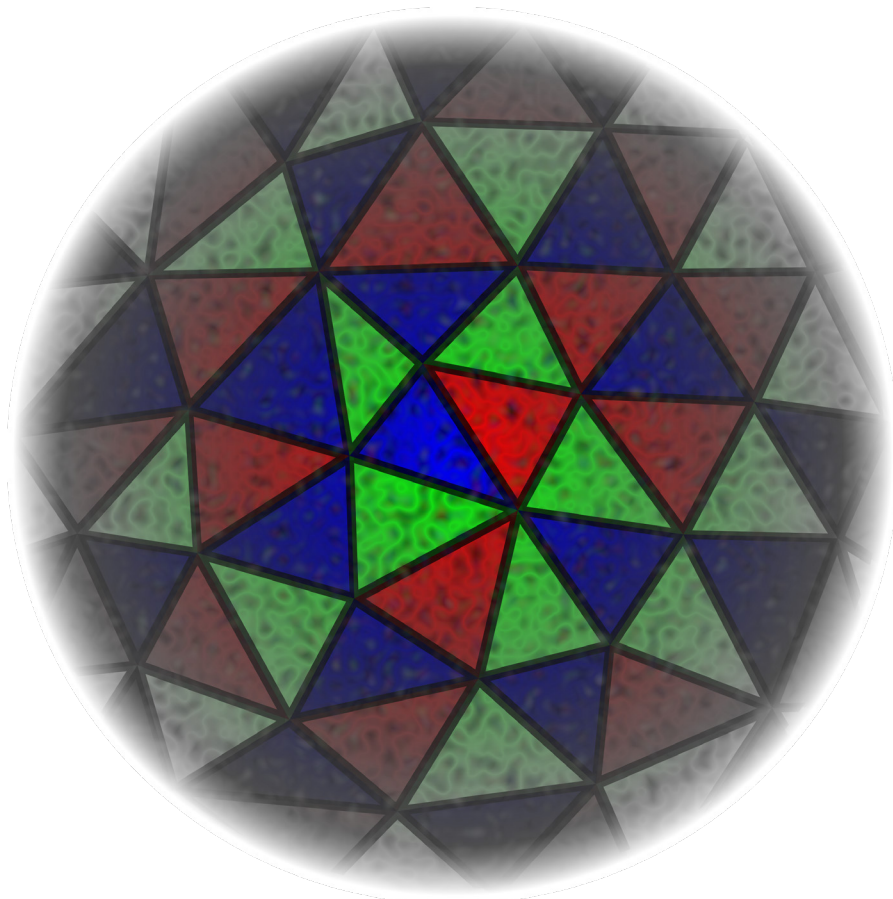Jani Penttala

Diffractive Processes at Next-to-Leading Order in the Dipole Picture

UNIVERSITY OF JYVÄSKYLÄ

FACULTY OF MATHEMATICS
AND SCIENCE

Jani Penttala

Diffractive Processes at Next-To-Leading Order in the Dipole Picture

Cover picture by Jani Penttala

Abstract

Penttala, Jani
Diffractive Processes at Next-to-Leading Order in the Dipole Picture

Diffractive processes are very sensitive to the target's gluon distribution in the high-energy limit, making them a good candidate for probing the target in the nonlinear region of quantum chromodynamics. The nonlinear effects are expected to eventually lead to gluon saturation which is naturally described in the color-glass condensate (CGC) effective field theory. While there are strong hints of gluon saturation in the currently available data, no unambiguous signal has been observed. It is then important to improve the theoretical understanding of processes sensitive to saturation to find a clear difference between predictions from the linear and nonlinear regions of QCD. This includes calculating diffractive processes beyond the leading order in perturbation theory.

In this thesis, we calculate diffractive processes at next-to-leading order (NLO) in the high-energy limit, with an emphasis on exclusive vector meson production and inclusive diffraction in deep inelastic scattering (DIS). Calculations in the high-energy limit can be done using the dipole picture, the basics of which are briefly reviewed. This includes using the CGC effective field theory to describe the nonperturbative dipole-target scattering amplitude which appears in practically all calculations in the dipole picture. The universality of the dipole-target scattering amplitude at NLO is shown numerically, in the sense that the same dipole-target scattering amplitude can be used to describe the data in both massless and massive quark production in inclusive DIS, and also in diffractive processes where exclusive vector meson production is considered. The analytical NLO calculations of exclusive vector meson production and inclusive diffraction in DIS are also explained. Exclusive vector meson production is calculated in the nonrelativistic limit for heavy mesons and the limit of large photon virtuality for light mesons. Also, the importance of including relativistic corrections to the heavy vector meson wave function in exclusive vector meson production is considered. For inclusive diffraction in DIS, we focus on the NLO corrections to the final state and show how the divergences cancel.

Tiivistelmä (Abstract in Finnish)

Penttala, Jani
Diffraktiiviset prosessit dipolikuvassa alinta seuraavassa kertaluvussa

Diffraktiiviset prosessit ovat korkean energian rajalla sensitiivisiä kohdehiukkasen gluonijakaumalle, mistä johtuen niiden avulla voidaan tutkia kohdetta kvanttiväridynamiikan epälineaarisessa alueessa. Näiden epälineaaristen ilmiöiden odotetaan johtavan gluonisaturaatioon, jota voidaan kuvata luontevasti värilasikondensaatiksi kutsutun efektiivisen kenttäteorian avulla. Vaikka saatavilla olevassa kokeellisessa datassa onkin vahvoja viitteitä gluonisaturaatiosta, yksiselitteistä merkkiä saturaatiosta ei ole havaittu. Tämän vuoksi on tärkeää parantaa saturaatiolle sensitiivisten prosessien teoreettista ymmärrystä, jotta pystytään löytämään selkeitä eroja kvanttiväridynamiikan lineaarisen ja epälineaarisen alueen ennusteiden väillä. Diffraktiivisten prosessien laskeminen korkeammille kertaluvuille häiriöteoriassa on osa tätä kehitystä.

Tässä väitöskirjassa lasketaan diffraktiivisia prosesseja korkean energian rajalla alinta seuraavassa kertaluvussa, ja näistä tarkastellaan erityisesti eksklusiivista vektorimesonituottoa sekä inklusiivista diffraktiota syvässä epäelastisessa sironnassa. Korkean energian rajalla laskuissa voidaan käyttää niin sanottua dipolikuvaa, jonka perusteet käydään lyhyesti läpi. Tähän kuuluu värilasikondensaattiteorian käyttäminen epäperturbatiivisen dipoliamplitudin kuvaamiseen, joka esiintyy oleellisesti kaikissa dipolikuvassa tehdyissä laskuissa. Dipoliamplitudin universaalius alinta seuraavassa kertaluvussa näytetään numeerisesti siinä mielessä, että samaa dipoliamplitudia voidaan käyttää sekä massattomien ja massallisten kvarkkien tuoton kuvaamiseen inklusiivisessa syvässä epäelastisessa sironnassa että diffraktiivisissa prosesseissa, joista tarkastellaan eksklusiivista vektorimesonituottoa. Eksklusiivisen vektorimesonituoton ja inklusiivisen diffraktion analyyttinen lasku alinta seuraavassa kertaluvussa käydään myös läpi. Näistä eksklusiivinen vektorimesonituotto lasketaan epärelativisella rajalla raskaiden mesonien tapauksessa ja suuren fotonin virtualiteetin rajalla kevyiden mesonien tapauksessa. Tämän lisäksi tarkastellaan relativististen korjausten tärkeyttä raskaiden mesonien aaltofunktioon tässä prosessissa. Inklusiivisen diffraktion tapauksessa keskitytään erityisesti alinta seuraavan kertaluvun korjauksiin lopputilassa sekä osoitetaan divergenssien kumoutuminen.

Author   Jani Penttala
                    Department of Physics
                    University of Jyväskylä
                    Finland

Supervisors   Dr. Heikki Mäntysaari
                    Department of Physics
                    University of Jyväskylä
                    Finland

                    Prof. Tuomas Lappi
                    Department of Physics
                    University of Jyväskylä
                    Finland

Reviewers   Prof. Zhongbo Kang
                    Department of Physics and Astronomy
                    University of California, Los Angeles (UCLA)
                    USA

                    Dr. Renaud Boussarie
                    CPHT, CNRS, École polytechnique
                    Institut polytechnique de Paris
                    France

Opponent   Prof. Lech Szymanowski
                    National Centre for Nuclear Research (NCBJ)
                    Poland

Preface

There is no magic.
There is only knowledge,
more or less hidden.

— Gene Wolfe, *The Claw of the Conciliator*

When I started studying physics everything seemed like magic, incomprehensible to the untrained eye. Even after many years of studying in the field a lot of things still do seem like that, but now I feel like I can see a glimpse of meaning behind it all. This does not mean that the magic has faded away, but instead everything starts to seem even more impressive. Of course, physics is still far from finished and there are a lot of questions unanswered. While working on this thesis it has become clear that there is still much work to be done.

List of Included Articles

I   Tuomas Lappi, Heikki Mäntysaari, Jani Penttala. Relativistic corrections to the vector meson light front wave function. *Physical Review D*, 102, 054020, (2020).

II   Heikki Mäntysaari, Jani Penttala. Exclusive heavy vector meson production at next-to-leading order in the dipole picture. *Physics Letters B*, 823, 136723, (2021).

III   Heikki Mäntysaari, Jani Penttala. Exclusive production of light vector mesons at next-to-leading order in the dipole picture. *Physical Review D*, 105, 114038, (2022).

IV   Heikki Mäntysaari, Jani Penttala. Complete calculation of exclusive heavy vector meson production at next-to-leading order in the dipole picture. *Journal of High Energy Physics*, 08, 247, (2022).

V   Henri Hänninen, Heikki Mäntysaari, Risto Paatelainen, Jani Penttala. Proton structure functions at NLO in the dipole picture with massive quarks. *Physical Review Letters*, 130, 192301, (2023).

The author performed all analytical and numerical calculations in Articles [I, II, III, IV]. For Article [V], the author implemented the massive structure functions into the existing code for the massless case. The author wrote the original drafts of the manuscripts for Articles [III, IV], and participated in writing Articles [I, II] and editing Article [V]. Chapter 5 contains discussion about an unpublished work with Guillaume Beuf, Tuomas Lappi, Heikki Mäntysaari and Risto Paatelainen, where the author has performed all analytical calculations.

Contents

1 INTRODUCTION

The recent century has brought us a vast amount of insight into the fine details of the smallest particles in the world. Especially interesting are the particles that form the atomic nuclei, protons and neutrons, as it turns out that their internal structure is much more complicated than what was originally thought. The first observations of this were found in the 1960s when it was realized that they are not actually elementary particles but contain a sub-structure of smaller constituents. These were later understood to be new particles called quarks, with protons and neutrons both comprised of three quarks each.

When the internal structure of nucleons was studied at higher energies, it was found that this simple quark model is not enough: a vast amount of gluons and virtual quarks also populate the nucleons. These constituents of nucleons are collectively called partons. At even higher energies, the inner structure is dominated by gluons [1]. This can be understood by the partons emitting gluons, with gluon emission becoming more likely with increasing energy. This makes the cross sections rise very steeply in energy. However, this steep increase cannot go on indefinitely. It was realized that this would eventually break the unitarity of quantum chromodynamics (QCD), and subsequently gluon absorption also has to become important at some point. Indeed, this was found to be a theoretical prediction of QCD, which gave rise to saturation models [2].

While these saturation effects are theoretically well-motivated, current experiments have not been able to distinguish between saturation and non-saturation models within the uncertainties of the theory and the experiment. However, there have been hints of saturation in heavy-ion collisions at the Relativistic Heavy-Ion Collider (RHIC) [3–5] and the Large Hadron Collider (LHC) [6–9], and it is hoped that even clearer signals will be found in electron-nucleus collisions at the future Electron-Ion Collider (EIC) [10]. These experimental endeavors for precise data make studying saturation effects very topical, and there has been a very active collaboration in the high-energy physics community to improve the theoretical understanding of saturation physics. This includes promoting calculations to the next-to-leading order (NLO), and this thesis is a part of that process focusing on a subset of diffractive processes. Diffractive processes are especially sensitive to the high-energy gluon dis-

tribution of the target, making them a good candidate for trying to find the "smoking gun" of saturation.

Diffraction in high-energy physics is briefly considered in Ch. 2, along with the dipole picture which forms the basis of calculations in the high-energy limit. Saturation physics is explained in Ch. 3 where the interaction of the probe with a highly energetic target is considered. We also discuss Article [V] which highlights the importance of including massive quarks for constraining the nonperturbative interaction with the target. Chapter 4 discusses higher-order corrections to exclusive vector meson production. We consider first relativistic effects to the heavy vector meson wave function, which is the topic of Article [I], and then the next-to-leading order corrections to exclusive vector meson production are discussed in detail. This discussion is based on the work in Articles [II, III, IV] where the NLO correction to the production of heavy vector mesons is considered in the nonrelativistic limit and the production of light vector mesons in the limit of large photon virtuality. Finally, inclusive diffraction is the topic of Sec. 3.3.1 where an unpublished NLO calculation of diffractive structure functions is briefly discussed.

2 DIFFRACTIVE PROCESSES IN THE DIPOLE PICTURE

2.1 High-energy diffraction

Interest in diffractive processes in high-energy physics began to rise in the 1990s when the results from the HERA collider in DESY started to become available. At HERA, it was found that in about 10% of Deep Inelastic Scattering (DIS) events there is a large rapidity gap present in the distribution of the final-state particles [11, 12]. The ratio of such events also remains roughly constant as a function of energy [13, 14]. This finding was largely surprising as one would expect the target to break up into a shower of particles filling the rapidity gap, and while this was true for the majority of events, events with a large rapidity gap were expected to get more suppressed with higher energies. In fact, this is true if one expects an exchange of color between the virtual photon and the target [15]. The large rapidity gap can then be understood as a signature of *diffractive* events where the interaction between the photon and the target is color neutral[1]. Especially, this means that the target and the projectile remain in a color-singlet state which is essential for the large rapidity gap: as a result of confinement, color-octet final states would start to radiate gluons as their separation grows, and this would produce a plethora of soft particles that would fill the whole rapidity spectrum.

The theory of high-energy diffraction dates back to 1960s when the Regge theory [16–18] was developed to give a qualitative explanation of a diffractive process as an exchange of the so-called *pomeron*[2], shown in Fig. 2.1. A pomeron is a theoretical quasiparticle that has the quantum numbers of a vacuum, and thus this process

---

[1]   This definition of diffraction has an analog in optics where diffraction refers to light meeting an obstacle that has a size comparable to the wavelength of the light. While this analogy between high-energy physics and optics is far from perfect, diffractive processes in the two fields have some properties in common. For example, diffractive cross sections tend to decrease rapidly as a function of the momentum transfer, expressing also *diffractive dips*.

[2]   A pomeron exchange corresponds to the dominating C-parity even interaction. The C-parity odd interactions corresponding to the so-called *odderon* exchange are more suppressed.
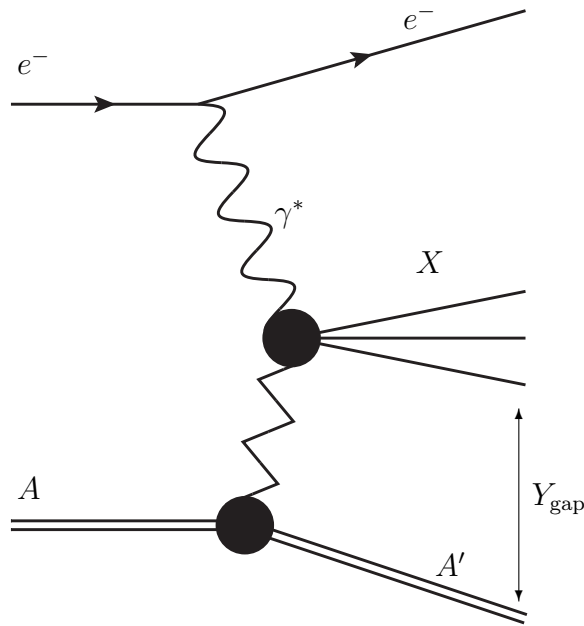
FIGURE 2.1 Diffractive DIS depicted as an exchange of a color-neutral quasiparticle. The large rapidity gap Y_{gap} is an experimental sign of a diffractive process.

satisfies the theoretical definition of diffraction as a color-neutral interaction. Even without understanding the whole structure of the pomeron, the Regge theory was quite successful in describing the general energy and momentum transfer dependence of the cross section [19]. While this explanation via a pomeron exchange is these days mostly of historical interest, the vocabulary dating to the Regge theory is still largely used also in modern literature.

After the discovery of QCD it was possible to give the pomeron a more rigorous definition starting from the first principles. It was understood that at high energies the gluon distribution starts to dominate in the nucleus, and thus the lowest-order color-neutral interaction is an exchange of two gluons between the target and a quark-antiquark pair [20, 21], shown in Fig. 2.2. This makes diffractive processes highly sensitive to the gluon distribution of the target. The enhancement of gluon emission at high energies also means that such a two-gluon exchange is not enough to fully describe the process, but instead one has to resum these gluon exchanges to all orders. This was first done by the Balitsky–Fadin–Kuraev–Lipatov (BFKL) equation [22–24]. The resummation of gluon exchanges in the high-energy limit is quite general and applies also to inclusive processes.

These theoretical endeavors to understand the interaction with the target run into problems at even higher energies. They predict a rapid rise of the gluon distribution which cannot go on indefinitely, as the power-like growth of the cross section predicted by the BFKL equation would eventually break the so-called Froissart–Martin bound [25, 26] for the energy dependence of the cross section. This is in violation of the unitarity of the S-matrix and thus the probability conservation in particle scattering. The enhancement of gluon radiation at high energies should eventually be compensated by nonlinear gluon recombination effects such that the
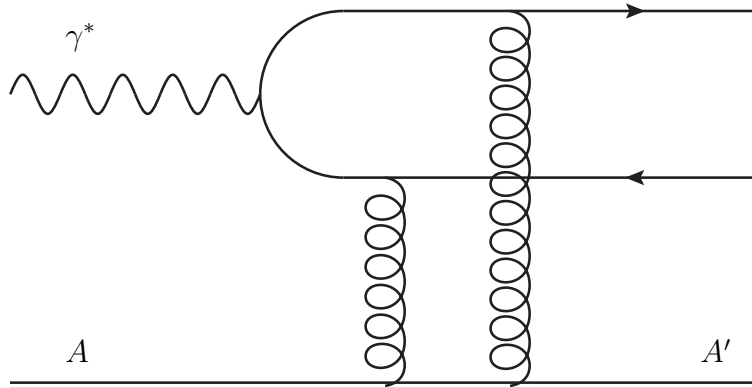
FIGURE 2.2   The leading-order picture for a color-neutral interaction with the target.

energy dependence of the cross section is tamed from power-like to logarithmic, which also results in a slower growth of the target's gluon distribution. This phenomenon is called gluon saturation. Saturation can be taken into account quite naturally by considering the interaction with the target in terms of nonperturbative *Wilson lines* instead of gluon exchanges, which leads to the celebrated Balitsky–Kovchegov (BK) [27, 28] and Jalilian-Marian–Iancu–McLerran–Weigert–Leonidov–Kovner (JIMWLK) [29–35] evolution equations for the interaction with the target. This is also the framework used in this thesis for describing the energy dependence of the nonperturbative *dipole-target scattering amplitude*. It turns out that this nonperturbative part can, in general, be treated separately from the rest of the process in the so-called *dipole picture* [2, 36–39] which allows for perturbative calculations of processes in the high-energy limit. The rest of this chapter is devoted to explaining the basics of this approach.

2.2 Factorization in the high-energy limit

The class of processes we are interested in involves a photon interacting with a target nucleus as shown in Fig. 2.3. This photon can be real, as in ultra-peripheral collisions, or virtual, as in DIS. In general, the interaction with the target is highly nonperturbative, but in the high-energy limit it can be written in a simplified form. This can be seen by considering the interaction in the light-cone coordinates

$$p^+ = \frac{1}{\sqrt{2}}(p^0 + p^3) \qquad p^- = \frac{1}{\sqrt{2}}(p^0 - p^3) \qquad \mathbf{p} = (p^1, p^2). \qquad (2.1)$$

It is also convenient to use *light-cone quantization* in the light-cone coordinates, which essentially means that the role of the Hamiltonian is played by the minus component of the momentum operator, $\hat{P}^-$, and the time is given by the light-cone time x^+. This also means that the components $(p^+, \mathbf{p})$ of the momenta are conserved during the interactions but the minus component p^- is not. Instead, it is determined by the on-shell condition $p^- = \frac{m^2 + \mathbf{p}^2}{2p^+}$.
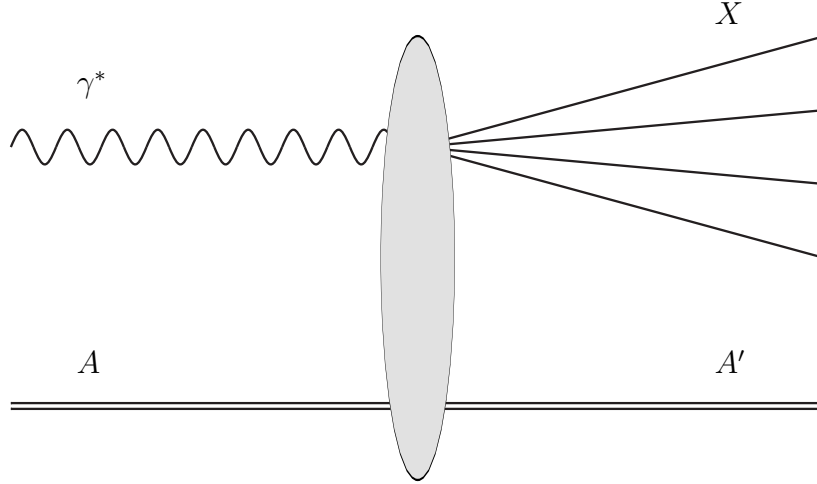
FIGURE 2.3   Diffractive interaction of a virtual photon with a target nucleus.

We will also choose a frame where the photon and the target are moving along the x^3-axis, with the photon going in the positive direction. For heavy nuclei, it is customary to consider the average momentum of a nucleon instead of the nucleus, which corresponds to dividing the momentum of the nucleus by its mass number. This makes it easier to study nuclear effects that modify the simple assumption that the nucleus consists of a number of free nucleons. The momenta of the photon and the average nucleon are then given by

$$q = (q^+, q^-, \mathbf{q}) = \left(q^+, -\frac{Q^2}{2q^+}, \mathbf{0}\right)$$
$$P_n = (P_n^+, P_n^-, \mathbf{P}_n) = \left(\frac{m_n^2}{2P_n^-}, P_n^-, \mathbf{0}\right) \tag{2.2}$$

where $Q^2 = -q^2 \geq 0$ is the photon virtuality and m_n is the mass of the nucleon. In the high-energy limit the center-of-mass energy is large, $W^2 \gg Q^2, m_n^2$, and thus the energy is given by

$$W^2 = (q + P_n)^2 = 2q^+ P_n^- - \frac{Q^2 m_n^2}{2q^+ P_n^-} - Q^2 + m_n^2 \approx 2q^+ P_n^-. \tag{2.3}$$

The photon-target interaction is dominated by strong interactions. As the photon is color neutral, it has to first fluctuate into a quark-antiquark pair which acts as a color dipole, and it can be shown that in the high-energy limit this fluctuation has to happen before the interaction. The reason for this is that the target gets Lorentz-contracted so that the duration of the interaction in the light-cone time is

$$x^+_{\text{interaction}} \sim \frac{1}{P_n^-} \tag{2.4}$$

which is much smaller the lifetime of the virtual photon[3]

$$x^+_\gamma \sim \frac{1}{|q^-|} = \frac{2q^+}{Q^2}. \tag{2.5}$$

---

[3]   By the Heisenberg uncertainty principle deviations from the on-shell condition for the minus momentum can live for a time $x^+_{\text{lifetime}} \sim \frac{1}{|\Delta p^-|}$ where $\Delta p^- = p^- - p_{\text{on-shell}}^-$.
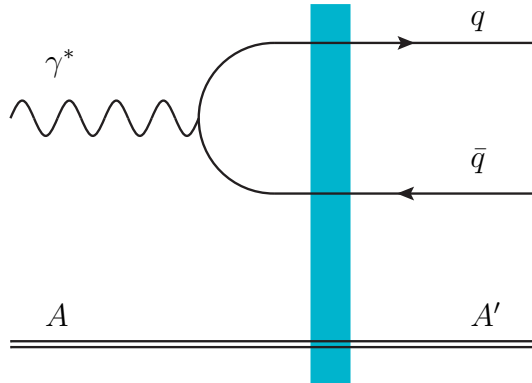
FIGURE 2.4   Factorization in the dipole picture at leading order. The blue rectangle depicts the nonperturbative interaction with the target.

This means that fluctuations into other particles during the interaction are suppressed by the factor $x^+_{\text{interaction}}/x^+_\gamma \sim Q^2/(2q^+P^-_n) = Q^2/W^2$, and hence it is much more likely that the photon has split before the interaction. This also holds in general for other types of particles interacting with the target as long as the minus momentum of the particle is not too large. Thus the probe, in this case a virtual photon, sees the target as an instantaneous shock wave. This high-energy condition is usually written in terms of the Bjorken x variable

$$x = \frac{Q^2}{2P_n \cdot q} = \frac{Q^2}{W^2 + Q^2 - m_n^2} \approx \frac{Q^2}{W^2 + Q^2}. \tag{2.6}$$

We can see that the high-energy limit $W^2 \gg Q^2$ is equivalent to a small Bjorken x.

The suppression of the Fock state fluctuations during the interaction allows us to factorize the process into three different parts [2, 36–39]:

1. The photon fluctuates into the Fock state n.

2. The Fock state n interacts with the target.

3. After the interaction, the Fock state n forms the final state X.

At leading order in perturbation theory, this happens by the photon going into the quark-antiquark dipole which interacts with the target, shown in Fig. 2.4. This is where the name dipole picture comes from. This factorization can be applied very generally to processes in the high-energy limit, and it allows us to write matrix elements as [40]

$$\left\langle X, A'(x^+ = +\infty) \right| \hat{S} - 1 \left| \gamma^*, A(x^+ = -\infty) \right\rangle$$
$$= \sum_{n,n'} \int d[\text{PS}]_n \, d[\text{PS}]_{n'} \, \langle X(+\infty)|n'\rangle \times \langle n'A'|\hat{S} - 1 |nA\rangle \times \langle n|\gamma^*(-\infty)\rangle \tag{2.7}$$

where $\hat{S}$ denotes the S-matrix, and n and n' correspond to the same Fock state but with possibly different momenta and quantum numbers. Here the phase space integrals are defined as

$$d[\text{PS}]_n = \prod_{i \in n} d\widetilde{k}_i \tag{2.8}$$

where
$$\mathrm{d}\widetilde{k} = \frac{\mathrm{d}k^+ \, \mathrm{d}^2\mathbf{k}}{2k^+(2\pi)^3}\theta(k^+). \tag{2.9}$$

From this factorization, we see that the nonperturbative interaction with the target is simplified to $\langle n'A'|\hat{S}-1\,|nA\rangle$. This matrix element is universal in the sense that it is independent from the rest of the process. The factors $\langle X(+\infty)|n'\rangle$, $\langle n|\gamma^*(-\infty)\rangle$ are in contrast dependent on the initial and final states, and they are most conveniently given by light-cone wave functions which can be calculated using light-cone perturbation theory discussed in Sec. 2.3.

The high-energy limit also simplifies the cross section. The differential element of the cross section for the scattering process $\gamma^* + A \to X + A'$ can be written as

$$\mathrm{d}\sigma^{\gamma^* A \to XA'} = \frac{1}{2W^2}\,\mathrm{d}[\mathrm{PS}]_X\,\mathrm{d}[\mathrm{PS}]_{A'}\,(2\pi)^4\delta^4(q+p_A-p_X-p_{A'})\Big|\mathcal{M}^{\gamma^* A \to XA'}\Big|^2. \tag{2.10}$$

In practice, it can be hard to measure the outgoing nucleus A'. For this reason, one usually considers quantities where the phase space of the nucleus A' has been integrated over. This leads to

$$\begin{aligned}\frac{\mathrm{d}\sigma^{\gamma^* A \to XA'}}{\mathrm{d}[\mathrm{PS}]_X} &= \frac{1}{2W^2}\frac{1}{2p_{A'}^-}(2\pi)\delta(q^+-p_X^+)\Big|\mathcal{M}^{\gamma^* A \to XA'}\Big|^2 \\ &= \frac{1}{(2W^2)^2}2q^+\delta(q^+-p_X^+)\Big|\mathcal{M}^{\gamma^* A \to XA'}\Big|^2\end{aligned} \tag{2.11}$$

where the corrections to this equation are of the order $\mathcal{O}\big(\frac{1}{W^2}\big)$. It is also customary to redefine the invariant amplitude such that the factor $1/(2W^2)$ is included in the amplitude. This will be discussed in more detail in Sec. 2.4.

2.3 Light-cone perturbation theory

Calculating the light-cone wave functions for the initial and final particles can be done in the so-called light-cone perturbation theory [40, 41] which is similar to canonical quantization in old-fashioned perturbation theory. The main idea is that the fields are quantized at equal light-cone times x^+ instead of the equal times t used in the standard formulation of the canonical quantization. This means that the fields satisfy commutation relations such as

$$\Big[\hat{\phi}(x^+, x^-, \mathbf{x}), \hat{\pi}(y^+ = x^+, y^-, \mathbf{y})\Big] = i\delta^2(\mathbf{x}-\mathbf{y})\delta(x^- - y^-) \tag{2.12}$$

in the case of a scalar field $\hat{\phi}(x)$ and its conjugate

$$\hat{\pi} = \frac{\partial\mathcal{L}}{\partial\big(\partial_+\hat{\phi}\big)}. \tag{2.13}$$

This is called the light-cone quantization of the fields. The role of the Hamiltonian in this quantization procedure is then given by the operator

$$\hat{P}^- = \int \mathrm{d}^2\mathbf{x}\,\mathrm{d}x^-\,\Big(\hat{\pi}\partial_+\hat{\phi} - \mathcal{L}\Big) \tag{2.14}$$

which corresponds to the minus component of the four-momentum. In general, this leads to a Hamiltonian that has a similar form as in equal-time quantization in the sense that we can divide the light-cone Hamiltonian $\hat{P}^- = \hat{P}_0^- + \hat{V}$ into the free-field part $\hat{P}_0^-$ and the interaction term $\hat{V}$. Perturbation theory is then done in the interaction picture where the free particles are eigenstates of the operator $\hat{P}_0^-$ with the on-shell condition $p^- = \frac{m^2 + \mathbf{p}^2}{2p^+}$. As a result of this quantization procedure, light-cone 3-momentum $(p^+, \mathbf{p})$ is conserved in the interactions whereas the minus component p^- is not[4]. Deriving perturbation theory then follows in a similar way to the old-fashioned perturbation theory. *A priori*, it is not clear that the physical results of light-cone quantization should then equal with the equal-time quantization, but considering the path integral formulation one can see that the quantization procedure should not have an effect on physical quantities.

While the results of light-cone perturbation theory agree with the equal-time quantization, the Feynman rules are quite different. First of all, light-cone perturbation theory is *time-ordered*. This means that Feynman diagrams with different time-orderings have to be calculated separately, which is more in line with the old-fashioned perturbation theory that was used in equal-time quantization until the 1960s [43]. Modern Feynman diagram calculations tend to calculate different time-ordered diagrams simultaneously using the covariant perturbation theory. Doing this for light-cone perturbation theory Feynman rules would result in the same covariant expressions, but this would defeat the advantages we get by light-cone quantization. For example, the time-ordering allows one to track the Fock states at each part of the process, and different parts of the process can also be combined using the light-cone wave functions. That being said, light-cone perturbation theory also has the major disadvantages of having to calculate much more Feynman diagrams for a single process and losing the explicit Lorentz invariance [44]. These are the main reasons why covariant perturbation theory is preferred in almost all calculations.

The main reason for doing light-cone perturbation theory in the high-energy limit is simple: as the interaction with the target is instantaneous in the light-cone time x^+, it is independent of the minus momenta p^-. The integrals over the minus components of the momenta in covariant perturbation theory can then be done using the residue theorem, with the different residues corresponding to the time-ordered Feynman diagrams in light-cone perturbation theory [45]. This leads to describing the initial and final states in terms of the light-cone wave functions as in Eq. (2.7). Thus, starting directly from light-cone perturbation theory one avoids the necessary step of using the residue theorem to calculate the integrals over the minus momenta.

To give the reader a concrete idea of light-cone perturbation theory, we provide a short derivation of the light-cone Feynman rules for calculating light-cone wave functions following Ref. [42]. To start, consider the following matrix element

$$\langle f(x_f^+)|i(x_i^+)\rangle = \langle f|U(x_f^+, x_i^+)|i\rangle \tag{2.15}$$

where the states are in the interaction picture and at the light-cone time x_0^+ they match the states in the Heisenberg picture: $\left|n(x_0^+)\right\rangle \equiv |n\rangle$. The time-evolution

---

[4]   For a more detailed analysis of the dynamics in the light cone the reader is referred to Ref. [42].

operator in the interaction picture for light-cone quantization is then given by

$$U(x_f^+, x_i^+) = e^{i\hat{P}_0^- x_f^+} e^{-i\hat{P}^-(x_f^+ - x_i^+)} e^{-i\hat{P}_0^- x_i^+}, \tag{2.16}$$

analogously to equal-time quantization. The light-cone Hamiltonian $\hat{P}^-$ has been divided into the free and interaction parts $\hat{P}^- = \hat{P}_0^- + \hat{V}$, and we write the free states as eigenstates of the free part of the Hamiltonian, $\hat{P}_0^- |n\rangle = p_n^- |n\rangle$. These states are normalized as

$$\langle n(p^+, \mathbf{p}) | n(k^+, \mathbf{k}) \rangle = 2p^+ (2\pi)^3 \delta(p^+ - k^+) \delta^2(\mathbf{p} - \mathbf{k}). \tag{2.17}$$

The separation of the Hamiltonian into free and interaction parts allows us to write

$$\langle f(x_f^+) | i(x_i^+) \rangle = e^{i p_f^- x_f^+ - i p_i^- x_i^+} \left\langle f \left| e^{-i\hat{P}^-(x_f^+ - x_i^+)} \right| i \right\rangle. \tag{2.18}$$

As $P^- \geq 0$ for all Fock states, the operator $\hat{P}^-$ is positive and we can use the residue theorem to rewrite

$$e^{-i\hat{P}^- \Delta x^+} = \int_{-\infty}^{\infty} \frac{d\epsilon}{2\pi} \frac{i}{\epsilon - \hat{P}^- + i\delta} e^{-i\epsilon \Delta x^+} \tag{2.19}$$

where $\delta > 0$ is an infinitesimal number taken to zero after the integration. Here we have assumed $\Delta x^+ > 0$; in the case $\Delta x^+ < 0$ we would have $\frac{-i}{\epsilon - \hat{P}^- - i\delta}$ instead.

We will then expand $\frac{1}{\epsilon - \hat{P}_0^- - \hat{V} + i\delta}$ as powers of $\hat{V}$ in order to do perturbation theory, which leads to the expression

$$\left\langle f \left| \frac{1}{\epsilon - \hat{P}^- + i\delta} \right| i \right\rangle = \left\langle f \left| \frac{1}{\epsilon - \hat{P}_0^- + i\delta} + \frac{1}{\epsilon - \hat{P}_0^- + i\delta} \hat{V} \frac{1}{\epsilon - \hat{P}_0^- + i\delta} + \dots \right| i \right\rangle$$

$$= \frac{1}{\epsilon - p_i^- + i\delta} \left\langle f \left| 1 + \frac{1}{\epsilon - \hat{P}_0^- + i\delta} \hat{V} + \dots \right| i \right\rangle. \tag{2.20}$$

The remaining operators $\frac{1}{\epsilon - \hat{P}_0^- + i\delta}$ can be written in terms of their spectral representation

$$\frac{1}{\epsilon - \hat{P}_0^- + i\delta} = \sum_n \int d[\mathrm{PS}]_n |n\rangle \frac{1}{\epsilon - p_n^- + i\delta} \langle n| \tag{2.21}$$

so that the original inner product becomes

$$\langle f(x_f^+) | i(x_i^+) \rangle = \int_{-\infty}^{\infty} \frac{d\epsilon}{2\pi} \frac{i}{\epsilon - p_i^- + i\delta} e^{i p_f^- x_f^+ - i p_i^- x_i^+} e^{-i\epsilon(x_f^+ - x_i^+)}$$

$$\times \left[\langle f | i \rangle + \frac{1}{\epsilon - p_f^- + i\delta} \langle f | \hat{V} | i \rangle \right.$$

$$\left. + \sum_n \int d[\mathrm{PS}]_n \frac{1}{\epsilon - p_f^- + i\delta} \langle f | \hat{V} | n \rangle \frac{1}{\epsilon - p_n^- + i\delta} \langle n | \hat{V} | i \rangle + \dots \right]. \tag{2.22}$$

At this point, we note that we are usually interested in inner products where $x_i^+ \to -\infty$. Using the identity

$$\lim_{T \to \infty} \frac{e^{-iTp}}{p + i\delta} = -2i\pi\delta(p) \tag{2.23}$$

we can write

$$\langle f(x_f^+) | i(-\infty) \rangle = e^{i(p_f^- - p_i^-)x_f^+}$$

$$\times \left[\langle f|i \rangle + \frac{1}{p_i^- - p_f^- + i\delta} \langle f|\hat{V}|i \rangle + \ldots \right] \tag{2.24}$$

$$\equiv e^{i(p_f^- - p_i^-)x_f^+} \left[\langle f|i \rangle + 2p_i^+(2\pi)^3\delta(p_f^+ - p_i^+)\delta^2(\mathbf{p}_f - \mathbf{p}_i)\Psi^{i \to f} \right]$$

where

$$2p_i^+(2\pi)^3\delta(p_f^+ - p_i^+)\delta^2(\mathbf{p}_f - \mathbf{p}_i)\Psi^{i \to f}$$

$$= \frac{1}{p_i^- - p_f^- + i\delta} \left[\langle f|\hat{V}|i \rangle + \sum_n \int \mathrm{d}[\mathrm{PS}]_n \langle f|\hat{V}|n \rangle \frac{1}{p_i^- - p_n^- + i\delta} \langle n|\hat{V}|i \rangle + \ldots \right] \tag{2.25}$$

and $\Psi^{i \to f}$ is the light-cone wave function for the process $i \to f$. Note that we leave the non-interacting case $\langle f|i \rangle$ out of the definition of the wave function. The delta functions come from the conservation of the light-cone 3-momentum $(p^+, \mathbf{p})$, and by definition they are not part of the light-cone wave function $\Psi^{i \to f}$.

As a side note, when calculating elements of the scattering matrix we also take the final state to be asymptotic so that $x_f^+ = +\infty$. Using the identity (2.23) again, this leads to

$$\langle f|\hat{S}|i \rangle = \langle f(+\infty)|i(-\infty) \rangle = \langle f|i \rangle$$

$$+ 2\pi i\delta(p_i^- - p_f^-) \left[\langle f|\hat{V}|i \rangle + \sum_n \int \mathrm{d}[\mathrm{PS}]_n \langle f|\hat{V}|n \rangle \frac{1}{p_i^- - p_n^- + i\delta} \langle n|\hat{V}|i \rangle + \ldots \right]$$

$$\equiv \langle f|i \rangle + (2\pi)^4\delta^4(p_i - p_f)i\mathcal{M}^{i \to f} \tag{2.26}$$

where $\hat{S} = \hat{1} + i\hat{T}$ is the S-matrix and $\mathcal{M}^{i \to f}$ is the scattering amplitude for the process $i \to f$.

From this derivation of the light-cone perturbation theory we can read the corresponding Feynman rules. There are some minor variations of the rules corresponding to a different metric and normalization of the light-cone wave function in the literature [41, 42, 45, 46]. With the conventions of this work, we end up with the following set of rules:

1. Draw all of the possible x^+-ordered Feynman diagrams corresponding to the process $i \to f$.

2. Assign an on-shell momentum for each line from left to right such that the light-cone 3-momentum $(p^+, \mathbf{p})$ is conserved.

3. For each vertex, assign a matrix element

$$\langle \text{out}|\hat{V}|\text{in}\rangle = (2\pi)^3 \delta(p_{\text{out}}^+ - p_{\text{in}}^+)\delta^2(\mathbf{p}_{\text{out}} - \mathbf{p}_{\text{in}})\Gamma^{\text{in}\to\text{out}} \tag{2.27}$$

where p_{in} is the sum of momenta flowing into the vertex and p_{out} out of the vertex, and $\Gamma^{\text{in}\to\text{out}}$ is the Feynman rule for the vertex.

4. For each intermediate state, assign an energy denominator

$$\frac{1}{p_i^- - p_{\text{intermediate}}^- + i\delta} \tag{2.28}$$

where p_i^- is the sum of minus components for the initial state and $p_{\text{intermediate}}^-$ for the intermediate state. The final state is considered to be an intermediate state.

5. For each internal line, i.e. lines that are not part of the initial or final state, sum over the helicities and integrate over the momenta p with the phase factors $\mathrm{d}\widetilde{p}$ from Eq. (2.9).

6. Include the required symmetry factors for identical particles and the additional factor (-1) for fermion loops and fermion lines beginning and ending in the initial state.

This gives us the expression $2p_i^+(2\pi)^3\delta(p_i^+ - p_f^+)\delta^2(\mathbf{p}_i - \mathbf{p}_f)\Psi^{i\to f}$ from which one can read the light-cone wave function. Scattering amplitudes are calculated analogously: leaving out the energy denominator for the final state in Rule 4 and setting $p_f^- = p_i^-$, one gets the expression $(2\pi)^3\delta(p_i^+ - p_f^+)\delta^2(\mathbf{p}_i - \mathbf{p}_f)\mathcal{M}^{i\to f}$.

The vertices $\Gamma^{\text{in}\to\text{out}}$ for QCD are listed in Refs. [45, 46]. This also includes *instantaneous interactions* which can be thought of as additional 4-point interactions between quarks and gluons that appear in the light-cone quantization. These Feynman rules use the light-cone gauge for gluons,

$$A^+ = 0, \tag{2.29}$$

which is a convenient gauge in light-cone perturbation theory. One advantage of this gauge is that it decouples the ghosts from the other particles, meaning that the ghosts can be integrated out trivially.

These rules for calculating the light-cone wave function assume that the initial state is asymptotic at $x_i^+ = -\infty$ and the final state is not an observed state but rather a state that will take part in further scattering processes, such as the interaction with the target in Eq. (2.7). These are the standard light-cone wave functions that are usually considered and we will denote them by Ψ_{in} to emphasize that they correspond to the asymptotic *incoming* particle. In practice, we also need the wave function for the actual observed outgoing state at $x_f^+ = +\infty$, in which case the initial state is not asymptotic but instead a part of a scattering process. To calculate this final-state wave function corresponding to the matrix element $\langle i(x_i^+)|f(+\infty)\rangle$, we note that we can repeat our previous derivation for the incoming-state wave function

such that the only difference is in Eq. (2.19) where the sign of $i\delta$ is now different. This leads to

$$
\begin{aligned}
\langle i(x_i^+)|f(+\infty)\rangle =& e^{i(p_i^- - p_f^-)x_i^+} \\
& \times \left[\langle i|f\rangle + \frac{1}{p_f^- - p_i^- - i\delta}\, \langle i|\hat{V}|f\rangle + \dots \right] \\
\equiv& e^{i(p_i^- - p_f^-)x_i^+} \left[\langle i|f\rangle + 2p_f^+(2\pi)^3\delta(p_f^+ - p_i^+)\delta^2(\mathbf{p}_f - \mathbf{p}_i)\Psi_{\text{out}}^{f\to i} \right]
\end{aligned}
\tag{2.30}
$$

where

$$
\begin{aligned}
& 2p_f^+(2\pi)^3\delta(p_f^+ - p_i^+)\delta^2(\mathbf{p}_f - \mathbf{p}_i)\Psi_{\text{out}}^{f\to i} \\
& = \frac{1}{p_f^- - p_i^- - i\delta}\left[\langle i|\hat{V}|f\rangle + \sum_n \int \mathrm{d}[\text{PS}]_n\, \langle i|\hat{V}|n\rangle\, \frac{1}{p_f^- - p_i^- - i\delta}\, \langle f|\hat{V}|i\rangle + \dots \right].
\end{aligned}
\tag{2.31}
$$

From this one can read the Feynman rules for calculating the outgoing-state wave function $\Psi_{\text{out}}^{f\to i}$. The only difference to the incoming state is in Rule 4 where we have now $-i\delta$ instead of $+i\delta$. The wave function for the matrix element $\langle f(+\infty)|i(x_i^+)\rangle$ is then given by the complex conjugate $\left(\Psi_{\text{out}}^{f\to i}\right)^*$.

One modification of the above rules concerns self-energy corrections to the asymptotic state. The LSZ reduction formula states that the self-energy corrections should be amputated from the light-cone wave function, and instead they introduce factors $\sqrt{Z_n}$ for the asymptotic state [40]. This means that the asymptotic state can be written as, in the case of the incoming state,

$$
|i(-\infty)\rangle = \sqrt{Z_i}\left[|i\rangle + \sum_n \int \mathrm{d}[\text{PS}]_n\, 2p_i^+(2\pi)^3\delta(p_i^+ - p_n^+)\delta(\mathbf{p}_i - \mathbf{p}_n)\Psi_{\text{in}}^{i\to n}\, |n\rangle \right].
\tag{2.32}
$$

Similar factors appear for the outgoing state.

Finally, we would like to mention that there are several different normalization conventions for the light-cone wave functions which correspond to different phase space integration measures. In this thesis, we use the conventions of Eqs. (2.8) and (2.9). These differ from Articles [I, II, III, IV] which follow the notation from Ref. [47]. There the integration measure for the plus momenta was defined as $\frac{\mathrm{d}z_i}{4\pi}$ instead of $\frac{\mathrm{d}z_i}{4\pi z_i} = \frac{\mathrm{d}k_i^+}{4\pi k_i^+}$, where $z_i = k_i^+/q^+$ are the plus-momentum fractions of the particles. This introduces an additional factor $\prod_{i\in n}\frac{1}{\sqrt{z_i}}$ into the wave functions.

2.4 Eikonal approximation

The high-energy limit can be used to also simplify the interaction with the target. To understand this, consider a quark-quark scattering process where the "probe" quark has a momentum q and the "target" quark has a momentum P as shown in
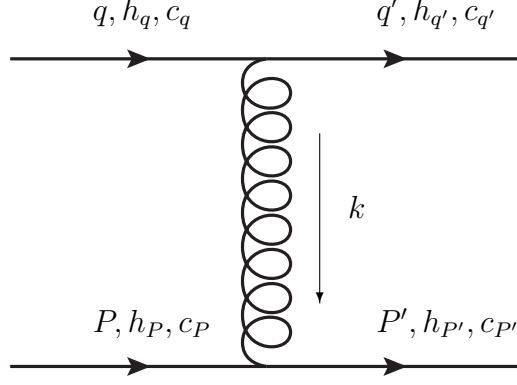
FIGURE 2.5 t-channel for the quark-quark scattering.

Fig. 2.5[5]. The two quarks collide with a high longitudinal momentum such that the center-of-mass energy $s = (q + P)^2 \approx 2q^+ P^- \gg m_q^2, m_P^2, \mathbf{q}^2, \mathbf{P}^2$ is large. This also means that the interaction happens mainly through the t-channel in Fig. 2.5 as the s-channel is suppressed by $1/s$. Demanding that the initial and final particles are on-shell one can show that the plus and minus momentum exchange is small compared to the transverse momentum exchange:

$$k^+ = (q - q')^+ = (P' - P)^+ \approx \frac{q^+}{s}(\mathbf{k}^2 + 2\mathbf{k} \cdot \mathbf{P}),$$
$$k^- = (q - q')^- = (P' - P)^- \approx \frac{P^-}{s}(-\mathbf{k}^2 + 2\mathbf{k} \cdot \mathbf{q}). \tag{2.33}$$

We can then assume that $q'^+ = q^+$ and $P'^- = P^-$ as the corrections are suppressed by $\mathbf{k}^2/s \ll 1$.

Using the Feynman rules from covariant perturbation theory, the scattering amplitude is given by

$$i\mathcal{M} = g_s^2 t_{c_{q'} c_q}^a t_{h_P h_{P'}}^a \frac{1}{\mathbf{k}^2} \bar{u}_{h'_q}(q') \gamma^\mu u_{h_q}(q) \bar{u}_{h'_P}(P') \gamma^\nu u_{h_P}(P) D_{\mu\nu}(k) \tag{2.34}$$

where $D_{\mu\nu}(k)$ is the gluon propagator. To stay consistent with the rest of this thesis, we consider the gluon propagator in the light-cone gauge where

$$D^{\mu\nu}(k) = g^{\mu\nu} - \frac{n^\mu k^\nu + n^\nu k^\mu}{n \cdot k} = -\begin{pmatrix} 0 & 0 & 0 & 0 \\ 0 & 2\frac{k^-}{k^+} & \frac{k^1}{k^+} & \frac{k^2}{k^+} \\ 0 & \frac{k^1}{k^+} & 1 & 0 \\ 0 & \frac{k^2}{k^+} & 0 & 1 \end{pmatrix} \tag{2.35}$$

with $n^\mu = \delta^{\mu-}$.

To calculate the scattering amplitude (2.34) we also need to specify a basis for the spinors. It turns out that in light-cone perturbation theory calculations

---

5   This example can be found in Ref. [45]. However, we do not assume that the individual components q^+ and P^- are large as we wish to present a boost-invariant motivation for the eikonal approximation. We also allow for non-zero transverse components $\mathbf{q}$ and $\mathbf{P}$ which is generally the case if one considers multiple gluon exchanges.

it is convenient to use a basis where quantities are boost invariant, and with this motivation in mind we choose to use Lepage–Brodsky basis [48]:

$$u_+(\vec{k}) = \frac{1}{\sqrt{2(E+k^3)}} \begin{pmatrix} E+k^3+m \\ k_R \\ E+k^3-m \\ k_R \end{pmatrix} \qquad u_-(\vec{k}) = \frac{1}{\sqrt{2(E+k^3)}} \begin{pmatrix} -k_L \\ E+k^3+m \\ k_L \\ -(E+k^3-m) \end{pmatrix}$$

$$v_+(\vec{k}) = \frac{1}{\sqrt{2(E+k^3)}} \begin{pmatrix} -k_L \\ E+k^3-m \\ k_L \\ -(E+k^3+m) \end{pmatrix} \qquad v_-(\vec{k}) = \frac{1}{\sqrt{2(E+k^3)}} \begin{pmatrix} E+k^3-m \\ k_R \\ E+k^3+m \\ k_R \end{pmatrix}$$

(2.36)

where $k_L = k^1 - ik^2 = |\mathbf{k}|e^{-i\varphi_\mathbf{k}}$ and $k_R = k^1 + ik^2 = |\mathbf{k}|e^{i\varphi_\mathbf{k}}$. Longitudinal boosts on these spinors do not mix the helicity states but only change the momenta so that

$$S(\Lambda)u_h(\vec{k}) = u_h(\Lambda\vec{k}) \tag{2.37}$$

where $S(\Lambda)$ is the action of the longitudinal boost Λ in the spinor representation of the Lorentz group. This is the main reason why this basis is ubiquitously used in the light-cone formalism. The spinors (2.36) are also the eigenstates of the so-called *light-cone helicity* which corresponds to the helicity in the "infinite-momentum frame" [49].

With the basis (2.36) one can find the following scaling relations for the spinor elements:

$$\begin{aligned} \bar{u}(q')\gamma^+ u(q) &\sim q^+ \\ \bar{u}(q')\gamma^- u(q) &\sim q^- \\ \bar{u}(q')\gamma^i u(q) &\sim \mathbf{q}^i \end{aligned} \tag{2.38}$$

and similarly for $\bar{u}(P')\gamma^\nu u(P)$. This allows us to find the dominating terms in the high-energy limit so that Eq. (2.33) becomes

$$i\mathcal{M} \approx -g_s^2 t^a_{c_{q'}c_q} t^a_{h_P h_{P'}} \frac{1}{\mathbf{k}^2} \bar{u}_{h'_q}(q')\gamma^+ u_{h_q}(q) \bar{u}_{h'_P}(P')\gamma^i u_{h_P}(P) D^{-i}(k) \tag{2.39}$$

where the other terms are suppressed by $1/s$. Explicitly evaluating the terms remaining terms this leads to[6]

$$i\mathcal{M} = 2s\delta_{h_q h'_q}\delta_{h_P h'_P} g_s^2 t^a_{c_{q'}c_q} t^a_{h_P h_{P'}} \frac{1}{\mathbf{k}^2}. \tag{2.40}$$

We can now read several things from this expression for the scattering amplitude that apply very generally to particle scattering in the high-energy limit:

1. The invariant amplitude is proportional to the center-of-mass energy s.

2. The helicities of the target and the probe are conserved.

---

[6] Strictly speaking, for the "target" one has to use a different basis of spinors so that the sign of k^3 in Eq. (2.36) is swapped. This is allowed as one can use different spinors bases for different spinors in the process.

3. The momentum transfer is dominated by the transverse component of the 4-momentum. From Eq. (2.33) we see especially that the plus momentum of the probe is conserved up to corrections in $1/s$, i.e. $q^+ \approx q'^+$.

4. The invariant amplitude depends only on the transverse momentum exchange $\mathbf{k}^2$.

In practice, the interaction with the target is not this simple. However, the properties noted above are quite general, and it can be shown that they are also satisfied for gluon targets. These properties then form the basis of the *eikonal approximation*[7] in the high-energy limit which states that the interaction with the target can be written as

$$i\mathcal{M}^{n+A \to n'+A'} \approx 2s \times 2p_n^+ (2\pi)\delta(p_n^+ - p_n'^+)\delta_{h_n h_n'}\delta_{h_A h_A'} S(\mathbf{k}) \tag{2.41}$$

where n can be a quark, an antiquark or a gluon, and $S(\mathbf{k})$ is a color matrix that depends only on the transverse momentum transfer $\mathbf{k} = \mathbf{p}_n' - \mathbf{p}_n$. The fact that $S(\mathbf{k})$ depends only on the momentum transfer and not on the individual momenta $\mathbf{p}_n$ and $\mathbf{p}_n'$ suggests that we should take a Fourier transform in the transverse plane. Writing

$$\int \frac{d^2\mathbf{p}_n \, d^2\mathbf{p}_n'}{(2\pi)^4} e^{i\mathbf{p}_n \cdot \mathbf{x}_n} e^{-i\mathbf{p}_n' \cdot \mathbf{x}_n'} S(\mathbf{k}) = \delta^2(\mathbf{x}_n - \mathbf{x}_n') \int \frac{d^2\mathbf{k}}{(2\pi)^2} e^{-i\mathbf{k}\cdot\mathbf{x}_n} S(\mathbf{k}) \tag{2.42}$$

we see that in the position space the transverse coordinates do not change during the interaction. This can be understood by noting that the interaction with the target is instantaneous and thus the change in the transverse coordinate has to be very small.

Combining the eikonal approximation (2.41) with the factorization in Eq. (2.7), we can write the invariant amplitude as

$$i\mathcal{M}^{\gamma^* A \to X A'} = \sum_n \int d[\widetilde{\text{PS}}]_n \, 2q^+(2\pi)\delta(q^+ - p_X^+) e^{-i\mathbf{b}_n \cdot \mathbf{\Delta}} \widetilde{\Psi}_{\text{in}}^{\gamma^* \to n} \left(\widetilde{\Psi}_{\text{out}}^{X \to n}\right)^* \left(1 - S_A^{(n)}(\mathbf{x}_i)\right) \tag{2.43}$$

where $\widetilde{\Psi}$ denotes the Fourier transform of the light-cone wave function, $S_A^{(n)}(\mathbf{x}_i)$ the eikonal approximation for the interaction of the Fock state n with the target A, and the integration measure in the mixed space is given by

$$d[\widetilde{\text{PS}}]_n = \prod_{i \in n} \left(d^2\mathbf{x}_i \frac{dk_i^+}{(2\pi)2k_i^+}\right). \tag{2.44}$$

---

7 Similarly to diffraction, the term "eikonal" also has its origin in optics. From Greek εἰκών ("image"), the eikonal approximation refers to the assumption that light encountering an object travels in a straight line, forming the "image" of the object. This is generally valid as long as the wavelength of the light is much smaller than the object, and an analogous thing is true in high-energy physics: a photon with a "wavelength" $x_\gamma^- \sim 1/q^+$ much smaller than the size of the target $x_A^- \sim 1/P_N^+ = 2P_N^-/m_N^2$ scatters eikonally.

The Fourier-transformed wave functions are defined by

$$
e^{i\mathbf{b}_n \cdot \sum_{i \in n} \mathbf{p}_i} \widetilde{\Psi}^{n \to m}(\mathbf{p}_i, z_{in}; \mathbf{x}_i, z_{im})
$$

$$
= \int \prod_{i \in m} \left(\frac{\mathrm{d}^2 \mathbf{k}_i}{(2\pi)^2} \right) (2\pi)^2 \delta^2 \left(\sum_{i \in m} \mathbf{k}_i - \sum_{i \in n} \mathbf{p}_i \right) e^{\sum_{i \in m} i\mathbf{k}_i \cdot \mathbf{x}_i} \Psi^{n \to m}(\mathbf{p}_i, z_{in}; \mathbf{k}_i, z_{im})
$$

$$(2.45)$$

where $\mathbf{b}_n = \sum_{i \in m} z_{im} \mathbf{x}_i$ is the impact parameter. Here we have denoted the momenta for the state n by $\mathbf{p}_i$ and $\mathbf{p}_i^+ = z_{in} q^+$, and for the state m by $\mathbf{k}_i$ and $\mathbf{k}_i^+ = z_{im} q^+$. Using the momentum fractions z instead of the plus momenta p^+ makes the boost invariance of the wave functions more explicit. It should be noted that this mixed space of coordinates $(\mathbf{x}_i, z_i)$ is very convenient for the eikonal approximation as these do not change during the interaction with the target. Also, here we have taken the factor $e^{-i\mathbf{b} \cdot \sum \mathbf{p}_i}$ out from the Fourier-transformed wave function as it turns out that with this definition the wave function $\widetilde{\Psi}$ depends only on the dipole sizes $\mathbf{x}_{ij} = \mathbf{x}_i - \mathbf{x}_j$ and the relative momenta $\mathbf{P}_{ij} \equiv z_{jn}\mathbf{p}_i - z_{in}\mathbf{p}_j$ but not on the impact parameter $\mathbf{b}$ or the total transverse momentum $\sum_i \mathbf{p}_i$. This makes the dependence on the transverse momentum transfer $\boldsymbol{\Delta} = \sum_{i \in X} \mathbf{p}_i$ in Eq. (2.43) explicit, and thus the dependence on the Mandelstam variable $t \approx -\boldsymbol{\Delta}^2$ is simple to calculate.

We have also rescaled the amplitude by the common factor $2s = 2W^2$ in Eq. (2.41). With the rescaled invariant amplitude from Eq. (2.43), the cross section now reads

$$
\frac{\mathrm{d}\sigma^{\gamma^* A \to XA'}}{\mathrm{d}[\mathrm{PS}]_X} = 2q^+ (2\pi)\delta(q^+ - p_X^+) \left| \mathcal{M}^{\gamma^* A \to XA'} \right|^2.
$$

$$(2.46)$$

Eqs. (2.43) and (2.46) hold in general in the high-energy limit, with the possible modification that in Eq. (2.43) we left out the non-interaction matrix element $\langle n | X \rangle$ for the case $X = n$ out for simplicity (see Eq. (2.30)). These equations will be used to calculate exclusive vector meson production in Ch. 4 and inclusive diffraction in DIS in Ch. 5.

3 DIPOLE-TARGET SCATTERING AMPLITUDE

To calculate any production amplitude for the process $\gamma^* + A \to X + A'$ in the dipole picture one still needs to understand the nonperturbative interaction with the target. At leading order, this interaction happens with the quark-antiquark dipole and the target, and it is described by the dipole-target scattering amplitude or the *dipole amplitude* for short. It turns out that interactions with even higher-order Fock states consisting of quarks and gluons can be given in terms of the dipole amplitude at certain limits, which will be discussed in Sec. 3.2 in more detail. Thus, a thorough understanding of the dipole amplitude is important for an accurate description of processes in the dipole picture.

3.1 Target as a classical color field

While the eikonal limit (2.41) significantly simplifies the interaction with the target, it is too general to give an actual model for the dipole amplitude. For this we need to consider the actual physical situation of the scattering and take input from QCD. The main idea is that at high energies the gluon distribution starts to dominate in the target and we can thus neglect the quark contribution. The second idea is to note that when the target is moving at a high velocity, it gets Lorentz-contracted such that the gluon field density μ^2 is very high, $\mu^2 \gg \Lambda_{\text{QCD}}^2$. This means that one is generally in the weak-coupling region $\alpha_s(\mu^2) \ll 1$ which allows us to treat the gluons as classical color fields. This is the basic starting point in the McLerran–Venugopalan model for high-energy scattering [50–52]. We can then model the target as a color field A_{cl} that is solved from the classical Yang-Mills equation

$$[D_\mu, F_{\text{cl}}^{\mu\nu}] = J^\nu \tag{3.1}$$

where $D_\mu = \partial_\mu - igA_\mu^{\text{cl}}$ is the covariant derivative, $F_{\text{cl}}^{\mu\nu} = [D^\mu, D^\nu]$ is the field strength tensor and $J^\nu(x)$ is the color current. As the target is moving in the minus direction

with a large momentum, we can model the current as

$$J^\nu(x) = \delta^{-\nu}\rho(x^+, \mathbf{x}) \tag{3.2}$$

so that only the minus component of the current is relevant. Here $\rho(x^+, \mathbf{x}) = t^a\rho^a(x^+, \mathbf{x})$ is the color charge density of the target, and the high-energy limit ensures that it is independent of the coordinate x^- and sharply peaked for the time of the interaction in x^+. These assumptions allow us to solve the field $A_{\rm cl}^\mu$ from Eq. (3.1), with the solution

$$\boldsymbol{\nabla}^2 A_{\rm cl}^-(x^+, \mathbf{x}) = -\rho(x^+, \mathbf{x})$$
$$A_{\rm cl}^+(x^+, \mathbf{x}) = A_{\rm cl}^i(x^+, \mathbf{x}) = 0 \tag{3.3}$$

in the light-cone gauge $A^+ = 0$. We note that this solution is not unique as there is still some gauge freedom left. Often it is more convenient to write a solution such that only the more physical transverse components of the gluon field remain, as the minus component A^- is not actually a dynamical field but a boundary condition for the gluon field [51]. However, for the purpose of this section it is simpler to work with the solution in Eq. (3.3).

The solution (3.3) for the target color field allows us to calculate the interaction with the target. This is done with the equations of motion in the background field $A_{\rm cl}$. For a quark field ψ this is given by

$$(i\slashed{D} - m)\psi = 0. \tag{3.4}$$

Note that the high-energy limit guarantees that during the interaction with the target the coordinates $(x^-, \mathbf{x})$ are roughly constant, and we are only interested in the change in the plus direction. Neglecting the other derivative terms and also the mass of the quark, this leads to the equation

$$\gamma^+\partial_+\psi = igA_{\rm cl}^-\gamma^+\psi. \tag{3.5}$$

The solution for this equation is given in terms of a Wilson line

$$\psi(x_f^+, \mathbf{x}) = V(x_f^+, x_i^+, \mathbf{x})\psi(x_i^+, \mathbf{x}), \tag{3.6}$$

$$V(x_f^+, x_i^+, \mathbf{x}) = \mathcal{P}\exp\left(ig\int_{x_i^+}^{x_f^+} \mathrm{d}y^+ \, A_{\rm cl}^{a-}(y^+, \mathbf{x})t^a\right) \tag{3.7}$$

where $\mathcal{P}$ denotes path-ordering for the integral and t^a are the color matrices in the fundamental representation. Similarly, for conjugate fields $\overline{\psi}$ one gets the Hermitean conjugate $V^\dagger(x_f^+, x_i^+\mathbf{x})$, and for gluon fields an adjoint Wilson line

$$U(x_f^+, x_i^+, \mathbf{x}) = \mathcal{P}\exp\left(ig\int_{x_i^+}^{x_f^+} \mathrm{d}y^+ \, A_{\rm cl}^{a-}(y^+, \mathbf{x})T^a\right) \tag{3.8}$$

where the color matrices T^a are now in the adjoint representation.

The connection to the dipole amplitude is that the eikonal interaction between a quark-antiquark pair and the target is given in terms of the Wilson lines as

$$\langle q_a(x_f^+, \mathbf{x}_0')\bar{q}_b(x_f^+, \mathbf{x}_1')|\hat{S}_A|q_c(x_i^+, \mathbf{x}_0)\bar{q}_d(x_i^+, \mathbf{x}_1)\rangle$$
$$= \delta^2(\mathbf{x}_0' - \mathbf{x}_0)\delta^2(\mathbf{x}_1' - \mathbf{x}_1)V_{ac}(x_f^+, x_i^+, \mathbf{x}_0)V_{db}^\dagger(x_f^+, x_i^+, \mathbf{x}_1) \tag{3.9}$$

where the subscripts refer to the color indices of the particles. This means that the particles only get color-rotated during the interaction with the target. In diffractive scattering the initial and final states are color singlets, so that in total the expression for the dipole amplitude leads to

$$
\frac{\delta^{ab}}{\sqrt{N_c}} \frac{\delta^{cd}}{\sqrt{N_c}} \langle q_a(\mathbf{x}_0')\bar{q}_b(\mathbf{x}_1')|1 - \hat{S}_A|q_c(\mathbf{x}_0)\bar{q}_d(\mathbf{x}_1)\rangle
$$
$$
= \delta^2(\mathbf{x}_0 - \mathbf{x}_0')\delta^2(\mathbf{x}_1 - \mathbf{x}_1')\left\{1 - \frac{1}{N_c}\mathrm{Tr}\big[V(\mathbf{x}_0)V^\dagger(\mathbf{x}_1)\big]\right\}. \tag{3.10}
$$

Here we have also taken $x_f^+ \to +\infty$, $x_i^+ \to -\infty$ as the dependence of the Wilson lines on the light-cone times x_f^+, x_i^+ is very slow, arising from the fact that $A_{\mathrm{cl}}^-(x^+)$ is highly suppressed for times $x^+ \neq 0$. A similar equation can be derived for any Fock state interacting with the target.

Using Eq. (3.10) still requires that we know the target color density ρ to solve for the field A_{cl}. This is, however, a nonperturbative quantity and needs to be modeled. One very successful model is the Gaussian approximation [50–52] which assumes that the target is a linear combination of all possible color configurations with a Gaussian weight. This corresponds to taking an average of expressions like Eq. (3.10) with

$$
\left\langle 1 - \frac{1}{N_c}\mathrm{Tr}\big[V(\mathbf{x}_0)V^\dagger(\mathbf{x}_1)\big]\right\rangle = \int \mathcal{D}\rho\,\mathcal{W}[\rho]\left\{1 - \frac{1}{N_c}\mathrm{Tr}\big[V(\mathbf{x}_0)V^\dagger(\mathbf{x}_1)\big]\right\} \tag{3.11}
$$

where

$$
\mathcal{W}[\rho] = \exp\left(-\int_{-\infty}^{\infty}\mathrm{d}x^+\int\mathrm{d}^2\mathbf{x}\,\frac{\mathrm{Tr}[\rho(x^+,\mathbf{x})^2]}{\mu^2(x^+,\mathbf{x})}\right) \tag{3.12}
$$

is the weight for the color density ρ, and μ^2 is the average color charge squared per unit volume in $\mathrm{d}x^+\,\mathrm{d}^2\mathbf{x}$ and unit color. The motivation for such a model is the central limit theorem which states that averages from probability distributions with a finite variance tend to a Gaussian distribution. It is also useful to note that the Gaussian approximation leads to the following correlator for the color densities ρ:

$$
\langle \rho^a(x^+,\mathbf{x})\rho^b(y^+,\mathbf{y})\rangle = \delta^{ab}\mu^2(x^+,\mathbf{x})\delta(x^+ - y^+)\delta^2(\mathbf{x} - \mathbf{y}). \tag{3.13}
$$

This states that the color densities at different light-cone times and transverse coordinates are not correlated, which is a natural assumption if one considers the target as a collection of point-like color charges.

With the Gaussian approximation Eq. (3.12), the path integral in Eq. (3.11) can be evaluated to give the dipole amplitude an expression in terms of the density $\mu^2(x^+,\mathbf{x})$. Assuming that the density $\mu^2(x^+,\mathbf{x})$ varies very slowly in terms of the transverse coordinate $\mathbf{x}$, this can be written as [53]

$$
N_{01} \equiv \left\langle 1 - \frac{1}{N_c}\mathrm{Tr}\big[V(\mathbf{x}_0)V^\dagger(\mathbf{x}_1)\big]\right\rangle \approx 1 - \exp\left(-\frac{\mathbf{x}_{01}^2 Q_s^2}{4}\ln\frac{1}{\Lambda^2\mathbf{x}_{01}^2}\right). \tag{3.14}
$$

Here Λ is an infrared regulator and $Q_s^2 = \alpha_s C_F \int \mathrm{d}x^+ \mu^2(x^+,\mathbf{b}')$ is the so-called *saturation scale*. The variable $\mathbf{b}' = \frac{1}{2}(\mathbf{x}_0 + \mathbf{x}_1)$ is the average of the quark and

antiquark coordinates, and hence the saturation scale depends on the transverse density profile of the target. This also means that the saturation scale is enhanced by the mass number of the target, as the density has only a slight dependence on the mass number but the radius behaves like $R \sim A^{1/3}$. This suggests that the saturation scale is enhanced by $Q_s^2 \sim A^{1/3}$ for heavy nuclei.

Several things can be noted from the form of the dipole amplitude (3.14). For small dipole sizes $\mathbf{x}_{01}^2$ the dipole amplitude behaves like $N_{01} \approx \frac{1}{4}\mathbf{x}_{01}^2 Q_s^2$, but for large dipoles the saturation scale tames the growth to the *black-disk limit* $N_{01} \to 1$. This behavior is important for the unitarity of the process: if the black-disk limit were violated, the unitarity of the S-matrix would be broken [53]. It is also useful to note that the dipole amplitude from the MV model satisfies the form of the eikonal approximation in Eq. (2.41): it depends only on the transverse coordinates and color indices of the scattering particles, and the mixed-space coordinates $(\mathbf{x}_i, z_i)$ and the helicities are conserved in the interaction.

3.2 High-energy evolution of the dipole amplitude

So far, the dependence on the center-of-mass energy W^2 has actually dropped out of Eqs. (2.43) and (2.46). This is a little bit puzzling, as generally cross sections tend to increase with energy. It turns out that indeed the dipole amplitude should have an energy dependence, and this will be important for higher-order equations to be finite. This energy dependence is related to the larger phase space available for gluon emission. This can be seen explicitly in next-to-leading order calculations where the emission of slow gluons with $z_g \ll 1$ starts to dominate. Resumming these gluon emissions leads to the JIMWLK equation for the energy dependence of the dipole amplitude.

The JIMWLK equation can be derived by considering the weight $\mathcal{W}[\rho]$ of the target's color configuration at some rapidity Y which is related to the energy of the system, $W^2 \sim e^Y$. Considering then a Fock state n interacting with the target, we can write the interaction using Eq. (3.11) as

$$\langle \hat{\mathcal{O}} \rangle = \int \mathcal{D}\rho \, \mathcal{W}[\rho] \, \mathcal{O}[\rho] \tag{3.15}$$

where the operator $\hat{\mathcal{O}}$ consists of the Wilson lines for the interacting Fock state n. The Fock state n may emit gluons with a momentum fraction z_g. It turns out that the gluon emission is enhanced by $1/z_g$ for gluons with a small momentum fraction, with the integral over z_g diverging at $z_g \to 0$. However, at small z_g the assumptions for the validity of the eikonal approximation break down as at some point the invariant mass of this $n + g$ state becomes comparable with the energy:

$$M_{n+g}^2 \approx \frac{\mathbf{k}_g^2}{z_g} \gtrsim W^2. \tag{3.16}$$

We should then limit the z_g-integral by some cut-off $z_{\min} \sim 1/W^2 \sim e^{-Y}$ so that we
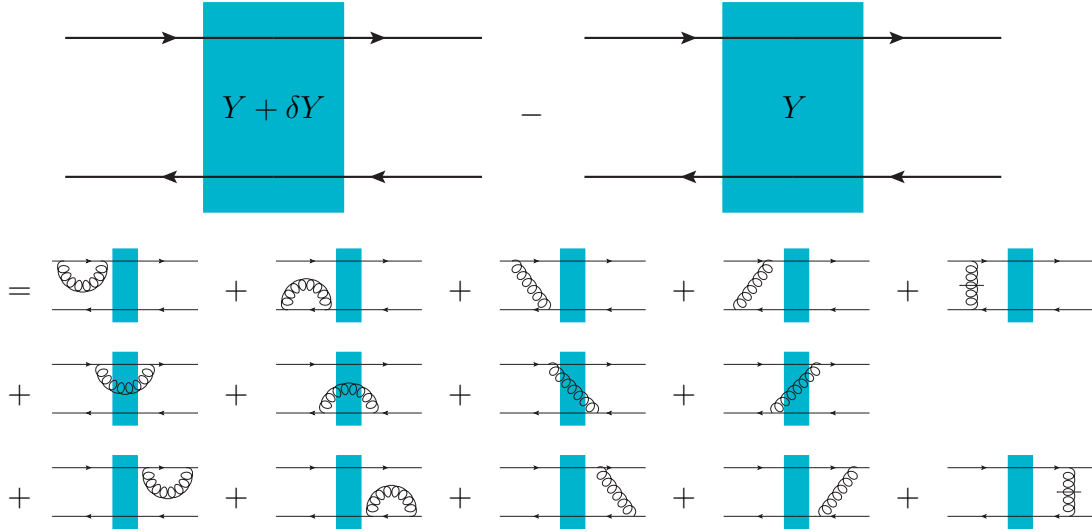
FIGURE 3.1   JIMWLK equation for a quark-antiquark dipole shown schematically in terms of the Feynman diagrams involving a slow gluon with $z_g \ll 1$. Here $Y + \delta Y$ and Y refer to the rapidity at which the target probed.

are only working in a region where the eikonal approximation is valid. The idea is that the slow gluons with $z_g < z_{\min}$ are then defined as a part of the target.

Demanding that the physical cross sections do not depend on the exact value of the cut-off $z_{\min}$ means that the weight $\mathcal{W}[\rho]$ has to have a dependence on the cut-off and thus also on the rapidity Y. This rapidity dependence can be calculated perturbatively by considering the difference between $\mathcal{W}[\rho]$ at rapidities Y and $Y + \delta Y$ where δY is small. For a quark-antiquark pair this then leads to an equation like shown in Fig. 3.1, but this can be generalized to more general Fock states. Taking $\delta Y \to 0$ one ends up with the JIMWLK equation [29–35]

$$\partial_Y \mathcal{W}_Y[\alpha] = -\mathcal{H}_{\mathrm{JIMWLK}} \mathcal{W}_Y[\alpha] \tag{3.17}$$

where the color field has been written in terms of $\partial^2 \alpha = \rho$. The JIMWLK Hamiltonian $\mathcal{H}_{\mathrm{JIMWLK}}$ is defined as

$$\mathcal{H}_{\mathrm{JIMWLK}} = -\frac{\alpha_s}{2} \int \mathrm{d}^2\mathbf{x}\, \mathrm{d}^2\mathbf{y}\, \frac{\partial}{\partial \alpha^a(\mathbf{x})} \eta^{ab}_{\mathbf{xy}} \frac{\partial}{\partial \alpha^b(\mathbf{y})} \tag{3.18}$$

where

$$\eta^{ab}_{\mathbf{xy}} = \frac{4}{g^2 \pi^2} \int \mathrm{d}^2\mathbf{z}\, \mathcal{K}(\mathbf{x}, \mathbf{y}, \mathbf{z}) \left[\left(1 - U(\mathbf{z})U^\dagger(\mathbf{x})\right)\left(1 - U(\mathbf{y})U^\dagger(\mathbf{z})\right)\right]^{ab} \tag{3.19}$$

and U is the adjoint Wilson lines from Eq. (3.8). The kernel $\mathcal{K}$ in $\eta^{ab}_{\mathbf{xy}}$ can be written as

$$\mathcal{K}(\mathbf{x}, \mathbf{y}, \mathbf{z}) = \frac{(\mathbf{z} - \mathbf{x}) \cdot (\mathbf{z} - \mathbf{y})}{(\mathbf{z} - \mathbf{x})^2 (\mathbf{z} - \mathbf{y})^2} \tag{3.20}$$

and it is related to the probability of an emission of a gluon with a coordinate $\mathbf{z}$ from a color dipole with coordinates $\mathbf{x}$ and $\mathbf{y}$. Rapidity evolution for the expectation value of the operator $\hat{\mathcal{O}}$ can then be written as

$$\partial_Y \langle \hat{\mathcal{O}} \rangle = - \left\langle \mathcal{H}_{\text{JIMWLK}} \hat{\mathcal{O}} \right\rangle \tag{3.21}$$

which follows from the hermiticity of $\mathcal{H}_{\text{JIMWLK}}$.

An important special case of Eq. (3.21) is the case of a quark-antiquark dipole scattering off the target, which corresponds to

$$\hat{\mathcal{O}} = \hat{S}_{01} = \frac{1}{N_c} \text{Tr} \left[V(\mathbf{x}_0) V^\dagger(\mathbf{x}_1) \right]. \tag{3.22}$$

The JIMWLK equation (3.21) in this case reads

$$\partial_Y \langle \hat{S}_{01} \rangle = \frac{\alpha_s C_{\text{F}}}{\pi^2} \int d^2 \mathbf{x}_2 \frac{\mathbf{x}_{10}^2}{\mathbf{x}_{20}^2 \mathbf{x}_{21}^2} \left\langle \hat{S}_{012} - \hat{S}_{01} \right\rangle \tag{3.23}$$

where

$$\hat{S}_{012} = \frac{1}{N_c C_{\text{F}}} \text{Tr} \left[V(\mathbf{x}_0) t^a V^\dagger(\mathbf{x}_1) t^b \right] [U(\mathbf{x}_2)]^{ba} \tag{3.24}$$

is the Wilson line operator for a $q\bar{q}g$ Fock state. Using Fierz identities for the Wilson lines it is possible to write this as

$$\hat{S}_{012} = \frac{N_c}{2 C_{\text{F}}} \left(\hat{S}_{02} \hat{S}_{12} - \frac{1}{N_c^2} \hat{S}_{01} \right) \tag{3.25}$$

so that Eq. (3.23) becomes

$$\partial_Y \langle \hat{S}_{01} \rangle = \frac{\alpha_s N_c}{2\pi^2} \int d^2 \mathbf{x}_2 \frac{\mathbf{x}_{10}^2}{\mathbf{x}_{20}^2 \mathbf{x}_{21}^2} \left\langle \hat{S}_{02} \hat{S}_{12} - \hat{S}_{01} \right\rangle. \tag{3.26}$$

This differential equation alone does not form a closed system as one then needs to know how the product of two dipole operators $\langle \hat{S} \hat{S} \rangle$ evolves. This can also be calculated using the JIMWLK equation, but its evolution equation will then contain operators with even more Wilson lines. This leads to an infinite system of coupled differential equations called the *Balitsky hierarchy* [27]. In practice, this infinite set of differential equations has to be truncated at some point. One way to do this is to use the Gaussian approximation (3.12) for the distribution of the target color field configurations, which allows higher-order Wilson line operators to be written in terms of the dipole operator [54]. Another way is to use the mean-field approximation $\langle \hat{S} \hat{S} \rangle \approx \langle \hat{S} \rangle \langle \hat{S} \rangle$, which is valid for example in the large-N_c limit. Using the mean-field approximation to Eq. (3.26) leads to

$$\partial_Y \langle \hat{S}_{01} \rangle = \frac{\alpha_s N_c}{2\pi^2} \int d^2 \mathbf{x}_2 \frac{\mathbf{x}_{10}^2}{\mathbf{x}_{20}^2 \mathbf{x}_{21}^2} \left(\langle \hat{S}_{02} \rangle \langle \hat{S}_{12} \rangle - \langle \hat{S}_{01} \rangle \right) \tag{3.27}$$

which is the famous BK equation [27, 28]. It is the differential equation for the rapidity evolution of the dipole amplitude $N_{01} = 1 - \langle \hat{S}_{01} \rangle$. No analytical solutions of the BK exist because of its nonlinear nature, but it can be solved numerically if
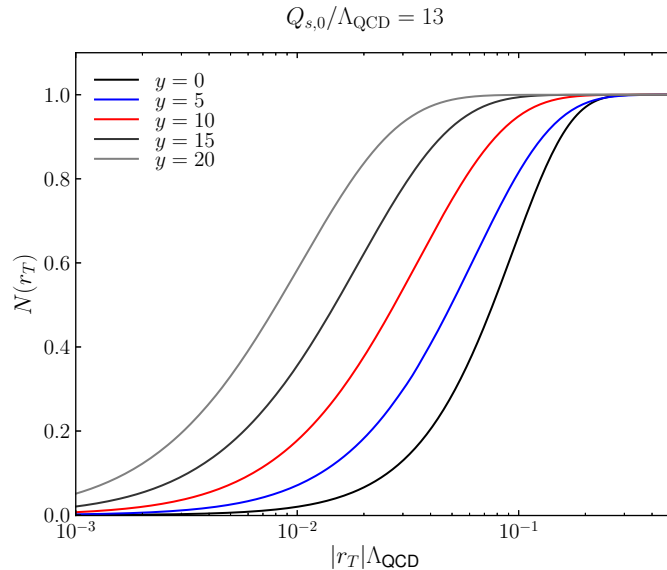
FIGURE 3.2   The BK-evolved dipole amplitude for different values of the rapidity Y as
a function of the dipole size r_T, with the MV model (3.14) as the initial
condition. Rapidity increases from right to left. Figure from Ref. [56].
Reprinted with permission from H. Mäntysaari.

the dipole amplitude at some initial rapidity $Y_{0,\text{BK}}$ is given. While the JIMWLK
equation (3.26) is formally the correct evolution equation for the dipole amplitude,
usually the simpler BK equation (3.27) is used in numerical calculations. This is
because the differences between the JIMWLK and BK equations are numerically
small, much less than the simple estimate $1/N_c^2 \approx 10\%$ from the large-N_c approxi-
mation [54, 55].

The BK equation depends on both the dipole sizes $\mathbf{x}_{ij}$ and the impact param-
eter $\mathbf{b}' = \frac{1}{2}(\mathbf{x}_i + \mathbf{x}_j)$. This impact parameter dependence of the BK equation is
problematic as it makes the evolution very sensitive to the infrared region, which
has to be remedied by including confinement effects [57–60]. For this reason, one
usually neglects the impact parameter dependence in the BK evolution such that
the dipole amplitudes $N_{ij} = 1 - \langle \hat{S}_{ij} \rangle$ are evaluated at the same impact parameter
and only the dependence on the dipole sizes remains. While this assumption should
be valid for heavy nuclei where the color density varies only slowly in $\mathbf{b}'$, for protons
this is less justified. However, for the time being it is not known how to implement
the impact parameter dependence of the evolution rigorously and thus it is neglected
for the dipole amplitudes considered in this thesis.

The nonlinearity of the BK equation (3.27) is crucial: without nonlinear effects
it reduces to the BFKL equation. The nonlinear effects ensure that, with the fixed
impact parameter, the black-disk limit $N_{01} \leq 1$ is satisfied which is important for
the unitarity of the S-matrix. In Fig. 3.2, we show how the BK evolution changes
the dipole amplitude: essentially, the dipole amplitude increases in rapidity, and for
large dipole sizes $\mathbf{x}_{01}$ it saturates to one. This saturation region of the target has
gained the name *color-glass condensate*, and it is a prediction of the BK equation
that it will be eventually reached at sufficiently high energies. However, direct

evidence of saturation has not been found at the energies available at the current experimental facilities. It is expected that the enhancement of saturation effects in heavy nuclei will allow us to probe the saturation region in the future [10]. The general framework of treating the target as a mixture of classical color fields that evolve with the JIMWLK equation (3.17) is usually referred to as the color-glass condensate effective field theory, and this is very commonly used for calculations in the dipole picture.

3.3 Numerical fits for the dipole amplitude

For an actual calculation in the dipole picture, one needs a specific model for the dipole amplitude $N_{01} = 1 - S_{01}$ that is suitable for numerics. The general way to do this is to take some simple model for the dipole amplitude with free parameters that are fitted to the data.

Several models exist in the literature, some of which are more physically motivated than others. One of the first models used for the dipole amplitude is the Golec-Biernat–Wüsthoff model [61, 62]

$$S_{01}(\mathbf{r}, Y = \log 1/x) = \sigma_0 \exp\left(-\frac{(\mathbf{r} \times 1\,\text{GeV})^2}{4}\left(\frac{x_0}{x}\right)^{\lambda/2}\right) \tag{3.28}$$

which has been integrated over the impact parameter $\mathbf{b}'$, and the constants σ_0, x_0 and λ are free parameters. This is purely a phenomenological model inspired by saturation and geometric scaling at HERA, but it is quite successful in describing the data [61, 62]. It essentially introduces the energy dependence of the saturation scale $Q_\text{s}^2 \sim \left(\frac{x_0}{x}\right)^{\lambda/2}$ as a power, which for small dipoles matches the power-like energy dependence of the cross section in the region where saturation effects are not relevant.

Another widely used model is the *impact parameter saturation* (IPsat) model [47, 63]

$$S_{01}(\mathbf{r}, \mathbf{b}', Y = \ln 1/x) = \exp\left(-\frac{\pi}{2N_\text{c}}\mathbf{r}^2\alpha_\text{s}(\mu^2)xg(x, \mu^2)T(\mathbf{b}')\right) \tag{3.29}$$

which depends on the gluon parton distribution function (PDF) $xg(x, \mu^2)$ and the transverse profile of the target $T(\mathbf{b}')$. The form of the gluon PDF is fitted to the data, and it satisfies the Dokshitzer–Gribov–Lipatov–Altarelli–Parisi (DGLAP) evolution [64–66] for the dependence on the factorization scale $\mu^2 \sim 1/\mathbf{r}^2$. This model relates the dipole amplitude directly to the gluon PDF, motivated by the idea of the interaction as a two-gluon exchange in Fig. 2.2. However, it is not clear how the dipole amplitude and the gluon PDF are related exactly beyond this leading-order picture.

A drawback of the two models mentioned above is that they do not satisfy the correct high-energy evolution given by the JIMWLK or BK equations. A more
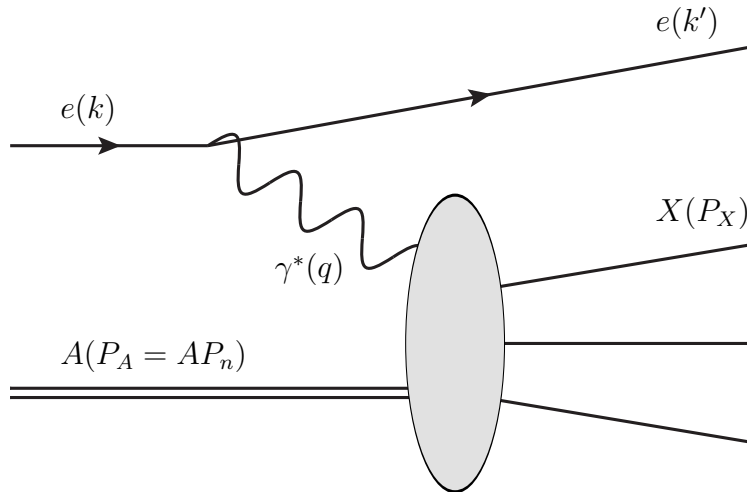
FIGURE 3.3   Inclusive deep inelastic scattering. The final states X are summed over.

physically motivated model is to fit the initial condition of the dipole amplitude to the data at some initial rapidity $Y_{0,\text{BK}}$ and then evolve the dipole amplitude to higher rapidities [67–69]. This "initial condition fit + rapidity evolution" is also the only one of these models that can be consistently used at NLO calculations where the large logarithms of the BK equation start to appear, and therefore we will mainly focus on this model in this thesis. It is interesting to note that the IPsat model is essentially orthogonal to this approach: there the dependence on the Bjorken x, and thus energy, is fitted to the data and the dependence on the dipole sizes is predicted by the DGLAP evolution. The BK-evolved approach instead fits the dependence on the dipole sizes at the initial rapidity to the data, and the dependence on the energy is then a prediction from the BK evolution.

All of these models have some freedom in the parametrization of the dipole amplitude. This freedom has to be constrained by the data, which is usually done by fitting the parameters to the HERA structure function data [70–73] because of its high precision. The high-energy factorization then guarantees that this same dipole amplitude can be used also in other calculations. Because the fitting procedure to the structure function data is so important for numerical calculations, we will briefly consider how the structure functions can be calculated in the dipole picture.

3.3.1   Inclusive deep inelastic scattering

In inclusive DIS we allow any final state in the $\gamma^* + A$ process as shown in Fig. 3.3. This can be calculated in the dipole picture using the framework we have presented in Sec. 2, and the optical theorem allows us to relate the inclusive cross section to the forward elastic scattering amplitude as

$$\sigma^{\gamma^* A} = 2 \operatorname{Im} \mathcal{M}^{\gamma^* A \to \gamma^* A} \tag{3.30}$$

with the scattering amplitude given by Eq. (2.43). This process is very inviting for measuring the dipole amplitude as everything else in the process is fully perturbative, and as an inclusive process the corresponding cross section is very large.

The cross section for inclusive DIS can be divided into longitudinal and transverse productions based on the photon polarization. These are, however, not directly measurable as the photon polarization itself is not observable. Instead, it is more useful to define the *structure functions*

$$F_\lambda(x, Q^2) = \frac{Q^2}{4\pi^2\alpha_{\text{em}}}\sigma^{\gamma_\lambda^* A}, \tag{3.31}$$

$$F_2(x, Q^2) = F_L(x, Q^2) + F_T(x, Q^2), \tag{3.32}$$

which allow us to define the experimentally measured *reduced cross section*

$$\sigma_r(y, x, Q^2) = F_2(x, Q^2) - \frac{y^2}{1 + (1-y)^2}F_L(x, Q^2). \tag{3.33}$$

The reduced cross section depends on the photon virtuality Q^2, the Bjorken x (2.6), and the inelasticity y defined as

$$y = \frac{2P_n \cdot q}{2P_n \cdot k} = \frac{W^2 + Q^2 - m_n^2}{s - m_e^2 - m_n^2} \approx \frac{W^2 + Q^2}{s} \tag{3.34}$$

where s is the center-of-mass energy of the lepton-nucleus system and the momenta are shown in Fig. 3.3. The structure functions only depend on the Bjorken x and the photon virtuality Q^2 but not on the inelasticity y. In principle, the structure functions F_2 and F_L could be determined from the reduced cross section by measuring it for different lepton-nucleus energies s and thus for different inelasticities y. In practice, this leads to less accurate data [74] and thus it is easier to simply calculate the reduced cross section from the structure functions for data comparisons.

3.3.2 Initial condition for the numerical fit

The BK equation needs a nonperturbative initial condition for the rapidity evolution. A common ansatz is the MV model in Eq. (3.14) which has a physical motivation for the general form of the dipole. This initial condition at $Y = Y_{0,\text{BK}}$ is often generalized to

$$S_{01}(\mathbf{r}, \mathbf{b}', Y_{0,\text{BK}}) = \exp\left[-\frac{1}{4}\left(\mathbf{r}^2 Q_{s,0}^2(\mathbf{b}')\right)^\gamma \ln\left(\frac{1}{|\mathbf{r}|\Lambda_{\text{QCD}}} + e\right)\right] \tag{3.35}$$

where the anomalous dimension γ is also introduced. The MV model predicts $\gamma = 1$ but in actual fits it may be taken as a parameter of the initial condition fitted to the data. This form is still quite general, and for the fits one needs to specify some form for the impact parameter dependence of the saturation scale $Q_{s,0}^2(\mathbf{b}')$. The dipole amplitude is usually fitted to the structure function data which only depends on the impact-parameter integrated dipole amplitude, and then the simplest assumption is to consider the integration as an overall factor to the dipole amplitude,

$$\int d^2\mathbf{b}'\, S_{01}(\mathbf{r}, \mathbf{b}', Y) = \frac{\sigma_0}{2}S_{01}(\mathbf{r}, Y), \tag{3.36}$$

which corresponds to assuming that the impact parameter dependence is given by a step function

$$Q_{s,0}^2(\mathbf{b}') = \theta(R - |\mathbf{b}'|)Q_{s,0}^2 \tag{3.37}$$

where R is the transverse radius of the target. With such a model, there are then three constants to fit for the initial condition: the anomalous dimensions γ, the saturation scale at the initial rapidity $Q_{s,0}^2$, and the target transverse area $\sigma_0/2$.

Such models (with some modifications) have been widely used to fit the dipole amplitude. For proton targets, there exist several fits for these parameters at LO [67–69] and also at NLO [75] by fitting the initial condition to the HERA structure function data. At LO, however, these fits suffer from the fact that it is not possible to describe simultaneously massless and massive quark production with the same parameters when using the BK equation to describe the target's evolution in energy [68]. It is not physical for the dipole amplitude to depend on the quark masses as they should be negligible in the high-energy interaction with the target, and thus one would expect that the massless and massive structure functions are given by the same dipole amplitude. This is one of the other reasons why it is important to go beyond the leading order in the dipole picture to check if this problem persists at higher orders. Indeed, the situation at NLO is already quite different as will be discussed in Sec. 3.3.4.

3.3.3 NLO fit with the massless structure function data

At the time of writing this thesis, the only dipole amplitude fits done at the full NLO are the ones in Ref. [75] which have been fitted to the HERA inclusive DIS data [70, 72] using NLO equations for the structure functions (3.31) with massless quarks. For this reason, these are the dipole amplitudes also used in Articles [II, III, IV] when predicting exclusive vector meson production from protons at NLO. There is some more freedom in the fitting procedure at NLO compared to the leading order, and as such we will go through the most important details of the fits in order to clarify the differences between them.

1. Two different data sets were used for the fitting. The first is the full HERA data set, and the second one is pseudodata consisting only of the light-quark contribution where the massive quark contribution was subtracted from the full HERA data using a prediction with the IPsat parametrization from Ref. [76]. The light-quark pseudodata is physically better motivated as the calculation of the structure functions in Ref. [75] uses only light quarks.

2. Three different versions of the BK evolution are used for the energy evolution of the dipole amplitude. These are called *kinematically constrained BK* (KCBK) [77], *resummed BK* (ResumBK) [78, 79], and *target rapidity BK* (TBK) [80]. The main reason for the different forms of the BK evolution is that they are different approximations of the full NLO BK evolution. To be completely consistent with the perturbation theory one should use the NLO BK equation in the NLO calculation, but because of its numerical complexity this is not really feasible in an already demanding numerical fit. The three

different BK evolutions used give in general a good approximation for the NLO
BK equation [81]. In KCBK, a kinematical constraint is introduced that forces
an explicit time ordering between subsequent gluon emissions. In ResumBK,
large single and double transverse logarithms that occur at higher orders are
resummed into the kernel of the BK equation. In TBK, one uses the target
rapidity instead of the projectile rapidity in the evolution. The target rapidity
is calculated from the projectile rapidity Y with the transformation

$$\eta = Y - \max\left\{0, \ln\left(\frac{1}{\mathbf{r}^2 Q_0^2}\right)\right\} \tag{3.38}$$

where $Q_0^2 \equiv 1\,\text{GeV}^2$ is the transverse scale of the target that is used to regulate
large dipole sizes.

3. Two different schemes for the running of the coupling constant α_s are used. In
both cases the dependence on the dipole size is given by

$$\alpha_s(\mathbf{r}^2) = \frac{4\pi}{\beta_0 \ln\left[\left(\frac{\mu_0^2}{\Lambda_{\text{QCD}}^2}\right)^{1/c} + \left(\frac{4C^2}{\mathbf{r}^2 \Lambda_{\text{QCD}}^2}\right)^{1/c}\right]^c} \tag{3.39}$$

where $\beta_0 = (11N_c - 2N_F)/3$, $N_F = 3$ and $\Lambda_{\text{QCD}} = 0.241\,\text{GeV}$. The constants
$\mu_0 = 2.5\Lambda_{\text{QCD}}$ and $c = 0.2$ regulate the running of the coupling in the infrared
region. The constant C^2 is a free parameter determined from the fit and it
controls how coordinate scales are related to momentum scales. From Fourier
analysis its predicted value is $C^2 = e^{-2\gamma_E}$ [82], but keeping it as a free param-
eter allows for absorbing some nonperturbative or higher-order contributions.
The two different schemes for the running of the coupling are then related to
what dipole sizes $\mathbf{r}$ are used in the coupling constant (3.39) for the $q\bar{q}g$ state.
In the *parent dipole* scheme the choice is $\mathbf{r}^2 = \mathbf{x}_{01}^2$ which corresponds to the
transverse size of the quark-antiquark dipole. The other scheme is called *Balit-
sky+smallest dipole*, and in this scheme one uses the Balitsky prescription [83]
for the running of the coupling when evolving the dipole amplitude. For the
impact factor the smallest dipole $\mathbf{r}^2 = \min\{\mathbf{x}_{01}^2, \mathbf{x}_{20}^2, \mathbf{x}_{21}^2\}$ is used instead. The
reason for this is that it is not clear how to use the Balitsky prescription in gen-
eral kinematics, and the smallest dipole can be thought of as an approximation
of the Balitsky prescription.

4. Two different starting points for the BK evolution of the dipole amplitude are
used, namely $Y_{0,\text{BK}} = 0$ and $Y_{0,\text{BK}} = \ln 1/0.01$. The later starting point for the
BK evolution, $Y_{0,\text{BK}} = \ln 1/0.01$, is typically more used in fitting the dipole
amplitude as it is not clear if the assumptions for deriving the MV model or
the BK evolution are valid for larger values of x (and hence smaller values of
Y).

These different setups have four free parameters. Three of them are related
to the MV model: the saturation scale at the initial rapidity $Q_{s,0}^2$, the anomalous
dimension γ, and the transverse area of the proton $\sigma_0/2$. The final fit parameter

is the constant C^2 controlling the running of the coupling constant. With this fitting procedure, one finds a set of these parameters for each of the different setups, resulting in $2 \times 2 \times 3 \times 2 = 24$ different fits. All of these fits describe the structure function data used in the fit extremely well, and as such one cannot distinguish between the fits based on this data alone. This changes, however, when one also takes into account the massive quark structure function data.

3.3.4 Structure functions with massive quarks at NLO

With the expressions for the massive quark structure functions at NLO now available [84–86], we can study how including the quark mass affects predictions for structure functions at NLO. It is especially important to see if both the total and charm production cross sections can be described by the same dipole amplitude, which was not possible at leading order if the evolution of the dipole amplitude is given by the BK equation [68]. This was the main motivation for Article [V] where the massive quark structure functions were calculated at NLO using the dipole amplitude fits described in Sec. 3.3.3.

Some words should be said about the numerical evaluation of the massive quark structure functions as the NLO equations including the quark mass are numerically quite demanding. They involve multi-dimensional integrals with a high number of dimensions, and getting these integrals to converge with a reasonable amount of integration points is quite tricky. To do this one has to be especially careful with the cancellation of possible numerical singularities. For example, numerical integration of the generalized Bessel functions

$$
\mathcal{G}_{(x)}^{(a;b)} = \int_0^\infty \frac{\mathrm{d}u}{u^a} \exp\left(-u\left[\overline{Q}_{(x)}^2 + m^2\right] - \frac{|\mathbf{x}_{3;(x)}|^2}{4u} \right)
$$
$$
\times \int_0^{u/\omega_{(x)}} \frac{\mathrm{d}t}{t^b} \exp\left(-t\omega_{(x)}\lambda_{(x)}m^2 - \frac{|\mathbf{x}_{2;(x)}|^2}{4t} \right)
$$

(3.40)

introduced in Refs. [84–86] is demanding in the limit $|\mathbf{x}_{2;(x)}|^2 \to 0$, as the t-integral develops a singularity at $t \to 0$ if $|\mathbf{x}_{2;(x)}|^2 = 0$. This problem is not severe if $b = 1$, as then the divergence is only logarithmic, but the power-like divergence in the case $b = 2$ leads to numerical instabilities. The convergence can be improved by subtracting the singular part in such a way that the remaining integral can be done analytically. A suitable subtraction is using the limit $\lambda_{(x)} \to 0$ as then the integrand has the same behavior at $t \to 0$, and we can calculate the integral analytically:

$$
\mathcal{G}_{(x)}^{(a;2)}(\lambda_{(x)} \to 0) = \frac{2^{2+a}}{|\mathbf{x}_{2;(x)}|^2} \left(\frac{\overline{Q}_{(x)}^2 + m^2}{|\mathbf{x}_{3;(x)}|^2 + \omega_{(x)}|\mathbf{x}_{2;(x)}|^2} \right)^{\frac{a-1}{2}}
$$
$$
\times K_{a-1}\left(\sqrt{\left(\overline{Q}_{(x)}^2 + m^2\right)\left(|\mathbf{x}_{3;(x)}|^2 + \omega_{(x)}|\mathbf{x}_{2;(x)}|^2\right)} \right).
$$

(3.41)

Such a subtraction leads to a much better convergence of the integrals which is crucial for a numerical implementation of the structure functions. Additionally, one

#	Data	BK equation	α_s	$Y_{0,\text{BK}}$	m_c [GeV]	χ_c^2/N	m_b [GeV]	χ_b^2/N	χ_{tot}^2/N
1	Light-q	ResumBK	PD	0	1.42	1.86	4.83	1.37	1.25
2	Light-q	KCBK	PD	0	1.49	2.55	4.96	1.58	1.23
3	Light-q	TBK	BSD	0	1.29	1.02	5.04	1.12	1.83

TABLE 3.1 Dipole amplitude fits from Ref. [75] that were found to be compatible with the massive quark structure function data from HERA. Here "light-q" refers to only using the light-quark pseudodata to fit the dipole amplitudes, and "PD" and "BSD" are the *parent dipole* and *Balitsky+smallest dipole* running coupling schemes for α_s. The optimal masses for the charm and bottom quarks are shown along with the χ^2/N values obtained with the optimal mass for the corresponding heavy quark production data. The values χ_{tot}^2/N refer to the total structure functions which contain both the light and heavy quarks. Table from Article [V].

can reduce the integration dimension by noting that with the change of variables $t \to y = t\omega_{(x)}/u$ the u-integral can be done analytically, leading to the expression

$$\mathcal{G}_{(x)}^{(a;b)} = \int_0^1 \frac{\mathrm{d}y}{y^{\frac{1}{2}(2-a+b)}} 2^{a+b-1} \omega_{(x)}^{b-1} \left(\frac{y\lambda_{(x)}m^2 + \overline{Q}_{(x)}^2 + m^2}{y|\mathbf{x}_{3;(x)}|^2 + \omega_{(x)}|\mathbf{x}_{2;(x)}|^2} \right)^{\frac{1}{2}(a+b-2)}$$
$$\times K_{a+b-2}\left(\sqrt{\frac{1}{y}\left(y\lambda_{(x)}m^2 + \overline{Q}_{(x)}^2 + m^2\right)\left(y|\mathbf{x}_{3;(x)}|^2 + \omega_{(x)}|\mathbf{x}_{2;(x)}|^2\right)} \right). \tag{3.42}$$

The subtraction in the numerical implementation is then done by subtracting Eq. (3.42) for $b = 2$ at the integral level, and adding the integrated result Eq. (3.41) to the rest of the calculation where the additional t- and u-integrals are not present.

Even after this, the remaining expressions are still numerically demanding. For this reason, instead of trying to perform fits to the charm data and inclusive data with quark masses included it was more feasible to first see if the fits to the massless quark structure function data can also be used to describe the massive data. This was the motivation for Article [V] where we calculated the total and charm quark structure functions at NLO with the NLO dipole amplitude fits described in Sec. 3.3.3. Out of the 24 fits only three were found to be compatible with both the charm quark and inclusive reduced cross section data from HERA [70, 72, 73], listed in Table 3.1. Results were also compared to the bottom quark production data from HERA [73] but due to the large data uncertainties this does not provide further constraints for the fits. The masses of the charm and bottom quarks were allowed to vary within reasonable limits, and the χ^2/N values are listed for the optimal mass. Results with these three dipole amplitude fits are shown in Fig. 3.4 where a good agreement with the data is found. It should be emphasized that, apart from varying the charm quark mass, these dipole amplitudes are not fitted to the charm quark data and thus these are genuine predictions using the previously obtained dipole amplitude fits.

Some comments can be made about these three fits. First, they have all been fitted to the light-quark pseudodata. This is expected as in the fitting procedure
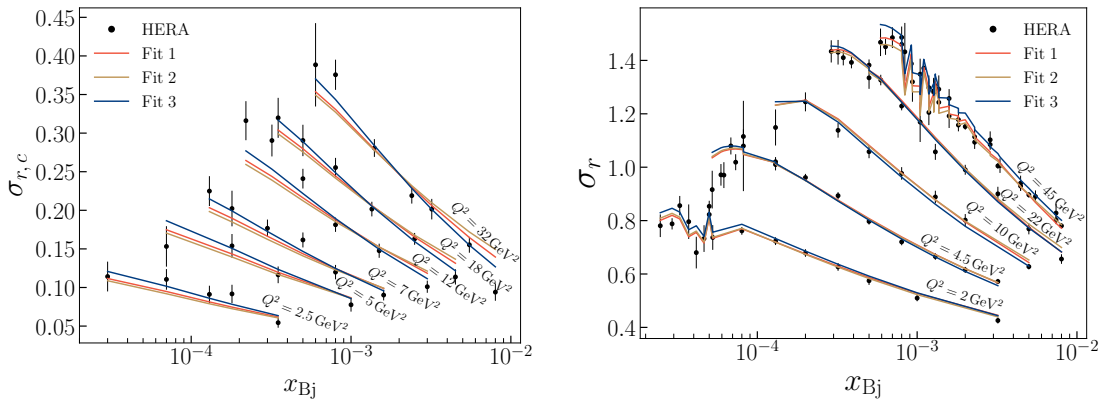
(a) Charm reduced cross section

(b) Total reduced cross section

FIGURE 3.4   Reduced cross section with massive quarks using the three dipole amplitude fits found to be compatible with the HERA data [70–73]. The reduced cross sections are plotted as a function of Bjorken x for various values of the photon virtuality. Note that the jumps in the lines for the total reduced cross section are not a result of numerical uncertainty, but rather they are a consequence of depicting points for different values of inelasticity y. Figures from Article [V], reproduced under the license CC BY 4.0.

only the massless quark structure functions were calculated, and thus fitting to the total reduced cross section which also includes the heavy quark contribution would overestimate the results. Second, these fits start the BK evolution at the earlier rapidity $Y_{0,\mathrm{BK}} = 0$. This can also be understood from the fitting procedure, as for both values of the initial rapidity $Y_{0,\mathrm{BK}}$ the dipole amplitude in the structure function is calculated down to the factorization rapidity $Y_{0,\mathrm{if}} = 0$, and the evolution of the dipole amplitude is frozen for values $Y_{0,\mathrm{if}} < Y < Y_{0,\mathrm{BK}}$. This is not entirely consistent as it leads to double counting in the rapidity region $Y_{0,\mathrm{if}} < Y < Y_{0,\mathrm{BK}}$. The contribution from this region, however, should be small, but it is important to remember that this procedure leads to a slight overestimation of the cross section. It would be more consistent to set $Y_{0,\mathrm{if}} = Y_{0,\mathrm{BK}}$ in which case no such ambiguity arrives.

The charm quark data seems to naturally disqualify the fits that are not consistent based on these two conditions. We are then still left with $6 = 3 \times 2$ fits with three different forms for the BK evolution and two different running coupling schemes. It is interesting to note that of these six fits only three are compatible with the charm quark production data, and these three fits all correspond to the different BK evolutions. Also, both of the running coupling schemes are present in this set of fits, with different BK evolutions seeming to prefer different schemes. While we do not have a clear reason for the different schemes preferred, we note that massive quark production data probes the dipole amplitude more in the perturbative region $\mathbf{r}^2\Lambda_{\mathrm{QCD}}^2 \ll 1$ compared to the light quark production. This explains why the heavy quark data provides more constraints for the dipole amplitude.

These fits show that it is possible to describe both inclusive and charm production data simultaneously with the same dipole amplitudes at NLO even when
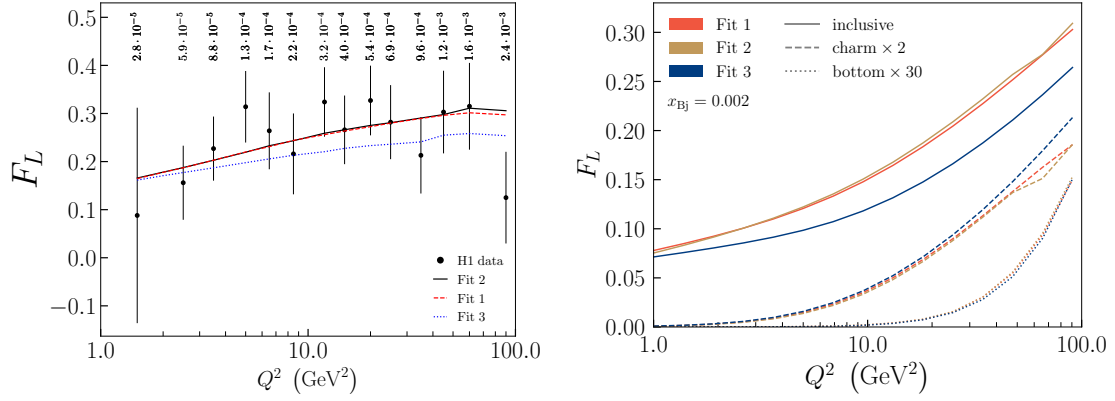
(a) HERA kinematics.

(b) EIC kinematics.

FIGURE 3.5   Longitudinal structure function F_L as a function of the photon virtuality Q^2 using the three dipole amplitude fits found to be compatible with the HERA data [70–73].
Left: Comparison to the HERA data [74]. The different values of Bjorken x for the data points are shown.
Right: Predictions for the EIC with a constant Bjorken x. The inclusive case is shown along with the charm and bottom quark structure functions multiplied by factors of 2 and 30 for visibility. Figure from Article [V], reproduced under the license CC BY 4.0.

using a BK evolution for the energy dependence of the dipole amplitude. This is not possible at leading order [68], even with an approximative NLO BK evolution [87], showing the importance of the full NLO calculation including the mass effects also in the impact factor. The NLO corrections modify both the evolution of the dipole amplitude and the mass dependence of the impact factor in such a way that to-gether these effects allow for a precise description of both the charm quark and inclusive production data simultaneously. This is important for the consistency of calculations in the dipole picture, as the dipole amplitude should be universal and independent of the quark mass in the high-energy limit.

With just the charm and inclusive reduced cross section data it is not possible to distinguish between the three remaining fits, and thus data comparisons for other processes are required to show differences between the fits. For example, while the longitudinal structure function F_L is not completely independent from the reduced cross section, it is generally more sensitive to the saturation region and can therefore give additional constraints for the dipole amplitude. As shown in Fig. 3.5, the current HERA data [74] for F_L is not enough to show differences between the three dipole amplitude fits, but in the EIC kinematics Fit 3 with the TBK evolution leads to different predictions. Diffractive processes are also more sensitive to the nuclear structure, and hence they are good candidates for a more precise determination of the dipole amplitude. In the future, one should do a global fit for the dipole amplitude using all of the available data for different processes to determine precisely the fit parameters with uncertainty estimates. In addition to the proton dipole amplitude, it would be interesting to fit also the nuclear dipole amplitude directly to the data,

which is not possible with the HERA data that is only for proton targets. With the EIC data in the future it will be possible to fit the dipole amplitude for heavy nuclei independently from protons [10].

4 EXCLUSIVE VECTOR MESON PRODUCTION

In an exclusive scattering process all of the produced particles are measured, and in a photon-nucleus scattering this means that the photon is essentially transformed into the produced particles. For single-particle final states, most likely particles produced in this way are vector mesons as they have the same quantum numbers $J^{PC} = 1^{--}$ as the photon, corresponding to a pomeron exchange in the terminology of the Regge theory. Exclusive vector meson production amounts to a significant amount, about 10%, of all diffractive processes [12].

At leading order in the dipole picture, exclusive vector meson production can be described by the Feynman diagram in Fig. 4.1, and the corresponding invariant amplitude reads

$$
\begin{aligned}
i\mathcal{M}_{\lambda_\gamma \lambda_V} = \int \mathrm{d}^2\mathbf{x}_{01}\,\mathrm{d}^2\mathbf{b} \int_0^1 \frac{\mathrm{d}z_0\,\mathrm{d}z_1}{(4\pi)^2 z_0 z_1} (4\pi)\delta(1 - z_0 - z_1) \\
\times\, e^{-i\mathbf{b}\cdot\boldsymbol{\Delta}} \widetilde{\Psi}_{\lambda_\gamma}^{\gamma^* \to q\bar{q}}(\mathbf{x}_{01}, z_i) \left(\widetilde{\Psi}_{\lambda_V}^{V \to q\bar{q}}(\mathbf{x}_{01}, z_i)\right)^* \left(1 - \hat{S}_{01}\right)
\end{aligned}
\tag{4.1}
$$

where the notations for the wave functions and the variables are explained in Sec. 2.4. The dipole amplitude depends on the rapidity variable in the process according to the JIMWLK equation in Sec. 3.2, and usually in the leading-order calculations the rapidity is chosen as $Y = \ln(1/x_{\mathbb{P}})$ where

$$
x_{\mathbb{P}} = \frac{q\cdot(P_n - P_n')}{q\cdot P_n} = \frac{Q^2 + M_V^2 - t}{W^2 + Q^2 - m_n^2}
\tag{4.2}
$$

is the momentum fraction carried by the pomeron in the high-energy limit, and the momentum-transfer squared is given by $t = (P_n - P_n')^2 \approx -\boldsymbol{\Delta}^2$. Note that here the impact parameter $\mathbf{b} = z_0\mathbf{x}_0 + z_1\mathbf{x}_1$ is defined as the center-of-mass position in the transverse plane, which is the Fourier conjugate of the momentum transfer $\boldsymbol{\Delta}$. In the literature, it is common to write the amplitude in terms of the average of the transverse coordinates, $\mathbf{b}' = \frac{1}{2}(\mathbf{x}_0 + \mathbf{x}_1) = \mathbf{b} + \left(\frac{1}{2} - z_0\right)\mathbf{x}_{01}$, and assume that the dipole amplitude $N(\mathbf{x}_{01}, \mathbf{b}') = \left\langle 1 - \hat{S}_{01} \right\rangle$ does not depend on the angle between $\mathbf{x}_{01}$ and $\mathbf{b}'$. This simplifies numerical calculations and was also done in Article [I].
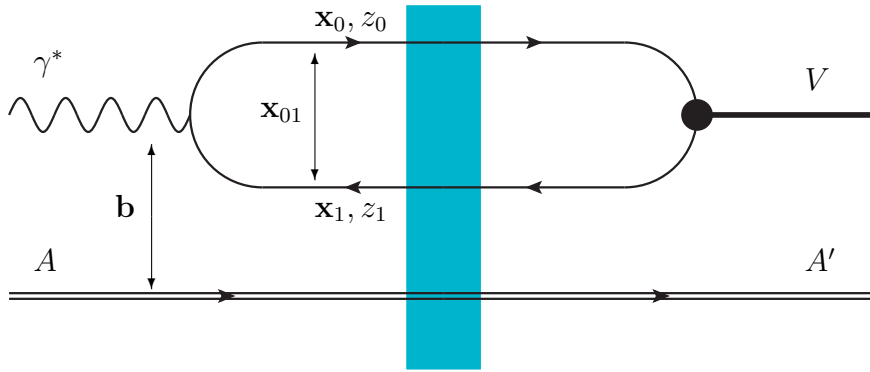
FIGURE 4.1   Exclusive vector meson production at leading order in the dipole picture. The blue rectangle depicts the instantaneous interaction with the target.

Experimentally, exclusive vector meson production is a very clean event, as the vector meson is the only particle produced. Then only the decay products of the vector meson need to be measured, which can be done very accurately by measuring the decay to a muon pair for example. For sufficiently high energies, $x_{\mathbb{P}} \lesssim 0.01$, there exists data from electron-proton collisions at HERA [88–93] and nuclear collisions at LHC [7, 8, 94–98]. The HERA data has been measured for various different center-of-mass energies W and photon virtualities Q^2, providing accurate data for both light and heavy vector mesons. At the LHC, the measurements have been done in nucleus-nucleus collisions where one of the nuclei emits the photon. In practice, measuring exclusive vector meson production in nuclear collisions requires a high impact parameter between the nuclei, which renders the photons to be quasi-real with a virtuality $Q^2 \approx 0$[1]. This has consequences for the perturbativity of the process, as the perturbative scale for exclusive vector meson production is given by $Q^2 + M_V^2$. Thus, for light vector mesons one cannot expect the process to be perturbative for small photon virtualities, whereas for heavy mesons the meson mass provides a perturbative scale. This allows us to compute exclusive heavy vector meson production also in the LHC kinematics, but for light vector mesons we have only the HERA data to compare to. In the future, more data will be expected to come from the future EIC where exclusive vector meson production will be measured in electron-nucleus collisions [10, 99, 100]. This will also allow measurements of production from heavy nuclei for non-zero photon virtualities.

In addition to measuring the dependence on the energy and the photon virtuality, exclusive vector meson production also allows for the measurement of the momentum transfer $t = -\boldsymbol{\Delta}^2$. Measuring the momentum transfer dependence gives us information about the impact parameter dependence of the interaction with the target, as is shown explicitly in Eq. (4.1) by the Fourier term $e^{-i\mathbf{b}\cdot\boldsymbol{\Delta}}$. Measuring the momentum-transfer dependent cross section also allows us to consider *coherent* and *incoherent* vector meson production separately. In the Good-Walker approach

---

[1]   Virtual photons have a lifetime $\sim 1/Q$, which means that for impact parameters higher than the nuclear radii only photons with $Q^2 \approx 0$ contribute.
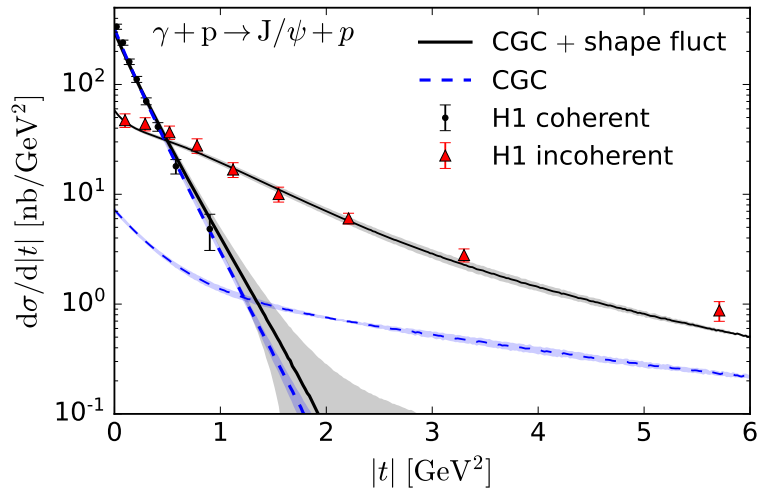
FIGURE 4.2   HERA data [93] for coherent and incoherent J/Ψ production with pre-
dictions from a CGC model. Note that including shape fluctuations (in
black solid line) is important for incoherent production as it measures tar-
get fluctuations. Figure from Ref. [102]: H. Mäntysaari, F. Salazar and
B. Schenke, *Nuclear geometry at high energy from exclusive vector meson
production*, *Phys. Rev. D* 106 (2022) no. 7 074019, DOI: 10.1103/Phys-
RevD.106.074019. Reproduced under the license CC BY 4.0.

to diffraction [101], these are defined as:

$$\frac{\mathrm{d}\sigma}{\mathrm{d}|t|} = \frac{1}{4\pi}\langle|\mathcal{M}|^2\rangle = \left(\frac{\mathrm{d}\sigma}{\mathrm{d}|t|}\right)_{\text{coherent}} + \left(\frac{\mathrm{d}\sigma}{\mathrm{d}|t|}\right)_{\text{incoherent}} \tag{4.3}$$

$$\left(\frac{\mathrm{d}\sigma}{\mathrm{d}|t|}\right)_{\text{coherent}} = \frac{1}{4\pi}|\langle\mathcal{M}\rangle|^2 \tag{4.4}$$

$$\left(\frac{\mathrm{d}\sigma}{\mathrm{d}|t|}\right)_{\text{incoherent}} = \frac{1}{4\pi}\left(\langle|\mathcal{M}|^2\rangle - |\langle\mathcal{M}\rangle|^2\right). \tag{4.5}$$

Note that the factor $1/(4\pi)$ in Eq. (4.3) is a convention that depends on the defini-
tion of the amplitude, and a different convention was used in Articles [I, II, III, IV].
Here $\langle\cdots\rangle$ denotes the average over the target configurations described in Sec. 3.1,
and thus the difference between the coherent and the total cross section is in the final
configuration of the nucleus: total production allows any color neutral configuration
of the target, whereas in coherent production the final state is in the same configu-
ration as the initial state. Incoherent production then corresponds to a "variance"
of the amplitude and it measures fluctuations in the target configuration.

Coherent and incoherent production are relevant at different scales for the
momentum exchange t as shown in Fig. 4.2. In general, coherent production is
more important for low values of $|t|$ where the data is also the most accurate. The
t-dependence of the coherent cross section has been experimentally found to be well
described by

$$\frac{\mathrm{d}\sigma}{\mathrm{d}|t|} \approx e^{-b_{\text{eff}}|t|}\frac{\mathrm{d}\sigma}{\mathrm{d}|t|}(t=0) \tag{4.6}$$

where b_{eff} is a parameter that should be fitted to the experimental data [88, 89, 92, 103]. It can be understood as the effective transverse area of the meson-target system. This phenomenological model for the t-dependence of coherent production allows one to estimate the t-integrated coherent cross section from the differential cross section at $t = 0$, as was done in Articles [II, III, IV] to avoid additional modeling for the impact parameter dependence of the dipole amplitude. Coherent production also allows one to use the target-averaged dipole amplitude that also appears in inclusive DIS. For this reason, only the coherent production was considered in Articles [I, II, III, IV].

Some notes should also be made about the difference in the dipole amplitude used in exclusive vector meson production and inclusive DIS. First of all, also the real part of the invariant amplitude (i.e. the imaginary part of the dipole amplitude) contributes to exclusive vector meson production as opposed to inclusive DIS which depends only on the imaginary part of the invariant amplitude (i.e. the real part of the dipole amplitude) by the optical theorem. Thus, if one wishes to use the dipole amplitude determined from inclusive DIS, one has to account for the real part of the production amplitude by other means. This contribution can be estimated to be small in the high-energy limit, and using Regge theory it is possible to write it as [104, 105]

$$\operatorname{Re}\mathcal{M} = \operatorname{Im}\mathcal{M} \times \tan\left(\frac{\pi}{2}\delta\right) \tag{4.7}$$

where

$$\delta = \frac{\partial}{\partial(1/x_{\mathbb{P}})} \operatorname{Im}\mathcal{M}. \tag{4.8}$$

Another difference between the dipole amplitude in exclusive vector meson production and inclusive DIS is that the dipole amplitude may depend on the minus-momentum exchange in the process. This means that when taking the average $\langle\cdots\rangle$ over the target configurations in exclusive vector meson production, the initial state A and the final state A' for the target have different momenta. This is in contrast to inclusive DIS where using the optical theorem to calculate the cross section corresponds to forward elastic scattering where the initial and final states have exactly the same momenta. While the plus-momentum is conserved in the interaction with the target, the transverse and minus components might differ for vector meson production, with the transverse-momentum exchange $t = -\boldsymbol{\Delta}^2$ and the minus-momentum exchange

$$\frac{P_n^- - P_n'^-}{P_n^-} \approx \frac{Q^2 + M_V^2 - t}{W^2 + Q^2 - m_n^2} = x_{\mathbb{P}}. \tag{4.9}$$

While the t-dependence can be understood from the Fourier transform of the dipole amplitude,

$$\int \mathrm{d}^2\mathbf{b}\, e^{-i\mathbf{b}\cdot\boldsymbol{\Delta}} N(\mathbf{x}_{01}, \mathbf{b}), \tag{4.10}$$

the minus-momentum exchange is more complicated. In terms of collinear factorization, this non-zero minus-momentum exchange is related to the fact that structure functions can be written in terms of the standard parton distribution functions

while exclusive vector meson production requires *generalized* parton distributions (GPDs) [106]. The difference coming from the minus-momentum exchange can be estimated in certain limits using collinear factorization where it is related to the *skewness* of the GPDs. In Ref. [107], the difference between maximally skewed GPDs and standard PDFs was calculated, and assuming that the interaction between the quark-antiquark dipole and the target happens through an exchange of two gluons one can estimate how this correction should appear in exclusive vector meson production. While this derivation of the skewness correction does not directly apply to the dipole picture, this skewness correction is often included in phenomenological data comparisons by multiplying the production amplitude by the factor [47, 108]

$$R_g = \frac{2^{2\delta+3}}{\sqrt{\pi}} \frac{\Gamma\left(\delta + \frac{5}{2}\right)}{\Gamma(\delta+4)}. \tag{4.11}$$

These corrections appear as a general overall factor that increases the cross section. The real-part correction is generally smaller, less than 20%, but the skewness correction can vary between 20% and 60% [109, 110]. The corrections also depend on the energy W and the photon virtuality Q^2, decreasing for higher energies and lower photon virtualities, i.e. the corrections become numerically less important for smaller $x_{\mathbb{P}}$. The real-part and skewness corrections were included for comparisons with the data in Article [I] but were left out of Articles [II, III, IV] where the main focus was on the calculation and not on data comparisons.

4.1 Vector meson wave function

The dependence on the produced vector meson is completely determined by the meson wave function. As a nonperturbative quantity, the vector meson wave function is also a major source of theoretical uncertainty for the process. The uncertainty can be somewhat reduced by considering symmetry relations for the meson wave function. In equal-time quantization, one could use the SO(3) rotational symmetry and spin-parity conservation to write the wave function for the $q\bar{q}$ state in the rest frame as

$$\Psi_{s\bar{s}}^\lambda(\vec{r}) = \sum_{Lm_Lm_s} \left\langle \frac{1}{2}s, \frac{1}{2}\bar{s} \middle| 1m_s \right\rangle \langle 1m_s, Lm_L | 1\lambda \rangle Y_L^{m_L}(\Omega_r)\phi^L(|\vec{r}|) \tag{4.12}$$

where $\langle \cdots, \cdots | \cdots \rangle$ are the Clebsch-Gordan coefficients, $Y_L^{m_L}$ spherical harmonics, Ω_r is the angular part of the 3-vector $\vec{r}$ and ϕ^L is the radial part of the wave function corresponding to the orbital angular momentum L. For vector mesons, the only possible values for the orbital angular momentum are $L = 0, 2$ which correspond to the S- and D-waves in the spectroscopic notation. In light-cone perturbation theory, one cannot write the light-cone wave function in this form. This follows from the fact that the SO(3) symmetry is broken by the light-cone quantization such that only the SO(2) rotation symmetry of the transverse plane remains. This means that

the total angular momentum is not explicitly conserved, but the magnetic quantum numbers, λ, m_s, m_L, corresponding to the angular momentum in the transverse plane are conserved. This can be used to factorize the dependence on the transverse angle φ out of the wave function by

$$\Psi_{s\bar{s}}^{\lambda}(\mathbf{r}, z) = e^{i\varphi m_L} \phi_{s\bar{s}}^{\lambda}(|\mathbf{r}|, z) \tag{4.13}$$

where $m_L = \lambda - (s + \bar{s})$ is the orbital magnetic quantum number and $\phi_{s\bar{s}}^{\lambda}(|\mathbf{r}|, z)$ is the part of the wave function that is independent of the transverse angle.

Parity is not a symmetry in light-cone perturbation theory as it requires also changing the sign of the x^3-axis, which corresponds to interchanging $x^+ \leftrightarrow x^-$. Instead, one can consider the *mirror parity* defined as $\hat{P}_x = \hat{R}_x(\pi)\hat{P}$, where $\hat{P}$ is the standard parity operator and $\hat{R}_x(\phi)$ corresponds to a rotation around the x^1-axis by the angle ϕ. This definition of the mirror parity corresponds to changing the sign of the x^1-axis [49, 111].

To see how the mirror parity and C-parity act on a meson, consider an eigenstate of the spin-parity J^{PC} with a definite polarization λ. We can write this as

$$\left| J^{PC}, \lambda \right\rangle = \int d^2\mathbf{x}_0 \, d^2\mathbf{x}_1 \int_0^1 \frac{dz}{z(1-z)} \sum_{s\bar{s}} \Psi_{s\bar{s}}^{\lambda}(\mathbf{x}_{01}, z) \left| q_s(\mathbf{x}_0, z)\bar{q}_{\bar{s}}(\mathbf{x}_1, 1-z) \right\rangle \tag{4.14}$$

at leading order. Charge conjugation interchanges the quark and antiquark such that

$$\hat{C} \left| J^{PC}, \lambda \right\rangle = \int d^2\mathbf{x}_0 \, d^2\mathbf{x}_1 \int_0^1 \frac{dz}{z(1-z)} \sum_{s\bar{s}} \Psi_{s\bar{s}}^{\lambda}(\mathbf{x}_{01}, z) \left| \bar{q}_s(\mathbf{x}_0, z)q_{\bar{s}}(\mathbf{x}_1, 1-z) \right\rangle$$

$$= -\int d^2\mathbf{x}_0 \, d^2\mathbf{x}_1 \int_0^1 \frac{dz}{z(1-z)} \sum_{s\bar{s}} \Psi_{\bar{s}s}^{\lambda}(-\mathbf{x}_{01}, 1-z) \left| q_s(\mathbf{x}_0, z)\bar{q}_{\bar{s}}(\mathbf{x}_1, 1-z) \right\rangle$$

$$= \int d^2\mathbf{x}_0 \, d^2\mathbf{x}_1 \int_0^1 \frac{dz}{z(1-z)} (-1)^{1+m_L} \Psi_{\bar{s}s}^{\lambda}(\mathbf{x}_{01}, 1-z) \left| q_s(\mathbf{x}_0, z)\bar{q}_{\bar{s}}(\mathbf{x}_1, 1-z) \right\rangle \tag{4.15}$$

which leads to the identity

$$C\Psi_{s\bar{s}}^{\lambda}(\mathbf{x}_{01}, z) = (-1)^{1+m_L} \Psi_{\bar{s}s}^{\lambda}(\mathbf{x}_{01}, 1-z). \tag{4.16}$$

Similarly, for mirror parity we get

$$\hat{P}_x \left| J^{PC}, \lambda \right\rangle = \int d^2\mathbf{x}_0 \, d^2\mathbf{x}_1 \int_0^1 \frac{dz}{z(1-z)} \sum_{s\bar{s}} \Psi_{s\bar{s}}^{\lambda}(\mathbf{x}_{01}, z) \left| q_{-s}(P_x\mathbf{x}_0, z)\bar{q}_{-\bar{s}}(P_x\mathbf{x}_1, 1-z) \right\rangle$$

$$= \int d^2\mathbf{x}_0 \, d^2\mathbf{x}_1 \int_0^1 \frac{dz}{z(1-z)} \sum_{s\bar{s}} \Psi_{-s,-\bar{s}}^{\lambda}(P_x\mathbf{x}_{01}, z) \left| q_s(\mathbf{x}_0, z)\bar{q}_{\bar{s}}(\mathbf{x}_1, 1-z) \right\rangle$$

$$= \int d^2\mathbf{x}_0 \, d^2\mathbf{x}_1 \int_0^1 \frac{dz}{z(1-z)}$$
$$\times \sum_{s\bar{s}} (-1)^{m_L} e^{-2im_L\varphi} \Psi_{-s,-\bar{s}}^{\lambda}(\mathbf{x}_{01}, z) \left| q_s(\mathbf{x}_0, z)\bar{q}_{\bar{s}}(\mathbf{x}_1, 1-z) \right\rangle \tag{4.17}$$

where $P_x\mathbf{r}$ corresponds to mirroring the vector $\mathbf{r}$ around the x^2-axis so that its x^1-component is flipped. Noting that mirror parity acts as [111]

$$\hat{P}_x \left| J^{PC}, \lambda \right\rangle = (-1)^J P \left| J^{PC}, -\lambda \right\rangle, \tag{4.18}$$

this leads to

$$(-1)^J P \Psi_{s\bar{s}}^{-\lambda}(\mathbf{x}_{01}, z) = (-1)^{m_L} e^{-2im_L\varphi} \Psi_{-s,-\bar{s}}^{\lambda}(\mathbf{x}_{01}, z). \tag{4.19}$$

Substituting the spin-parity $J^{PC} = 1^{--}$ of the vector meson in Eqs. (4.16) and (4.19) leads to a set of relations between different components of the light-cone wave function which somewhat restricts the degrees of freedom. It should be mentioned that these relations assume the sign convention $\varepsilon^\lambda = \frac{1}{\sqrt{2}}(-\lambda, -i)$ for the polarization vectors which is consistent with the Condon-Shortley convention for spherical harmonics. Also, it is assumed that the spinors are eigenstates of the x^3-component of the total angular momentum operator $\hat{J}_3 = \hat{L}_3 + \hat{S}_3$, and the quark and antiquark spinors are related by charge conjugation, $v_s(\vec{k}) = -i\gamma^2 u_s(\vec{k})$. These assumptions about the spinors are true for most spinor bases used in the literature, and especially the Lepage–Brodsky basis (2.36) satisfies these.

Using the angular dependence of the meson wave function (4.13), it is possible to show that vector meson production is highly suppressed unless the polarizations of the photon and meson are the same [112]. In fact, if one assumes that the dipole amplitude $N(\mathbf{x}_{01}, \mathbf{b})$ does not depend on the angle between $\mathbf{x}_{01}$ and $\mathbf{b}$, the leading-order production amplitude for differing polarizations vanishes. Therefore the contribution from polarization-changing components is usually ignored, and one considers only the case $\lambda_\gamma = \lambda_V$.

4.1.1 Relativistic corrections to the heavy vector meson wave function

When talking about heavy vector mesons, one usually means heavy quarkonia states such as J/Ψ or Υ. The main advantage of these particles is that they can be treated as nonrelativistic states such that the relative velocity v of the quark and antiquark is small, $v \ll 1$. There are multiple ways to describe a nonrelativistic state mathematically. For example, potential models using the Schrödinger equation have been quite successful in explaining qualitatively the existing quarkonium states [113–116], and by solving the Schrödinger equation one can obtain a rest-frame wave function that can be used for other calculations.

Another possibility is to use the effective field theory of nonrelativistic quantum chromodynamics (NRQCD) which has been developed for describing quarkonium states [117]. The main idea of NRQCD is to expand quantities as a power series of the velocity of the heavy quark v, such that the nonperturbative physics is described by universal long-distance matrix elements (LDMEs) that appear both in the decay and production of quarkonia. The LDMEs can then be related to the rest-frame wave function and its derivatives at the origin. The leading-order approach in NRQCD is to treat the quark-antiquark pair moving at zero velocity, meaning that the rest-frame wave function is a delta function in momentum space, $\Psi(\vec{k}) \sim (2\pi)^3 \delta^3(\vec{k})$, or equivalently a constant in position space, $\widetilde{\Psi}(\vec{r}) \sim 1$. These wave functions are

proportional to the LDME $\langle \mathcal{O}_1 \rangle$ which can be determined e.g. from the leptonic width of the corresponding quarkonium state.

Higher-order terms in NRQCD can be included order by order in terms of the heavy quark velocity, which can also be used to add relativistic corrections to the vector meson wave function. Assuming that the meson wave function is peaked around $\vec{k} = 0$, the standard expectation value

$$\int \frac{\mathrm{d}^3 k}{(2\pi)^3} k^{2n} \left| \Psi(\vec{k}) \right|^2 = \langle k^{2n} \rangle \tag{4.20}$$

also suggests that

$$\int \frac{\mathrm{d}^3 k}{(2\pi)^3} k^{2n} \Psi(\vec{k}) \sim \langle k^{2n} \rangle \int \frac{\mathrm{d}^3 k}{(2\pi)^3} \Psi(\vec{k}) \tag{4.21}$$

which in the position space corresponds to

$$\nabla^{2n} \widetilde{\Psi}(0) \sim \langle k^{2n} \rangle \widetilde{\Psi}(0). \tag{4.22}$$

Writing then the wave function $\widetilde{\Psi}(\vec{r})$ as a Taylor series, we can note that each term in the series is suppressed by the velocity v as

$$\widetilde{\Psi}(\vec{r}) = \underbrace{\widetilde{\Psi}(0)}_{\mathcal{O}(v^0)} + \underbrace{r^i \partial_i \widetilde{\Psi}(0)}_{\mathcal{O}(v^1)} + \underbrace{\frac{1}{2} r^i r^j \partial_i \partial_j \widetilde{\Psi}(0)}_{\mathcal{O}(v^2)} + \mathcal{O}(v^3). \tag{4.23}$$

This series can then be truncated at the desired point to include corrections of the order $\mathcal{O}(v^n)$, and after this the wave function uncertainty is reduced to a finite number of unknown constants corresponding to derivatives of the wave function at the origin $\partial^n \widetilde{\Psi}(0)$. These unknown constants can then be written in terms of the universal LDMEs of NRQCD [118].

In addition to the suppression of higher orders in the expansion (4.23), the non-dominant orbital angular momentum and spin components are velocity-suppressed. For example, for the lowest-energy heavy vector mesons J/Ψ and Υ the dominant spin component is the S-wave, and correspondingly the D-wave is suppressed by v^2 [117]. The D-wave is suppressed even further in the decay and production of these particles, as the D-wave component has to be combined with terms proportional to $\vec{k}^2$ to give a non-zero result. This means that the D-wave component is in total suppressed by v^4 in the production of J/Ψ and Υ. The situation is similar for non-dominant spin components which are proportional to $e^{i\varphi m_L}$ according to Eq. (4.13). These have to be combined similarly with terms proportional to $k^{|m_L|} e^{-i\varphi m_L}$ to yield a non-zero contribution, which brings an additional suppression of $v^{|m_L|}$.

These ideas of using NRQCD to add relativistic corrections were used in Article [I] where we considered the order v^2 correction to the rest-frame wave function. At this order, we can neglect the D-wave such that we only have the S-wave contribution, and by rotational symmetry only the first and third terms in Eq. (4.23) are non-zero, which corresponds to having two unknown constants in the wave function. Numerical values for these constants have been determined in Ref. [118] for J/Ψ and in Ref. [119] for Υ by considering electromagnetic decays of quarkonia.

The potential models and the NRQCD approach give us the rest-frame wave function which is not the same thing as the light-cone wave function required for calculating processes in light-cone perturbation theory. The exact relation between the two wave functions is not known as it is highly nontrivial because of the different quantizations leading to the wave functions. Discarding the differences in the Fock state expansions of the states corresponding to different quantization schemes, one can treat the differences between the two wave functions arising from the differences in the spinors and the variables.

For the rest-frame wave function, it is more convenient to use the standard 3-momentum or -position coordinates as variables. The standard spinor basis for the rest frame is the Bjorken–Drell basis [120]:

$$u_s = \sqrt{E+m} \begin{pmatrix} \xi_s \\ \frac{\vec{\sigma}\cdot\vec{k}}{E+m}\xi_s \end{pmatrix} \qquad v_s = \sqrt{E+m} \begin{pmatrix} \frac{\vec{\sigma}\cdot\vec{k}}{E+m}\chi_s \\ \chi_s \end{pmatrix} \qquad (4.24)$$

where

$$\xi_\uparrow = \begin{pmatrix} 1 \\ 0 \end{pmatrix} \qquad \xi_\downarrow = \begin{pmatrix} 0 \\ 1 \end{pmatrix} \qquad \chi_\uparrow = \begin{pmatrix} 0 \\ -1 \end{pmatrix} \qquad \chi_\downarrow = \begin{pmatrix} 1 \\ 0 \end{pmatrix}. \qquad (4.25)$$

Here E is the energy of the particle and σ_i are the Pauli matrices. They satisfy the relations $v_s(\vec{k}) = -i\gamma^2 u_s(\vec{k})^*$ and $\chi_s = i\sigma_2\xi_s^*$ which are useful when considering the conservation of C-parity. These spinors are also the eigenstates of the spin-operator $\hat{S}_3$ boosted to the particle's rest frame [121]. This is the reason why the Bjorken–Drell basis is sometimes called the *spin* basis, and it also allows us to use the conservation of angular momentum to describe the wave function as a combination of eigenstates of the operators $\hat{L}_3$ and $\hat{S}_3$. This leads to the decomposition of the wave function in terms of components with specific L and S quantum numbers in Eq. (4.12).

As described in Sec. 2.4, in light-cone perturbation theory the convenient basis for the spinors is the Lepage–Brodsky basis (2.36). This is the reason why this choice for the spinors is usually also made for describing the light-cone wave function. To describe the light-cone wave function in terms of the rest-frame wave function correctly, one needs to correct for this difference in the spinor basis. This can be done by a simple change of the basis in the vector space of the spinors. Note that we can write the Lepage–Brodsky spinors in the form of Eq. (4.24) using the following 2-spinors[2]:

$$\xi_+(\vec{k}) = N \begin{pmatrix} E + k^3 + m \\ k_R \end{pmatrix} \qquad \xi_-(\vec{k}) = N \begin{pmatrix} -k_L \\ E + k^3 + m \end{pmatrix} \qquad (4.26)$$

$$\chi_+(\vec{k}) = N \begin{pmatrix} k_L \\ -(E + k^3 + m) \end{pmatrix} \qquad \chi_-(\vec{k}) = N \begin{pmatrix} E + k^3 + m \\ k_R \end{pmatrix} \qquad (4.27)$$

---

[2] In fact, it is possible to write *any* choice of the spinors in the Bjorken–Drell form with suitably chosen 2-spinors. This follows from the fact that the solutions for the Dirac equations $(\not{k} - m)u(k) = 0$ and $(\not{k} + m)v(k) = 0$ form 2-dimensional vector spaces.

where $N = \frac{1}{\sqrt{2(E+m)(E+k^3)}}$ is a normalization factor. The change for the spinor basis can then be written as

$$\Psi_{h\bar{h}} = \sum_{s=\uparrow,\downarrow} \sum_{\bar{s}=\uparrow,\downarrow} \xi_h^\dagger \xi_s \chi_{\bar{s}}^\dagger \chi_{\bar{h}} \Psi_{s\bar{s}}. \tag{4.28}$$

This procedure is also called the *Melosh rotation* [122]. It should be noted that the Melosh rotation preserves the symmetry relations (4.13), (4.16), (4.19) between the different components of the wave functions as both the Lepage–Brodsky and Bjorken–Drell bases satisfy the assumptions required for these relations.

The Melosh rotation is sometimes thought of as a boost to the "infinite-momentum frame" [123, 124]. To see this, note that a longitudinal boost with a rapidity Y acts on the Bjorken–Drell spinors as

$$\exp\left(\frac{1}{4}[\gamma^0, \gamma^3]Y\right) u_s(\vec{k}) = \sqrt{E'+m} \begin{pmatrix} \xi_s' \\ \frac{\vec{\sigma}\cdot\vec{k}'}{E'+m}\xi_s' \end{pmatrix} \tag{4.29}$$

where

$$E' = E\cosh Y + k^3 \sinh Y, \qquad k^{3\prime} = E\cosh Y + k^3 \sinh Y, \qquad \mathbf{k}' = \mathbf{k}, \tag{4.30}$$

correspond to the boosted energy and momenta and the 2-spinor is transformed into

$$\xi_s' = \frac{1}{\sqrt{(E+m)(E'+m)}} \left[\cosh\left(\frac{Y}{2}\right)(E'+m) - \sinh\left(\frac{Y}{2}\right)\sigma \cdot \vec{k}'\sigma^3\right] \xi_s. \tag{4.31}$$

We can now consider the quark to be moving with a very high momentum k^3, and we wish to boost it closer to the rest frame. This corresponds to taking $Y \to -\infty$ which then changes the form of the 2-spinors to match the Lepage–Brodsky basis by $\xi_\uparrow' \to \xi_+(\vec{k}')$ and $\xi_\downarrow' \to \xi_-(\vec{k}')$. This means that the spinors in the Lepage–Brodsky basis can be thought of as the Bjorken–Drell spinors boosted to the "infinite-momentum frame". It should be stressed, however, that such an infinite boost is not *required* for the Melosh rotation. Instead, we view it as a mathematical transformation between the two different spinor bases without any physical meaning. One is free to choose the spinor basis as one wishes, and in this case the convenient bases for the rest frame and the light cone simply happen to be different.

The other correction one has to make when going from the rest-frame wave function to the light-cone wave function is the change in the variables. Essentially, one has to change $k^3 \to k^+$, which is nontrivial as in the rest-frame the total energy is not conserved and in the light cone it is the minus component of the momentum that is not conserved. A common approach is to assume the conservation of the plus-momentum, which in the rest frame of the quark-antiquark pair leads to the expression

$$k^3 = M_{q\bar{q}}\left(z - \frac{1}{2}\right) \tag{4.32}$$

where

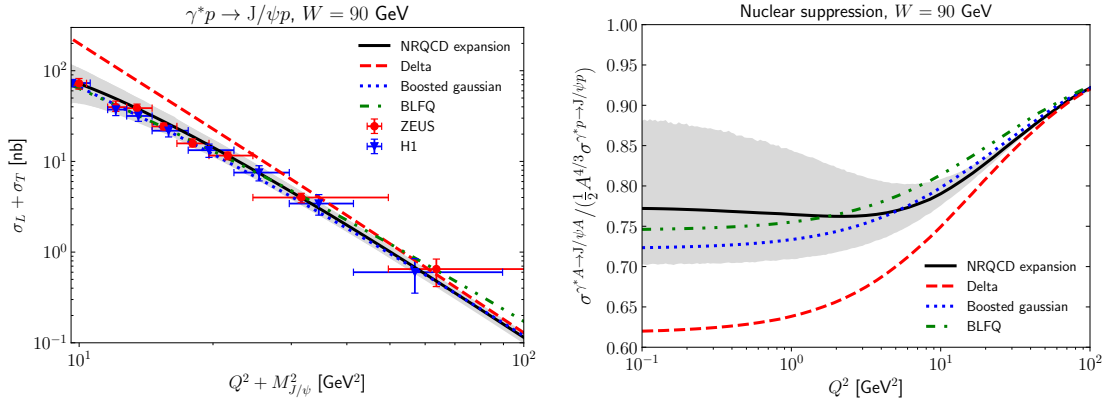$$M_{q\bar{q}}^2 = \frac{\mathbf{k}^2 + m^2}{z(1-z)} \tag{4.33}$$

(a) Total exclusive J/Ψ production.

(b) Nuclear suppression for J/Ψ production.

FIGURE 4.3   Exclusive J/Ψ production as a function of the photon virtuality Q^2 compared to the HERA data [90, 91] for different wave functions. *Delta* is the fully nonrelativistic limit for the wave function and *NRQCD expansion* includes the v^2 relativistic corrections. *Boosted gaussian* [47] and *BLFQ* [132] are phenomenological wave functions fitted to the leptonic width of J/Ψ and the charmonium mass spectrum, respectively. The IPsat parametrization from Ref. [76] was used for the dipole amplitude. Figures from Article [I], reproduced under the license CC BY 4.0.

is the invariant mass of the quark-antiquark pair. This change of variables is also known as the *Terentev substitution* [125]. The main problem with this is that it is impossible to conserve both the energy and the plus momentum in the wave function, or in other words the center-of-mass energy of the quark-antiquark pair $M_{q\bar{q}}$ does not agree with the mass of the meson M_V, and thus this relation cannot be truly exact. In Article [I], this appears through the fact that the leptonic widths for longitudinal and transverse modes differ depending on whether it is the $M_{q\bar{q}}$ or M_V that appears in the equations. The difference between the two masses can be seen as corrections from higher-order Fock states, related to the fact that the vector meson is the (approximate) eigenstate of the full Hamiltonian and the quark-antiquark pair only of the free Hamiltonian. Thus, we can treat the ambiguity in changing the variables as a higher-order correction that would need to be remedied if one were to consider corrections higher order in both velocity and α_s.

This combination of the Melosh rotation and the Terentev substitution is a common way to get a light-cone wave function from the rest-frame wave function. In Refs. [126–131] it has been used for a potential-model wave function, and in Article [I] we used it for the NRQCD-based wave function to include the relativistic v^2 corrections. From the explicit form of this *NRQCD expansion* wave function one can note several things as a consistency check. First, the symmetry relations (4.13), (4.16) and (4.19) are satisfied without imposing them directly. Second, the non-dominant spin components have the additional suppression of $v^{|m_L|}$ as explained previously.

The results of including these v^2 corrections in NRQCD to J/Ψ production at leading order in α_s are shown in Fig. 4.3a. The agreement with the HERA data

is extremely good, although the error band coming from the uncertainties of the LDMEs is quite large. Nevertheless, comparing the results to the fully nonrelativistic case we see that these relativistic corrections are important for small photon virtualities near $Q^2 = 0$. For large photon virtualities the relativistic corrections lose their importance, in agreement with explicit calculations in the limit $Q^2 \to \infty$ [133]. The dependence of relativistic effects on the photon virtuality can be understood by noting that the dipole sizes probed in the process are roughly $\mathbf{r}^2 \sim 1/(Q^2 + M_V^2)$, which means that for small virtualities larger dipoles become important. It is this dependence on large dipoles in the meson wave function that is modified by the relativistic corrections as can be seen from the expansion in Eq. (4.23). It should be noted that for the Υ particle the relativistic corrections are not expected to be important even for low photon virtualities, as the estimates for the average heavy quark velocity are very low [119].

In Fig. 4.3b, we show estimates for nuclear suppression of J/Ψ production in the EIC kinematics. Nuclear suppression is defined as the ratio

$$R_A = \frac{\sigma^{\gamma^* + A \to \mathrm{J}/\Psi + A}}{cA^{4/3}\sigma^{\gamma^* + p \to \mathrm{J}/\Psi + p}} \tag{4.34}$$

which can be used as a measure of nonlinear effects in the nucleus. The nuclear dipole amplitude $N_A(\mathbf{r}, \mathbf{b}', Y) = 1 - S_A(\mathbf{r}, \mathbf{b}', Y)$ has been approximated from the proton's dipole amplitude $N_p(\mathbf{r}, \mathbf{b}', Y) = 1 - S_p(\mathbf{r}, \mathbf{b}', Y)$, $S_p(\mathbf{r}, \mathbf{b}', Y) = \exp(-T_p(\mathbf{b}')f(\mathbf{r}, Y))$, by writing [63]

$$S_A(\mathbf{r}, \mathbf{b}') = \exp(-AT_A(\mathbf{b}')f(\mathbf{r}, Y)) \tag{4.35}$$

where $T_p(\mathbf{b}')$, $T_A(\mathbf{b}')$ are the transverse density profiles of the proton and the nucleus, and $f(\mathbf{r}, Y)$ is a function describing the dependence on the dipole size and rapidity $Y = \ln 1/x_{\mathbb{P}}$. Noting that $f(\mathbf{r}, Y) \to 0$ when $\mathbf{r} \to 0$, we can see that in the limit $Q^2 \to \infty$ the ratio (4.34) becomes

$$R_A(Q^2 \to \infty) = \frac{1}{c}\frac{A^2 \int \mathrm{d}^2\mathbf{b}'\, T_A(\mathbf{b}')^2}{A^{4/3}\int \mathrm{d}^2\mathbf{b}'\, T_p(\mathbf{b}')^2} \equiv 1 \tag{4.36}$$

which defines the normalization constant c. The factor $A^{4/3}$ in Eq. (4.34) has been chosen to minimize the dependence of the constant c on the mass number A. Note that the effects of the wave function cancel in this limit. The estimates for nuclear suppression in Fig. 4.3b indicate that while this cancellation of the wave function is true in the asymptotic limit, for values $Q^2 \lesssim M_V^2$ the wave function effects start to become visible. Thus, the form of the wave function does not cancel in this ratio, and a naïve nonrelativistic approximation does not give a realistic picture of the saturation effects. In general, relativistic corrections suppress the contribution from large dipoles, which results in a smaller sensitivity to nonlinear effects. This is especially visible for smaller photon virtualities where the production is more sensitive to larger dipole sizes. It is thus important to use a realistic wave function for J/Ψ when looking for saturation in heavy nuclei.

4.2 Exclusive vector meson production at next-to-leading order

At next-to-leading order, there are essentially two modifications that we need to make to the leading-order amplitude Eq. (4.1). First, we need to also include the case where the photon fluctuates into a $q\bar{q}g$ state that interacts with the target. This can be included in the production amplitude by writing

$$
\begin{aligned}
i\mathcal{M} = &\int \mathrm{d}^2\mathbf{x}_0\,\mathrm{d}^2\mathbf{x}_1 \int_0^1 \frac{\mathrm{d}z_0\,\mathrm{d}z_1}{(4\pi)^2 z_0 z_1}(4\pi)\delta(1 - z_0 - z_1)\\
&\times e^{-i\mathbf{b}\cdot\boldsymbol{\Delta}}\widetilde{\Psi}^{\gamma\to q\bar{q}}(\mathbf{x}_{01}, z_i)\left(\widetilde{\Psi}^{V\to q\bar{q}}(\mathbf{x}_{01}, z_i)\right)^*\left(1 - \hat{S}_{01}\right)\\
&+ \int \mathrm{d}^2\mathbf{x}_0\,\mathrm{d}^2\mathbf{x}_1\,\mathrm{d}^2\mathbf{x}_2 \int_0^1 \frac{\mathrm{d}z_0\,\mathrm{d}z_1\,\mathrm{d}z_2}{(4\pi)^3 z_0 z_1 z_2}(4\pi)\delta(1 - z_0 - z_1 - z_2)\\
&\times e^{-i\mathbf{b}\cdot\boldsymbol{\Delta}}\widetilde{\Psi}^{\gamma\to q\bar{q}g}(\mathbf{x}_i, z_i)\left(\widetilde{\Psi}^{V\to q\bar{q}g}(\mathbf{x}_i, z_i)\right)^*\left(1 - \hat{S}_{012}\right).
\end{aligned}
\tag{4.37}
$$

Note that here we also include the dependence on the total momentum transfer $\boldsymbol{\Delta}$ that was missing from Articles [II, III, IV] where only the case $t = -\boldsymbol{\Delta}^2 = 0$ was considered. Second, the wave functions $\widetilde{\Psi}^{\gamma\to q\bar{q}}$, $\widetilde{\Psi}^{V\to q\bar{q}}$ need to be calculated at next-to-leading order. The photon wave functions are perturbative also at NLO and have been calculated in Refs. [134–136] for massless quarks and in Refs. [84–86] for massive quarks. For the meson, we need to calculate Feynman diagrams in Figs. 4.4 and 4.5 where the $V \to q\bar{q}$ vertex is given by the leading-order wave function. The self-energy diagrams 4.4a and 4.4b contribute to the renormalization factor $\sqrt{Z_V}$ of the meson, and the gluon exchange diagrams 4.4c, 4.4d and 4.4e are then genuine NLO corrections to the wave function. For the Fock state $q\bar{q}g$, the perturbative contribution to the meson wave function $\Psi^{V\to q\bar{q}g}$ can be calculated in a similar manner using Diagrams 4.5a and 4.5b. Diagram 4.5c corresponds to a nonperturbative contribution to the $\Psi^{V\to q\bar{q}g}$ wave function. In principle, it should be included in the calculation, but it turns out that in the limits considered in Articles [II, III, IV] this nonperturbative contribution can be neglected. The required meson wave functions at NLO have been calculated in Ref. [137] for heavy vector mesons and in Article [III] for light vector mesons and will be explained briefly in Secs. 4.2.1 and 4.2.2.

The next-to-leading order calculation also requires that we are careful with the regularization of loop integrals. As light-cone perturbation theory breaks the explicit Lorentz symmetry, a Lorentz invariant regularization scheme such as dimensional regularization cannot be used. Instead, a common regularization scheme suitable for light-cone calculations is to consider longitudinal and transverse directions separately. In the transverse direction, one uses dimensional regularization so that the integrals are done in $D - 2 = 2 - 2\varepsilon$ transverse dimensions. For the longitudinal direction, one introduces a cut-off for gluons' plus-momenta such that $k_2^+ > \alpha q^+$ where $\alpha > 0$. This means that we encounter two different kinds of divergences: infrared (IR) or ultraviolet (UV) divergences of the transverse momenta when $\varepsilon \to 0$, and divergences in the gluon's plus momentum when $\alpha \to 0$.

(a)

(b)

(c)
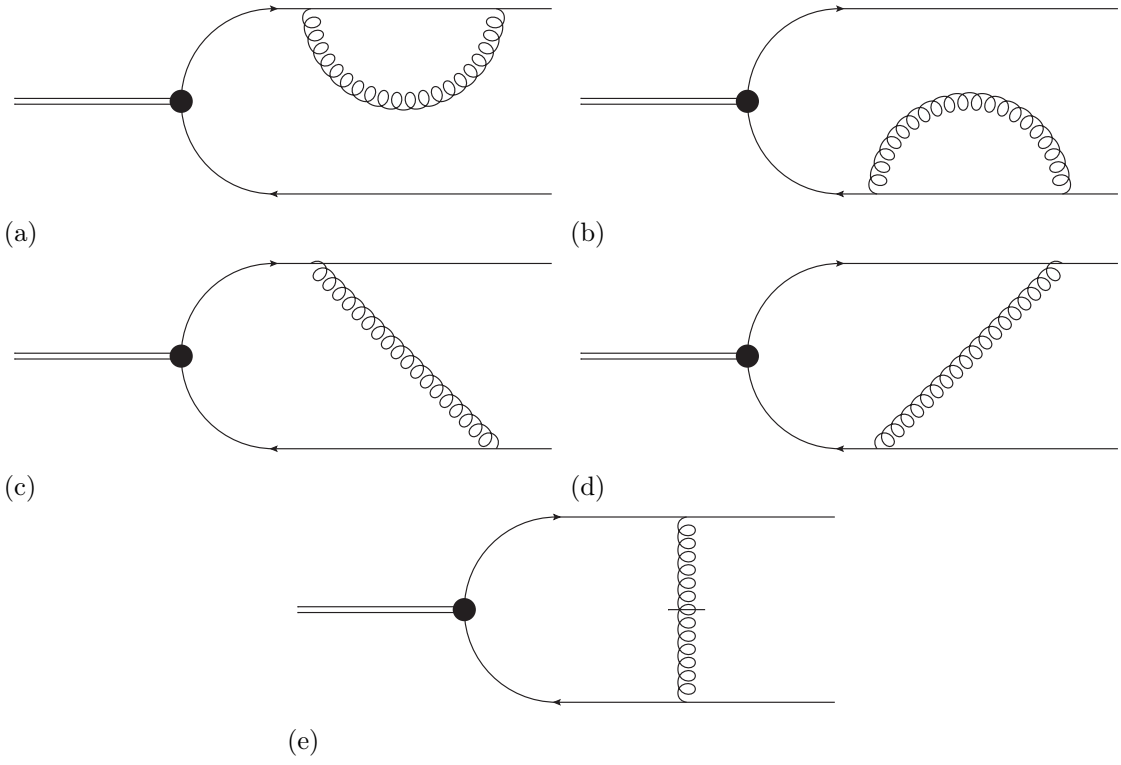
(d)

(e)

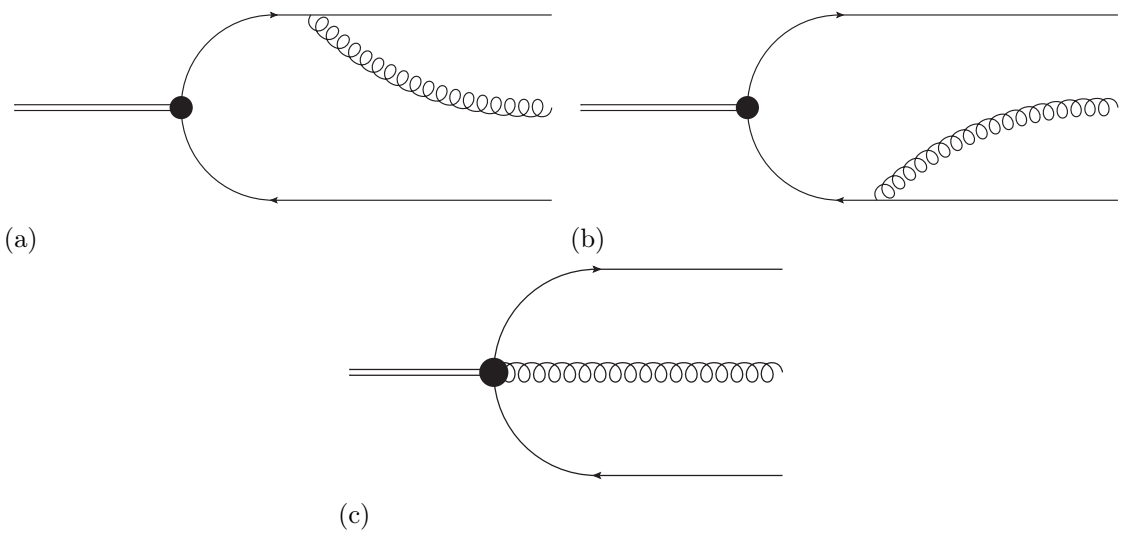FIGURE 4.4   The NLO corrections to the meson wave function $\Psi^{V \to q\bar{q}}$.

(a)

(b)

(c)

FIGURE 4.5   Contributions to the meson wave function $\Psi^{V \to q\bar{q}g}$ at NLO.

Several things need to be considered when summing different NLO contributions to get a finite result in the end. First of all, the two different parts in the production amplitude, Eq. (4.37), are separately divergent but many of the divergences cancel in their sum. This is because the $q\bar{q}g$-contribution contains divergent gluon loops similar to Diagrams 4.4a and 4.4b, with the exception that the gluon also crosses the shock wave describing the interaction with the target. In addition to this the nonperturbative parts of the calculation, i.e. the dipole amplitude and the vector meson wave function, need to be renormalized. The renormalization of the dipole amplitude is done by the BK equation, which leads to the rapidity dependence of the dipole amplitude. The NLO calculations in Articles [II, III, IV] suggest that this rapidity scale should be chosen as $Y_{\mathrm{dip}} = Y_0 + \ln\left((1-z_0)\frac{W^2+Q^2-m_n^2}{Q_0^2}\right)$ in the leading-order part, where Q_0^2 is the transverse scale of the target and $Y_{0,\mathrm{if}}$ is the factorization rapidity scale discussed in Sec. 3.3.3. This differs somewhat from the common choice $Y_{\mathbb{P}} = \ln 1/x_{\mathbb{P}} = \ln\left(\frac{W^2+Q^2-m_n^2}{Q^2+M_V^2-t}\right)$ used in the leading-order calculations. For the meson wave function, only the leading-order wave function corresponding to the $V \to q\bar{q}$ vertex needs to be renormalized. This is done differently for heavy and light vector mesons and will be discussed in more detail in Secs. 4.2.1 and 4.2.2.

4.2.1 Heavy vector meson production in the nonrelativistic limit

A framework to include higher-order corrections systematically in α_{s} and heavy quark velocity v has been developed in Ref. [137], where the meson wave functions are expanded as a power series of corrections in the heavy quark velocity v and the coupling constant α_{s} as

$$\widetilde{\Psi}_V^n = \sum_{k,l} C_{n\leftarrow l}^k \int_0^1 \frac{\mathrm{d}z'}{4\pi} \left(\frac{1}{m}\widetilde{\nabla}\right)^k \phi^l(\mathbf{r} = \mathbf{0}, z'). \tag{4.38}$$

This equation describes how the light-cone wave function Ψ_V for a Fock state n can be written in terms of the leading-order wave function ϕ for the Fock state l. The coefficients $C_{n\leftarrow l}^k$ can be calculated perturbatively, and they contain the α_{s} corrections from Feynman diagrams. The derivatives $\widetilde{\nabla} = \left(\mathbf{\nabla}_{\mathbf{r}}, 2mi\left[z' - \frac{1}{2}\right]\right)$ correspond to relativistic corrections where the order of the term is given by the power k, with the exception that non-dominant spin components have additional relativistic suppression as explained in Sec. 4.1.1. This allows one to expand the wave function as a power series in both α_{s} and v, and in a sense it is a generalization of Eq. (4.23) to the mixed space including also corrections in α_{s}. The NRQCD estimate for the velocity of the heavy quark is $v \gtrsim \alpha_{\mathrm{s}}$ [117], and numerical estimates confirm that for J/Ψ we have roughly $v^2 \sim \alpha_{\mathrm{s}}$ [118]. This leads to the estimate $1 \gg \alpha_{\mathrm{s}} \gtrsim v^2 \gg \alpha_{\mathrm{s}}v^2$ for different terms in the expansion, which suggests that the most important correction to the leading order is the NLO correction in the nonrelativistic limit. This is also the limit where the coefficients $C_{n\leftarrow l}^k$ have been calculated in Ref. [137]. Note, however, that the importance of the relativistic corrections depends on the kinematical region as discussed in Sec. 4.1.1.

Taking the nonrelativistic limit for the NLO calculation leads to a significant simplification of the calculation. For example, the only nonperturbative part of the

vector meson wave function is then the leading-order wave function for the $q\bar{q}$ state, as the wave functions for the other states are suppressed by v or $\alpha_{\rm s}$. For example, the leading-order wave function for the $q\bar{q}g$ state corresponding to Diagram 4.5c is suppressed by $\alpha_{\rm s}v^2$ in the production amplitude. Also, in the nonrelativistic limit only the integrated leading-order wave function

$$\int_0^1 \frac{{\rm d}z'}{4\pi} \phi^{q\bar{q}}(\mathbf{r} = \mathbf{0}, z') \tag{4.39}$$

survives, meaning that the nonperturbative physics of vector meson formation is given by a single constant. It should be mentioned that this is in agreement with the approach where one starts from the nonrelativistic limit in the rest frame as described in Sec. 4.1.1.

This nonperturbative constant still needs to be renormalized, which in a general scheme can be written as [137]

$$\int_0^1 \frac{{\rm d}z'}{4\pi} \phi^{q\bar{q}}(\mathbf{0}, z') = \int_0^1 \frac{{\rm d}z'}{4\pi} \phi^{q\bar{q}}_{\rm renorm}(\mathbf{0}, z') \left[1 - \frac{\alpha_{\rm s} C_F}{2\pi} \left(\frac{1}{\alpha} + f_{\rm scheme}\right)\right]. \tag{4.40}$$

Choosing the finite part $f_{\rm scheme}$ can be done in several different ways. The simplest way is to choose $f_{\rm scheme} = 0$ as then it turns out that $\phi^{q\bar{q}}_{\rm renorm}$ corresponds to using dimensional regularization in all space-time dimensions [137]. This regularization scheme for the wave function has been used in Refs. [118, 119] to determine non-perturbative LDMEs for J/Ψ and Υ, and as such using this scheme allows one to use those results without additional scheme matching. This is especially useful if one wants to consider relativistic corrections at leading order on top of the NLO corrections.

Another choice for the scheme is to consider the leptonic width of the meson at NLO [137]

$$\Gamma\left(V \to e^- e^+\right) = \frac{2N_c e_f^2 e^4}{3\pi M_V} \left|\int \frac{{\rm d}z'}{4\pi} \phi^{q\bar{q}}(\mathbf{0}, z')\right|^2 \left[1 + \frac{\alpha_{\rm s} C_F}{\pi} \left(\frac{1}{\alpha} - 4\right)\right] \tag{4.41}$$

and solve the leading-order wave function from this equation. This corresponds to the choice $f_{\rm scheme} = -4$. While this is simpler as it directly relates the nonperturbative leading-order wave function to the physical leptonic width, it is not as convenient in actual calculations. For example, when taking into account the running of the coupling it is not clear if the running is the same in the leptonic width and the production amplitude. For these reasons, in Article [IV] we recommend using the scheme with $f_{\rm scheme} = 0$ for calculating vector meson production. The dependence of the production on the renormalization scheme is mostly mild at high energies, but in certain kinematical regions it can have a significant numerical contribution to the production cross section [IV].

In addition to the leading-order wave function, one also needs to renormalize the mass of the heavy quark. This was done in the pole mass scheme which is set by demanding that the mass of the quark agrees with the pole of the quark propagator. The mass renormalization is more complicated in the light-cone quantization compared to the covariant formalism, as the breaking of the Lorentz symmetry brings
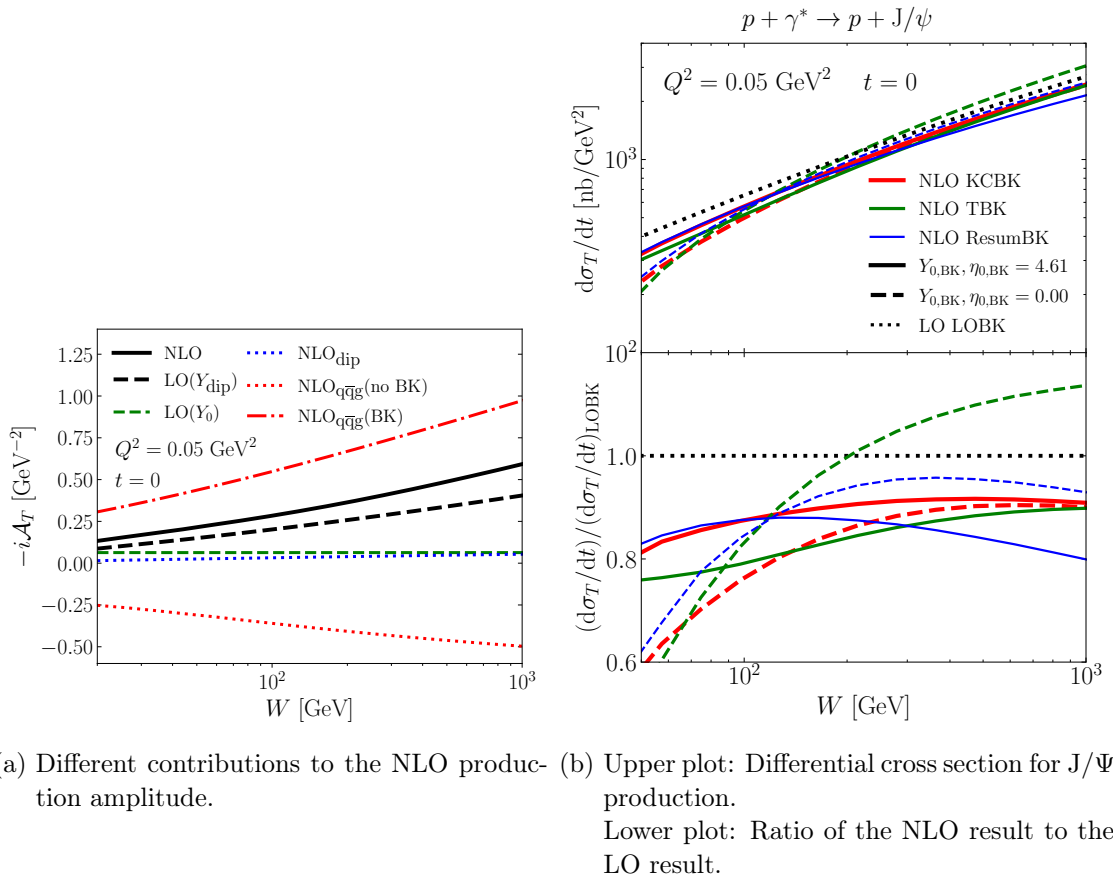
$p + \gamma^* \to p + \mathrm{J}/\psi$

(a) Different contributions to the NLO produc-
tion amplitude.

(b) Upper plot: Differential cross section for J/Ψ
production.
Lower plot: Ratio of the NLO result to the
LO result.

FIGURE 4.6   Tranverse J/Ψ production at next-to-leading order as a function of the
center-of-mass energy W. Figures from Article [III], reproduced under the
license CC BY 4.0.

additional complications. This is discussed in detail in Ref. [86] where the effect
of using the pole mass scheme in the photon wave function is calculated using the
Lorentz invariance of the photon form factors. A different approach for mass renor-
malization is described in Ref. [137] where the mass renormalization for the meson
wave function is calculated using an approach closer to the covariant formalism. We
have checked that these two approaches for the pole mass scheme agree, meaning
that no additional scheme matching has to be done to use the two wave functions.

After these renormalizations and absorbing the remaining rapidity divergence
$\ln \alpha$ to the BK evolution of the dipole amplitude, the invariant amplitude for the
vector meson production is finite and can be calculated. The final result is compli-
cated and contains high-dimensional integrals, but it is possible to evaluate these
expressions numerically. The NLO expressions and their numerical solutions were
computed in Article [II] for longitudinal production and Article [IV] for transverse
production. The main results of these articles are summarized in Fig. 4.6. The NLO
results are shown using the NLO dipole amplitude fits discussed in Sec. 3.3.3 that
were fitted to the full HERA structure function data with the *Balitsky+smallest
dipole* running coupling scheme. In general, the NLO results are fairly close to the
LO result, although there is some dependence on the dipole amplitude used. This
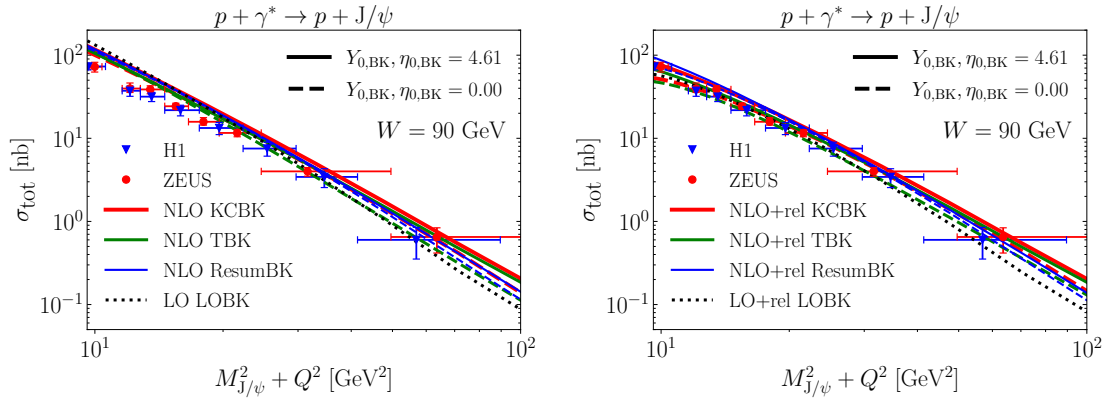
(a) Nonrelativistic limit.

(b) With relativistic $\alpha_s^0 v^2$ corrections.

FIGURE 4.7   Total coherent J/Ψ production as a function of the photon virtuality Q^2 compared to the HERA data [89–91, 93]. Figures from Article [IV], reproduced under the license CC BY 4.0.

is especially visible at lower energies, $W \lesssim 100\,\mathrm{GeV}$, where the BK evolution is not as dominant.

Remembering that the dipole amplitudes were fitted to the same HERA structure function data, it is interesting to see differences in vector meson production between the results corresponding to different fits. One reason for this is that vector meson production probes the dipole amplitude at length scales $1/(Q^2 + M_V^2)$ as opposed to $1/Q^2$ in inclusive DIS, making vector meson production more sensitive to the behavior of the dipole amplitude at smaller dipoles. Another reason for the differences between the different dipole amplitudes is that when calculating the cross section we choose to drop terms of the order $\mathcal{O}(\alpha_s^2)$ for consistency with the power counting. To do this, we need to determine the LO part from the result which is not unique. Our choice for this is the LO amplitude calculated with the rapidity Y_dip that is motivated by the NLO part of the calculation. This choice corresponds to resumming large logarithms $\sim \alpha_s \ln 1/x$ with the BK equation and including them as a part of the LO result. The caveat with this approach is that the resulting $\mathcal{O}(\alpha_s^2)$ terms may be quite large, which can be seen in Fig. 4.6a as the difference between the "NLO" and "LO(Y_dip)" results. The effect of dropping the $\mathcal{O}(\alpha_s^2)$ contributions is especially large at lower energies where dropping these contributions may result in negative cross sections. One does not need to do this division of the LO result and the genuine NLO corrections when calculating the inclusive DIS cross section and fitting the dipole amplitude, and dependence on this choice is an additional uncertainty to exclusive vector meson production. If one does not drop the $\mathcal{O}(\alpha_s^2)$ higher-order terms, one will get results that are closer to each other and more in line with the fitting procedure. This approach, however, is not consistent with the perturbative expansion and for this reason we did not choose to do so in Articles [II, IV]. It is left for future work to better understand the division between the LO and NLO terms.

In addition to the NLO corrections in the nonrelativistic limit, we also included the relativistic corrections $\mathcal{O}(v^2)$ at leading order. Their contribution is shown

in Fig. 4.7 as a function of the photon virtuality, where it can be seen that the relativistic corrections are important even at NLO when considering J/Ψ production at small photon virtualities. In fact, in photoproduction the relativistic corrections seem to be even more important than the NLO corrections. For Υ production, the relativistic effects are estimated to be so small that they can be neglected for all photon virtualities, and the NLO effects are more important [IV].

Finally, we would like to highlight that the main purpose of Articles [II, IV] was to calculate the NLO expression for heavy vector meson production in the nonrelativistic limit, and thorough phenomenological analyses are left for future work. For example, varying the heavy quark mass m within the uncertainties of the experimentally measured value has a large effect for small Q^2 [47], which needs to be taken into account when comparing against the data. Also, there exists data for t-differential J/Ψ production, which can be used to gain information about the impact parameter dependence of the dipole amplitude. Another interesting prospect is to consider heavy vector meson production from heavy nuclei which is more sensitive to saturation. There is already a reasonable amount of data for J/Ψ production from Pb-Pb collisions measured in the ultra-peripheral collisions at the LHC [7, 8, 94–98], with similar data for Υ expected to come soon. Calculating this requires modeling the nuclear dipole amplitude in terms of the proton dipole amplitude using a relation such as Eq. (4.35), which is yet to be done with the NLO dipole amplitude fits.

4.2.2 Light vector meson production at large photon virtualities

For light vector meson production to be perturbative one has to have a high enough photon virtuality. An additional simplification of the process can be done by assuming that the photon virtuality is higher than any momentum scale on the meson side, meaning that we can essentially neglect the meson mass and the transverse momenta of the quark and antiquark in the meson. This can be given a precise mathematical formulation in the mixed space by noting that in the high-photon virtuality limit only dipoles of the size $1/Q^2$ contribute. We can then write the leading-order wave function as a Taylor series in the transverse dipole sizes,

$$\widetilde{\Psi}^{q\bar{q}}(\mathbf{r}, z) = \widetilde{\Psi}^{q\bar{q}}(\mathbf{0}, z) + \mathcal{O}(\mathbf{r}^2), \tag{4.42}$$

and in the limit $Q^2 \to \infty$ only the first term contributes to light vector meson production. This $\mathbf{r}$-independent term can be written in terms of the leading-twist distribution amplitude of the meson $\phi(z)$ which for longitudinal polarization has twist 2 [106, 138]. For transverse polarization, the leading term is proportional to $\mathbf{r} \cdot \boldsymbol{\varepsilon}_\lambda$, corresponding to a twist-3 term [138]. The expansion (4.42) can be considered as a twist expansion where higher-twist terms are suppressed by powers of Q, which also allows us to neglect transverse production in comparison to the longitudinal one as the transverse production is then suppressed by $|\mathbf{r} \cdot \boldsymbol{\varepsilon}_\lambda|^2 \sim 1/Q^2$. Such an expansion also shows that the leading-order wave function for the Fock state $q\bar{q}g$ has twist 3, meaning that the nonperturbative diagram 4.5c can be neglected [139, 140]. Thus, the leading-twist contribution to light vector meson production at NLO can be written in terms of the twist-2 distribution amplitude for longitudinal polarization. This

leads to a simplification of the calculation as the first term in the expansion (4.42) corresponds to a delta function $\delta^2(\mathbf{k})$ in momentum space. Also, all of the nonperturbative physics on the meson side is included in the twist-2 distribution amplitude $\phi(z)$.

The distribution amplitude $\phi(z)$ still needs to be renormalized in the calculation. This is done with the well-known Efremov–Radyushkin–Brodsky–Lepage (ERBL) equation [48, 141] which corresponds to a resummation of gluon exchanges between the quark and antiquark with transverse momenta $\mathbf{k}^2 < Q^2$. In general, the renormalized distribution amplitude $\phi(z, \mu_F)$ can be written in terms of the bare distribution amplitude $\phi_0(z)$ as

$$
\begin{aligned}
\phi(z, \mu_F) = {} & \phi_0(z) \\
& + \frac{\alpha_{\mathrm{s}} C_F}{2\pi} \int_0^1 \mathrm{d}z' \, \phi_0(z') \left[K(z, z') \left(\frac{2}{D-4} + \gamma_E - \ln(4\pi) + \ln\left(\frac{\mu_F^2}{\mu^2}\right) \right) + f_{\mathrm{scheme}} \right]
\end{aligned}
\tag{4.43}
$$

where $K(z, z')$ is the ERBL kernel

$$
\begin{aligned}
K(z, z') = {} & \frac{z}{z'} \left(1 + \frac{1}{z' - z} \right) \theta(z' - z - \alpha) + \frac{1-z}{1-z'} \left(1 + \frac{1}{z - z'} \right) \theta(z - z' - \alpha) \\
& + \left(\frac{3}{2} + \ln \frac{\alpha^2}{z(1-z)} \right) \delta(z' - z),
\end{aligned}
\tag{4.44}
$$

μ is the scale from dimensional regularization and f_{scheme} is a finite scheme-dependent term. This introduces a dependence on the factorization scale μ_F to the distribution amplitude, which is given by the ERBL equation

$$
\frac{\partial}{\partial \ln \mu_F^2} \phi(z, \mu_F) = \frac{\alpha_{\mathrm{s}} C_F}{2\pi} \int_0^1 \mathrm{d}z' \, K(z, z') \phi(z', \mu_F).
\tag{4.45}
$$

The ERBL equation can be solved exactly by

$$
\phi(z, \mu_F) = \sum_{n=0}^{\infty} a_n(\mu_F) f_n(z)
\tag{4.46}
$$

where the dependence on the factorization scale is contained in the coefficients a_n, and the eigenfunctions f_n of the ERBL equation can be written in terms of the Gegenbauer polynomials $C_n^{\left(\frac{3}{2}\right)}$ as

$$
f_n(z) = 6z(1 - z) C_n^{\left(\frac{3}{2}\right)}(2z - 1).
\tag{4.47}
$$

It is interesting to note that in the limit $\mu_F \to \infty$ the solutions of the ERBL equation are driven towards the asymptotic limit $\phi(z, \mu_F = \infty) = 6z(1 - z)a_0$.

In Article [III], we choose $f_{\mathrm{scheme}} = 0$ in accordance with the $\overline{\mathrm{MS}}$ scheme. We note, however, that a regularization-scheme dependent choice might also be suitable. We do the NLO calculation in a formalism that allows one to use two different
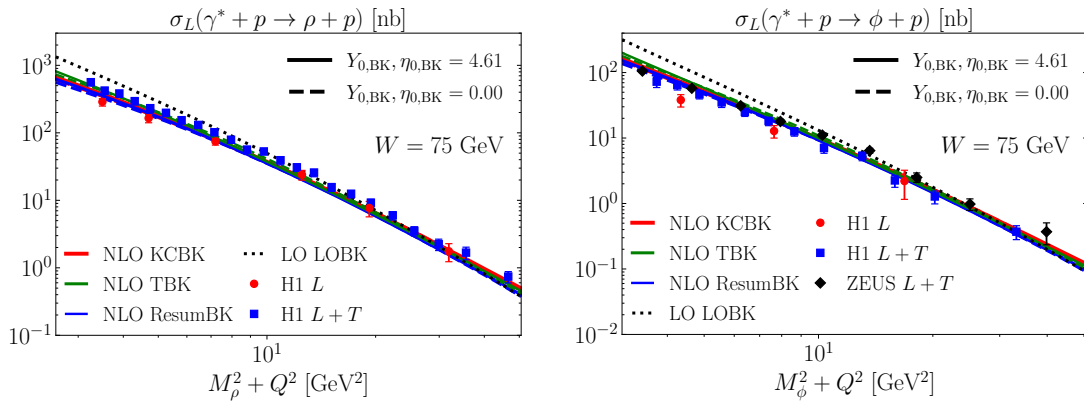
(a) Exclusive ρ production.　　　　(b) Exclusive ϕ production.

FIGURE 4.8　　Exclusive light vector meson at next-to-leading order as a function of the photon virtuality Q^2. Figures from Article [III], reproduced under the license CC BY 4.0.

regularization schemes for gluon polarization vectors, the so-called "conventional dimensional regularization" and the "four-dimensional helicity" schemes [142, 143]. With the $\overline{\text{MS}}$ scheme, the resulting equations still contain a constant dependent on the regularization scheme which could be included in the renormalization of the distribution amplitude. This scheme dependence arises because the distribution amplitude is a nonperturbative quantity, and a similar scheme-dependent part should appear in other processes involving the distribution amplitude as well. In the case of exclusive light vector meson production this scheme-dependent constant has an extremely small contribution [III], and it vanishes if one takes the asymptotic form of the distribution amplitude.

The factorization scale μ_F should be chosen as the relevant scale of the process. The NLO calculation suggests the choice $\mu_F^2 = 4e^{-2\gamma_E}/\mathbf{r}^2$ which is also in line with the Fourier transform estimates for the running of the coupling constant [82]. Another possible choice is $\mu_F^2 = Q^2$ which has the attractive property that the factorization scale is constant in the calculation. The differences between these two choices are fairly small for reasonable forms of the distribution amplitude, less than 5% [III].

The resulting expression for the longitudinal production amplitude is finite and can be numerically evaluated. It has been calculated before in a different framework in Ref. [144] where the resulting expressions are presented in momentum space. This makes comparisons between the two calculations difficult, as one has to perform complicated Fourier transforms from the momentum space to the coordinate space. So far, only parts of the calculation have been compared with agreeing results.

The main numerical results for ρ and ϕ meson production from Article [III] are shown in Fig. 4.8. These calculations use a distribution amplitude that is close to the asymptotic form, including also the $n = 2$ correction in Eq. (4.46) using numerical estimates from Refs. [145, 146]. The contributions from this correction to the asymptotic form are almost negligible in these figures, less than 10%. In general, we find a very good agreement with the NLO results to the longitudinal

production data. Note that the total production, longitudinal + transverse, should be dominated by the longitudinal production in the $Q^2 \to \infty$ limit, and thus it is consistent to compare to the total production data also. Only for smaller photon virtualities our results seem to overestimate the longitudinal production data, and it is expected that there the higher-twist effects should also contribute. Here the agreement between the different dipole amplitude fits is better than in the case of heavy vector meson production. This can be understood by the fact that in inclusive DIS, where the dipole amplitude fit is done, the same dipole sizes $1/Q^2$ are probed as in light vector meson production. In contrast, for heavy vector meson production the probed dipole sizes are modified by the heavy meson mass as $1/(Q^2 + M_V^2)$.

5   INCLUSIVE DIFFRACTION

Exclusive vector meson production is an example of an exclusive process where all of the produced particles are explicitly measured. The opposite of this is an inclusive process where the final states are summed over. We have already briefly considered total inclusive particle production in Sec. 3.3.1 where the final state is not restricted. In addition to this, we can consider inclusive diffraction where the interaction with the target is color neutral, resulting in final states that are in a color singlet. This corresponds to the process in Fig. 2.1 with a sum over the final states X.

Inclusive diffraction has several advantages compared to exclusive vector meson production. First, we are not as restricted in our final state, leading to a higher cross section. Second, the only nonperturbative part of the process is the interaction with the target, making inclusive diffraction a very clean probe of the target structure. When compared to the total inclusive production, the advantage of inclusive diffraction is its higher sensitivity to the small-x gluon distribution, enhancing the nonlinear effects. Also, more differential quantities can be measured, such as the dependence on the momentum transfer t and the invariant mass of the final state $M_X^2 = P_X^2$. The momentum-transfer dependence gives us information about the geometry of the target in the transverse plane, similarly as in exclusive vector meson production in Ch. 4. The dependence on the invariant mass is related to the relevant Fock states in the process as will be explained shortly.

Inclusive diffraction can be naturally calculated using Eqs. (2.43) and (2.46) from Sec. 2.4. This leads to the cross section

$$\frac{\mathrm{d}\sigma_{\gamma_\lambda^* + A}^{\mathrm{D}}}{\mathrm{d}|t|\,\mathrm{d}M_X^2} = \sum_{\substack{\text{color-singlet} \\ \text{states } n}} \int \mathrm{d}[\mathrm{PS}]_n\, 2q^+(2\pi)\delta(q^+ - q_n^+)\big|\mathcal{M}_{\gamma_\lambda^* \to n}\big|^2 \delta(M_X^2 - M_n^2)\delta\left(|t| - \boldsymbol{\Delta}^2\right)$$

(5.1)

where the delta functions specify the given momentum transfer t and invariant mass M_X^2 of the final state. At leading order, only the final state $X = q\bar{q}$ contributes, and calculating the cross section corresponds to evaluating the Feynman diagram in
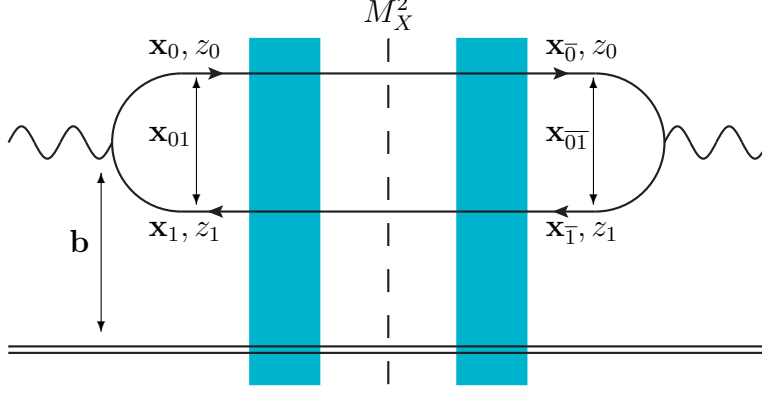
59

FIGURE 5.1   Inclusive diffractive DIS at leading order in the dipole picture. The blue rectangle depicts the interaction with the target, and the dashed line corresponds to the final state which is set to have an invariant mass M_X^2.

Fig. 5.1. The leading-order cross section evaluates to [147, 148]

$$\frac{\mathrm{d}\sigma_{\gamma_\lambda^*+A}^{\mathrm{D}}}{\mathrm{d}|t|\,\mathrm{d}M_X^2} = 2\pi\alpha_{\mathrm{em}}N_c Q^2 \sum_f e_f^2 \int \frac{\mathrm{d}^2\mathbf{x}_0\,\mathrm{d}^2\mathbf{x}_1\,\mathrm{d}^2\mathbf{x}_{\bar{0}}\,\mathrm{d}^2\mathbf{x}_{\bar{1}}}{(2\pi)^4} \int_0^1 \mathrm{d}z_0\,\mathrm{d}z_1\,\delta(1-z_0-z_1)$$

$$\times \frac{1}{4\pi} J_0\big(|t||\mathbf{b}-\overline{\mathbf{b}}|\big) J_0\big(|\mathbf{x}_{01}-\mathbf{x}_{\overline{01}}|M_X\sqrt{z_0 z_1}\big)\mathcal{F}_\lambda \left\langle 1-\hat{S}_{01}\right\rangle\left\langle 1-\hat{S}_{\overline{01}}\right\rangle^* \tag{5.2}$$

where

$$\mathcal{F}_\lambda = \begin{cases} 4z_0^3 z_1^3 K_0(|\mathbf{x}_{01}|Q\sqrt{z_0 z_1})K_0(|\mathbf{x}_{\overline{01}}|Q\sqrt{z_0 z_1}) & \lambda = L \\ z_0^2 z_1^2 (z_0^2 + z_1^2) K_1(|\mathbf{x}_{01}|Q\sqrt{z_0 z_1})K_1(|\mathbf{x}_{\overline{01}}|Q\sqrt{z_0 z_1})\frac{\mathbf{x}_{01}\cdot\mathbf{x}_{\overline{01}}}{|\mathbf{x}_{01}||\mathbf{x}_{\overline{01}}|} & \lambda = T \end{cases} \tag{5.3}$$

depends on the photon polarization λ. It should be mentioned that this is the *coherent* production cross section, in line with the notation used in Ch. 4. Total (i.e. coherent+incoherent) cross section corresponds to Eq. (5.2) with the average over the target fluctuations taken as $\left\langle \left(1-\hat{S}_{01}\right)\left(1-\hat{S}_{\overline{01}}\right)^\dagger\right\rangle$ instead.

The inclusive diffractive cross section can be related to the diffractive structure functions, defined as

$$x_{\mathbb{P}}F_\lambda^{\mathrm{D}(4)}(\beta, Q^2, x_{\mathbb{P}}, t) = \frac{Q^2}{(2\pi)^2\alpha_{\mathrm{em}}}\frac{Q^2}{\beta}\frac{\mathrm{d}\sigma_{\gamma_\lambda^*+A}^{\mathrm{D}}}{\mathrm{d}|t|\,\mathrm{d}M_X^2}. \tag{5.4}$$

The superscript indicates how many variables the structure function $x_{\mathbb{P}}F_\lambda^{\mathrm{D}(4)}$ depends on. The variables β and $x_{\mathbb{P}}$ are defined for inclusive diffraction as

$$\beta = \frac{Q^2}{2q\cdot(P_n - P_n')} = \frac{Q^2}{Q^2 + M_X^2 - t} \approx \frac{Q^2}{Q^2 + M_X^2}, \tag{5.5}$$

$$x_{\mathbb{P}} = \frac{q\cdot(P_n - P_n')}{q\cdot P_n} = \frac{Q^2 + M_X^2 - t}{W^2 + Q^2 - m_n^2} \approx \frac{Q^2 + M_X^2}{W^2 + Q^2}. \tag{5.6}$$
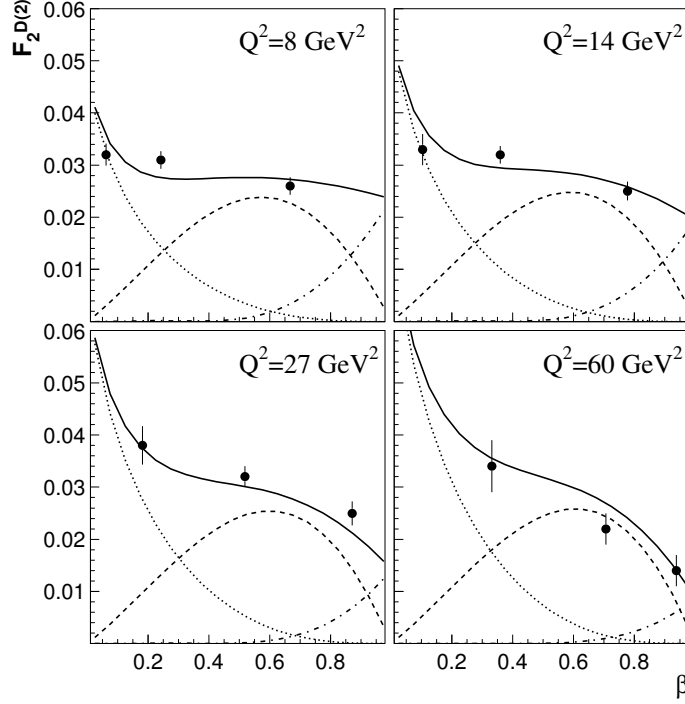
ZEUS 1994

FIGURE 5.2   Theoretical predictions for the diffractive structure function $F_2^{\mathrm{D}(2)}(\beta, Q^2)$ compared against the HERA data [149].
Dashed line: Leading-order $q\bar{q}$ contribution for transverse photons.
Dot-dashed line: Leading-order $q\bar{q}$ contribution for longitudinal photons.
Dotted line: Large-Q^2 contribution for the $q\bar{q}g$ state for transverse photons.
Reprinted figure with permission from K. Golec-Biernat, and M. Wusthoff, Phys. Rev. D, 60, 114023, 1999. Copyright (1999) by the American Physical Society.

Other interesting observables are the t-integrated diffractive structure functions

$$F_\lambda^{\mathrm{D}(3)}(\beta, Q^2, x_{\mathbb{P}}) = \int_0^\infty \mathrm{d}|t|\, F_\lambda^{\mathrm{D}(4)}(\beta, Q^2, x_{\mathbb{P}}, t), \tag{5.7}$$

$$F_2^{\mathrm{D}(3)}(\beta, Q^2, x_{\mathbb{P}}) = F_L^{\mathrm{D}(3)}(\beta, Q^2, x_{\mathbb{P}}) + F_T^{\mathrm{D}(3)}(\beta, Q^2, x_{\mathbb{P}}), \tag{5.8}$$

and the most precise data is given in terms of the diffractive reduced cross section

$$\sigma_r^{\mathrm{D}(3)}(\beta, Q^2, x_{\mathbb{P}}) = F_2^{\mathrm{D}(3)}(\beta, Q^2, x_{\mathbb{P}}) - \frac{y^2}{1 + (1-y)^2} F_L^{\mathrm{D}(3)}(\beta, Q^2, x_{\mathbb{P}}) \tag{5.9}$$

analogously to the inclusive case (3.33).

Experimental measurements of inclusive diffraction at DIS have been done at HERA [13, 14, 149–160] where it has been measured in $p+e^-$ collisions. Comparisons of the data and theory then showed that the leading-order picture is not enough to describe diffractive DIS at low values of β [149]. This is shown in Fig. 5.2 where it can

be seen that the leading-order results (5.2) fall to zero when $\beta \to 0$, in contradiction with the measured data. This started calculations of the process at next-to-leading order, as it was found that gluon emission starts to dominate in the limit $\beta \to 0$, which was first calculated in Refs. [62, 161–163] in the large-Q^2 limit. Including these gluonic contributions to the cross section results in a very good agreement with the data as can be seen in Fig. 5.2. The more natural large-M_X^2 limit has later been calculated by several authors in Refs. [164–169], and it has been connected to the large-Q^2 result in Ref. [147].

The reason for the importance of the gluonic contribution to the cross section stems from large logarithms $\ln 1/\beta$ that start to appear at NLO. These logarithms are related to the rapidity interval $Y_X = \ln 1/\beta$ between the electron and the parton shower X, and they can be resummed with the Kovchegov–Levin evolution equation [164] for the diffractive dipole amplitude. In practice, the rapidity gap $Y_{\text{gap}} = \ln 1/x_{\mathbb{P}}$ between the parton shower X and the target has to be large enough to be detectable, which means that $\ln 1/\beta = \ln x_{\mathbb{P}}/x$ is not too large in the HERA (or EIC) kinematics [148]. Thus, it is expected that keeping only the first large logarithm $\ln 1/\beta$ of the gluonic contribution at NLO is enough for comparisons to the currently available data.

The above-mentioned calculations contained only a part of the full NLO calculation in certain limits. They were brought into a more systematic NLO framework in the dipole picture in Ref. [170] where it was shown they can be obtained from the part of the NLO calculation where a gluon emission happens before the shock wave in the amplitude and its complex conjugate[1]. That article started the more systematic calculation of the full NLO equation for inclusive diffraction, which is being completed in an ongoing work of the author where the rest of the NLO diagrams are computed. That work will present the full NLO cross section for inclusive diffraction for the first time, and the purpose of this chapter is to give a rough outline of the full calculation.

5.1 Diffractive DIS at next-to-leading order

The full NLO calculation contains a lot of different diagrams that need to be accounted for. Perhaps the most simple classification of the calculation can be done by considering different Fock states at the shock wave and at the final state. At NLO, this results in dividing the calculation into four terms shown in Fig. 5.3. The full cross section can then be written as

$$\frac{\mathrm{d}\sigma_{\gamma_\lambda^*+A}^{\mathrm{D}}}{\mathrm{d}|t|\,\mathrm{d}M_X^2} = \left[\frac{\mathrm{d}\sigma_{\gamma_\lambda^*+A}^{\mathrm{D}}}{\mathrm{d}|t|\,\mathrm{d}M_X^2}\right]_{q\bar{q}} + \left[\frac{\mathrm{d}\sigma_{\gamma_\lambda^*+A}^{\mathrm{D}}}{\mathrm{d}|t|\,\mathrm{d}M_X^2}\right]_{q\bar{q}g} \tag{5.10}$$

---

[1] The large-M_X^2 limit in Ref. [168] also requires an additional contribution from gluon emission after the shock wave.
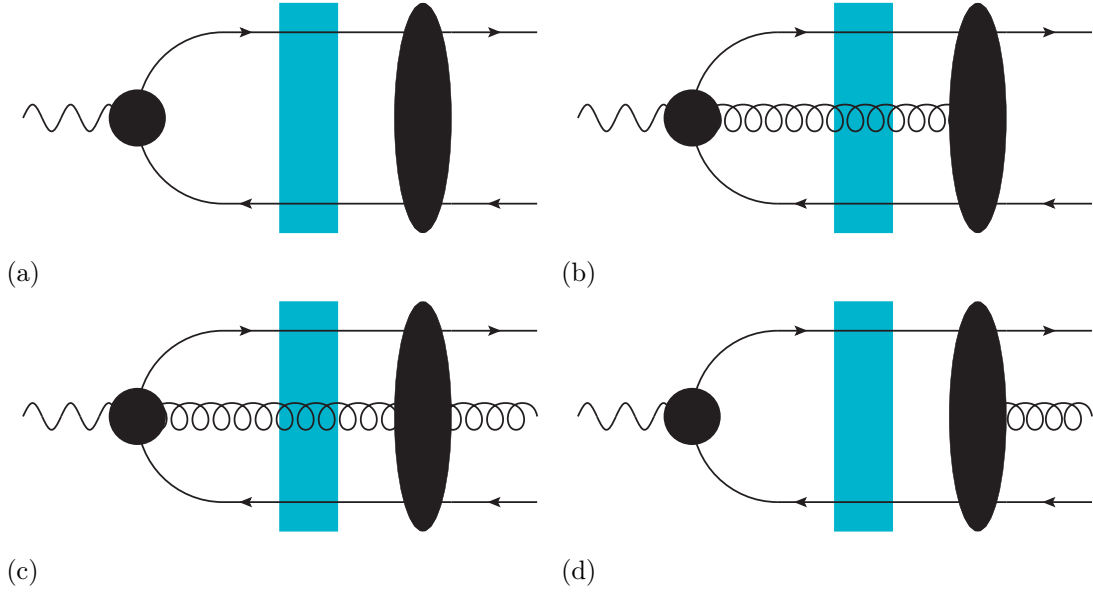
(a)

(b)

(c)

(d)

FIGURE 5.3   Contributions to the NLO invariant amplitude in diffractive DIS. The blue
rectangle represents the interaction with the target, and the black ellipse
effectively represents the wave function $\Psi^{n \to m}$ including the non-interacting
case (see Eq. (2.30)). Note that the black blob for the $\gamma^* \to m$ vertex corre-
sponds to the photon wave function $\Psi^{\gamma^* \to m}$ where also the NLO corrections
are included.

where

$$
\left[\frac{\mathrm{d}\sigma^{\mathrm{D}}_{\gamma^*_\lambda + A}}{\mathrm{d}|t| \, \mathrm{d}M_X^2} \right]_{q\bar{q}} = \int \mathrm{d}[\mathrm{PS}]_{q\bar{q}} \, 2q^+ (2\pi) \delta(q^+ - q^+_{q\bar{q}}) |\mathcal{M}_{q\bar{q}}|^2 \delta(M_X^2 - M_{q\bar{q}}^2) \delta\left(|t| - \boldsymbol{\Delta}^2\right),
$$

(5.11)

$$
\left[\frac{\mathrm{d}\sigma^{\mathrm{D}}_{\gamma^*_\lambda + A}}{\mathrm{d}|t| \, \mathrm{d}M_X^2} \right]_{q\bar{q}g} = \int \mathrm{d}[\mathrm{PS}]_{q\bar{q}g} \, 2q^+ (2\pi) \delta(q^+ - q^+_{q\bar{q}g}) |\mathcal{M}_{q\bar{q}g}|^2 \delta(M_X^2 - M_{q\bar{q}g}^2) \delta\left(|t| - \boldsymbol{\Delta}^2\right),
$$

(5.12)

and the corresponding invariant amplitudes are

$$
\mathcal{M}_{q\bar{q}} = \mathcal{M}^{(a)}_{q\bar{q}} + \mathcal{M}^{(b)}_{q\bar{q}},
$$

(5.13)

$$
\mathcal{M}_{q\bar{q}g} = \mathcal{M}^{(c)}_{q\bar{q}g} + \mathcal{M}^{(d)}_{q\bar{q}g}.
$$

(5.14)

Squaring the amplitudes, we end up with the following terms in the cross
section:

$$
\begin{aligned}
\frac{\mathrm{d}\sigma^{\mathrm{D}}_{\gamma^*_\lambda + A}}{\mathrm{d}^2\boldsymbol{\Delta} \, \mathrm{d}M_X^2} =& \left[\frac{\mathrm{d}\sigma^{\mathrm{D}}_{\gamma^*_\lambda + A}}{\mathrm{d}^2\boldsymbol{\Delta} \, \mathrm{d}M_X^2} \right]_{|(a)|^2} + \left[\frac{\mathrm{d}\sigma^{\mathrm{D}}_{\gamma^*_\lambda + A}}{\mathrm{d}^2\boldsymbol{\Delta} \, \mathrm{d}M_X^2} \right]_{|(b)|^2} \\
&+ \left[\frac{\mathrm{d}\sigma^{\mathrm{D}}_{\gamma^*_\lambda + A}}{\mathrm{d}^2\boldsymbol{\Delta} \, \mathrm{d}M_X^2} \right]_{|(c)|^2} + \left[\frac{\mathrm{d}\sigma^{\mathrm{D}}_{\gamma^*_\lambda + A}}{\mathrm{d}^2\boldsymbol{\Delta} \, \mathrm{d}M_X^2} \right]_{|(d)|^2} \\
&+ 2 \operatorname{Re} \left[\frac{\mathrm{d}\sigma^{\mathrm{D}}_{\gamma^*_\lambda + A}}{\mathrm{d}^2\boldsymbol{\Delta} \, \mathrm{d}M_X^2} \right]_{(a)\times(b)^*} + 2 \operatorname{Re} \left[\frac{\mathrm{d}\sigma^{\mathrm{D}}_{\gamma^*_\lambda + A}}{\mathrm{d}^2\boldsymbol{\Delta} \, \mathrm{d}M_X^2} \right]_{(c)\times(d)^*}
\end{aligned}
$$

(5.15)

where the subscript $i \times j^*$ refers to the product of invariant amplitudes $\mathcal{M}_i \times \mathcal{M}_j^*$ in the cross section. The different contributions can be understood as follows:

- $|(a)|^2$: Contains the leading-order part, the NLO corrections to the photon wave function, the self-energy correction $\sqrt{Z_{q\bar{q}}}$ of the quark-antiquark pair, and a part of the final-state corrections corresponding to a gluon exchange between the quark-antiquark pair.

- $|(b)|^2$: A gluon is emitted and absorbed before the final state in both the amplitude and the complex conjugate. This contribution comes at the order $\mathcal{O}(\alpha_s^2)$ and can be neglected at NLO.

- $|(c)|^2$: A gluon is emitted before the shock wave in both the amplitude and its complex conjugate, and it is not absorbed in the final state. This is a finite contribution to the NLO cross section and has already been calculated in Ref. [170].

- $|(d)|^2$: Contains the final-state corrections where a gluon is emitted after the shock wave in both the production amplitude and its complex conjugate.

- $(a) \times (b)^*$: Contains the NLO corrections where a gluon crosses the shock wave and is absorbed in the final state.

- $(c) \times (d)^*$: Contains the cross-terms where the gluon is emitted before the shock wave in the amplitude and after the shock wave in the complex conjugate, or vice versa. This contribution is finite.
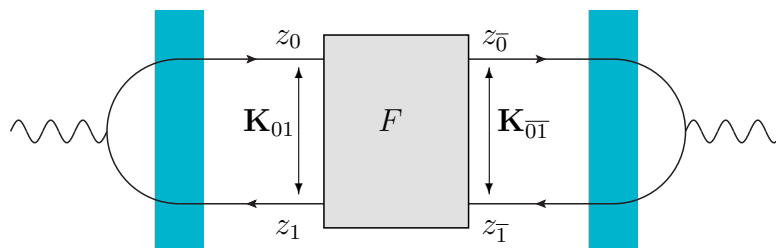
To calculate these different terms, the wave functions $\Psi_{\text{in}}^{\gamma^* \to q\bar{q}}$ and $\Psi_{\text{out}}^{q\bar{q} \to q\bar{q}}$ are needed at the order $\mathcal{O}(g_s^2)$, and the wave functions $\Psi_{\text{in}}^{\gamma^* \to q\bar{q}g}$, $\Psi_{\text{out}}^{q\bar{q} \to q\bar{q}g}$ and $\Psi_{\text{out}}^{q\bar{q}g \to q\bar{q}}$ at the order $\mathcal{O}(g_s)$. The wave functions with the photon have already been calculated in Refs. [134–136], but the rest of the wave functions are new and have not been calculated before. Feynman diagrams containing these wave functions, however, have already been calculated in Ref. [171], so that the expressions for the wave functions can be compared to some extent to the results presented there.

With these wave functions, one can then calculate each term in Eq. (5.15) separately. However, contributions related to the final-state corrections in $|(a)|^2$ and $|(d)|^2$ turn out to be especially difficult to calculate, as we need to Fourier transform the wave function $\Psi_{\text{out}}^{q\bar{q} \to q\bar{q}}$ to the mixed space used in the rest of the calculation. It is not known how to do this Fourier transform analytically, and thus one is left with an additional integral which makes showing the cancellation of divergences in the full cross section highly nontrivial. The purpose of the next section is to demonstrate how to deal with the final-state corrections in a more clever way.

5.1.1 Final-state corrections

The final-state corrections can be factorized out of the rest of the calculation. This is shown in Fig. 5.4a where

$$F = \sum_{i \in \text{ diagrams}} F_i \qquad (5.16)$$

(a) Factorization of the final-state corrections.

(b) Diagram A0

(c) Diagram A1

(d) Diagram A2

(e) Diagram B0

(f) Diagram B1

(g) Diagram B2

(h) Diagram C0

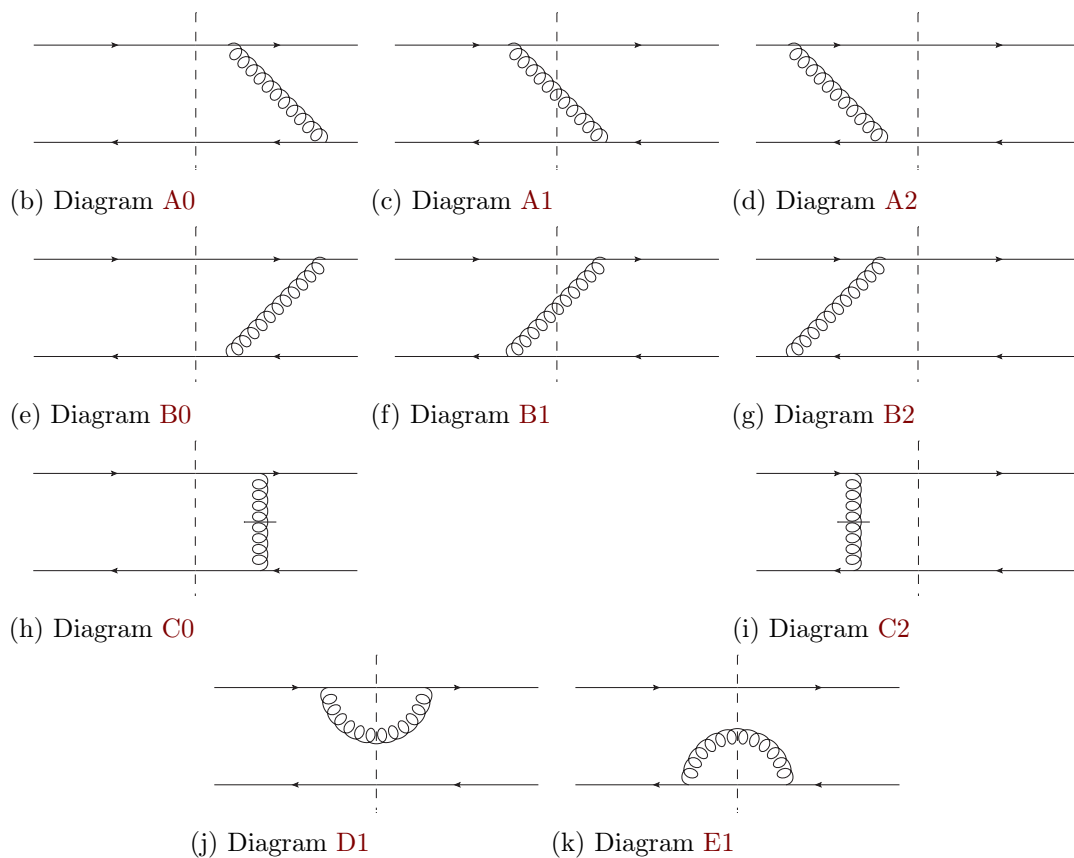(i) Diagram C2

(j) Diagram D1

(k) Diagram E1

FIGURE 5.4   Feynman diagrams contributing to the final-state corrections at NLO.

denotes the sum of the diagrams in Fig. 5.4. As the final-state corrections, and thus their divergences, are deeply related to each other it is more natural to first sum them together in the momentum space and only then take the transverse Fourier transforms to the mixed space. This is most convenient to do by grouping the different diagrams corresponding to the rows in Fig. 5.4.

Let us first consider the first row with the diagrams labeled as Ai. The corresponding contributions can be written as

$$
F_{Ai} \propto \int \frac{d^2\mathbf{K}_{01}\, d^2\mathbf{K}_{\overline{01}}}{(2\pi)^4} e^{i\mathbf{K}_{\overline{01}}\cdot\mathbf{x}_{\overline{01}} - i\mathbf{K}_{01}\cdot\mathbf{x}_{01}} \frac{1}{(z_0 - z_{\bar0})^3}(z_{\bar0}\mathbf{K}_{01} - z_0\mathbf{K}_{\overline{01}})\cdot(z_{\bar1}\mathbf{K}_{01} - z_1\mathbf{K}_{\overline{01}})
$$
$$
\times \frac{\delta(M_X^2 - M_{Ai}^2)}{[M_{Ai}^2 - M_{Aj}^2 \pm i\delta][M_{Ai}^2 - M_{Ak}^2 \pm i\delta]}
$$

(5.17)

where M_{Ai}^2 are the invariant masses at different parts of the Feynman diagrams, which come from the energy denominators in the light-cone perturbation theory. The signs of the infinitesimals $\pm i\delta$ are determined by whether the energy denominator is in the amplitude or the complex conjugate. The contributions F_{A0}, F_{A1} and F_{A2} differ only in the invariant masses and the signs of the infinitesimals, and thus they can be easily summed to obtain

$$
F_{A0} + F_{A1} + F_{A2} \propto \int \frac{d^2\mathbf{K}_{01}\, d^2\mathbf{K}_{\overline{01}}}{(2\pi)^4} e^{i\mathbf{K}_{\overline{01}}\cdot\mathbf{x}_{\overline{01}} - i\mathbf{K}_{01}\cdot\mathbf{x}_{01}} \frac{1}{(z_0 - z_{\bar0})^3}
$$
$$
\times (z_{\bar0}\mathbf{K}_{01} - z_0\mathbf{K}_{\overline{01}})\cdot(z_{\bar1}\mathbf{K}_{01} - z_1\mathbf{K}_{\overline{01}})\left\{ \frac{\delta(M_{A0}^2 - M_X^2)}{(M_{A0}^2 - M_{A1}^2 - i\delta)(M_{A0}^2 - M_{A2}^2 - i\delta)} \right.
$$
$$
\left. + \frac{\delta(M_{A1}^2 - M_X^2)}{(M_{A1}^2 - M_{A0}^2 + i\delta)(M_{A1}^2 - M_{A2}^2 - i\delta)} + \frac{\delta(M_{A2}^2 - M_X^2)}{(M_{A2}^2 - M_{A0}^2 + i\delta)(M_{A2}^2 - M_{A1}^2 + i\delta)} \right\}.
$$

(5.18)

We can get rid of the delta functions by writing

$$
\delta(x) = \frac{1}{2\pi i}\left[\frac{1}{x - i\delta} - \frac{1}{x + i\delta} \right].
$$

(5.19)

This is especially useful as there are cancellations between the three terms in Eq. (5.18), resulting in

$$
\frac{\delta(M_{A0}^2 - M_X^2)}{(M_{A0}^2 - M_{A1}^2 - i\delta)(M_{A0}^2 - M_{A2}^2 - i\delta)} + \frac{\delta(M_{A1}^2 - M_X^2)}{(M_{A1}^2 - M_{A0}^2 + i\delta)(M_{A1}^2 - M_{A2}^2 - i\delta)}
$$
$$
+ \frac{\delta(M_{A2}^2 - M_X^2)}{(M_{A2}^2 - M_{A0}^2 + i\delta)(M_{A2}^2 - M_{A1}^2 + i\delta)}
$$
$$
= \frac{1}{2\pi i}\left[\frac{1}{(M_X^2 - M_{A0}^2 - i\delta)(M_X^2 - M_{A1}^2 - i\delta)(M_X^2 - M_{A2}^2 - i\delta)} \right.
$$
$$
\left. - \frac{1}{(M_X^2 - M_{A0}^2 + i\delta)(M_X^2 - M_{A1}^2 + i\delta)(M_X^2 - M_{A2}^2 + i\delta)} \right].
$$

(5.20)

Note that the correct signs for the infinitesimals $\pm i\delta$, discussed in Sec. 2.3, are crucial for this trick. While it is now easier to perform the Fourier transform without the delta function, Fourier transforms with three different denominators are still in general quite complicated. This can be simplified by noting that

$$
\begin{aligned}
(z_{\overline{0}}\mathbf{K}_{01} &- z_0\mathbf{K}_{\overline{01}}) \cdot (z_{\overline{1}}\mathbf{K}_{01} - z_1\mathbf{K}_{\overline{01}}) \\
&= \frac{1}{2}(z_0 - z_{\overline{0}})\bigg[z_0 z_{\overline{1}}(M_X^2 - M_{A0}^2) + z_0 z_{\overline{1}}(M_X^2 - M_{A2}^2) \\
&\qquad\qquad - (z_{\overline{0}}z_1 + z_0 z_{\overline{1}})(M_X^2 - M_{A1}^2) - (z_0 - z_{\overline{0}})M_X^2\bigg]
\end{aligned}
\tag{5.21}
$$

which allows us to cancel some of the denominators. This leads to

$$
\begin{aligned}
F_{A0} + F_{A1} + F_{A2} &\propto \int \frac{\mathrm{d}^2\mathbf{K}_{01}\,\mathrm{d}^2\mathbf{K}_{\overline{01}}}{(2\pi)^4} e^{i\mathbf{K}_{\overline{01}}\cdot\mathbf{x}_{\overline{01}} - i\mathbf{K}_{01}\cdot\mathbf{x}_{01}} \frac{1}{(z_0 - z_{\overline{0}})^2} \\
&\quad \times \bigg[z_0 z_{\overline{1}}D_{A01} + z_0 z_{\overline{1}}D_{A12} - (z_{\overline{0}}z_1 + z_0 z_{\overline{1}})D_{A02} - (z_0 - z_{\overline{0}})M_X^2 D_{A012}\bigg]
\end{aligned}
\tag{5.22}
$$

where we have denoted

$$
\begin{aligned}
D_{Aij} &= \frac{1}{\pi}\,\mathrm{Im}\left\{\frac{1}{[M_X^2 - M_{Ai}^2 - i\delta][M_X^2 - M_{Aj}^2 - i\delta]}\right\}, \\
D_{Aijk} &= \frac{1}{\pi}\,\mathrm{Im}\left\{\frac{1}{[M_X^2 - M_{Ai}^2 - i\delta][M_X^2 - M_{Aj}^2 - i\delta][M_X^2 - M_{Ak}^2 - i\delta]}\right\}.
\end{aligned}
\tag{5.23}
$$

The crucial simplification here is that different terms in Eq. (5.22) correspond to different divergences in terms of the gluon's plus-momentum cut-off α. The divergences come from the gluon's plus momentum going to zero, which corresponds to $z_2 = z_0 - z_{\overline{0}} \to 0$, and we can see that Eq. (5.22) is divergent in this limit. Note that the energy denominators also depend on $z_0 - z_{\overline{0}}$ so that we have roughly

$$
\frac{1}{M_X^2 - M_{A1}^2 - i\delta} \sim (z_0 - z_{\overline{0}})\ln(z_0 - z_{\overline{0}})
\tag{5.24}
$$

after the Fourier integrals, which alleviates the divergence for terms with this denominator. Other energy denominators do not have such a dependence on $z_0 - z_{\overline{0}}$. This allows us to read the divergences of the different terms as follows:

1. D_{A01} and D_{A12}: a logarithmic divergence $\ln^2 \alpha$

2. D_{A02}: a power divergence $1/\alpha$

3. D_{A012}: no divergences

Especially, the term D_{A012} with three denominators is free of divergences. The other terms with divergences contain only two denominators and are thus simpler to study.

Similarly to Diagrams Ai, the second row in Fig. 5.4 corresponding to Diagrams Bi can be shown to simplify in this way. For the third row with the instantaneous

gluon exchange, Diagrams Ci, we get a slightly different combination of denominators. The contributions of Diagrams C0 and C2 read:

$$F_{\mathrm{C0}} \propto \int \frac{\mathrm{d}^2\mathbf{K}_{01}\,\mathrm{d}^2\mathbf{K}_{\overline{01}}}{(2\pi)^4} e^{i\mathbf{K}_{\overline{01}}\cdot\mathbf{x}_{\overline{01}} - i\mathbf{K}_{01}\cdot\mathbf{x}_{01}} \frac{1}{(z_0 - z_{\overline{0}})^2} \times \frac{\delta(M_X^2 - M_{\mathrm{A2}}^2)}{M_{\mathrm{A0}}^2 - M_{\mathrm{A2}}^2 - i\delta}, \qquad (5.25)$$

$$F_{\mathrm{C2}} \propto \int \frac{\mathrm{d}^2\mathbf{K}_{01}\,\mathrm{d}^2\mathbf{K}_{\overline{01}}}{(2\pi)^4} e^{i\mathbf{K}_{\overline{01}}\cdot\mathbf{x}_{\overline{01}} - i\mathbf{K}_{01}\cdot\mathbf{x}_{01}} \frac{1}{(z_0 - z_{\overline{0}})^2} \times \frac{\delta(M_X^2 - M_{\mathrm{A0}}^2)}{M_{\mathrm{A2}}^2 - M_{\mathrm{A0}}^2 + i\delta}. \qquad (5.26)$$

These can be summed together using the identity

$$\frac{\delta(M_X^2 - M_{\mathrm{A2}}^2)}{M_{\mathrm{A0}}^2 - M_{\mathrm{A2}}^2 - i\delta} + \frac{\delta(M_X^2 - M_{\mathrm{A0}}^2)}{M_{\mathrm{A2}}^2 - M_{\mathrm{A0}}^2 + i\delta} = -D_{\mathrm{C02}} \qquad (5.27)$$

which gives us

$$F_{\mathrm{C0}} + F_{\mathrm{C2}} \propto -\int \frac{\mathrm{d}^2\mathbf{K}_{01}\,\mathrm{d}^2\mathbf{K}_{\overline{01}}}{(2\pi)^4} e^{i\mathbf{K}_{\overline{01}}\cdot\mathbf{x}_{\overline{01}} - i\mathbf{K}_{01}\cdot\mathbf{x}_{01}} \frac{1}{(z_0 - z_{\overline{0}})^2} D_{\mathrm{C02}}. \qquad (5.28)$$

It turns out that we can combine the terms with the similar denominator structure D_{A02}, D_{B02} and D_{C02} as we have

$$D_{\mathrm{C02}} = \begin{cases} D_{\mathrm{A02}} & \text{if } z_0 - z_{\overline{0}} > 0 \\ D_{\mathrm{B02}} & \text{if } z_0 - z_{\overline{0}} < 0. \end{cases} \qquad (5.29)$$

While the coefficients in Eqs. (5.22) and (5.28) differ, one can show that the divergences $1/(z_0 - z_{\overline{0}})^2$ and $1/(z_0 - z_{\overline{0}})$ cancel in their sum so that the end result is finite.

This means that after summing together Diagrams Ai, Bi and Ci in the first three rows of Fig. 5.4 the only divergences left come from terms with the energy denominator structure D_{A01}, D_{A12}, D_{B01} and D_{B12}. The corresponding divergences are $\ln^2\alpha$ in terms of the gluon's plus-momentum regulator α. The remaining divergences are then simpler to handle and can be shown to cancel with the rest of the calculation. This concludes the handling of final-state corrections that have a form of a gluon exchange between the quark and the antiquark, i.e. Diagrams Ai, Bi and Ci.

One still needs to evaluate Diagrams D1 and E1 that are similar to the self-energy corrections of the quark and the antiquark. For these diagrams, the Fourier integrals can be done analytically without any additional left-over integrals which makes treating the divergences simpler. Thus, no tricks are needed for calculating Diagrams D1 and E1. These diagrams contain both IR divergences in ε and plus-momentum divergences of the form $\ln^2\alpha$. It turns out that this $\ln^2\alpha$ cancels exactly with the other final-state corrections so that the remaining plus-momentum divergences have only a $\ln\alpha$ dependence on the cut-off.

5.1.2 Cancellation of divergences

It is important to highlight the nontrivial cancellation of different kinds of divergences appearing in the calculation. The appearing divergences can be classified into the following categories based on the Feynman diagrams of their origin:

1. $|(a)|^2$: Self-energy corrections to the final $q\bar{q}$ state. These contain both IR and UV divergences in terms of the ε of dimensional regularization. These divergences cancel each other when using the same ε for both IR and UV divergences, and actually the self-energy corrections are identically zero in dimensional regularization.

2. $|(a)|^2$: NLO corrections to the $\gamma^* \to q\bar{q}$ wave function. These bring UV divergences in ε and plus-momentum divergences of the form $\ln \alpha$.

3. $(b) \times (a)^*$: Gluons crossing the shock wave that are emitted and absorbed by the same particle. These are related to the self-energy corrections, except now the IR region is made finite by the different energy denominator structure on the photon side. Hence, these only contain UV divergences that do not cancel as in Point 1. Also, plus-momentum divergences of the form $\ln \alpha$ are present.

4. $(b) \times (a)^*$: Gluons crossing the shock wave that correspond to a gluon exchange between the quark and the antiquark. These only bring a plus-momentum divergence $\ln \alpha$.

5. $|(d)|^2$: Final-state corrections where the gluon is emitted by the same particle both in the amplitude and its complex conjugate, i.e. Diagrams D1 and E1 in Fig. 5.4. In terms of Feynman diagrams, these can be related to the self-energy corrections with a delta function setting the invariant mass of the intermediate $q\bar{q}g$ state to be M_X^2. This delta function regulates the UV region, and thus these only contain IR divergences in ε. Also, plus-momentum divergences $\ln^2 \alpha$ are present.

6. $|(a)|^2$ and $|(d)|^2$: Final-state corrections that diagrammatically correspond to a gluon exchange between the quark and the antiquark, i.e. Diagrams Ai, Bi and Ci in Fig. 5.4. As described in Sec. 5.1.1, these contain $\ln^2 \alpha$ divergences when summed together.

As the cancellation of these divergences is in general quite involved, we will not go through it here in its full complexity. However, some general comments can be said about the cancellation. First of all, the final-state IR divergences in Point 5 are directly related to the IR divergences in the self-energy corrections. The overall effect of the self-energy corrections can be thought of as converting the IR divergences to UV divergences which then cancel with the rest of the calculation. With this in mind, the combined divergence structure of the final-state corrections in Points 5 and 6 is the same as the photon wave function $\gamma^* \to q\bar{q}$ in Point 2. This can be understood by noting that the difference to the forward elastic scattering amplitude in inclusive DIS, Eq. 3.30, is in the final state and thus for both processes to be finite the divergence structure of the final state has to be the same. Combining the final-state divergences with the rest of the calculation, the UV divergences cancel but there are still some logarithmic $\ln \alpha$ divergences left. These are related to the JIMWLK evolution of the dipole amplitudes in the production amplitude and its complex conjugate. Absorbing this $\ln \alpha$ divergence to the evolution of the dipole amplitudes then cancels the final divergence, rendering the NLO cross section finite.

After canceling the divergences, the resulting expressions can be numerically evaluated for comparisons to the HERA data and predictions for the EIC [10, 99, 100]. It will be especially interesting to compare diffractive structure functions for protons and heavy nuclei at the NLO accuracy to see the effects of saturation. The numerical computations for these predictions are left for future work.

6 CONCLUSIONS

The focus of this thesis has been on diffractive processes in the high-energy limit where the nonlinear effects of QCD start to become relevant. To probe this nonlinear region of QCD, it is crucial to get a better understanding of processes sensitive to saturation, which includes diffractive processes. Calculations in the high-energy limit can be done in the dipole picture with the color-glass condensate effective field theory, outlined in Chs. 2 and 3. The NLO calculations considered in this thesis are state-of-the-art in the dipole picture.

In Ch. 4, we discuss higher-order corrections to exclusive vector meson production. This includes relativistic corrections to heavy vector meson production, and NLO corrections to both heavy and light vector meson production. In Article [I], it was shown that the relativistic corrections can be numerically important for small photon virtualities in heavy vector meson production. The NLO corrections to heavy vector meson production in the nonrelativistic limit were calculated in Articles [II] and [IV], where it was found that the NLO corrections are numerically moderate when also using a dipole amplitude fitted at NLO. In general, a good agreement with the experimental data was found if also the relativistic corrections at leading order were included. The NLO corrections to light vector meson production in the limit of large photon virtuality calculated in Article [III] were also considered. Similarly to the heavy vector meson case, the NLO results were found to be comparable to the leading-order results, with an excellent agreement with the experimental data for values $Q^2 \gg M_V^2$ where the calculations are valid.

In phenomenological applications, an important part of calculations in the dipole picture is the dipole amplitude discussed in Ch. 3. Constraints for the dipole amplitude from massive quarks were considered in Article [V] where heavy quark production was calculated numerically. It was then shown that with properly parametrized initial conditions the dipole amplitude is universal in the sense that the same dipole amplitude can be used to calculate both total and charm quark production in DIS. This was not possible at leading order when using a BK-evolved dipole amplitude, and thus the NLO corrections were found to be crucial for precision computations in the dipole picture.

Some discussion about an unpublished work on NLO corrections to inclusive

diffraction in DIS was included in Ch. 5. The main difference to exclusive vector meson production is in the final state, where in inclusive diffraction the final state is defined to be any multiparticle state with a definite invariant mass M_X^2. This means that calculating the NLO corrections to the final state is more complicated than in exclusive vector meson production and includes more Feynman diagrams, shown in Fig. 5.4. The general strategy for dealing with these diagrams is discussed in Sec. 5.1.1. Including all of the NLO corrections, along with the JIMWLK evolution of the dipole amplitude, one can then show that the end result is finite and suitable for numerical calculations. While the NLO corrections have not been implemented numerically yet, it will be interesting to see if they will modify the behavior of the diffractive structure functions.

This thesis is a part of a bigger picture of striving for precise predictions using the dipole picture. We note that other NLO calculations using the framework of this work also exist, some of which we have already addressed: single inclusive hadron production [172–185], total structure functions with massless [134–136] and massive quarks [84–86], the dominating gluonic contribution to diffractive structure functions [170], exclusive production of light vector mesons [144], diffractive jet production [186, 187], inclusive dijet production in DIS [171, 188, 189], diffractive dihadron production [190], and inclusive dihadron production in DIS [191, 192]. Also, NLO corrections to the rapidity evolution of the dipole amplitude have been calculated, namely the NLO BK [193] and NLO JIMWLK [194–196] equations. Analytical calculations in the high-energy limit have thus been largely promoted to the NLO precision era, with numerical implementations on the way.

Other interesting calculations in the dipole picture involve going beyond the eikonal approximation and including the so-called sub-eikonal effects [197–206]. While no numerical estimates of these sub-eikonal corrections exist at the moment of writing this thesis, it is expected that they will become important for lower energies. Computing these will give us guidelines for the accuracy of the eikonal approximation and the validity of the high-energy factorization.

With these higher-order calculations in the dipole picture becoming available, it will be very interesting to implement them numerically and see if the results obtained at leading order are modified. It will also be very important to compare results from saturation models to calculations that do not involve saturation to see which observables can be used to search for saturation from the experimental data. Non-saturation calculations of these processes involve calculations in the BFKL framework and also the collinear framework: see for example Refs. [207–209] for NLO exclusive heavy vector meson production in collinear factorization. Numerical comparisons to these results will be crucial for distinguishing between saturation and non-saturation effects.

References

[1] **ZEUS** collaboration, S. Chekanov *et. al.*, *A ZEUS next-to-leading-order QCD analysis of data on deep inelastic scattering*, *Phys. Rev. D* **67** (2003) 012007 [`arXiv:hep-ex/0208023`].

[2] A. H. Mueller, *Unitarity and the BFKL pomeron*, *Nucl. Phys. B* **437** (1995) 107 [`arXiv:hep-ph/9408245`].

[3] E. Braidot, *Two-particle azimuthal correlations at forward rapidity in STAR*. PhD thesis, Utrecht U., 2011. `arXiv:1102.0931 [nucl-ex]`.

[4] **PHENIX** collaboration, A. Adare *et. al.*, *Suppression of back-to-back hadron pairs at forward rapidity in d+Au Collisions at $\sqrt{s_{NN}} = 200$ GeV*, *Phys. Rev. Lett.* **107** (2011) 172301 [`arXiv:1105.5112 [nucl-ex]`].

[5] **STAR** collaboration, M. S. Abdallah *et. al.*, *Evidence for Nonlinear Gluon Effects in QCD and Their Mass Number Dependence at STAR*, *Phys. Rev. Lett.* **129** (2022) no. 9 092501 [`arXiv:2111.10396 [nucl-ex]`].

[6] **ALICE** collaboration, B. Abelev *et. al.*, *Transverse momentum distribution and nuclear modification factor of charged particles in p-Pb collisions at $\sqrt{s_{NN}} = 5.02$ TeV*, *Phys. Rev. Lett.* **110** (2013) no. 8 082302 [`arXiv:1210.4520 [nucl-ex]`].

[7] **ALICE** collaboration, B. Abelev *et. al.*, *Coherent J/ψ photoproduction in ultra-peripheral Pb-Pb collisions at $\sqrt{s_{NN}} = 2.76$ TeV*, *Phys. Lett. B* **718** (2013) 1273 [`arXiv:1209.3715 [nucl-ex]`].

[8] **CMS** collaboration, V. Khachatryan *et. al.*, *Coherent J/ψ photoproduction in ultra-peripheral PbPb collisions at $\sqrt{s_{NN}} = 2.76$ TeV with the CMS experiment*, *Phys. Lett. B* **772** (2017) 489 [`arXiv:1605.06966 [nucl-ex]`].

[9] **LHCb** collaboration, R. Aaij *et. al.*, *Measurement of the Nuclear Modification Factor and Prompt Charged Particle Production in $p - Pb$ and pp Collisions at $\sqrt{s_{NN}}$=5 TeV*, *Phys. Rev. Lett.* **128** (2022) no. 14 142004 [`arXiv:2108.13115 [hep-ex]`].

[10] R. Abdul Khalek *et. al.*, *Science Requirements and Detector Concepts for the Electron-Ion Collider: EIC Yellow Report*, *Nucl. Phys. A* **1026** (2022) 122447 [`arXiv:2103.05419 [physics.ins-det]`].

[11] **ZEUS** collaboration, M. Derrick *et. al.*, *Observation of events with a large rapidity gap in deep inelastic scattering at HERA*, *Phys. Lett. B* **315** (1993) 481.

[12] **H1** collaboration, T. Ahmed *et. al.*, *Deep inelastic scattering events with a large rapidity gap at HERA*, *Nucl. Phys. B* **429** (1994) 477.

[13] **H1** collaboration, C. Adloff *et. al.*, *Inclusive measurement of diffractive deep inelastic ep scattering*, *Z. Phys. C* **76** (1997) 613 [`arXiv:hep-ex/9708016`].

[14] **ZEUS** collaboration, J. Breitweg *et. al.*, *Measurement of the diffractive structure function $F_2^{D(4)}$ at HERA*, *Eur. Phys. J. C* **1** (1998) 81 [`arXiv:hep-ex/9709021`].

[15] J. D. Bjorken, *Rapidity gaps and jets as a new physics signature in very high-energy hadron hadron collisions*, *Phys. Rev. D* **47** (1993) 101.

[16] T. Regge, *Introduction to complex orbital momenta*, *Nuovo Cim.* **14** (1959) 951.

[17] G. F. Chew and S. C. Frautschi, *Principle of Equivalence for All Strongly Interacting Particles Within the S Matrix Framework*, *Phys. Rev. Lett.* **7** (1961) 394.

[18] V. N. Gribov, *Partial waves with complex orbital angular momenta and the asymptotic behavior of the scattering amplitude*, *Zh. Eksp. Teor. Fiz.* **41** (1961) 1962.

[19] V. Barone and E. Predazzi, *High-Energy Particle Diffraction*, vol. v.565 of *Texts and Monographs in Physics*. Springer-Verlag, Berlin Heidelberg, 2002.

[20] F. E. Low, *A Model of the Bare Pomeron*, *Phys. Rev. D* **12** (1975) 163.

[21] S. Nussinov, *A Perturbative Recipe for Quark Gluon Theories and Some of Its Applications*, *Phys. Rev. D* **14** (1976) 246.

[22] L. N. Lipatov, *Reggeization of the Vector Meson and the Vacuum Singularity in Nonabelian Gauge Theories*, *Sov. J. Nucl. Phys.* **23** (1976) 338.

[23] E. A. Kuraev, L. N. Lipatov and V. S. Fadin, *The Pomeranchuk Singularity in Nonabelian Gauge Theories*, *Sov. Phys. JETP* **45** (1977) 199.

[24] I. I. Balitsky and L. N. Lipatov, *The Pomeranchuk Singularity in Quantum Chromodynamics*, *Sov. J. Nucl. Phys.* **28** (1978) 822.

[25] M. Froissart, *Asymptotic behavior and subtractions in the Mandelstam representation*, *Phys. Rev.* **123** (1961) 1053.

[26] A. Martin, *Unitarity and high-energy behavior of scattering amplitudes*, *Phys. Rev.* **129** (1963) 1432.

[27] I. Balitsky, *Operator expansion for high-energy scattering*, *Nucl. Phys. B* **463** (1996) 99 [`arXiv:hep-ph/9509348`].

[28] Y. V. Kovchegov, *Small x F(2) structure function of a nucleus including multiple pomeron exchanges*, *Phys. Rev. D* **60** (1999) 034008 [`arXiv:hep-ph/9901281`].

[29] E. Iancu, A. Leonidov and L. D. McLerran, *Nonlinear gluon evolution in the color glass condensate. 1.*, *Nucl. Phys. A* **692** (2001) 583 [`arXiv:hep-ph/0011241`].

[30] E. Iancu, A. Leonidov and L. D. McLerran, *The Renormalization group equation for the color glass condensate*, *Phys. Lett. B* **510** (2001) 133 [`arXiv:hep-ph/0102009`].

[31] E. Iancu and L. D. McLerran, *Saturation and universality in QCD at small x*, *Phys. Lett. B* **510** (2001) 145 [`arXiv:hep-ph/0103032`].

[32] E. Ferreiro, E. Iancu, A. Leonidov and L. McLerran, *Nonlinear gluon evolution in the color glass condensate. 2.*, *Nucl. Phys. A* **703** (2002) 489 [`arXiv:hep-ph/0109115`].

[33] J. Jalilian-Marian, A. Kovner, L. D. McLerran and H. Weigert, *The Intrinsic glue distribution at very small x*, *Phys. Rev. D* **55** (1997) 5414 [`arXiv:hep-ph/9606337`].

[34] J. Jalilian-Marian, A. Kovner, A. Leonidov and H. Weigert, *The Wilson renormalization group for low x physics: Towards the high density regime*, *Phys. Rev. D* **59** (1998) 014014 [`arXiv:hep-ph/9706377`].

[35] J. Jalilian-Marian, A. Kovner, A. Leonidov and H. Weigert, *The BFKL equation from the Wilson renormalization group*, *Nucl. Phys. B* **504** (1997) 415 [`arXiv:hep-ph/9701284`].

[36] N. N. Nikolaev and B. G. Zakharov, *Color transparency and scaling properties of nuclear shadowing in deep inelastic scattering*, *Z. Phys. C* **49** (1991) 607.

[37] N. Nikolaev and B. G. Zakharov, *Pomeron structure function and diffraction dissociation of virtual photons in perturbative QCD*, *Z. Phys. C* **53** (1992) 331.

[38] A. H. Mueller, *Soft gluons in the infinite momentum wave function and the BFKL pomeron*, *Nucl. Phys. B* **415** (1994) 373.

[39] A. H. Mueller and B. Patel, *Single and double BFKL pomeron exchange and a dipole picture of high-energy hard processes*, *Nucl. Phys. B* **425** (1994) 471 [`arXiv:hep-ph/9403256`].

[40] J. D. Bjorken, J. B. Kogut and D. E. Soper, *Quantum Electrodynamics at Infinite Momentum: Scattering from an External Field*, *Phys. Rev. D* **3** (1971) 1382.

[41] J. B. Kogut and D. E. Soper, *Quantum Electrodynamics in the Infinite Momentum Frame*, *Phys. Rev. D* **1** (1970) 2901.

[42] S. J. Brodsky, H.-C. Pauli and S. S. Pinsky, *Quantum chromodynamics and other field theories on the light cone*, *Phys. Rept.* **301** (1998) 299 [`arXiv:hep-ph/9705477`].

[43] M. D. Schwartz, *Quantum Field Theory and the Standard Model*. Cambridge University Press, 3, 2014.

[44] S. J. Brodsky, G. McCartor, H. C. Pauli and S. S. Pinsky, *The Challenge of light cone quantization of gauge field theory*, *Part. World* **3** (1993) no. 3 109.

[45] Y. V. Kovchegov and E. Levin, *Quantum Chromodynamics at High Energy*, vol. 33 of *Cambridge Monographs on Particle Physics, Nuclear Physics and Cosmology (33)*. Cambridge University Press, 11, 2022.

[46] T. Lappi and R. Paatelainen, *The one loop gluon emission light cone wave function*, *Annals Phys.* **379** (2017) 34 [`arXiv:1611.00497 [hep-ph]`].

[47] H. Kowalski, L. Motyka and G. Watt, *Exclusive diffractive processes at HERA within the dipole picture*, *Phys. Rev. D* **74** (2006) 074016 [`arXiv:hep-ph/0606272`].

[48] G. P. Lepage and S. J. Brodsky, *Exclusive Processes in Perturbative Quantum Chromodynamics*, *Phys. Rev. D* **22** (1980) 2157.

[49] D. E. Soper, *Infinite-momentum helicity states*, *Phys. Rev. D* **5** (1972) 1956.

[50] L. D. McLerran and R. Venugopalan, *Gluon distribution functions for very large nuclei at small transverse momentum*, *Phys. Rev. D* **49** (1994) 3352 [`arXiv:hep-ph/9311205`].

[51] L. D. McLerran and R. Venugopalan, *Computing quark and gluon distribution functions for very large nuclei*, *Phys. Rev. D* **49** (1994) 2233 [`arXiv:hep-ph/9309289`].

[52] L. D. McLerran and R. Venugopalan, *Green's functions in the color field of a large nucleus*, *Phys. Rev. D* **50** (1994) 2225 [`arXiv:hep-ph/9402335`].

[53] E. Iancu and R. Venugopalan, *The Color glass condensate and high-energy scattering in QCD*, pp. 249–363. World Scientific, 2004. `arXiv:hep-ph/0303204`.

[54] Y. V. Kovchegov, J. Kuokkanen, K. Rummukainen and H. Weigert, *Subleading-N(c) corrections in non-linear small-x evolution*, *Nucl. Phys. A* **823** (2009) 47 [`arXiv:0812.3238 [hep-ph]`].

[55] T. Lappi, H. Mäntysaari and A. Ramnath, *Next-to-leading order Balitsky-Kovchegov equation beyond large N_c*, *Phys. Rev. D* **102** (2020) no. 7 074027 [`arXiv:2007.00751 [hep-ph]`].

[56] H. Mäntysaari, *Scattering off the Color Glass Condensate*. PhD thesis, Jyvaskyla U., 2015. `arXiv:1506.07313 [hep-ph]`.

[57] K. J. Golec-Biernat and A. M. Stasto, *On solutions of the Balitsky-Kovchegov equation with impact parameter*, *Nucl. Phys. B* **668** (2003) 345 [`arXiv:hep-ph/0306279`].

[58] J. Berger and A. Stasto, *Numerical solution of the nonlinear evolution equation at small x with impact parameter and beyond the LL approximation*, *Phys. Rev. D* **83** (2011) 034015 [`arXiv:1010.0671 [hep-ph]`].

[59] J. Berger and A. M. Stasto, *Small x nonlinear evolution with impact parameter and the structure function data*, *Phys. Rev. D* **84** (2011) 094022 [`arXiv:1106.5740 [hep-ph]`].

[60] J. Berger and A. M. Stasto, *Exclusive vector meson production and small-x evolution*, *JHEP* **01** (2013) 001 [`arXiv:1205.2037 [hep-ph]`].

[61] K. J. Golec-Biernat and M. Wusthoff, *Saturation effects in deep inelastic scattering at low Q^2 and its implications on diffraction*, *Phys. Rev. D* **59** (1998) 014017 [`arXiv:hep-ph/9807513`].

[62] K. J. Golec-Biernat and M. Wusthoff, *Saturation in diffractive deep inelastic scattering*, *Phys. Rev. D* **60** (1999) 114023 [`arXiv:hep-ph/9903358`].

[63] H. Kowalski and D. Teaney, *An Impact parameter dipole saturation model*, *Phys. Rev. D* **68** (2003) 114005 [`arXiv:hep-ph/0304189`].

[64] V. N. Gribov and L. N. Lipatov, *Deep inelastic ep scattering in perturbation theory*, *Sov. J. Nucl. Phys.* **15** (1972) 438.

[65] Y. L. Dokshitzer, *Calculation of the Structure Functions for Deep Inelastic Scattering and e^+e^- Annihilation by Perturbation Theory in Quantum Chromodynamics.*, *Sov. Phys. JETP* **46** (1977) 641.

[66] G. Altarelli and G. Parisi, *Asymptotic Freedom in Parton Language*, *Nucl. Phys. B* **126** (1977) 298.

[67] J. L. Albacete, N. Armesto, J. G. Milhano and C. A. Salgado, *Non-linear QCD meets data: A Global analysis of lepton-proton scattering with running coupling BK evolution*, *Phys. Rev. D* **80** (2009) 034031 [`arXiv:0902.1112 [hep-ph]`].

[68] J. L. Albacete, N. Armesto, J. G. Milhano, P. Quiroga-Arias and C. A. Salgado, *AAMQS: A non-linear QCD analysis of new HERA data at small-x including heavy quarks*, *Eur. Phys. J. C* **71** (2011) 1705 [`arXiv:1012.4408 [hep-ph]`].

78

[69] T. Lappi and H. Mäntysaari, *Single inclusive particle production at high energy from HERA data to proton-nucleus collisions*, *Phys. Rev. D* **88** (2013) 114020 [`arXiv:1309.6963 [hep-ph]`].

[70] **H1, ZEUS** collaboration, F. D. Aaron *et. al.*, *Combined Measurement and QCD Analysis of the Inclusive $e^{\pm}p$ Scattering Cross Sections at HERA*, *JHEP* **01** (2010) 109 [`arXiv:0911.0884 [hep-ex]`].

[71] **H1, ZEUS** collaboration, H. Abramowicz *et. al.*, *Combination and QCD Analysis of Charm Production Cross Section Measurements in Deep-Inelastic ep Scattering at HERA*, *Eur. Phys. J. C* **73** (2013) no. 2 2311 [`arXiv:1211.1182 [hep-ex]`].

[72] **H1, ZEUS** collaboration, H. Abramowicz *et. al.*, *Combination of measurements of inclusive deep inelastic $e^{\pm}p$ scattering cross sections and QCD analysis of HERA data*, *Eur. Phys. J. C* **75** (2015) no. 12 580 [`arXiv:1506.06042 [hep-ex]`].

[73] **H1, ZEUS** collaboration, H. Abramowicz *et. al.*, *Combination and QCD analysis of charm and beauty production cross-section measurements in deep inelastic ep scattering at HERA*, *Eur. Phys. J. C* **78** (2018) no. 6 473 [`arXiv:1804.01019 [hep-ex]`].

[74] **H1** collaboration, V. Andreev *et. al.*, *Measurement of inclusive ep cross sections at high Q^2 at $\sqrt{s}$ = 225 and 252 GeV and of the longitudinal proton structure function F_L at HERA*, *Eur. Phys. J. C* **74** (2014) no. 4 2814 [`arXiv:1312.4821 [hep-ex]`].

[75] G. Beuf, H. Hänninen, T. Lappi and H. Mäntysaari, *Color Glass Condensate at next-to-leading order meets HERA data*, *Phys. Rev. D* **102** (2020) 074028 [`arXiv:2007.01645 [hep-ph]`].

[76] H. Mäntysaari and P. Zurita, *In depth analysis of the combined HERA data in the dipole models with and without saturation*, *Phys. Rev. D* **98** (2018) 036002 [`arXiv:1804.05311 [hep-ph]`].

[77] G. Beuf, *Improving the kinematics for low-x QCD evolution equations in coordinate space*, *Phys. Rev. D* **89** (2014) no. 7 074039 [`arXiv:1401.0313 [hep-ph]`].

[78] E. Iancu, J. D. Madrigal, A. H. Mueller, G. Soyez and D. N. Triantafyllopoulos, *Collinearly-improved BK evolution meets the HERA data*, *Phys. Lett. B* **750** (2015) 643 [`arXiv:1507.03651 [hep-ph]`].

[79] E. Iancu, J. D. Madrigal, A. H. Mueller, G. Soyez and D. N. Triantafyllopoulos, *Resumming double logarithms in the QCD evolution of color dipoles*, *Phys. Lett. B* **744** (2015) 293 [`arXiv:1502.05642 [hep-ph]`].

[80] B. Ducloué, E. Iancu, A. H. Mueller, G. Soyez and D. N. Triantafyllopoulos, *Non-linear evolution in QCD at high-energy beyond leading order*, *JHEP* **04** (2019) 081 [`arXiv:1902.06637 [hep-ph]`].

[81] H. Hänninen, *Deep inelastic scattering in the dipole picture at next-to-leading order*. PhD thesis, Jyväskylä U., 2021. `arXiv:2112.08818 [hep-ph]`.

[82] Y. V. Kovchegov and H. Weigert, *Triumvirate of Running Couplings in Small-x Evolution*, *Nucl. Phys. A* **784** (2007) 188 [`arXiv:hep-ph/0609090`].

[83] I. Balitsky, *Quark contribution to the small-x evolution of color dipole*, *Phys. Rev. D* **75** (2007) 014001 [`arXiv:hep-ph/0609105`].

[84] G. Beuf, T. Lappi and R. Paatelainen, *Massive quarks in NLO dipole factorization for DIS: Longitudinal photon*, *Phys. Rev. D* **104** (2021) no. 5 056032 [`arXiv:2103.14549 [hep-ph]`].

[85] G. Beuf, T. Lappi and R. Paatelainen, *Massive Quarks at One Loop in the Dipole Picture of Deep Inelastic Scattering*, *Phys. Rev. Lett.* **129** (2022) no. 7 072001 [`arXiv:2112.03158 [hep-ph]`].

[86] G. Beuf, T. Lappi and R. Paatelainen, *Massive quarks in NLO dipole factorization for DIS: Transverse photon*, `arXiv:2204.02486 [hep-ph]`.

[87] B. Ducloué, E. Iancu, G. Soyez and D. N. Triantafyllopoulos, *HERA data and collinearly-improved BK dynamics*, *Phys. Lett. B* **803** (2020) 135305 [`arXiv:1912.09196 [hep-ph]`].

[88] **ZEUS** collaboration, J. Breitweg *et. al.*, *Exclusive electroproduction of ρ^0 and J/ψ mesons at HERA*, *Eur. Phys. J. C* **6** (1999) 603 [`arXiv:hep-ex/9808020`].

[89] **ZEUS** collaboration, S. Chekanov *et. al.*, *Exclusive photoproduction of J/ψ mesons at HERA*, *Eur. Phys. J. C* **24** (2002) 345 [`arXiv:hep-ex/0201043`].

[90] **ZEUS** collaboration, S. Chekanov *et. al.*, *Exclusive electroproduction of J/ψ mesons at HERA*, *Nucl. Phys. B* **695** (2004) 3 [`arXiv:hep-ex/0404008`].

[91] **H1** collaboration, A. Aktas *et. al.*, *Elastic J/ψ production at HERA*, *Eur. Phys. J. C* **46** (2006) 585 [`arXiv:hep-ex/0510016`].

[92] **H1** collaboration, F. D. Aaron *et. al.*, *Diffractive Electroproduction of ρ and ϕ Mesons at HERA*, *JHEP* **05** (2010) 032 [`arXiv:0910.5831 [hep-ex]`].

[93] **H1** collaboration, C. Alexa *et. al.*, *Elastic and Proton-Dissociative Photoproduction of J/ψ Mesons at HERA*, *Eur. Phys. J. C* **73** (2013) no. 6 2466 [`arXiv:1304.5162 [hep-ex]`].

[94] **ALICE** collaboration, E. Abbas *et. al.*, *Charmonium and e^+e^- pair photoproduction at mid-rapidity in ultra-peripheral Pb-Pb collisions at $\sqrt{s_{\mathrm{NN}}}$=2.76 TeV*, *Eur. Phys. J. C* **73** (2013) no. 11 2617 [`arXiv:1305.1467 [nucl-ex]`].

[95] **ALICE** collaboration, S. Acharya *et. al.*, *Coherent J/ψ photoproduction at forward rapidity in ultra-peripheral Pb-Pb collisions at $\sqrt{s_{\mathrm{NN}}} = 5.02$ TeV*, *Phys. Lett. B* **798** (2019) 134926 [`arXiv:1904.06272 [nucl-ex]`].

[96] **ALICE** collaboration, S. Acharya *et. al.*, *Coherent J/ψ and ψ' photoproduction at midrapidity in ultra-peripheral Pb-Pb collisions at $\sqrt{s_{\mathrm{NN}}} = 5.02$ TeV*, *Eur. Phys. J. C* **81** (2021) no. 8 712 [`arXiv:2101.04577 [nucl-ex]`].

[97] **LHCb** collaboration, R. Aaij *et. al.*, *Study of coherent J/ψ production in lead-lead collisions at $\sqrt{s_{\mathrm{NN}}} = 5$ TeV*, *JHEP* **07** (2022) 117 [`arXiv:2107.03223 [hep-ex]`].

[98] **CMS** collaboration, A. Tumasyan *et. al.*, *Probing small Bjorken-x nuclear gluonic structure via coherent J/ψ photoproduction in ultraperipheral PbPb collisions at $\sqrt{s_{\mathrm{NN}}} = 5.02$ TeV*, `arXiv:2303.16984 [nucl-ex]`.

[99] A. Accardi *et. al.*, *Electron Ion Collider: The Next QCD Frontier: Understanding the glue that binds us all*, *Eur. Phys. J. A* **52** (2016) no. 9 268 [`arXiv:1212.1701 [nucl-ex]`].

[100] E. C. Aschenauer, S. Fazio, J. H. Lee, H. Mäntysaari, B. S. Page, B. Schenke, T. Ullrich, R. Venugopalan and P. Zurita, *The electron–ion collider: assessing the energy dependence of key measurements*, *Rept. Prog. Phys.* **82** (2019) no. 2 024301 [`arXiv:1708.01527 [nucl-ex]`].

[101] M. L. Good and W. D. Walker, *Diffraction disssociation of beam particles*, *Phys. Rev.* **120** (1960) 1857.

[102] H. Mäntysaari, F. Salazar and B. Schenke, *Nuclear geometry at high energy from exclusive vector meson production*, *Phys. Rev. D* **106** (2022) no. 7 074019 [`arXiv:2207.03712 [hep-ph]`].

[103] **ZEUS** collaboration, S. Chekanov *et. al.*, *Exclusive electroproduction of ϕ mesons at HERA*, *Nucl. Phys. B* **718** (2005) 3 [`arXiv:hep-ex/0504010`].

[104] V. N. Gribov and A. A. Migdal, *The Pomeranchuk quasi-stable pole and diffraction scattering at ultrahigh-energy*, *Yad. Fiz.* **8** (1968) 1213.

[105] J. Nemchik, N. N. Nikolaev, E. Predazzi and B. G. Zakharov, *Color dipole phenomenology of diffractive electroproduction of light vector mesons at HERA*, *Z. Phys. C* **75** (1997) 71 [`arXiv:hep-ph/9605231`].

[106] J. C. Collins, L. Frankfurt and M. Strikman, *Factorization for hard exclusive electroproduction of mesons in QCD*, *Phys. Rev. D* **56** (1997) 2982 [arXiv:hep-ph/9611433].

[107] A. G. Shuvaev, K. J. Golec-Biernat, A. D. Martin and M. G. Ryskin, *Off diagonal distributions fixed by diagonal partons at small x and ξ*, *Phys. Rev. D* **60** (1999) 014015 [arXiv:hep-ph/9902410].

[108] A. D. Martin, M. G. Ryskin and T. Teubner, Q^2 *dependence of diffractive vector meson electroproduction*, *Phys. Rev. D* **62** (2000) 014022 [arXiv:hep-ph/9912551].

[109] H. Mäntysaari and B. Schenke, *Revealing proton shape fluctuations with incoherent diffraction at high energy*, *Phys. Rev. D* **94** (2016) no. 3 034042 [arXiv:1607.01711 [hep-ph]].

[110] H. Mäntysaari and B. Schenke, *Probing subnucleon scale fluctuations in ultraperipheral heavy ion collisions*, *Phys. Lett. B* **772** (2017) 832 [arXiv:1703.09256 [hep-ph]].

[111] Y. Li, P. Maris, X. Zhao and J. P. Vary, *Heavy Quarkonium in a Holographic Basis*, *Phys. Lett. B* **758** (2016) 118 [arXiv:1509.07212 [hep-ph]].

[112] H. Mäntysaari, K. Roy, F. Salazar and B. Schenke, *Gluon imaging using azimuthal correlations in diffractive scattering at the Electron-Ion Collider*, *Phys. Rev. D* **103** (2021) no. 9 094026 [arXiv:2011.02464 [hep-ph]].

[113] E. Eichten, K. Gottfried, T. Kinoshita, K. D. Lane and T.-M. Yan, *Charmonium: Comparison with Experiment*, *Phys. Rev. D* **21** (1980) 203.

[114] N. Barik and S. N. Jena, *Fine-hyperfine splittings of quarkonium levels in an effective power-law potential*, *Phys. Lett. B* **97** (1980) 265.

[115] C. Quigg and J. L. Rosner, *Quarkonium Level Spacings*, *Phys. Lett. B* **71** (1977) 153.

[116] W. Buchmuller and S. H. H. Tye, *Quarkonia and Quantum Chromodynamics*, *Phys. Rev. D* **24** (1981) 132.

[117] G. T. Bodwin, E. Braaten and G. P. Lepage, *Rigorous QCD analysis of inclusive annihilation and production of heavy quarkonium*, *Phys. Rev. D* **51** (1995) 1125 [arXiv:hep-ph/9407339]. [Erratum: Phys.Rev.D 55, 5853 (1997)].

[118] G. T. Bodwin, H. S. Chung, D. Kang, J. Lee and C. Yu, *Improved determination of color-singlet nonrelativistic QCD matrix elements for S-wave charmonium*, *Phys. Rev. D* **77** (2008) 094017 [arXiv:0710.0994 [hep-ph]].

82

[119] H. S. Chung, J. Lee and C. Yu, *NRQCD matrix elements for S-wave bottomonia and* $\Gamma[\eta_b(nS) \to \gamma\gamma]$ *with relativistic corrections*, *Phys. Lett. B* **697** (2011) 48 [`arXiv:1011.1554 [hep-ph]`].

[120] J. D. Bjorken and S. D. Drell, *Relativistic Quantum Mechanics.* International Series In Pure and Applied Physics. McGraw-Hill, New York, 1965.

[121] N. N. Bogolyubov, A. A. Logunov and I. T. Todorov, *Introduction to Axiomatic Quantum Field Theory.* Mathematical Physics Monograph Series, No. 18. W. A. Benjamin, Inc., Reading, Mass.-London-Amsterdam, 1975. Translated from the Russian by Stephen A. Fulling and Ludmila G. Popova, Edited by Stephen A. Fulling.

[122] H. J. Melosh, *Quarks: Currents and constituents*, *Phys. Rev. D* **9** (1974) 1095.

[123] M. Beyer, C. Kuhrts and H. J. Weber, *Relativistic spin-flavor states in light front dynamics*, *Annals Phys.* **269** (1998) 129 [`arXiv:nucl-th/9804021`].

[124] J. Hufner, Y. P. Ivanov, B. Z. Kopeliovich and A. V. Tarasov, *Photoproduction of charmonia and total charmonium proton cross-sections*, *Phys. Rev. D* **62** (2000) 094022 [`arXiv:hep-ph/0007111`].

[125] M. V. Terentev, *On the Structure of Wave Functions of Mesons as Bound States of Relativistic Quarks*, *Sov. J. Nucl. Phys.* **24** (1976) 106.

[126] M. Krelina, J. Nemchik, R. Pasechnik and J. Cepila, *Spin rotation effects in diffractive electroproduction of heavy quarkonia*, *Eur. Phys. J. C* **79** (2019) no. 2 154 [`arXiv:1812.03001 [hep-ph]`].

[127] M. Krelina, J. Nemchik and R. Pasechnik, *D-wave effects in diffractive electroproduction of heavy quarkonia from the photon-like* $V \to Q\bar{Q}$ *transition*, *Eur. Phys. J. C* **80** (2020) no. 2 92 [`arXiv:1909.12770 [hep-ph]`].

[128] J. Cepila, J. Nemchik, M. Krelina and R. Pasechnik, *Theoretical uncertainties in exclusive electroproduction of S-wave heavy quarkonia*, *Eur. Phys. J. C* **79** (2019) no. 6 495 [`arXiv:1901.02664 [hep-ph]`].

[129] I. Babiarz, V. P. Goncalves, R. Pasechnik, W. Schäfer and A. Szczurek, $\gamma^*\gamma^* \to \eta_c(1S, 2S)$ *transition form factors for spacelike photons*, *Phys. Rev. D* **100** (2019) no. 5 054018 [`arXiv:1908.07802 [hep-ph]`].

[130] I. Babiarz, R. Pasechnik, W. Schäfer and A. Szczurek, *Hadroproduction of scalar P-wave quarkonia in the light-front* k_T *-factorization approach*, *JHEP* **06** (2020) 101 [`arXiv:2002.09352 [hep-ph]`].

[131] I. Babiarz, R. Pasechnik, W. Schäfer and A. Szczurek, *Probing the structure of* $\chi_{c1}(3872)$ *with photon transition form factors*, `arXiv:2303.09175 [hep-ph]`.

[132] Y. Li, P. Maris and J. P. Vary, *Quarkonium as a relativistic bound state on the light front*, *Phys. Rev. D* **96** (2017) 016022 [arXiv:1704.06968 [hep-ph]].

[133] P. Hoodbhoy, *Wave function corrections and off forward gluon distributions in diffractive J/ψ electroproduction*, *Phys. Rev. D* **56** (1997) 388 [arXiv:hep-ph/9611207].

[134] H. Hänninen, T. Lappi and R. Paatelainen, *One-loop corrections to light cone wave functions: the dipole picture DIS cross section*, *Annals Phys.* **393** (2018) 358 [arXiv:1711.08207 [hep-ph]].

[135] G. Beuf, *Dipole factorization for DIS at NLO: Loop correction to the $\gamma^*_{T,L} \to q\bar{q}$ light-front wave functions*, *Phys. Rev. D* **94** (2016) no. 5 054016 [arXiv:1606.00777 [hep-ph]].

[136] G. Beuf, *Dipole factorization for DIS at NLO: Combining the $q\bar{q}$ and $q\bar{q}g$ contributions*, *Phys. Rev. D* **96** (2017) no. 7 074033 [arXiv:1708.06557 [hep-ph]].

[137] M. A. Escobedo and T. Lappi, *Dipole picture and the nonrelativistic expansion*, *Phys. Rev. D* **101** (2020) no. 3 034030 [arXiv:1911.01136 [hep-ph]].

[138] V. L. Chernyak and A. R. Zhitnitsky, *Asymptotic Behavior of Exclusive Processes in QCD*, *Phys. Rept.* **112** (1984) 173.

[139] P. Ball, V. M. Braun, Y. Koike and K. Tanaka, *Higher twist distribution amplitudes of vector mesons in QCD: Formalism and twist - three distributions*, *Nucl. Phys. B* **529** (1998) 323 [arXiv:hep-ph/9802299].

[140] V. M. Braun and I. E. Filyanov, *Conformal Invariance and Pion Wave Functions of Nonleading Twist*, *Z. Phys. C* **48** (1990) 239.

[141] A. V. Efremov and A. V. Radyushkin, *Factorization and Asymptotical Behavior of Pion Form-Factor in QCD*, *Phys. Lett. B* **94** (1980) 245.

[142] Z. Bern and D. A. Kosower, *The Computation of loop amplitudes in gauge theories*, *Nucl. Phys. B* **379** (1992) 451.

[143] Z. Bern, A. De Freitas, L. J. Dixon and H. L. Wong, *Supersymmetric regularization, two loop QCD amplitudes and coupling shifts*, *Phys. Rev. D* **66** (2002) 085002 [arXiv:hep-ph/0202271].

[144] R. Boussarie, A. V. Grabovsky, D. Y. Ivanov, L. Szymanowski and S. Wallon, *Next-to-Leading Order Computation of Exclusive Diffractive Light Vector Meson Production in a Saturation Framework*, *Phys. Rev. Lett.* **119** (2017) no. 7 072002 [arXiv:1612.08026 [hep-ph]].

[145] F. Gao, L. Chang, Y.-X. Liu, C. D. Roberts and S. M. Schmidt, *Parton distribution amplitudes of light vector mesons*, *Phys. Rev. D* **90** (2014) no. 1 014011 [`arXiv:1405.0289 [nucl-th]`].

[146] M. V. Polyakov and H.-D. Son, *Second Gegenbauer moment of a ρ-meson distribution amplitude*, *Phys. Rev. D* **102** (2020) no. 11 114005 [`arXiv:2008.06270 [hep-ph]`].

[147] C. Marquet, *A Unified description of diffractive deep inelastic scattering with saturation*, *Phys. Rev. D* **76** (2007) 094017 [`arXiv:0706.2682 [hep-ph]`].

[148] H. Kowalski, T. Lappi, C. Marquet and R. Venugopalan, *Nuclear enhancement and suppression of diffractive structure functions at high energies*, *Phys. Rev. C* **78** (2008) 045201 [`arXiv:0805.4071 [hep-ph]`].

[149] **ZEUS** collaboration, J. Breitweg *et. al.*, *Measurement of the diffractive cross-section in deep inelastic scattering using ZEUS 1994 data*, *Eur. Phys. J. C* **6** (1999) 43 [`arXiv:hep-ex/9807010`].

[150] **H1** collaboration, T. Ahmed *et. al.*, *First measurement of the deep inelastic structure of proton diffraction*, *Phys. Lett. B* **348** (1995) 681 [`arXiv:hep-ex/9503005`].

[151] **H1** collaboration, A. Aktas *et. al.*, *Diffractive deep-inelastic scattering with a leading proton at HERA*, *Eur. Phys. J. C* **48** (2006) 749 [`arXiv:hep-ex/0606003`].

[152] **H1** collaboration, A. Aktas *et. al.*, *Measurement and QCD analysis of the diffractive deep-inelastic scattering cross-section at HERA*, *Eur. Phys. J. C* **48** (2006) 715 [`arXiv:hep-ex/0606004`].

[153] **H1** collaboration, F. D. Aaron *et. al.*, *Measurement of the Diffractive Longitudinal Structure Function F_L^D at HERA*, *Eur. Phys. J. C* **71** (2011) 1836 [`arXiv:1107.3420 [hep-ex]`].

[154] **H1** collaboration, F. D. Aaron *et. al.*, *Inclusive Measurement of Diffractive Deep-Inelastic Scattering at HERA*, *Eur. Phys. J. C* **72** (2012) 2074 [`arXiv:1203.4495 [hep-ex]`].

[155] **H1, ZEUS** collaboration, F. D. Aaron *et. al.*, *Combined inclusive diffractive cross sections measured with forward proton spectrometers in deep inelastic ep scattering at HERA*, *Eur. Phys. J. C* **72** (2012) 2175 [`arXiv:1207.4864 [hep-ex]`].

[156] **ZEUS** collaboration, M. Derrick *et. al.*, *Measurement of the diffractive structure function in deep elastic scattering at HERA*, *Z. Phys. C* **68** (1995) 569 [`arXiv:hep-ex/9505010`].

[157] **ZEUS** collaboration, M. Derrick *et. al.*, *Measurement of the diffractive cross-section in deep inelastic scattering*, *Z. Phys. C* **70** (1996) 391 [`arXiv:hep-ex/9602010`].

[158] **ZEUS** collaboration, S. Chekanov *et. al.*, *Measurement of the Q^2 and energy dependence of diffractive interactions at HERA*, *Eur. Phys. J. C* **25** (2002) 169 [`arXiv:hep-ex/0203039`].

[159] **ZEUS** collaboration, S. Chekanov *et. al.*, *Study of deep inelastic inclusive and diffractive scattering with the ZEUS forward plug calorimeter*, *Nucl. Phys. B* **713** (2005) 3 [`arXiv:hep-ex/0501060`].

[160] **ZEUS** collaboration, S. Chekanov *et. al.*, *Deep inelastic inclusive and diffractive scattering at Q^2 values from 25 to 320 GeV^2 with the ZEUS forward plug calorimeter*, *Nucl. Phys. B* **800** (2008) 1 [`arXiv:0802.3017 [hep-ex]`].

[161] M. Wusthoff, *Large rapidity gap events in deep inelastic scattering*, *Phys. Rev. D* **56** (1997) 4311 [`arXiv:hep-ph/9702201`].

[162] M. Wusthoff and A. D. Martin, *The QCD description of diffractive processes*, *J. Phys. G* **25** (1999) R309 [`arXiv:hep-ph/9909362`].

[163] J. Bartels and M. Wusthoff, *The Triple Regge limit of diffractive dissociation in deep inelastic scattering*, *Z. Phys. C* **66** (1995) 157.

[164] Y. V. Kovchegov and E. Levin, *Diffractive dissociation including multiple pomeron exchanges in high parton density QCD*, *Nucl. Phys. B* **577** (2000) 221 [`arXiv:hep-ph/9911523`].

[165] J. Bartels, H. Jung and M. Wusthoff, *Quark-antiquark-gluon jets in DIS diffractive dissociation*, *Eur. Phys. J. C* **11** (1999) 111 [`arXiv:hep-ph/9903265`].

[166] B. Z. Kopeliovich, A. Schafer and A. V. Tarasov, *Nonperturbative effects in gluon radiation and photoproduction of quark pairs*, *Phys. Rev. D* **62** (2000) 054022 [`arXiv:hep-ph/9908245`].

[167] Y. V. Kovchegov, *Diffractive gluon production in proton nucleus collisions and in DIS*, *Phys. Rev. D* **64** (2001) 114016 [`arXiv:hep-ph/0107256`]. [Erratum: Phys.Rev.D 68, 039901 (2003)].

[168] S. Munier and A. Shoshi, *Diffractive photon dissociation in the saturation regime from the Good and Walker picture*, *Phys. Rev. D* **69** (2004) 074022 [`arXiv:hep-ph/0312022`].

[169] K. J. Golec-Biernat and C. Marquet, *Testing saturation with diffractive jet production in deep inelastic scattering*, *Phys. Rev. D* **71** (2005) 114005 [`arXiv:hep-ph/0504214`].

[170] G. Beuf, H. Hänninen, T. Lappi, Y. Mulian and H. Mäntysaari, *Diffractive deep inelastic scattering at NLO in the dipole picture: The qq̄g contribution*, *Phys. Rev. D* **106** (2022) no. 9 094014 [`arXiv:2206.13161 [hep-ph]`].

[171] P. Caucal, F. Salazar and R. Venugopalan, *Dijet impact factor in DIS at next-to-leading order in the Color Glass Condensate*, *JHEP* **11** (2021) 222 [`arXiv:2108.06347 [hep-ph]`].

[172] G. A. Chirilli, B.-W. Xiao and F. Yuan, *One-loop Factorization for Inclusive Hadron Production in pA Collisions in the Saturation Formalism*, *Phys. Rev. Lett.* **108** (2012) 122301 [`arXiv:1112.1061 [hep-ph]`].

[173] G. A. Chirilli, B.-W. Xiao and F. Yuan, *Inclusive Hadron Productions in pA Collisions*, *Phys. Rev. D* **86** (2012) 054005 [`arXiv:1203.6139 [hep-ph]`].

[174] A. M. Staśto, B.-W. Xiao, F. Yuan and D. Zaslavsky, *Matching collinear and small x factorization calculations for inclusive hadron production in pA collisions*, *Phys. Rev. D* **90** (2014) no. 1 014047 [`arXiv:1405.6311 [hep-ph]`].

[175] Z.-B. Kang, I. Vitev and H. Xing, *Next-to-leading order forward hadron production in the small-x regime: rapidity factorization*, *Phys. Rev. Lett.* **113** (2014) 062002 [`arXiv:1403.5221 [hep-ph]`].

[176] B.-W. Xiao and F. Yuan, *Comment on "Next-to-leading order forward hadron production in the small-x regime: rapidity factorization" arXiv:1403.5221 by Kang et al*, `arXiv:1407.6314 [hep-ph]`.

[177] T. Altinoluk, N. Armesto, G. Beuf, A. Kovner and M. Lublinsky, *Single-inclusive particle production in proton-nucleus collisions at next-to-leading order in the hybrid formalism*, *Phys. Rev. D* **91** (2015) no. 9 094016 [`arXiv:1411.2869 [hep-ph]`].

[178] K. Watanabe, B.-W. Xiao, F. Yuan and D. Zaslavsky, *Implementing the exact kinematical constraint in the saturation formalism*, *Phys. Rev. D* **92** (2015) no. 3 034026 [`arXiv:1505.05183 [hep-ph]`].

[179] E. Iancu, A. H. Mueller and D. N. Triantafyllopoulos, *CGC factorization for forward particle production in proton-nucleus collisions at next-to-leading order*, *JHEP* **12** (2016) 041 [`arXiv:1608.05293 [hep-ph]`].

[180] B. Ducloué, T. Lappi and Y. Zhu, *Single inclusive forward hadron production at next-to-leading order*, *Phys. Rev. D* **93** (2016) no. 11 114016 [`arXiv:1604.00225 [hep-ph]`].

[181] B. Ducloué, E. Iancu, T. Lappi, A. H. Mueller, G. Soyez, D. N. Triantafyllopoulos and Y. Zhu, *Use of a running coupling in the NLO calculation of forward hadron production*, *Phys. Rev. D* **97** (2018) no. 5 054020 [`arXiv:1712.07480 [hep-ph]`].

[182] B. Ducloué, T. Lappi and Y. Zhu, *Implementation of NLO high energy factorization in single inclusive forward hadron production*, *Phys. Rev. D* **95** (2017) no. 11 114007 [arXiv:1703.04962 [hep-ph]].

[183] H.-Y. Liu, Y.-Q. Ma and K.-T. Chao, *Improvement for Color Glass Condensate factorization: single hadron production in pA collisions at next-to-leading order*, *Phys. Rev. D* **100** (2019) no. 7 071503 [arXiv:1909.02370 [nucl-th]].

[184] H.-Y. Liu, Z.-B. Kang and X. Liu, *Threshold resummation for hadron production in the small-x region*, *Phys. Rev. D* **102** (2020) no. 5 051502 [arXiv:2004.11990 [hep-ph]].

[185] F. Bergabo and J. Jalilian-Marian, *Single inclusive hadron production in DIS at small x: next to leading order corrections*, *JHEP* **01** (2023) 095 [arXiv:2210.03208 [hep-ph]].

[186] R. Boussarie, A. V. Grabovsky, L. Szymanowski and S. Wallon, *Impact factor for high-energy two and three jets diffractive production*, *JHEP* **09** (2014) 026 [arXiv:1405.7676 [hep-ph]].

[187] R. Boussarie, A. V. Grabovsky, L. Szymanowski and S. Wallon, *On the one loop $\gamma^{(*)} \to q\bar{q}$ impact factor and the exclusive diffractive cross sections for the production of two or three jets*, *JHEP* **11** (2016) 149 [arXiv:1606.00419 [hep-ph]].

[188] P. Caucal, F. Salazar, B. Schenke and R. Venugopalan, *Back-to-back inclusive dijets in DIS at small x: Sudakov suppression and gluon saturation at NLO*, *JHEP* **11** (2022) 169 [arXiv:2208.13872 [hep-ph]].

[189] P. Caucal, F. Salazar, B. Schenke, T. Stebel and R. Venugopalan, *Back-to-back inclusive di-jets in DIS at small x_{Bj}: Gluon Weizsäcker-Williams distribution at NLO*, arXiv:2304.03304 [hep-ph].

[190] M. Fucilla, A. V. Grabovsky, E. Li, L. Szymanowski and S. Wallon, *NLO computation of diffractive di-hadron production in a saturation framework*, *JHEP* **03** (2023) 159 [arXiv:2211.05774 [hep-ph]].

[191] F. Bergabo and J. Jalilian-Marian, *One-loop corrections to dihadron production in DIS at small x*, *Phys. Rev. D* **106** (2022) no. 5 054035 [arXiv:2207.03606 [hep-ph]].

[192] F. Bergabo and J. Jalilian-Marian, *Dihadron production in DIS at small x at next-to-leading order: Transverse photons*, *Phys. Rev. D* **107** (2023) no. 5 054036 [arXiv:2301.03117 [hep-ph]].

[193] I. Balitsky and G. A. Chirilli, *Next-to-leading order evolution of color dipoles*, *Phys. Rev. D* **77** (2008) 014019 [arXiv:0710.4330 [hep-ph]].

[194] A. Kovner, M. Lublinsky and Y. Mulian, *Jalilian-Marian, Iancu, McLerran, Weigert, Leonidov, Kovner evolution at next to leading order*, *Phys. Rev. D* **89** (2014) no. 6 061704 [`arXiv:1310.0378 [hep-ph]`].

[195] M. Lublinsky and Y. Mulian, *High Energy QCD at NLO: from light-cone wave function to JIMWLK evolution*, *JHEP* **05** (2017) 097 [`arXiv:1610.03453 [hep-ph]`].

[196] L. Dai and M. Lublinsky, *NLO JIMWLK evolution with massive quarks*, *JHEP* **07** (2022) 093 [`arXiv:2203.13695 [hep-ph]`].

[197] T. Altinoluk, N. Armesto, G. Beuf, M. Martínez and C. A. Salgado, *Next-to-eikonal corrections in the CGC: gluon production and spin asymmetries in pA collisions*, *JHEP* **07** (2014) 068 [`arXiv:1404.2219 [hep-ph]`].

[198] T. Altinoluk, N. Armesto, G. Beuf and A. Moscoso, *Next-to-next-to-eikonal corrections in the CGC*, *JHEP* **01** (2016) 114 [`arXiv:1505.01400 [hep-ph]`].

[199] P. Agostini, T. Altinoluk and N. Armesto, *Non-eikonal corrections to multi-particle production in the Color Glass Condensate*, *Eur. Phys. J. C* **79** (2019) no. 7 600 [`arXiv:1902.04483 [hep-ph]`].

[200] T. Altinoluk, G. Beuf, A. Czajka and A. Tymowska, *Quarks at next-to-eikonal accuracy in the CGC: Forward quark-nucleus scattering*, *Phys. Rev. D* **104** (2021) no. 1 014019 [`arXiv:2012.03886 [hep-ph]`].

[201] T. Altinoluk and G. Beuf, *Quark and scalar propagators at next-to-eikonal accuracy in the CGC through a dynamical background gluon field*, *Phys. Rev. D* **105** (2022) no. 7 074026 [`arXiv:2109.01620 [hep-ph]`].

[202] P. Agostini, T. Altinoluk, N. Armesto, F. Dominguez and J. G. Milhano, *Multiparticle production in proton–nucleus collisions beyond eikonal accuracy*, *Eur. Phys. J. C* **82** (2022) no. 11 1001 [`arXiv:2207.10472 [hep-ph]`].

[203] T. Altinoluk, G. Beuf, A. Czajka and A. Tymowska, *DIS dijet production at next-to-eikonal accuracy in the CGC*, *Phys. Rev. D* **107** (2023) no. 7 074016 [`arXiv:2212.10484 [hep-ph]`].

[204] T. Altinoluk, N. Armesto and G. Beuf, *Probing quark transverse momentum distributions in the Color Glass Condensate: quark-gluon dijets in Deep Inelastic Scattering at next-to-eikonal accuracy*, `arXiv:2303.12691 [hep-ph]`.

[205] G. A. Chirilli, *Sub-eikonal corrections to scattering amplitudes at high energy*, *JHEP* **01** (2019) 118 [`arXiv:1807.11435 [hep-ph]`].

[206] G. A. Chirilli, *High-energy operator product expansion at sub-eikonal level*, *JHEP* **06** (2021) 096 [`arXiv:2101.12744 [hep-ph]`].

[207] K. J. Eskola, C. A. Flett, V. Guzey, T. Löytäinen and H. Paukkunen,
*Next-to-leading order perturbative QCD predictions for exclusive J/ψ
photoproduction in oxygen-oxygen and lead-lead collisions at the LHC*,
`arXiv:2210.16048 [hep-ph]`.

[208] K. J. Eskola, C. A. Flett, V. Guzey, T. Löytäinen and H. Paukkunen,
*Exclusive J/ψ photoproduction in ultraperipheral Pb+Pb collisions at the
CERN Large Hadron Collider calculated at next-to-leading order perturbative
QCD*, *Phys. Rev. C* **106** (2022) no. 3 035202 [`arXiv:2203.11613 [hep-ph]`].

[209] K. J. Eskola, C. A. Flett, V. Guzey, T. Löytäinen and H. Paukkunen,
*Predictions for exclusive Υ photoproduction in ultraperipheral $Pb + Pb$
collisions at the LHC at next-to-leading order in perturbative QCD*,
`arXiv:2303.03007 [hep-ph]`.

ORIGINAL PAPERS

I

RELATIVISTIC CORRECTIONS TO THE VECTOR MESON LIGHT FRONT WAVE FUNCTION

by

Tuomas Lappi, Heikki Mäntysaari, Jani Penttala (2020)

Relativistic corrections to the vector meson light front wave function

T. Lappi◉, H. Mäntysaari, and J. Penttala◉

*Department of Physics, University of Jyväskylä, P.O. Box 35, 40014 University of Jyväskylä, Finland
and Helsinki Institute of Physics, P.O. Box 64, 00014 University of Helsinki, Finland*

We compute a light front wave function for heavy vector mesons based on long-distance matrix elements constrained by decay width analyses in the nonrelativistic QCD framework. Our approach provides a systematic expansion of the wave function in quark velocity. The first relativistic correction included in our calculation is found to be significant and crucial for a good description of the HERA exclusive J/ψ production data. When looking at cross section ratios between nuclear and proton targets, the wave function dependence does not cancel out exactly. In particular the fully nonrelativistic limit is found not to be a reliable approximation even in this ratio. The important role of the Melosh rotation to express the rest frame wave function on the light front is illustrated.

I. INTRODUCTION

At large densities or small Bjorken-x, nonlinear QCD dynamics is expected to manifest itself in nuclear structure. To describe the QCD matter in this nonlinear regime, an effective field theory known as the color glass condensate has been developed; see e.g., [1,2]. Diffractive scattering processes at high energies are especially powerful probes of this region of phase space. The advantage in diffractive, with respect to inclusive, scattering is that since no color charge transfer is allowed, even at leading order in perturbative QCD at least two gluons have to be exchanged with the target. Consequently, the cross sections approximatively probe the square of the gluon density [3] and can be expected to be highly sensitive to nonlinear dynamics.

An especially interesting diffractive process is exclusive vector meson production in collisions of real or virtual photons with the target, where only one meson with the same quantum numbers as the photon is produced. In these processes only vacuum quantum numbers are exchanged between the target and the diffractive system. Thus the target can remain intact, and the transverse momentum transfer can be used to probe the spatial structure of the target. This momentum transfer is by definition the Fourier conjugate to the impact parameter. As such, it becomes possible to study the target structure differentially in the transverse plane. A particularly important channel is the production of J/ψ mesons. The charm quark is heavy enough to enable a weak coupling description of its elementary interactions. Nevertheless the quark mass is not large enough to make the process insensitive to saturation effects. Also experimentally the J/ψ is relatively easily identifiable and produced with large enough cross sections to be seen.

Exclusive J/ψ production in electron-proton deep inelastic scattering has been studied in detail at HERA by the H1 and ZEUS experiments [4–9]. Additionally, lighter ρ and ϕ [10–12] and heavier Υ states [13,14] have been measured. Recently, it has also become possible to measure exclusive vector meson production at the RHIC and at the LHC in ultraperipheral collisions [15,16] where the impact parameter between the two hadrons is large enough such that the scattering is mediated by quasireal photons; see Refs. [17–26] for recent measurements. These developments have also enabled vector meson photoproduction studies with nuclear targets, which are more sensitive to gluon saturation. Indeed signatures of strong nuclear effects (e.g., saturation, or gluon shadowing) are seen in J/ψ photoproduction (see e.g., Refs. [27–29]). The effects seen in these exclusive processes are consistent with inclusive measurements such as particle spectra in proton-nucleus collisions (see e.g., [30–35]). However, in exclusive scattering the nonlinear effects are larger, since inclusive cross sections at leading order are only sensitive to the first power of the gluon density.

One major source of model uncertainties in the theoretical description of vector meson production follows from the nonperturbative vector meson wave function. For the J/ψ, a natural first approximation is to treat it as a fully nonrelativistic bound charm-anticharm state, which is the limit taken in the seminal work in Ref. [3]. The calculation of Ref. [36] recovers the same nonrelativistic result in the

dipole picture (see also Ref. [37]). Already early on, it has been argued that this nonrelativistic approximation obtains important corrections from the motion of the charm quark pair in the bound state [38,39]. More recently, much of the phenomenological literature on J/ψ photoproduction has used phenomenological light cone wave functions to describe the meson bound state. This has the advantage that the light cone wave function is invariant under boosts in the longitudinal direction and is thus naturally more suited to high-energy collision phenomena. A disadvantage of some recent phenomenological parametrizations has been that they do not fully use the information on the nonperturbative bound state physics, most importantly decay widths, of quarkonium states that are usually analyzed in terms of nonrelativistic wave functions.

In recent literature, the applied different phenomenological wave functions result in e.g., J/ψ production cross sections that differ up to $\sim 30\%$ from each other [27,40,41]. This is a large model uncertainty, compared to the precise data that is already available from HERA and the LHC and especially given that the Electron Ion Collider (EIC) [42,43] is in the horizon (and similar plans exist at CERN [44] and in China [45]). The EIC will perform vast amounts of precise deep inelastic scattering (DIS) measurements over a wide kinematical range, which calls for robust theoretical predictions.

To reduce the model uncertainty related to the vector meson wave function, we propose in this work a new method to constrain the wave function for heavy mesons based on input from the nonrelativistic QCD (NRQCD) matrix elements. These matrix elements capture nonperturbative long-distance physics and can be obtained by computing the vector meson decay widths in different channels as a systematic expansion in both the coupling constant α_s and the quark velocity v. As we will demonstrate, these matrix elements can be used to determine the value and the derivative of the vector meson wave function at the origin. As such, this approach provides more constraints than the phenomenological parametrizations widely used in the literature. In particular, starting from manifestly rotationally invariant rest frame wave functions, one by construction obtains consistent parametrizations of longitudinally and tranversally polarized vector mesons simultaneously, which is not obvious in many light cone approaches.

This manuscript is organized as follows. First, in Sec. II we review how vector meson production is computed in the dipole picture within the color glass condensate framework and how the cross section depends on the vector meson light front wave function. In Sec. III we first present how to obtain the rest frame wave function in terms of the NRQCD matrix elements and then show how this is transformed to the light cone by applying the Melosh rotation [46,47]. We compare the obtained NRQCD-based wave function to other widely used wave functions that are reviewed in

Sec. IV. The numerical analysis including vector meson-photon overlaps and J/ψ production cross sections is presented in Sec. V.

II. VECTOR MESON PRODUCTION IN THE DIPOLE PICTURE

A. Exclusive scattering

At high energies exclusive vector meson production in virtual photon-proton (or nucleus) scattering can be described in a factorized form. The necessary ingredients are the virtual photon wave function Ψ_γ^λ describing the $\gamma^* \to q\bar{q}$ splitting, the dipole-target scattering amplitude N and the vector meson wave function Ψ_V describing the transition $q\bar{q} \to V$. The scattering amplitude reads [48] (note that the correct phase factor coupling the dipole size $\mathbf{r}$ to the transverse momentum transfer Δ is determined in Ref. [49])

$$
\mathcal{A}^\lambda = 2i \int d^2\mathbf{b}\, d^2\mathbf{r}\, \frac{dz}{4\pi} e^{-i(\mathbf{b}+(\frac{1}{2}-z)\mathbf{r})\cdot\Delta}
$$
$$
\times \Psi_\gamma^{\lambda*}(\mathbf{r}, Q^2, z)\Psi_V(\mathbf{r}, z) N(\mathbf{r}, \mathbf{b}, x_\mathbb{P}). \qquad (1)
$$

Here Q^2 is the photon virtuality, $\mathbf{r}$ the transverse size of the dipole, $\mathbf{b}$ the impact parameter and z the fraction of the photon light cone plus momentum carried by the quark. The photon polarization is λ, with $\lambda = \pm 1$ referring to the transverse polarization and $\lambda = 0$ to the longitudinal one.

In this work will study coherent vector meson V production. The coherent cross section refers to the scattering process where the target proton (or nucleus) remains intact. In this case, the cross section as a function of squared momentum transfer $t \approx -\Delta^2$ can be written as

$$
\frac{d\sigma^{\gamma^* p \to Vp}}{dt} = R_g^2(1+\beta^2)\frac{1}{16\pi}|\mathcal{A}_{T,L}|^2. \qquad (2)
$$

The dipole amplitude N depends on the longitudinal momentum fraction $x_\mathbb{P}$ the target loses in the scattering process, which reads

$$
x_\mathbb{P} = \frac{M_V^2 + Q^2 - t}{W^2 + Q^2 - m_N^2}. \qquad (3)
$$

Here M_V is the mass of the vector meson V and m_N is the proton mass. The scattering amplitude $\mathcal{A}_{T,L}$ is obtained from Eq. (1) by summing over the quark helicities and, in the case of transverse (T) polarization, averaging over the photon polarization states $\lambda = \pm 1$.

In Eq. (2) two phenomenological corrections are included following Ref. [48]. First, $\beta = \tan(\frac{\pi\delta}{2})$ is the ratio between the real and imaginary parts of the scattering amplitude. It can be obtained from an analyticity argument as

$$\delta = \frac{\partial \ln \mathcal{A}_{T,L}}{\partial \ln(1/x_{\mathbb{P}})}. \qquad (4)$$

The so-called skewedness correction is included in terms of the factor R_g, which reads

$$R_g = \frac{2^{2\delta+3}}{\sqrt{\pi}} \frac{\Gamma(\delta + 5/2)}{\Gamma(\delta + 4)}. \qquad (5)$$

This correction can be derived by considering the vector meson production in the two-gluon exchange limit, assuming that the two gluons carry very different fractions of the target longitudinal momentum [50]. In this case, the cross section can be related to the collinearly factorized parton distribution functions scaled by the factor R_g. In the dipole picture applied here, where the two quarks are color rotated in the target color field and undergo multiple scattering, this limit is not reached. In this work we include both of the real part and skewedness corrections widely used in the previous literature but emphasize that these numerically large corrections should be used with caution when predicting absolute normalizations for the cross sections.

In addition to coherent scattering, one can study incoherent diffraction where the target breaks up, but there is still no exchange of color charge between the produced vector meson and the target remnants. These processes are recently studied extensively in the literature as they probe, in addition to saturation effects [41], also the event-by-event fluctuations of the scattering amplitude resulting from the target structure fluctuations; see e.g., Refs. [51–54] or Ref. [55] for a review. As the focus in this work is on the vector meson wave function which enters in calculations of both incoherent and coherent cross sections similarly, from now on we only consider coherent scattering here.

B. Virtual photon wave function

The virtual photon splitting to a $c\bar{c}$ dipole is a simple QED process, and the photon wave function Ψ_γ can be computed directly by applying the light cone perturbation theory (see e.g., [56,57]). Using the diagrammatic rules of light front perturbation theory and the conventions used in Refs. [58,59], the wave function can be written as

$$\Psi^\lambda_{\gamma,h\bar{h}}(k) = \frac{e_f e \sqrt{N_c}}{q^- - k^- - k'^-} \frac{\bar{u}_h(k)\not{\varepsilon}^\lambda(q)v_{\bar{h}}(k')}{4\sqrt{\pi}k^+k'^+q^+}. \qquad (6)$$

Here e_f is the fractional charge of the quark (in this work we consider only charm quarks with $e_f = 2/3$), k, k' and q are the quark, antiquark and photon momenta, respectively, $e = \sqrt{4\pi\alpha_{em}}$ and h and $\bar{h}$ refer to the quark and antiquark light front helicities [60]. The factor $\sqrt{N_c}$ is included to obtain a squared wave function proportional to the number of colors N_c. The spinors which are the eigenstates of light front helicity read, in the Lepage-Brodsky convention,

$$u_h(k) = \frac{1}{2^{1/4}\sqrt{p^+}}(\sqrt{2}p^+ + \gamma^0 m + \alpha_T \cdot \mathbf{k})\bar{\chi}_h, \qquad (7)$$

$$v_h(k) = \frac{1}{2^{1/4}\sqrt{p^+}}(\sqrt{2}p^+ - \gamma^0 m + \alpha_T \cdot \mathbf{k})\bar{\chi}_{-h}, \qquad (8)$$

where the four-component helicity spinors read $\bar{\chi}_{h=+1} = \frac{1}{\sqrt{2}}(1,0,1,0)^T$ and $\bar{\chi}_{h=-1} = \frac{1}{\sqrt{2}}(0,1,0,-1)^T$, and $\alpha_T = (\gamma^0\gamma^1, \gamma^0\gamma^2)$. We use the light cone variables defined as $p^\pm = \frac{1}{\sqrt{2}}(p^0 \pm p^3)$. The spinor normalization convention is $\bar{u}_h u_{\bar{h}} = -\bar{v}_h v_{\bar{h}} = 2m\delta_{h\bar{h}}$, where m is the quark mass.

In the light cone gauge, in which $\varepsilon^+ = 0$, the photon polarization vectors read

$$\varepsilon^{\lambda=0}(q) = \left(0, 0, 0, \frac{Q}{q^+}\right), \qquad (9)$$

$$\varepsilon^{\lambda=\pm1} = \left(0, \varepsilon^\lambda_T, \frac{\mathbf{q} \cdot \varepsilon^\lambda_T}{q^+}\right), \qquad (10)$$

where

$$\varepsilon^{\lambda=\pm1}_T = (\mp 1, -i)/\sqrt{2} \qquad (11)$$

and $Q^2 = -q^2$.

The wave function can be evaluated by substituting the polarization vectors and explicit expressions for the spinors in Eq. (6) and setting the photon transverse momentum $\mathbf{q}$ to zero. It is convenient here to define a wave function in terms of the momentum fraction z and pull out a factor 4π. This should be done so that probability is conserved:

$$\int \mathrm{d}k^+ |\Psi^\lambda_{\gamma,h\bar{h}}(k^+, \mathbf{k})|^2 = \int \frac{\mathrm{d}z}{4\pi} |\Psi^\lambda_{\gamma,h\bar{h}}(z, \mathbf{k})|^2, \qquad (12)$$

so that we can write $\Psi^\lambda_{\gamma,h\bar{h}}(z, \mathbf{k}) = \sqrt{4\pi q^+}\Psi^\lambda_{\gamma,h\bar{h}}(k^+, \mathbf{k})$. In momentum space, the wave functions read

$$\Psi^{\lambda=0}_{\gamma,h\bar{h}}(z, \mathbf{k}) = -e_f e \sqrt{N_c} \frac{2Qz(1-z)}{(\mathbf{k}^2 + \epsilon^2)}\delta_{h,-\bar{h}}, \qquad (13)$$

$$\Psi^{\lambda=+1}_{\gamma,h\bar{h}}(z, \mathbf{k}) = -\frac{e_f e \sqrt{2N_c}}{(\mathbf{k}^2 + \epsilon^2)}[ke^{i\theta_k}(z\delta_{h+}\delta_{\bar{h}-} \\ -(1-z)\delta_{h-}\delta_{\bar{h}+}) + m\delta_{h+}\delta_{\bar{h}+}], \qquad (14)$$

$$\Psi^{\lambda=-1}_{\gamma,h\bar{h}}(z, \mathbf{k}) = -\frac{e_f e \sqrt{2N_c}}{(\mathbf{k}^2 + \epsilon^2)}[ke^{-i\theta_k}((1-z)\delta_{h+}\delta_{\bar{h}-} \\ -z\delta_{h-}\delta_{\bar{h}+}) + m\delta_{h-}\delta_{\bar{h}-}], \qquad (15)$$

where $\epsilon^2 = Q^2 z(1-z) + m^2$ and $ke^{i\theta_k} = k_x + ik_y$. The wave function in the mixed transverse coordinate, longitudinal momentum fraction space entering in the vector

meson production cross section (1) is then obtained by performing a Fourier transform:

$$\Psi^\lambda_{\gamma,h\bar{h}}(z,\mathbf{r}) = \int \frac{d^2\mathbf{k}}{(2\pi)^2} e^{i\mathbf{k}\cdot\mathbf{r}} \Psi^\lambda_{\gamma,h\bar{h}}(z,\mathbf{k}). \quad (16)$$

The mixed space wave function for the longitudinal polarization is

$$\Psi^{\lambda=0}_{\gamma,h\bar{h}}(z,\mathbf{r}) = -e_f e \sqrt{N_c}\,\delta_{h,-\bar{h}} 2Qz(1-z)\frac{K_0(\epsilon r)}{2\pi}. \quad (17)$$

Similarly, for the transverse photon with $\lambda = \pm 1$ the wave function reads

$$\Psi^{\lambda=+1}_{\gamma,h\bar{h}}(z,\mathbf{r}) = -e_f e \sqrt{2N_c}\left[ie^{i\theta_r}\frac{\epsilon K_1(\epsilon r)}{2\pi}(z\delta_{h+}\delta_{\bar{h}-} \right.$$
$$\left. -(1-z)\delta_{h-}\delta_{\bar{h}+}) + m\frac{K_0(\epsilon r)}{2\pi}\delta_{h+}\delta_{\bar{h}+}\right],$$

$$\Psi^{\lambda=-1}_{\gamma,h\bar{h}}(z,\mathbf{r}) = -e_f e \sqrt{2N_c}\left[ie^{-i\theta_r}\frac{\epsilon K_1(\epsilon r)}{2\pi}((1-z)\delta_{h+}\delta_{\bar{h}-} \right.$$
$$\left. -z\delta_{h-}\delta_{\bar{h}+}) + m\frac{K_0(\epsilon r)}{2\pi}\delta_{h-}\delta_{\bar{h}-}\right]. \quad (18)$$

We note that the these wave functions agree with those derived in Ref. [59] using the same convention, except for the overall sign in case of transverse polarizations which does not affect any of our results. On the other hand, when compared to the widely used wave functions reported in Ref. [48], the relative sign between the mass term and z terms in the $\lambda = +1$ case is different.

We emphasize that the quark light cone helicity structure above does not exactly correspond to the spin structure in the rest frame of the meson (there is no rest frame for the spacelike photon). In particular, when transformed to the meson rest frame, there are both S- and D-wave contributions in both longitudinally and transversely polarized photons. The transformation between the light front wave function expressed in terms of the quark light front helicities and the rest frame wave function in terms of the quark spins is discussed in Sec. III B. We will discuss the decomposition of light cone wave functions, including the virtual photon one, into the S- and D-wave components in more detail in Appendix A.

C. Dipole-target scattering

The dipole-target scattering amplitude N in Eq. (1) is a correlator of Wilson lines, corresponding to the eikonal propagation of the quarks in the target color field. In principle, it satisfies perturbative evolution equations describing the dependence on momentum fraction $x_\mathbb{P}$, the so-called Jalilian-Marian–Iancu–McLerran–Weigert–Leonidov–Kovner equation (JIMWLK) equation [61–67], or the BK equation [68,69] that is obtained in the large-N_c

limit. These perturbative evolution equations, combined with a nonperturbative input obtained by fitting some experimental data, can in principle be used to evaluate the dipole amplitude at any (small) $x_\mathbb{P}$. This has been a successful approach when considering structure functions in DIS or inclusive particle production in hadronic collisions; see e.g., Refs. [31–35,70,71].

In diffractive scattering considered here one explicitly measures the transverse momentum transfer $\boldsymbol{\Delta}$, which is the Fourier conjugate to the impact parameter. Consequently, the dependence on the transverse geometry needs to be included accurately in the calculation. However, perturbative evolution equations generate long-distance Coulomb tails that should be regulated by some nonperturbative physics in order to avoid unphysical growth of the cross section [72]. There have been attempts to include effective confinement scale contributions in the BK and JIMWLK evolutions and use the obtained dipole amplitudes in phenomenological calculations of e.g., vector meson production [73–76] (see also [77]). As the main focus of this work is in vector meson wave functions, we apply a simpler approach and use the so called IPsat parametrization to describe the dipole-proton scattering amplitude.

The IPsat parametrization [78] consists of an eikonalized Dokshitzer–Gribov–Lipatov–Altarelli–Parisi equation (DGLAP)-evolved [79–82] gluon distribution, combined with an impact parameter $\mathbf{b}$ dependent transverse density profile. The advantage of this parametrization is that it matches perturbative QCD result in the dilute (small dipole size $|\mathbf{r}|$) limit and respects unitary in the saturation regime. The dipole amplitude in the IPsat parametrization reads

$$N(\mathbf{r},\mathbf{b},x) = 1 - \exp\left(-\frac{\pi^2}{2N_c}\mathbf{r}^2\alpha_s(\mu^2)xg(x,\mu^2)T_p(\mathbf{b})\right), \quad (19)$$

where the proton transverse density profile is assumed to be Gaussian:

$$T_p(\mathbf{b}) = \frac{1}{2\pi B_p}e^{-b^2/(2B_p)} \quad (20)$$

with $B = 4$ GeV^{-2}. The initial condition for the DGLAP evolution is obtained by fitting the HERA structure function data [83–86], and the fit results in an excellent description of the total reduced cross section and the charm contribution [87]. The scale choice is $\mu^2 = C/r^2 + \mu_0^2$, with the parameters C and μ_0, among with the DGLAP initial condition, are determined in the fit performed in Ref. [87] (see also [88]).

Following Ref. [78] (see also [87]), the dipole-proton scattering amplitude can be generalized to coherent scattering in the dipole-nucleus case as

$$N_A(\mathbf{r}, \mathbf{b}, x) = 1 - \exp\left(-\frac{\pi^2}{2N_c}\mathbf{r}^2\alpha_s(\mu^2)xg(x,\mu^2)AT_A(\mathbf{b})\right).$$
(21)

This estimate is valid in case of large nuclei, assuming that the dipole size $|\mathbf{r}|$ is not very large, which is the case in heavy vector meson production. Here $T_A(\mathbf{b})$ is the Woods-Saxon distribution integrated over the longitudinal coordinate, with the normalization $\int d^2\mathbf{b}T_A(\mathbf{b}) = 1$. The nuclear radius used here is $R_A = (1.13A^{1/3} - 0.86A^{-1/3})$ fm.

In order to calculate vector meson production, it is still necessary to determine the vector meson wave function. It cannot be computed perturbatively, and consequently there are many phenomenological parametrizations used in the literature. The main goal of this paper is to obtain the meson wave function in a systematic expansion in quark velocities given by the NRQCD approach. We will also discuss, for comparison, some other wave function parametrizations in Sec. IV.

III. LIGHT CONE WAVE FUNCTION FROM NRQCD

NRQCD is an effective field theory describing QCD in the limit where quark masses are large, or $v = p/m$ is small, where p is e.g., quark momentum and m is the quark mass. In this approach, it becomes possible to factorize cross sections into universal long-distance matrix elements and perturbatively calculated process-dependent hard factors.

A. Vector meson wave function in the rest frame

The J/ψ decay width in the NRQCD approach is written as an expansion in the quark velocity v [89]. At lowest order in v, the decay width is only sensitive to the long-distance matrix element $\langle\mathcal{O}_1\rangle_{J/\psi}$, which itself is determined by the value of the (renormalized) wave function at the origin. At next order, one finds a contribution proportional to the long-distance matrix element $\langle\vec{q}^2\rangle_{J/\psi}$ which is suppressed by a relative v^2. This matrix element is sensitive to the derivative of the wave function at the origin (see also Refs. [90,91] for a discussion of the velocity suppressed contributions to the distribution amplitude).

In this work we follow Ref. [92], where these matrix elements are determined. There, a subset of higher order (in v) contributions to the decay width including higher powers of ∇^2 are resummed to all orders following Ref. [93]. As a result, the J/ψ decay width in the leptonic channel can be written as

$$\Gamma(J/\psi \rightarrow e^-e^+)$$
$$= \frac{8\pi e_q^2\alpha_{\text{em}}^2}{3M_V^2}\left[1 - f\left(\frac{\langle\vec{q}^2\rangle_{J/\psi}}{m_{c,NR}^2}\right) - 2C_F\frac{\alpha_s}{\pi}\right]^2\langle\mathcal{O}_1\rangle_{J/\psi}$$
(22)

with

$$f(x) = \frac{x}{3(1 + x + \sqrt{1 + x})}.$$
(23)

Here, $e_q = 2/3$ is the fractional charge of the charm quark and M_V is the J/ψ mass. At this order in v, the J/ψ is a pure S-wave state, and its wave function can be factorized into a spin part and a scalar part. We will discuss the spin and angular momentum structure in more detail later.

The extraction of the matrix elements that we use [92] has been done in a calculation that includes both velocity and α_s corrections, such as in (22). Here, on the other hand, we will be using the light cone wave functions in a leading order calculation of cross sections, including only velocity corrections to the wave function. In a strict NRQCD power counting sense in α_s, the α_s corrections could be considered more important. Although steps have been taken to take them into account in the dipole picture exclusive cross section calculations [94] (see also recent work in a different formalism [95]), fully including them in the cross section is not yet possible at this point since the full photon to heavy quark pair wave function is not known to one-loop accuracy. Thus we will leave a computation that includes also the perturbative α_s calculations to future work and continue with our focus on the velocity corrections to the wave function here.

Since our cross section calculation does not include pure α_s corrections, taking the wave function to be given by just the operator $\langle\mathcal{O}_1\rangle_{J/\psi}$ in (22) would lead to an inconsistent treatment of the α_s corrections between the decay width and the cross section. Even in a more general sense, the α_s contributions that appear as corrections to the decay widths or cross sections expressed in terms of nonrelativistic wave functions should, in light cone perturbation theory, be thought of as perturbative corrections to the light cone wave function itself [39,94]. This can be understood in the sense that the degrees of freedom in the nonrelativistic wave function are constituent quarks as opposed to bare quarks in the light cone wave function; see the discussion in [39]. To obtain a consistent picture here, we will absorb the α_s correction to the scalar part of the wave function $\phi(r)$, which is then transformed to the light cone wave function. We thus relate the value and derivative at the origin of $\phi(r)$ to the long-distance matrix elements as

$$\left[1 - 2C_F\frac{\alpha_s}{\pi}\right]^2\langle\mathcal{O}_1\rangle_{J/\psi} = 2N_c|\phi(0)|^2 + \mathcal{O}(v^4),$$
(24)

$$\langle\vec{q}^2\rangle_{J/\psi} = -\frac{\nabla^2\phi(0)}{\phi(0)} + \mathcal{O}(v^2).$$
(25)

The nonperturbative long-distance matrix elements have been determined in Ref. [92] by considering simultaneously the $J/\psi \rightarrow e^+e^-$ and $\eta_c \rightarrow 2\gamma$ decays. As a result of this analysis, the matrix elements for J/ψ read

$$\langle \mathcal{O}_1 \rangle_{J/\psi} = 0.440^{+0.067}_{-0.055} \text{ GeV}^3, \tag{26}$$

$$\langle \vec{q}^2 \rangle_{J/\psi} = 0.441^{+0.140}_{-0.140} \text{ GeV}^2. \tag{27}$$

The analysis in Ref. [92] is done by using the charm quark mass $m_{c,NR} = 1.4$ GeV. In general, the charm quark mass in NRQCD can differ from the charm quark mass used in the IPsat fits discussed in Sec. II. In our numerical analysis, we will use the NRQCD value for the charm quark mass in both the meson and photon wave functions when using the NRQCD results. Everywhere else in this work we use the charm mass $m_c = 1.3528$ GeV obtained in the IPsat fit to the HERA structure function data.

The uncertainties quoted above for the long-distance matrix elements are not independent, and the correlation matrix is also provided in Ref. [92]. To implement these correlated uncertainties, we use a Monte Carlo method and sample parameter values from the Gaussian distribution taking into account the full covariance matrix. The uncertainty is then obtained by calculating the one standard deviation band with respect to the result obtained by using the best fit values.

To construct the meson wave function, we start from the meson rest frame where we can use the NRQCD matrix elements to constrain the wave function as discussed above. In the rest frame, we require that the quark spins are coupled into a triplet state and the total spin and angular momentum to a $J = 1$ vector state. Thus we can in general write the spin structure of the wave function in the following form:

$$\psi^\lambda_{s\bar{s}}(\vec{r}) = \sum_{L,m_L,m_S} \langle L\, m_L\, 1\, m_S | 1\, \lambda \rangle$$
$$\times \left\langle \frac{1}{2} s \frac{1}{2} \bar{s} \middle| 1\, m_S \right\rangle Y_L^{m_L}(\theta, \phi) \psi_L(r). \tag{28}$$

Here $Y_L^{m_L}$ are the spherical harmonics, ψ_L is the radial wave function corresponding to the orbital angular momentum L and $\langle j_1 m_{j_1} j_2 m_{j_2} | J m_J \rangle$ are Clebsch-Gordan coefficients. In general, the conservation of spin parity tells us that for J/ψ the orbital angular momentum can only take values $L = S, D$. Since J/ψ should be dominated by the S-wave contribution, we will from now on consider the case where only the S-wave component is nonzero. We note that in principle in the NRQCD approach one finds the D-wave contribution to the vector meson wave function to be suppressed by v^2 compared to the S wave, and this is of the same order as the first relativistic correction included in terms of the wave function derivative above. However, the D-wave contribution to the decay width is suppressed by an additional v^2 and as such the D-wave contribution is not constrained by the decay widths at this order. Thus it is most consistent to set it to zero. In this case the wave function simplifies to

$$\psi^\lambda_{s\bar{s}}(\vec{r}) = \left\langle \frac{1}{2} s \frac{1}{2} \bar{s} \middle| 1\, \lambda \right\rangle \phi(r), \tag{29}$$

where $\phi(r)$ is the scalar part of the wave function and related to the long-distance matrix elements as shown in Eqs. (24) and (25). Using the three-dimensional polarization vectors in Eq. (11) we can also write this as

$$\psi^\lambda_{s\bar{s}}(\vec{r}) = U^\lambda_{s\bar{s}} \phi(r), \tag{30}$$

where

$$U^\lambda_{s\bar{s}} = \frac{1}{\sqrt{2}} \xi^\dagger_s \vec{\epsilon}_\lambda \cdot \vec{\sigma} \tilde{\xi}_{\bar{s}} \tag{31}$$

in the case of transverse polarization and

$$U^{\lambda=0}_{s\bar{s}} = \frac{1}{\sqrt{2}} \xi^\dagger_s \sigma_3 \tilde{\xi}_{\bar{s}} \tag{32}$$

when the vector meson is longitudinally polarized. Here $\xi_+ = (1, 0)$ and $\xi_- = (0, 1)$ are the two-component spinors describing spin-up and spin-down states and $\tilde{\xi}_{\bar{s}} = i\sigma_2 \xi^*_s$ is the antiquark spinor.

The behavior of the quarkonium wave function at long distances is determined by nonperturbative physics. This long-distance physics affects short distances through the requirement of the normalization of the wave function. The NRQCD approach broadly speaking consists of parametrizing the nonperturbative long-distance physics by measurable coefficients that serve as coefficients in the short-distance expansion, which is used to calculate a physical process happening at short-distance scales. In practice this amounts to expressing the wave function as a Taylor expansion around the origin:

$$\phi(\vec{r}) = A + B\vec{r}^2. \tag{33}$$

The linear term does not appear to ensure that the Laplacian of the wave function is finite at the origin. The coefficients can also be written as $A = \phi(0)$ and $B = \frac{1}{6}\nabla^2\phi(0)$, and using Eqs. (24) and (25) we get the values

$$A = \left[1 - 2C_F \frac{\alpha_s}{\pi}\right] \sqrt{\frac{1}{2N_c} \langle \mathcal{O}_1 \rangle_{J/\psi}} = 0.213 \text{ GeV}^{3/2}, \tag{34}$$

$$B = -\frac{1}{6} A \langle \vec{q}^2 \rangle_{J/\psi} = -0.0157 \text{ GeV}^{7/2}. \tag{35}$$

The uncertainties in the long-distance matrix elements are correlated as discussed above, and in our numerical calculations this correlated uncertainty is propagated to the coefficients A and B.

We then want to write our wave function ansatz (33) in light cone coordinates $(\mathbf{k}, z)$. We do this by first going to momentum space:

$$
\psi^\lambda_{s\bar{s}}(\vec{k}) = \int \mathrm{d}^3\vec{r}\, e^{-i\vec{k}\cdot\vec{r}} \psi^\lambda_{s\bar{s}}(\vec{r}) = U^\lambda_{s\bar{s}}\phi(k)
$$
$$
= U^\lambda_{s\bar{s}}(2\pi)^3(A\delta^3(\vec{k}) - B\nabla^2_{\vec{k}}\delta^3(\vec{k})), \qquad (36)
$$

where $\vec{k} = (\mathbf{k}, k^3)$. We then want to change the longitudinal momentum variable from k^3 to the plus momentum fraction carried by the quark: z. Unfortunately there is no unique way to do this, due to the different nature of instant form and light cone quantization. In principle we would want to define z as the ratio of the quark k^+ to the meson $P^+ = M_V/\sqrt{2}$, working in the rest frame of the meson. However, a quark inside a bound state described as a superposition of different $\vec{k}$ modes is not exactly on shell, its energy being affected by the binding potential. Thus we do not precisely know the k^0 required to calculate k^+ from k^3. The rest frame wave function also includes values of k^3 that are very large, leading to values of k^+ that are larger than $M_V/\sqrt{2}$. This is perfectly possible in instant form quantization with the time variable t. However, in light cone quantization k^+ is a conserved momentum variable and has to satisfy $0 < k^+ < P^+$. The procedure that we adopt here is (similarly to e.g., [96]) to define the momentum fraction in practice as $z = k^+_q/(k^+_q + k^+_{\bar{q}})$, where k_q and $k_{\bar{q}}$ are the quark and antiquark momenta, with k^+ calculated assuming $k^0 = \sqrt{m^2_{c,NR} + \vec{k}^2}$. In other words, we normalize by the total plus momentum of the quark-antiquark pair, instead of the meson plus momentum, and assume an on-shell dispersion relation. This choice has the advantage that it leads to $0 < z < 1$ by construction. This leads us to the expression for the longitudinal momentum in the meson rest frame k^3 as

$$
k^3 = M\left(z - \frac{1}{2}\right), \qquad (37)
$$

where

$$
M = \sqrt{\frac{\mathbf{k}^2 + m^2_{c,NR}}{z(1-z)}} \qquad (38)
$$

is the invariant mass of the quark-antiquark pair. We emphasize that since this choice is not unique, we might expect corrections or ambiguities proportional to powers of the difference between the meson mass and the quark-antiquark pair invariant mass $M^2_V - M^2$ to appear. Such corrections are, however, higher order corrections in the nonrelativistic limit and also numerically very small for J/ψ for the values of $m_{c,NR}$ and $\langle \vec{q}^2 \rangle$ used here. We could also hope that since the invariant mass is a rotationally invariant quantity, these ambiguities would not lead to serious violations of rotational invariance (which expresses itself here as the equality of physical properties such as decay widths of transverse and longitudinal polarization states). We will see an example of such a correction explicitly in Appendix B.

To change the variables in our wave function, one needs to be careful with the delta functions and their derivatives. We therefore make the change by requiring that the overlap

$$
\int \frac{\mathrm{d}^3\vec{k}}{(2\pi)^3} \psi^\lambda_{s\bar{s}}(\vec{k})\varphi(\vec{k}) = \int \frac{\mathrm{d}^2\mathbf{k}}{(2\pi)^2}\frac{\mathrm{d}z}{4\pi} \psi^\lambda_{s\bar{s}}(\mathbf{k}, z)\varphi(\mathbf{k}, z), \quad (39)
$$

where φ is an arbitrary wave function, does not change under the change of variables. This requirement tells us that the scalar part $\phi(\vec{k})$ changes to

$$
\phi(\mathbf{k}, z) = (2\pi)^3\sqrt{2\frac{\partial z}{\partial k^3}}\left(A\delta\left(z - \frac{1}{2}\right)\delta^2(\mathbf{k}) - B\left(\partial_z\left[\frac{\partial z}{\partial k^3}\partial_z\left[\frac{\partial z}{\partial k^3}\delta\left(z - \frac{1}{2}\right)\right]\right]\delta^2(\mathbf{k}) + \delta\left(z - \frac{1}{2}\right)\nabla^2_{\mathbf{k}}\delta^2(\mathbf{k})\right)\right), \qquad (40)
$$

where

$$
\frac{\partial z}{\partial k^3} = \frac{4z(1-z)}{M}. \qquad (41)
$$

Equation (40) is the scalar part of the NRQCD-based vector meson wave function in the meson rest frame, expressed in momentum space. We note that this wave function is not normalizable due to the presence of the delta functions. However, as the NRQCD approach can only be used to constrain the coordinate space wave function and its derivative at the origin, we are forced to use the expansion

of Eq. (33) which cannot result in a normalizable wave function. However, for the purposes of this work this is not a problem, as the vector meson production is sensitive to the vector meson wave function overlap with the virtual photon wave function, and the photon wave function is heavily suppressed at long distances where the expansion (33) is not reliable.

B. Wave function on the light front

The NRQCD wave function obtained in the previous section is written in the vector meson rest frame in terms of

the quark and antiquark spin states s and $\bar{s}$. In order to calculate overlaps with the virtual photon wave function (17) and (18), we need to express it in terms of the light cone helicities h and $\bar{h}$. The transformation between these two bases, usually expressed in terms of the 2-spinors, is known as the "Melosh rotation" [46,47].

The Dirac spinors that are used to factorize the non-relativistic wave function into a spin and scalar part are eigenstates of the spin-z operator in the zero transverse momentum limit. In terms of the two-component spin vectors ξ defined above in Eqs. (31) and (32) they read

$$u_s(p) = \frac{1}{\sqrt{N}} \begin{pmatrix} \xi_s \\ \frac{\vec{\sigma} \cdot \vec{p}}{E_p + m} \xi_s \end{pmatrix}, \qquad (42)$$

$$v_s(p) = \frac{1}{\sqrt{N}} \begin{pmatrix} \frac{\vec{\sigma} \cdot \vec{p}}{E_p + m} \tilde{\xi}_s \\ \tilde{\xi}_s \end{pmatrix}. \qquad (43)$$

The normalization factor N is determined from the condition $\bar{u}_s u_{\bar{s}} = -\bar{v}_s v_{\bar{s}} = 2m\delta_{s,\bar{s}}$.

Both the Dirac spinors in terms of the spin-z component u_s and the helicity spinors u_h [see Eqs. (7) and (8)] are solutions to the Dirac equation and as such can be obtained as linear combinations of each other. This mapping is the Melosh rotation R^{sh}. It can be computed from the spinor inner products (see also Ref. [97]) as

$$R^{sh}(\mathbf{k}, z) = \frac{1}{2m} \bar{u}_s(\mathbf{k}, z) u_h(\mathbf{k}, z), \qquad (44)$$

where $k^+ = zq^+$ and q^+ is the meson plus momentum and s and h refer to the spin and light front helicity, respectively.

The helicity spinors u_h and v_h can also be written in a similar form as the spinors in the spin basis, Eqs. (42) and (43), by introducing the two-component helicity spinors χ_h. To do this we write the helicity spinors (7) and (8) in the form

$$u_h(p) = \frac{1}{\sqrt{N}} \begin{pmatrix} \chi_h \\ \frac{\vec{\sigma} \cdot \vec{p}}{E_p + m} \chi_h \end{pmatrix}, \qquad (45)$$

$$v_h(p) = \frac{1}{\sqrt{N}} \begin{pmatrix} \frac{\vec{\sigma} \cdot \vec{p}}{E_p + m} \tilde{\chi}_h \\ \tilde{\chi}_h \end{pmatrix}, \qquad (46)$$

where N is again determined by the normalization requirement and $\tilde{\chi}_h = i\sigma_2 \chi_h^*$. Using this form one can check that the Melosh rotation also connects the two-component spin and helicity spinors as

$$R^{sh}(\mathbf{k}, z) = \xi_s^\dagger \chi_h. \qquad (47)$$

The coefficients R^{sh} can also be expressed as a 2×2 matrix rotating the 2-spinors

$$R(\mathbf{k}, z) = \frac{m_{c,NR} + zM - i(\vec{\sigma} \times \vec{n}) \cdot (\mathbf{k}, k^3)}{\sqrt{(m_{c,NR} + zM)^2 + \mathbf{k}^2}}. \qquad (48)$$

Here M is the invariant mass of the $q\bar{q}$ system from Eq. (38) and $n = (0, 0, 1)$ is the unit vector in the longitudinal direction. In terms of this matrix the 2-spinors ξ_s and χ_h are related by

$$\chi_\pm = R(\mathbf{k}, z)\xi_\pm. \qquad (49)$$

Using Eq. (47) we can now express the NRQCD wave function in the light front helicity basis. We write

$$\Psi_{h\bar{h}}^\lambda(\mathbf{k}, z) = U_{h\bar{h}}^\lambda \phi(\mathbf{k}, z), \qquad (50)$$

where the scalar part is given in Eq. (40). The helicity structure $U_{h\bar{h}}^\lambda$ is obtained by applying the transform (47) in Eqs. (31) and (32), i.e.,

$$U_{h\bar{h}}^\lambda = \sum_{s\bar{s}} R^{*sh}(\mathbf{k}, z) R^{*\bar{s}\bar{h}}(-\mathbf{k}, 1 - z) U_{s\bar{s}}^\lambda. \qquad (51)$$

After the Melosh rotation, we compute the Fourier transform to obtain the light front wave function in the mixed transverse coordinate–longitudinal momentum fraction space as

$$\Psi_{h\bar{h}}^\lambda(\mathbf{r}, z) = \int \frac{d^2\mathbf{k}}{(2\pi)^2} e^{i\mathbf{k} \cdot \mathbf{r}} \Psi_{h\bar{h}}^\lambda(\mathbf{k}, z)$$
$$= \int \frac{d^2\mathbf{k}}{(2\pi)^2} e^{i\mathbf{k} \cdot \mathbf{r}} U_{h\bar{h}}^\lambda(\mathbf{k}, z) \phi(\mathbf{k}, z). \qquad (52)$$

The different helicity components of the final light front wave function resulting from this procedure are

$$\Psi_{+-}^{\lambda=0}(\mathbf{r}, z) = \Psi_{-+}^{\lambda=0}(\mathbf{r}, z) = \frac{\pi\sqrt{2}}{\sqrt{m_{c,NR}}} \left[A\delta(z - 1/2) + \frac{B}{m_{c,NR}^2} \left(\left(\frac{5}{2} + \mathbf{r}^2 m_{c,NR}^2 \right) \delta(z - 1/2) - \frac{1}{4} \partial_z^2 \delta(z - 1/2) \right) \right],$$

$$\Psi_{++}^{\lambda=1}(\mathbf{r}, z) = \Psi_{--}^{\lambda=-1}(\mathbf{r}, z) = \frac{2\pi}{\sqrt{m_{c,NR}}} \left[A\delta(z - 1/2) + \frac{B}{m_{c,NR}^2} \left(\left(\frac{7}{2} + \mathbf{r}^2 m_{c,NR}^2 \right) \delta(z - 1/2) - \frac{1}{4} \partial_z^2 \delta(z - 1/2) \right) \right],$$

$$\Psi_{+-}^{\lambda=1}(\mathbf{r}, z) = -\Psi_{-+}^{\lambda=1}(\mathbf{r}, z) = (\Psi_{-+}^{\lambda=-1}(\mathbf{r}, z))^* = (-\Psi_{+-}^{\lambda=-1}(\mathbf{r}, z))^* = -\frac{2\pi i}{m_{c,NR}^{3/2}} B\delta(z - 1/2)(r_1 + ir_2),$$

$$\Psi_{--}^{\lambda=1}(\mathbf{r}, z) = \Psi_{++}^{\lambda=-1}(\mathbf{r}, z) = \Psi_{++}^{\lambda=0}(\mathbf{r}, z) = \Psi_{--}^{\lambda=0}(\mathbf{r}, z) = 0. \qquad (53)$$

The first relativistic correction to the wave function, proportional to B or the wave function derivative, mixes the helicity and spin states. In particular, in the case of transverse polarization the $h, \bar{h} = \pm \mp$ terms are non-vanishing when the relativistic correction is included. These terms also bring a nonzero contribution to photon-vector meson overlaps. In general, we expect that if higher order corrections in v were included in the wave function parametrization, we would also find other components to be nonvanishing.

The Melosh rotation is crucial here, as it generates helicity structures that are not visible in the spin basis. This is in contrast to some early attempts to transform the wave functions obtained by solving the potential models to the light front as done e.g., in Ref. [78]. The role of the Melosh rotation in the context of vector meson light front wave functions and exclusive scattering was first emphasized in Ref. [47]. More recently it was applied to J/ψ production in the dipole picture in Ref. [98], and in [99] different quark-antiquark potentials were studied in this context. In the case of excited states such as $\psi(2S)$ the role of the Melosh rotation is expected to be even more significant [100].

Let us in passing briefly compare our approach to the one in the recent work of Krelina, Nemchik, and Pasechnik in Ref. [98]. In our approach, we take the NRQCD wave function which only includes the S-wave contribution (D-wave part is suppressed by v^2). The quark spin dependence is now trivial, as the total angular momentum must be provided by the quark spins which gives us the structure of Eq. (30). In Ref. [98], the authors assume, unlike we do here, that the spin structure of the vector meson wave function in the rest frame has the same form as the light cone helicity structure of the photon light cone wave function, Eqs. (17) and (18). This structure is then supplemented by a wave function obtained from the potential model, and a Melosh rotation to the light front is applied at the end. Such a procedure leads to a large D-wave contribution in the wave function, which we do not have. We discuss the structure of the wave functions in terms of S and D waves in more detail in Appendix A.

To determine the role of the relativistic corrections in the vector meson wave function, we will also study for comparison the fully nonrelativistic wave function where our starting point for the scalar part is

$$\phi(\vec{r}) = A'. \tag{54}$$

Following the previous procedure, the final result for the light cone wave function can be read from Eq. (53) with the substitutions $A = A'$ and $B = 0$. One notices that this can now be written as

$$\Psi^\lambda_{J/\psi, h\bar{h}}(\mathbf{r}, z) = \frac{\pi \sqrt{2}}{\sqrt{m_{c,NR}}} U^\lambda_{h\bar{h}} A' \delta \left(z - \frac{1}{2} \right). \tag{55}$$

In this extreme nonrelativistic limit ($\mathbf{k} = 0, z = 1/2$) the Melosh rotation simply corresponds to an identity matrix so that the spin and helicity bases are interchangeable here. The normalization A' is obtained from the van Royen–Weisskopf equation for the leptonic width [101], which is also obtained from Eq. (22) by neglecting the relativistic correction proportional to $\langle \mathbf{q}^2 \rangle_{J/\psi}/m^2_{c,NR}$, and the higher order QCD correction $\sim \alpha_s$ (note that parametrically $\alpha_s \sim v$):

$$\Gamma(J/\psi \rightarrow e^- e^+) = \frac{16\pi e_f^2 \alpha_{\text{em}}}{M^2_{J/\psi}} |\phi(0)|^2. \tag{56}$$

By using the experimental value for leptonic width [102], we can calculate the coefficient A' to be

$$A' = \phi(0) = 0.211 \text{ GeV}^{3/2}. \tag{57}$$

C. Overlap with photon

Using the obtained J/ψ wave function on the light front, Eq. (53), we can directly compute overlaps with the virtual photon, Eqs. (17) and (18). In these overlaps, we also include the phase factor $\exp\left(i(z - \frac{1}{2})\mathbf{r} \cdot \mathbf{\Delta}\right)$ present in the vector meson production amplitude in Eq. (1). We also assume that the dipole amplitude does not depend on the orientation θ_r of $\mathbf{r}$ as is the case in the IPsat parametrization and integrate over θ_r. The overlaps summed over the quark helicities read

$$r \sum_{h\bar{h}} \int_0^{2\pi} d\theta_r \int_0^1 \frac{dz}{4\pi} (\Psi^L_{J/\psi})^* \Psi^L_\gamma e^{i(z-1/2)\mathbf{r} \cdot \mathbf{\Delta}} = \frac{r e e_f Q}{2} \sqrt{\frac{N_c}{2m_{c,NR}}} \Bigg[A K_0(r\bar{e})$$

$$+ \frac{B}{m^2_{c,NR}} \left(\frac{9}{2} K_0(r\bar{e}) + m^2_{c,NR} r^2 K_0(r\bar{e}) - \frac{Q^2 r}{4\bar{e}} K_1(r\bar{e}) + \frac{1}{4} \Delta^2 r^2 K_0(r\bar{e}) \right) \Bigg] \tag{58}$$

and

$$r \sum_{h\bar{h}} \int_0^{2\pi} \mathrm{d}\theta_r \int_0^1 \frac{\mathrm{d}z}{4\pi} (\Psi_{J/\psi}^T)^* \Psi_\gamma^T e^{i(z-1/2)\mathbf{r}\cdot\boldsymbol{\Delta}} = r e e_f \sqrt{\frac{N_c m_{c,NR}}{2}} \Bigg[A K_0(r\bar{\epsilon})$$

$$+ \frac{B}{m_{c,NR}^2} \left(\frac{7}{2} K_0(r\bar{\epsilon}) + m_{c,NR}^2 r^2 K_0(r\bar{\epsilon}) - \frac{r}{2\bar{\epsilon}}(Q^2 + 2m_{c,NR}^2) K_1(r\bar{\epsilon}) + \frac{1}{4}\Delta^2 r^2 K_0(r\bar{\epsilon}) \right) \Bigg], \tag{59}$$

where $\bar{\epsilon}^2 = Q^2/4 + m_{c,NR}^2$, $\Delta = |\boldsymbol{\Delta}|$, and $r = |\mathbf{r}|$. In the case of transverse polarization, the result is identical in cases with $\lambda = +1$ and $\lambda = -1$. We will study these overlaps numerically in Sec. VA. We note that thanks to the delta function structure in z in our wave function (53), many phenomenological applications become numerically more straightforward as the z integral can be performed analytically.

IV. PHENOMENOLOGICAL WAVE FUNCTIONS

To provide a quantitative point of comparison for the effect of the relativistic corrections, we want to compare the light cone wave functions obtained in Sec. III to other parametrizations used in the literature. For this purpose, let us now discuss two specific alternative approaches used for phenomenological applications in the literature.

A. Boosted Gaussian

A commonly used phenomenological approach to construct the vector meson wave function is to assume that it has the same polarization and helicity structure as the virtual photon. This can be done by replacing the scalar part of the photon wave functions (17) and (18) by an unknown function as [48]

$$e_f e z(1-z) \frac{K_0(\epsilon r)}{2\pi} \to \phi_{T,L}(r,z), \tag{60}$$

with the explicit factor Q in the longitudinal wave function replaced by the meson mass as $2Q \to M_V$. The scalar function $\phi(r, z)$ is then parametrized, and the parameters can be determined by requiring that the resulting wave function is normalized to unity and reproduces the experimental leptonic decay width. As we will discuss in more detail in Appendix B, this procedure does not correspond to the most general possible helicity structure. Nevertheless, our result at this order in the nonrelativistic expansion can in fact also be written in terms of the "scalar part of light cone wave functions." However, at higher orders in v different a different structure could appear.

In the boosted Gaussian parametrization, the $q\bar{q}$ invariant mass distribution is assumed to be Gaussian, with the width of the distribution $\mathcal{R}$ and the normalization factors $N_{T,L}$ being free parameters. In mixed space, the parametrization reads

$$\phi_{T,L}(r,z) = \mathcal{N}_{T,L} z(1-z)$$
$$\times \exp\left(-\frac{m_c^2 \mathcal{R}^2}{8z(1-z)} - \frac{2z(1-z)r^2}{\mathcal{R}^2} + \frac{m_c^2 \mathcal{R}^2}{2} \right). \tag{61}$$

In this work we use the parameters constrained in Ref. [87] by using the same charm quark mass $m_c = 1.3528$ GeV as is used when fitting the IPsat dipole amplitude to the HERA data. The parameters are determined by requiring that the longitudinal polarization can be used to reproduce the experimental decay width. The obtained parameters are $\mathcal{R} = 1.507$ GeV^{-1}, $N_T = 0.589$ and $N_L = 0.586$ with $M_V = 3.097$ GeV.

The specific functional form and helicity structure of the boosted Gaussian parametrization imply that in the vector meson rest frame there are both S- and D-wave contributions. This is demonstrated explicitly in Appendix A by performing a Melosh rotation from the light front back to the J/ψ rest frame. This feature is hard to describe in potential model calculations, and our NRQCD-based wave function in particular has only the S-wave component in the rest frame. The D-wave contribution in the boosted Gaussian wave function is, however, quite small.

B. Basis light-front quantization (BLFQ)

The second wave function we study here for comparisons is based on explicit calculations on the light front. In this approach, one constructs a light front Hamiltonian H_{eff}, which consists of a one-gluon exchange interaction and a nonperturbative confining potential inspired by light-front holography. The formalism is developed in Refs. [103–109].

The quarkonium states are obtained by solving the eigenvalue problem

$$H_{\mathrm{eff}} |\psi_{m_J}^{J^{PC}}\rangle = M_V^2 |\psi_{m_J}^{J^{PC}}\rangle. \tag{62}$$

As a solution, one obtains the invariant mass M_V^2 spectrum and the light front wave functions in momentum space

$$\psi_{m_J}^{J^{PC}}(\mathbf{k}, z, h, \bar{h}) = \langle \mathbf{k}, z, h, \bar{h} | \psi_{m_J}^{J^{PC}}\rangle. \tag{63}$$

Here J, P, C and m_J are the total angular momentum, parity, C parity and the magnetic quantum number of the state, respectively. The free parameters, value of the coupling constant, strength of the confining potential, quark mass and the effective gluon mass, can be
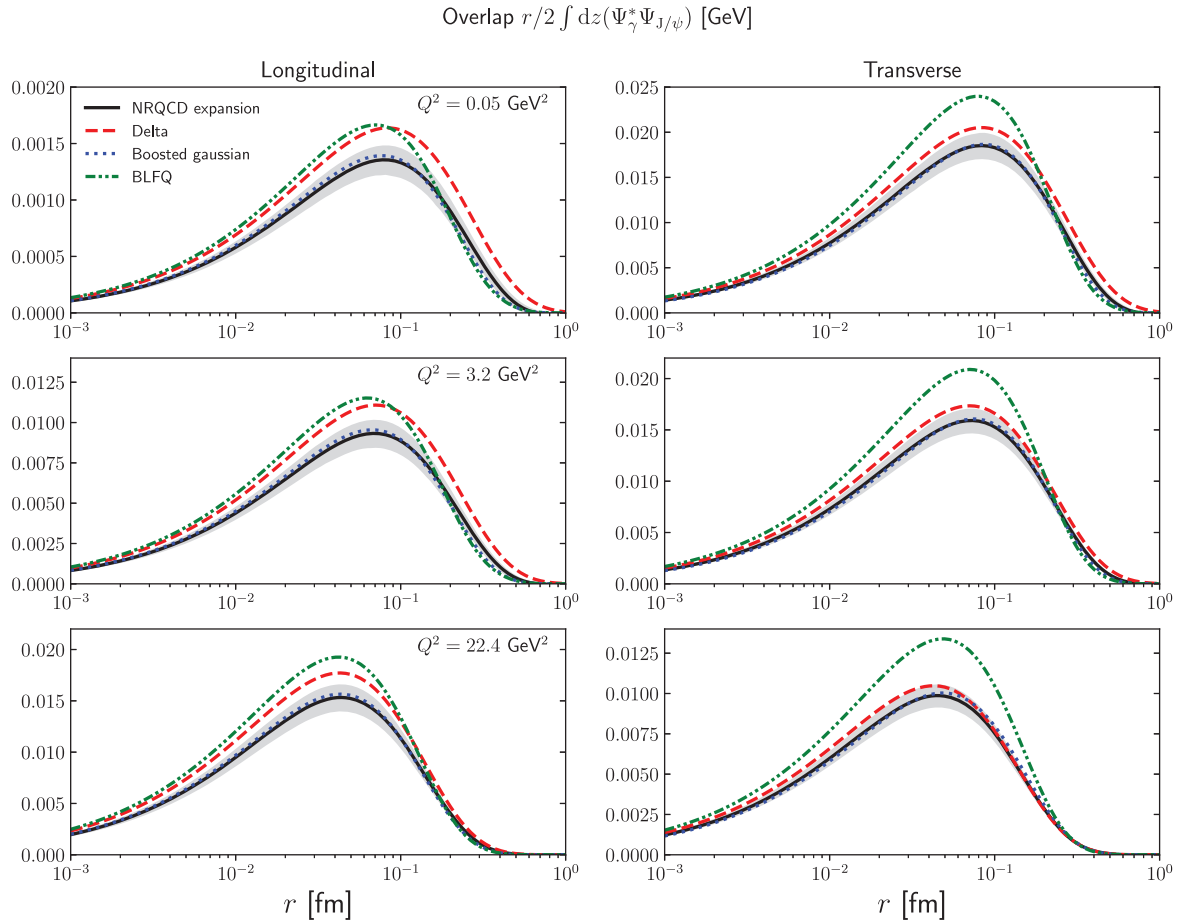
Overlap $r/2 \int \mathrm{d}z (\Psi_\gamma^* \Psi_{J/\psi})$ [GeV]

FIG. 1. Forward ($\Delta = 0$) virtual photon-J/ψ wave function overlaps computed using the different vector meson wave functions as a function of the dipole size r at different photon virtualities.

constrained by the charmonium and bottomonium mass spectra [110,111]. In this work, we use the most up-to-date parametrizations from Ref. [111].

The obtained BLFQ wave functions have been applied in studies of the J/ψ production in the dipole picture at HERA [112] and in the context of exclusive J/ψ production in ultraperipheral heavy ion collisions at the LHC in Ref. [113]. Following the prescription used in Refs. [112,113], we consider the fitted quark mass $m_c^{\text{BLFQ}} = 1.603$ GeV in the "BLFQ wave function" to be an effective mass of the quarks in the confining potential, including some nonperturbative contributions. Consequently, when calculating the overlaps we use, as in [112,113], $m_c = 1.3528$ GeV for the charm mass in the photon wave function, as constrained by the charm structure function data in the IPsat fit [87].

V. VECTOR MESON PRODUCTION

A. Photon overlap

The exclusive vector meson production cross section depends on the overlap between the $c\bar{c}$ component of the virtual photon wave function with the vector meson wave

function; see Eq. (1). In Fig. 1 these overlaps for $\Delta = 0$ are shown as a function of the transverse size $r = |\mathbf{r}|$ of the intermediate dipole, using four vector meson wave functions:

1. *NRQCD expansion*, which is constructed by parametrizing the wave function and its derivative at the origin based on NRQCD matrix elements including corrections $\sim v^2$ and performing the Melosh rotation to the light front. This is our result from Sec. III.
2. *Delta*, which is the fully nonrelativistic limit [Eq. (55)] of the above wave function, without any information about the wave function derivative.
3. *Boosted Gaussian*, the phenomenological parametrization discussed in Sec. IV A.
4. *BLFQ* wave function based on basis light-front quantization, discussed in Sec. IV B.

In Fig. 2 we show the same overlaps plotted as ratios to the fully nonrelativistic limit, i.e., the *Delta* parametrization. For the NRQCD expansion-based wave function, we also show the model uncertainty related to the NRQCD matrix elements that control the value of the wave function and its derivative at the origin. The uncertainty band is in this case computed as discussed in Sec. III.
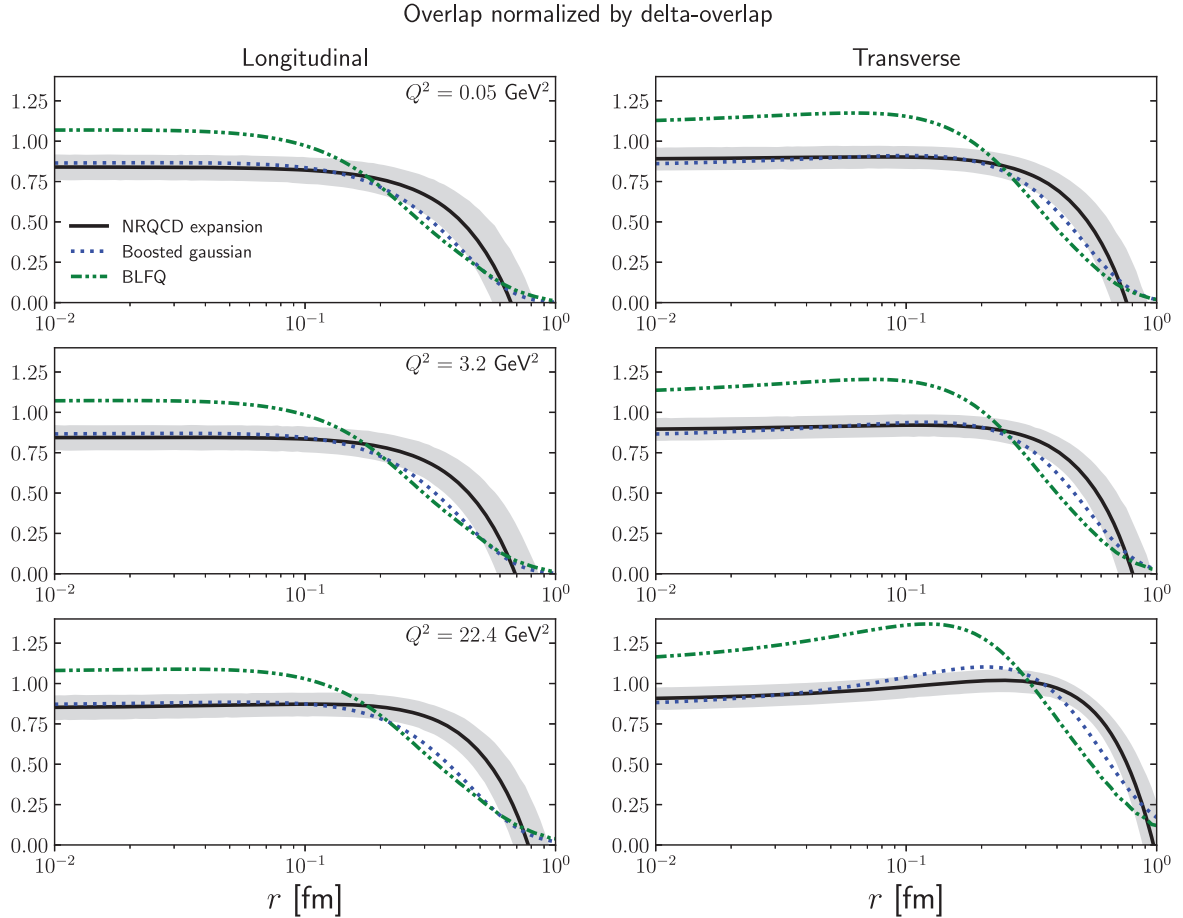
FIG. 2.   Ratios of the forward ($\Delta = 0$) virtual photon-J/ψ wave function overlaps computed using the different vector meson wave functions to the fully nonrelativistic *Delta* parametrization as a function of the dipole size r at different photon virtualities.

The effect of the first relativistic correction can be determined by comparing the *Delta* and *NRQCD expansion* wave functions. At large dipoles the negative velocity suppressed $\sim \mathbf{r}^2$ contribution suppresses the vector meson wave function[1] compared to the fully nonrelativistic form. This is especially visible at small Q^2. At larger photon virtualities, the exponential suppression in the photon wave function becomes dominant before the relativistic $-\mathbf{r}^2$ correction becomes numerically important. Thus, while the effect of the relativistic correction is dramatic in the ratio in Fig. 2, at large Q^2 it is insignificant for the actual overlap, as is seen in Fig. 1.

For small dipoles the wave functions are most strictly constrained by the quarkonium decay widths. The NRQCD parametrization does not, however, reduce exactly to the fully nonrelativistic *Delta* parametrization in the small r

FIG. 3.   Total J/ψ production cross section as a function of virtuality computed using different vector meson wave functions compared with H1 [4] and ZEUS [8] data.

---

[1]The wave function would change sign at $r_0 = 0.73$ fm. As there should be no node in the J/ψ wave function, we set the wave function to zero at $r > r_0$. We have checked that this cutoff has a negligible effect on our numerical results.

limit. This can be traced back to the fact that the gradient correction also affects the decay width, as seen in Eq. (22) [and from the fact that the constants A in (34) and A' in (57) are different]. A part of the three-dimensional gradient correction becomes a correction to the functional form in z even at $\mathbf{r} = 0$. This leads to the overlaps at small r being slightly different, even though the same decay width data are used to obtain the parameters of the rest frame wave functions.

Both the boosted Gaussian and BLFQ wave functions are even more suppressed at large dipole sizes than the NRQCD parametrization. This is most clearly seen on the ratio plot, Fig. 2. This is a straightforward consequence of the fact that in these parametrizations the wave function normalization imposes an additional suppression at large r. For the boosted Gaussian parametrization this additional suppression happens at such a large r that the overlap is already very small and thus has a negligible effect on the overall overlap in Fig. 1. The boosted Gaussian parametrization is very close to our NRQCD also for small dipoles. The BLFQ parametrization yields a somewhat larger wave function overlap at small r than our NRQCD one or the boosted Gaussian.[2]

The suppression with respect to the nonrelativistic limit is larger for the longitudinal polarization state than for the transverse one. This can be understood as follows. The longitudinal virtual photon wave function depends on the quark momentum fraction as $\sim z(1 - z)$ [see Eq. (17)] and as such is peaked at $z = 1/2$. The z structure of the fully nonrelativistic wave function is $\delta(z - 1/2)$, and when the first relativistic corrections are included, the $z = 1/2$ region still dominates the overlap. On the other hand, the transverse photon wave function is not peaked at $z = 1/2$; see Eq. (18). Thus, the suppression from the $\partial_z^2\delta(z - 1/2)$ term in the relativistic correction is smaller for the transverse polarization.

B. J/ψ production

The total exclusive DIS J/ψ production cross section for a proton target at $W = 90$ GeV is shown in Fig. 3, compared with the H1 [4] and ZEUS [8] data. The overall normalization of the cross section has a relatively large theoretical uncertainty. We note that the two corrections discussed in Sec. II, the real part and especially the skewedness correction are numerically significant, up to $\sim 50\%$ (see e.g., Ref. [40]). As discussed in Sec. II, especially the skewedness correction is not very robust and its applicability in the dipole picture used here is not

clear. In addition to the possibly problematic skewedness corrections, the fact that our NRQCD-based wave functions are not normalized affects the absolute normalization of the vector meson production cross sections. Thus our focus here is rather on the relative effects of different meson wave functions and the dependence on Q^2.

The vector meson cross section is dominated by dipole sizes of the order of $1/(Q^2 + M_V^2)$ as can be seen[3] from Fig. 1. Consequently, it is more instructive to look at the dependence of the J/ψ cross section on Q^2 than the overall normalization. From Fig. 3 one sees that the fully non-relativistic wave function results in a too steep Q^2 dependence compared to the HERA data. The first relativistic correction slows down the Q^2 evolution close to the photoproduction region and leads to a better agreement with the experimental data. This is a consequence of the basic behavior of the relativistic correction as a $\sim -\mathbf{r}^2$ modification that suppresses the vector meson wave function strongly at large dipoles. Thus the reduction from the relativistic correction is larger for smaller Q^2. At large Q^2 the exponential suppression from the photon wave function starts to dominate at smaller dipole sizes, and the relativistic $-\mathbf{r}^2$ correction becomes negligible. However, the relativistic contribution to the momentum fraction z structure is present at all Q^2 and suppresses the longitudinal cross section more than the transverse one.

A similar trend in the Q^2 dependence is also visible with both the boosted Gaussian and BLFQ wave functions. For the boosted Gaussian case, the agreement with HERA data has been established numerous times in the previous literature, e.g., in Ref. [48]. The Q^2 dependence of the cross section is slightly weaker when the BLFQ wave function is used, but the difference is comparable to the experimental uncertainties. We note that in Ref. [112] the BLFQ wave function is found to result in a cross section underestimating the HERA data in the photoproduction region. In this work, compared to the setup used in Ref. [112], we use an updated BLFQ parametrization from Ref. [111] which was shown in Ref. [113] to result in a good description of the J/ψ production in ultraperipheral proton-proton collisions at the LHC, which in practice probe vector meson photoproduction [15,16].

To cancel normalization uncertainties, we next study cross section ratios. In Fig. 4 the longitudinal-to-transverse ratio of the J/ψ production cross section is shown as a function of the photon virtuality. The results are compared with the H1 and ZEUS data from Refs. [4,8]. The first relativistic correction reduces the longitudinal cross section more than the transverse one. As discussed above, this is due to the fact that a part of the correction shifts the meson wave function away from the $\delta(z - 1/2)$, which is the

---

[2]The parameters in the BLFQ wave function are constrained by the charmonium mass spectrum and not the decay widths that probe the wave function at $r = 0$. Consequently the BLFQ wave function is not required to result in exactly the same decay width as the other wave functions, which explains the difference at small r.

[3]Note, however, that as the dipole amplitude scales as $N \sim r^2$ at small r, the dominant dipole size scale for the cross section is larger than the maximum of the overlap peaks in Fig. 1.
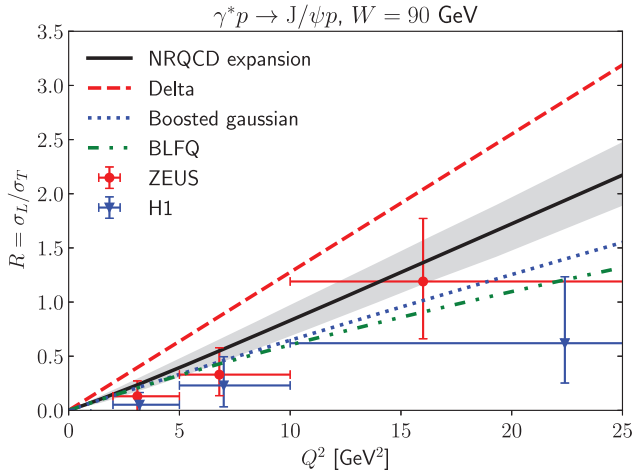
FIG. 4. Longitudinal J/ψ production cross section divided by the transverse cross section as a function of photon virtuality. Results obtained with different wave functions are compared with the H1 [4] and ZEUS [8] data.
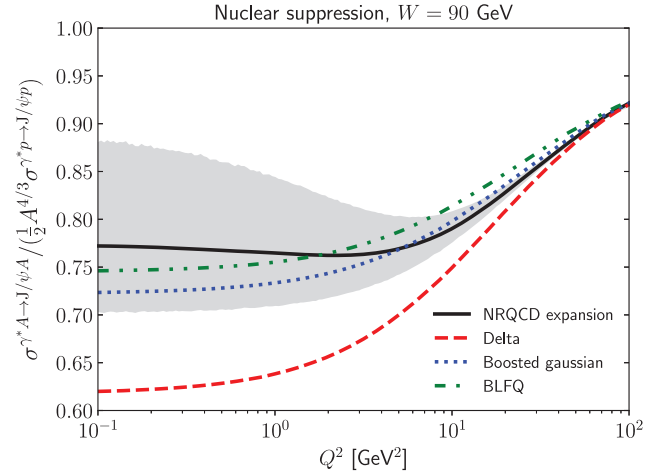

FIG. 5. Nuclear suppression factor for total coherent J/ψ production as a function of Q^2 computed using the different vector meson wave functions.

structure preferred by longitudinal photons but not by transverse photons. This shows up as a decrease in the longitudinal to transverse ratio as a function of Q^2. The effect is even stronger with the boosted Gaussian and BLFQ wave functions.

Finally, we study vector meson production in the future Electron Ion Collider. As the diffractive cross section at leading order in perturbative QCD is approximatively proportional to the squared gluon density, exclusive vector meson production is a promising observable to look for saturation effects at the future Electron Ion Collider (see e.g., [114]).

To quantify the nonlinear effects, we compute the nuclear suppression factor

$$\frac{\sigma^{\gamma^* A \to J/\psi A}}{c A^{4/3} \sigma^{\gamma^* p \to J/\psi p}}. \tag{64}$$

The denominator corresponds to the so-called impulse approximation, which is used to transform the photon-proton cross section to the photon-nucleus case in the absence of nuclear effects, but taking into account the different form factors (transverse density profiles Fourier transformed to the momentum space). The $A^{4/3}$ scaling can be understood to originate from the fact that the coherent cross section at $t = 0$ scales as $\sim A^2$, and the width of the coherent spectra (location of the first diffractive minimum) is proportional to $1/R_A^2 \sim A^{-2/3}$. The numerical factor c depends on the proton and nuclear form factors and is found to be very close to $c = \frac{1}{2}$ in Ref. [87]. In the absence of nonlinear effects (or shadowing effects in the gluon distribution), with dipole amplitudes (19) and (21) that depend linearly on $\mathbf{r}^2 x g(x, \mu^2)$, this ratio is exactly 1.

The obtained nuclear suppression factor is shown in Fig. 5 in the Q^2 range accessible at the Electron Ion Collider. We emphasize that all the nuclear modifications in this figure are calculated with exactly the same dipole cross sections, corresponding to the same nuclear shadowing (as measured e.g., by the nuclear suppression in F_L or F_2). Thus the difference between the curves results purely from vector meson wave function effects. When using the NRQCD wave function with the relativistic correction, the boosted Gaussian wave function or the BLFQ wave function, the obtained nuclear suppression factors are practically identical. Even though large mass of the vector meson renders the scale in the process large, a moderate suppression ~ 0.75 is found at small and moderate Q^2. In the small Q^2 region the uncertainty obtained by varying the NRQCD matrix elements is large.

The fully nonrelativistic wave function results in a much stronger suppression at small Q^2. This can be understood, as it was already seen in Fig. 1 that this wave function gives more weight on larger dipoles compared to the other studied wave functions. As the larger dipoles are more sensitive to nonlinear effects, a larger nuclear suppression in this case is anticipated. The first relativistic correction $\sim -\mathbf{r}^2$ suppresses the overlap at large dipole sizes and consequently the nuclear suppression. At higher Q^2 the photon wave function again cuts out the large dipole part of the overlap in all cases, and as such the results obtained by applying the fully nonrelativistic wave function do not differ from other wave functions any more. At asymptotically large Q^2 only small dipoles contribute and the dipole amplitudes can be linearized. Consequently, the suppression factor approaches unity at large Q^2 independently of the applied wave function.

The fact that the fully nonrelativistic wave function results in a very different nuclear suppression demonstrates

that the dependence on the meson wave function does not completely cancel in the nucleus-to-proton cross section ratios. Consequently, a realistic (and relativistic) description of the vector meson wave function is necessary for interpreting the measured nuclear suppression factors. This indicates that there is a large theoretical uncertainty in using the fully nonrelativistic formula of Ryskin [3], not only for extracting absolute gluon distributions, but even for extracting nuclear modifications to the dipole cross section (or the gluon density) from cross section ratios.

VI. CONCLUSIONS

In this work we proposed a new parametrization for the heavy vector meson wave function based on NRQCD long-distance matrix elements. These matrix elements can be used to simultaneously constrain both the value and the derivative of the vector meson wave function at the origin using quarkonium decay data. This approach provides a systematic method to compute the vector meson wave function as an expansion in the strong coupling constant α_s and the quark velocity v.

Compared to many phenomenological approaches used in the literature, our approach uses two independent constraints (the wave function value and its derivative). The obtained wave function is rotationally symmetric in the rest frame and contains only the S-wave component. Consequently, we simultaneously obtain a consistent parametrization for both polarization states. This is unlike in some widely used phenomenological parametrizations where the virtual photon like helicity structure is assumed on the light front. Relating light cone wave functions to rest frame ones also provides a consistent way to discuss the effect of a potential D-wave contribution to the meson wave function. We do not see indications, neither theoretically nor phenomenologically, that a significant D-wave contribution would be required or favored for the J/ψ.

The first relativistic correction to the wave function, controlled by the wave function derivative at the origin, is found to have a sizable effect on the cross section. The negative $\sim -\mathbf{r}^2$ relativistic contribution in terms of the transverse size $\mathbf{r}$ suppresses the obtained wave function at larger dipole sizes. The momentum fraction part of the correction partially compensates for this effect for the transverse photon by shifting the wave function away from the fully nonrelativistic configuration where both quarks carry the same fraction of the longitudinal momentum, a configuration which is not preferred by the transverse photon.

A disadvantage in our approach is that it is not possible to obtain a wave function which is normalized to unity. In the NRQCD framework the value of the wave function at long distances is parametrized by a nonperturbative matrix element, whose effect is felt in the value of the wave function near the origin. This can lead to an overestimation of the cross section at $Q^2 = 0$, where one is most sensitive

to the long-distance behavior of the wave function. In practice, however, we obtain cross sections that are quite similar to what is given by e.g., the boosted Gaussian parametrization. The wave function overlap with the photon is also smaller than with the BLFQ approach. Thus the lack of normalization in the wave function does not seem to be an important effect for J/ψ. The situation would be different for lighter vector mesons.

The structure of the wave function can be probed by studying cross sections (and cross section ratios) at different photon virtualities where the dipole sizes contributing to the cross section vary. The first relativistic correction is found to weaken the Q^2 dependence of the total J/ψ production cross section and the longitudinal-to-transverse ratio. These effects are broadly similar to predictions obtained by the boosted Gaussian parametrization or by the BLFQ wave function that is based on an explicit calculation on the light front including confinement effects.

When comparing vector meson production off protons to heavy nuclei, we find that the wave function does not completely cancel in the nuclear suppression factor, which compares the $\gamma^* A$ cross section to the $\gamma^* p$ in the impulse approximation. This demonstrates that a realistic vector meson wave function is necessary to properly interpret the nuclear suppression results, and in particular a fully nonrelativistic approach cannot be reliably used to extract the nonlinear effects on the nuclear structure.

In addition to the corrections in velocity, it would be important to include perturbative corrections in the strong coupling α_s in the calculation of exclusive vector meson production. Indeed some recent advances [94,115] are gradually making it possible to do so in the dipole picture. However, a study of the phenomenological implications of these α_s corrections remains to be done. In terms of understanding current and future experimental collider data, it would also be important to explore whether this approach can be extended to excited states such as the $\psi(nS)$.

APPENDIX A: ORBITAL DECOMPOSITION

In Sec. III we highlighted how it is crucial to properly transform the NRQCD-based vector meson wave function

to the light front by performing the Melosh rotation. In particular, we demonstrated that this rotation gives rise to the helicity structures absent in the rest frame spin structure (e.g., nonzero $\Psi^{\lambda=\pm1}_{h=\pm1,\bar{h}=\mp1}$).

In this section, we illustrate the role of the Melosh rotation by considering both the J/ψ and virtual photon (in the case of charm quarks) wave functions and determining the contributions from the S- and D-wave components. The NRQCD-based wave function obtained in Sec. III contains only the S-wave structure. For the J/ψ wave function, we study here the commonly used boosted Gaussian parametrization (see Sec. IV A).

The S and D waves are properly defined in the rest frame. Consequently, we take the vector meson or the virtual photon wave functions on the light front written in momentum space and perform the Melosh rotation to transform them to the meson rest frame. In the rest frame we then remove either the S- or D-wave contribution and transform the final wave function back to the light front and Fourier transform to transverse coordinate space.

The boosted Gaussian parametrization of the J/ψ wave function is decomposed to S and D components in Fig. 6. In principle the angular momentum structure of the parametrization could turn out to correspond to a large D-wave component in the rest frame. Indeed it is mostly constrained by the choice of having helicity structure on the light front exactly the same as that of the photon, which has a large D-wave component as we will see. However, in practice the

S-wave-only result is a good approximation of the full result. This is due to the small quark velocities contributing to the wave function, as in the momentum space the boosted Gaussian wave function is exponentially suppressed at large invariant mass $M^2 = \frac{\mathbf{k}^2 + m_c^2}{z(1-z)}$. Thus, large transverse momentum $|\mathbf{k}|$ or large longitudinal momentum ($z \to 0$ or $z \to 1$) contributions are heavily suppressed and do not generate a significant D-wave component.

A similar discussion can be carried out for the BLFQ wave function described in Sec. IV A. As shown in [116], in the rest frame, the squared J/ψ BLFQ wave function is dominated by the S-wave component, the D wave contributing only a small fraction of the order of 0.1%…4% (depending on the polarization). In heavier mesons, this contribution is even smaller. This is comparable to the boosted Gaussian case discussed above.

Overall, based on neither the boosted Gaussian nor the BLFQ parametrizations, we do not see any confirmation for the result of Ref. [98], where the D-wave part of the J/ψ wave function was found to result in tens of percent contribution on the vector meson production cross section. Part of this discrepancy might be merely a question of terminology. In our discussion here, we have insisted that the terms S wave and D wave refer to the angular momentum components of the three-dimensional wave function in the meson rest frame. Thus the mere presence, in the light cone wave function, of terms proportional to transverse momenta originating from the Melosh rotation cannot be taken as an indication of a D-wave component in the meson.

Let us now move to the case of a virtual photon. Since a spacelike virtual photon does not have a rest frame and is not a bound state, it is not customarily thought of in terms of an S-D-wave decomposition. Now, however, we have an explicit light cone wave function for the photon just like for the meson, and we can use the same procedure to determine its S- and D-wave components in the meson rest frame. The resulting squared light front wave functions summed over quark helicities are shown in Fig. 7. The full photon wave function, written in Eqs. (17) and (18), is denoted by $S + D$, as it can be written as a sum of these two components. When compared to the full result, the squared D-wave-only contribution is found to be strongly suppressed. There is also a contribution originating from the overlap between the S- and D-wave contributions. This term would vanish if we integrated over all the angles. Here, we only integrate over the azimuthal direction of $\mathbf{r}$. Integration over the momentum fraction z corresponds to the evaluation of the coordinate space wave function at $x^3 = 0$, and consequently one angular integral is not performed and the overlap does not vanish. The relative importance of different contributions is found to be approximatively independent of Q^2.

The $S - D$ overlap contribution is numerically significant, which is reflected by the large difference between the
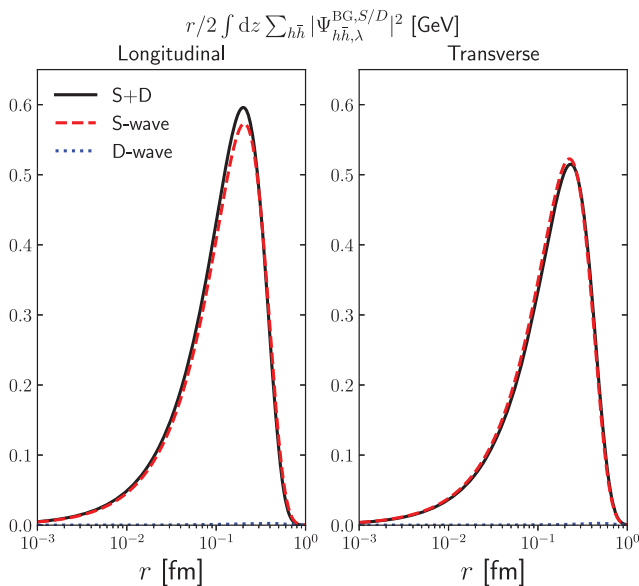

$$r/2 \int \mathrm{d}z \sum_{h\bar{h}} |\Psi^{\mathrm{BG},S/D}_{h\bar{h},\lambda}|^2 \ [\mathrm{GeV}]$$

FIG. 6.   Vector meson wave function from the boosted Gaussian parametrization decomposed into S- and D-wave components in the J/ψ rest frame as a function of the quark-antiquark transverse separation. The left panel shows the longitudinal polarization and the right panel transverse polarization.
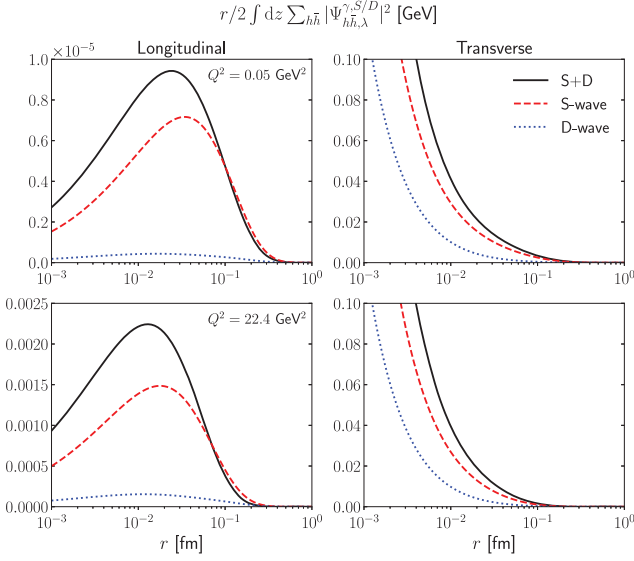
$$r/2 \int \mathrm{d}z \sum_{h\bar{h}} |\Psi^{\gamma,S/D}_{h\bar{h},\lambda}|^2 \text{ [GeV]}$$

FIG. 7. Virtual photon wave function integrated over the longitudinal momentum fraction z decomposed to S- and D-wave components as a function of the quark-antiquark transverse separation.

full result and the S-wave-only contribution. This suggests that even though the D-wave contribution is suppressed by the quark velocity, the charm quark mass is not large enough to render this contribution negligible. This is due to the fact that the photon wave function in the momentum space behaves as $\sim 1/\mathbf{k}^2$, where $\mathbf{k}$ is the quark transverse momentum, and this powerlike tail brings numerically large contributions from relatively large momenta. Additionally, the integration over the longitudinal momentum fraction z includes high momentum contributions, as the photon wave function has a support over a large range of z.

The contribution from the $S-D$ overlap changes sign at large transverse separations in case of the longitudinal polarization. There is no node in the radial part of the wave function, but the spherical harmonic function describing the angular part of the D-wave component changes sign, which explains the sign flip. In the $S-D$ overlap mostly the helicity-$+-$ and $-+$ components of the D-wave contribute by coupling to the S wave. On the other hand, in the D-wave squared wave function, one sums all helicity components. As the D-wave component itself is a relativistic correction, none of the helicity structures dominates unlike in the S-wave part. Moreover, only the $+-$ and $-+$ helicity components change sign at large distances, and as the $++$ and $--$ components do not vanish in this region, no node appears in the squared D wave result. In the case of transverse polarization with $\lambda = \pm 1$, the helicity component $\pm\pm$ in the D wave also changes the sign at large distances, but this effect is not easily visible in Fig. 7 as the other helicity components that do not change sign dominate.

APPENDIX B: PHOTONLIKE PARAMETRIZATIONS OF LIGHT CONE WAVE FUNCTIONS

As discussed in Sec. IV, an often used approach to parametrize vector meson wave functions is to start from the helicity structure of the virtual photon light cone wave functions (17) and (18). One then replaces the Bessel function K_0 in the photon wave functions (17) and (18) by an unknown function as [48]

$$e_f e z(1-z) \frac{K_0(\epsilon r)}{2\pi} \to \phi_{T,L}(r, z), \qquad (\text{B1})$$

with the explicit factor Q in the longitudinal wave function replaced by the meson mass as $2Q \to M_V$. This leads, with our sign conventions, to the wave function being written as

$$\psi^{\lambda=0}_{h\bar{h}}(\mathbf{r}, z) = \sqrt{N_c}\delta_{h,-\bar{h}}$$
$$\times \left[M_V + \frac{m_c^2 - \nabla_{\mathbf{r}}^2}{M_V z(1-z)} \right] \phi_L(\mathbf{r}, z), \qquad (\text{B2})$$

$$\psi^{\lambda=\pm 1}_{h\bar{h}}(\mathbf{r}, z) = \sqrt{2N_c} \frac{1}{z(1-z)} (m_c \delta_{h,\pm}\delta_{\bar{h},\pm}$$
$$\mp i e^{\pm i\theta_r}(z\delta_{h,\pm}\delta_{\bar{h},\mp} - (1-z)\delta_{h,\mp}\delta_{\bar{h},\pm})\partial_r)\phi_T(\mathbf{r}, z). \qquad (\text{B3})$$

The scalar functions $\phi_{T,L}(\mathbf{r}, z)$ are then parametrized, and the parameters can be determined by requiring that the resulting wave function is normalized to unity and reproduces the experimental leptonic decay width. In terms of Lorentz-invariant form factors this means that the meson is assumed to have a nonzero Dirac form factor but a vanishing Pauli form factor, since this is the structure dictated by the gauge-boson-fermion vertex at leading order perturbation theory. The procedure therefore does not generate the most general possible helicity structure.

This photonlike parametrization approach starts from a spacelike photon, where the photon momentum breaks rotational symmetry that is manifested here as a symmetry between longitudinal and transverse meson polarization states. The common approach is to separately parametrize the longitudinal and transverse functions $\phi_{T,L}(\mathbf{r}, z)$. The helicity structure obtained by generalization from the photon wave function is of course consistent with rotational symmetry, since the decay of a timelike virtual photon is rotationally symmetric. Thus one could derive a constraint relating $\phi_L(\mathbf{r}, z)$ and $\phi_T(\mathbf{r}, z)$ by requiring the meson rest frame wave functions to be the same. To our knowledge this approach has not, however, been used in the literature. Using separate parametrizations for $\phi_{T,L}(\mathbf{r}, z)$ should be contrasted with the approach in this paper. Here, we maintain rotational invariance in the meson rest frame, in particular starting from the same decay constants

calculated from the rest frame wave functions. Our procedure for going from the rest frame to the light cone wave function therefore simultaneously determines the wave function for both longitudinal and transverse polarization states.

One can take the parametrization (B2) and (B3) in momentum space, perform the inverse Melosh rotation and separate the S- and D-wave components to get a rest frame three-dimensional wave function. Assuming that the Fourier transforms of the scalar functions are rotationally invariant, i.e., $\phi_{T,L}(\mathbf{k}, z)$ depend only on $k = |\vec{k}| = \sqrt{(M/2)^2 - m_c^2}$, the result of this exercise in momentum space is

$$\psi_S^{\lambda=0} = \phi_L(k)\left(M_V + \frac{4E^2}{M_V}\right)$$
$$\times \sqrt{N_c\pi}\frac{2}{(E + m_c)(2E)^{3/2}}\left(\frac{1}{3}k^2 + (E + m)^2\right),$$
$$(B4)$$

$$\psi_S^{\lambda=+1,-1} = \phi_T(k) \cdot 4E$$
$$\times \sqrt{N_c\pi}\frac{2}{(E + m_c)(2E)^{3/2}}\left(\frac{1}{3}k^2 + (E + m)^2\right),$$
$$(B5)$$

$$\psi_D^{\lambda=0} = \phi_L(k)\left(M_V + \frac{4E^2}{M_V}\right)$$
$$\times \sqrt{N_c\pi}\frac{2}{(E + m_c)(2E)^{3/2}}\frac{4}{3\sqrt{2}}k^2, \quad (B6)$$

$$\psi_D^{\lambda=+1,-1} = \phi_T(k) \cdot 4E$$
$$\times \sqrt{N_c\pi}\frac{2}{(E + m_c)(2E)^{3/2}}\frac{4}{3\sqrt{2}}k^2. \quad (B7)$$

These expressions are written in terms of the energy of the quark in the meson rest frame $E = \sqrt{\vec{k}^2 + m_c^2} = M/2$, and $k = |\vec{k}|$. Let us point out a few aspects of these expressions. Firstly, as discussed above, in the photonlike parametrization there is always a D-wave component in the meson wave function. It is, as expected, explicitly a relativistic correction, i.e., proportional to the squared 3-momentum of the quark. Secondly, the rest frame wave functions of the transverse and longitudinal polarizations are not the same but differ by a factor $(M_V + \frac{4E^2}{M_V})/(4E) \approx 1 + \mathcal{O}((M - M_V)^2)$, where M is the invariant mass of the quark pair and M_V the mass of the meson. As discussed earlier in Sec. III, the coordinate transformation from k^3 to z inevitably introduces ambiguities that are proportional to this difference, so this should not come as a surprise. In an NRQCD power counting, this

difference is of the order of the binding energy of the meson, which is higher order than we are considering here.

In spite of this discussion, the wave function that we obtained in Sec. IV can in fact be written in a photonlike form in terms of scalar parts of light cone wave functions. In the notation of [48] these read

$$\phi_L(\mathbf{r}, z) = \frac{\pi}{\sqrt{N_c}(2m_{c,NR})^{3/2}}\frac{4M_V m_{c,NR}}{4m_{c,NR}^2 + M_V^2}$$
$$\cdot \left[A\delta(z - 1/2)\right.$$
$$+ \frac{B}{m_{c,NR}^2}\left(\left(\frac{34m_{c,NR}^2 + \frac{5}{2}M_V^2}{4m_{c,NR}^2 + M_V^2} + m_{c,NR}^2\mathbf{r}^2\right)\delta(z - 1/2)\right.$$
$$\left.\left. - \frac{1}{4}\partial_z^2\delta(z - 1/2)\right)\right],$$
$$(B8)$$

$$\phi_T(\mathbf{r}, z) = \frac{\pi}{\sqrt{N_c}(2m_{c,NR})^{3/2}}\left[A\delta(z - 1/2)\right.$$
$$+ \frac{B}{m_{c,NR}^2}\left(\left(\frac{11}{2} + m_{c,NR}^2\mathbf{r}^2\right)\delta(z - 1/2)\right.$$
$$\left.\left. - \frac{1}{4}\partial_z^2\delta(z - 1/2)\right)\right].$$
$$(B9)$$

We emphasize that we do not expect that writing down such a parameterization in terms of two scalar parts of a light cone wave function having the helicity structure of a photon would be possible at higher orders in the nonrelativistic expansion.

As a side remark, we discussed above that the photonlike structure generically implies a nonzero D-wave component; see Eqs. (B6) and (B7). On the other hand, our NRQCD-based wave function by construction has no D component. However, the D-wave component resulting from inserting the scalar parts (B8) and (B9) into the formulas for the D-wave contribution, Eqs. (B6) and (B7), behaves as $\sim k^2\nabla_k^2\delta^{(3)}(\vec{k})$. Such a function actually yields zero when convoluted with any test function $f(\vec{k})$, since the angular integral picks out the $\ell = 2$ component of f, which must vanish at $k = 0$. Thus the D-wave contribution corresponding to (B8) and (B9) is in fact zero in a distribution sense.

It is interesting to note that, when one calculates from these expressions the decay constants for the different polarization states using the light cone perturbation theory expressions (26) and (27) in Ref. [48], one obtains

$$f_L = \sqrt{\frac{2N_c}{m_{c,NR}}}e_f\left(A + \frac{5}{2}\frac{B}{m_{c,NR}^2}\right), \quad (B10)$$

$$f_T = \sqrt{\frac{2N_c}{m_{c,NR}}} e_f \frac{2m_{c,NR}}{M_V} \left(A - \frac{1}{2} \frac{B}{m_{c,NR}^2} \right). \qquad \text{(B11)}$$

The results are not exactly equal. However, as discussed above, if one approximates the meson mass by the quark pair invariant mass, as we did in transforming to the momentum fraction z, they do reduce to the same result. This can be seen explicitly by replacing M_V in (B11) by $\langle M \rangle \approx 2\sqrt{m_{c,NR}^2 + \langle \mathbf{q}^2 \rangle}$ and using Eq. (35) to write, at lowest nontrivial order in the quark velocity, $2m_{c,NR}/M_V \approx$

$1 + 3B/(m_{c,NR}^2 A)$ (note that $B < 0$). In this approximation Eqs. (B10) and (B11) also give back the same decay width expression that we are using to determine the rest frame wave function. We reiterate that a difference such as this can be expected in our procedure. We are constructing our wave functions by requiring the decay widths calculated from the rest frame wave functions to have the correct value and to be the same for the different polarization states. The coordinate transformation to light cone wave functions does not conserve these properties exactly, but only up to a given order in the nonrelativistic expansion.

[1] F. Gelis, E. Iancu, J. Jalilian-Marian, and R. Venugopalan, The color glass condensate, Annu. Rev. Nucl. Part. Sci. **60,** 463 (2010).

[2] J. L. Albacete and C. Marquet, Gluon saturation and initial conditions for relativistic heavy ion collisions, Prog. Part. Nucl. Phys. **76,** 1 (2014).

[3] M. G. Ryskin, Diffractive J/ψ electroproduction in LLA QCD, Z. Phys. C **57,** 89 (1993).

[4] A. Aktas *et al.* (H1 Collaboration), Elastic J/ψ production at HERA, Eur. Phys. J. C **46,** 585 (2006).

[5] S. Chekanov *et al.* (ZEUS Collaboration), Exclusive photoproduction of J/ψ mesons at HERA, Eur. Phys. J. C **24,** 345 (2002).

[6] S. Chekanov *et al.* (ZEUS Collaboration), Measurement of proton dissociative diffractive photoproduction of vector mesons at large momentum transfer at HERA, Eur. Phys. J. C **26,** 389 (2003).

[7] A. Aktas *et al.* (H1 Collaboration), Diffractive photoproduction of J/ψ mesons with large momentum transfer at HERA, Phys. Lett. B **568,** 205 (2003).

[8] S. Chekanov *et al.* (ZEUS Collaboration), Exclusive electroproduction of J/ψ mesons at HERA, Nucl. Phys. **B695,** 3 (2004).

[9] C. Alexa *et al.* (H1 Collaboration), Elastic and proton-dissociative photoproduction of J/ψ mesons at HERA, Eur. Phys. J. C **73,** 2466 (2013).

[10] C. Adloff *et al.* (H1 Collaboration), Elastic electroproduction of ρ mesons at HERA, Eur. Phys. J. C **13,** 371 (2000).

[11] S. Chekanov *et al.* (ZEUS Collaboration), Exclusive electroproduction of ϕ mesons at HERA, Nucl. Phys. **B718,** 3 (2005).

[12] F. D. Aaron *et al.* (H1 Collaboration), Diffractive electroproduction of ρ and ϕ mesons at HERA, J. High Energy Phys. 05 (2010) 032.

[13] S. Chekanov *et al.* (ZEUS Collaboration), Exclusive photoproduction of Υ mesons at HERA, Phys. Lett. B **680,** 4 (2009).

[14] C. Adloff *et al.* (H1 Collaboration), Elastic photoproduction of J/ψ and upsilon mesons at HERA, Phys. Lett. B **483,** 23 (2000).

[15] C. A. Bertulani, S. R. Klein, and J. Nystrand, Physics of ultra-peripheral nuclear collisions, Annu. Rev. Nucl. Part. Sci. **55,** 271 (2005).

[16] S. R. Klein and H. Mäntysaari, Imaging the nucleus with high-energy photons, Nat. Rev. Phys. **1,** 662 (2019).

[17] S. Afanasiev *et al.* (PHENIX Collaboration), Photoproduction of J/ψ and of high mass e^+e^- in ultra-peripheral Au + Au collisions at $\sqrt{s} = 200$ GeV, Phys. Lett. B **679,** 321 (2009).

[18] B. B. Abelev *et al.* (ALICE Collaboration), Exclusive J/ψ Photoproduction Off Protons in Ultra-Peripheral p-Pb Collisions at $\sqrt{s_{NN}} = 5.02$ TeV, Phys. Rev. Lett. **113,** 232504 (2014).

[19] S. Acharya *et al.* (ALICE Collaboration), Energy dependence of exclusive J/ψ photoproduction off protons in ultra-peripheral p-Pb collisions at $\sqrt{s_{NN}} = 5.02$ TeV, Eur. Phys. J. C **79,** 402 (2019).

[20] E. Abbas *et al.* (ALICE Collaboration), Charmonium and e^+e^- pair photoproduction at mid-rapidity in ultra-peripheral Pb-Pb collisions at $\sqrt{s_{NN}} = 2.76$ TeV, Eur. Phys. J. C **73,** 2617 (2013).

[21] B. Abelev *et al.* (ALICE Collaboration), Coherent J/ψ photoproduction in ultra-peripheral Pb-Pb collisions at $\sqrt{s_{NN}} = 2.76$ TeV, Phys. Lett. B **718,** 1273 (2013).

[22] V. Khachatryan *et al.* (CMS Collaboration), Coherent J/ψ photoproduction in ultra-peripheral PbPb collisions at $\sqrt{s_{NN}} = 2.76$ TeV with the CMS experiment, Phys. Lett. B **772,** 489 (2017).

[23] A. M. Sirunyan *et al.* (CMS Collaboration), Measurement of exclusive Υ photoproduction from protons in pPb collisions at $\sqrt{s_{NN}} = 5.02$ TeV, Eur. Phys. J. C **79,** 277 (2019).

[24] J. Adam (STAR Collaboration), Coherent J/ψ photoproduction in ultra-peripheral collisions at STAR, Proc. Sci. DIS2019 (**2019**) 042.

[25] A. Bursche (LHCb Collaboration), Study of coherent J/ψ production in lead-lead collisions at $\sqrt{s_{NN}} = 5$ TeV with the LHCb experiment, Nucl. Phys. **A982,** 247 (2019).

[26] H. Li (LHCb Collaboration), Z production in pPb collisions and charmonium production in PbPb ultra-peripheral collisions at LHCb, in *Proceedings of the 28th International Conference on Ultrarelativistic Nucleus-*

Nucleus Collisions (Quark Matter 2019) Wuhan, China, 2019 (2020) [arXiv:2002.01863].

[27] T. Lappi and H. Mantysaari, J/ψ production in ultra-peripheral $Pb + Pb$ and $p + Pb$ collisions at energies available at the CERN Large Hadron Collider, Phys. Rev. C **87,** 032201 (2013).

[28] V. Guzey and M. Zhalov, Exclusive J/ψ production in ultraperipheral collisions at the LHC: Constrains on the gluon distributions in the proton and nuclei, J. High Energy Phys. 10 (2013) 207.

[29] V. Guzey, E. Kryshen, and M. Zhalov, Coherent photo-production of vector mesons in ultraperipheral heavy ion collisions: Update for run 2 at the CERN Large Hadron Collider, Phys. Rev. C **93,** 055206 (2016).

[30] J. L. Albacete and C. Marquet, Single inclusive hadron production at RHIC and the LHC from the color glass condensate, Phys. Lett. B **687,** 174 (2010).

[31] J. L. Albacete, A. Dumitru, H. Fujii, and Y. Nara, CGC predictions for p + Pb collisions at the LHC, Nucl. Phys. **A897,** 1 (2013).

[32] T. Lappi and H. Mäntysaari, Single inclusive particle production at high energy from HERA data to proton-nucleus collisions, Phys. Rev. D **88,** 114020 (2013).

[33] B. Ducloué, T. Lappi, and H. Mäntysaari, Forward J/ψ production in proton-nucleus collisions at high energy, Phys. Rev. D **91,** 114005 (2015).

[34] B. Ducloué, T. Lappi, and H. Mäntysaari, Forward J/ψ production at high energy: Centrality dependence and mean transverse momentum, Phys. Rev. D **94,** 074031 (2016).

[35] H. Mäntysaari and H. Paukkunen, Saturation and forward jets in proton-lead collisions at the LHC, Phys. Rev. D **100,** 114029 (2019).

[36] S. J. Brodsky, L. Frankfurt, J. F. Gunion, A. H. Mueller, and M. Strikman, Diffractive leptoproduction of vector mesons in QCD, Phys. Rev. D **50,** 3134 (1994).

[37] S. Anand and T. Toll, Exclusive diffractive vector meson production: A comparison between the dipole model and the leading twist shadowing approach, Phys. Rev. C **100,** 024901 (2019).

[38] P. Hoodbhoy, Wave function corrections and off forward gluon distributions in diffractive J/ψ electroproduction, Phys. Rev. D **56,** 388 (1997).

[39] L. Frankfurt, W. Koepf, and M. Strikman, Diffractive heavy quarkonium photoproduction and electroproduction in QCD, Phys. Rev. D **57,** 512 (1998).

[40] H. Mäntysaari and B. Schenke, Probing subnucleon scale fluctuations in ultraperipheral heavy ion collisions, Phys. Lett. B **772,** 832 (2017).

[41] T. Lappi and H. Mantysaari, Incoherent diffractive J/ψ-production in high energy nuclear DIS, Phys. Rev. C **83,** 065202 (2011).

[42] A. Accardi et al., Electron ion collider: The next QCD frontier, Eur. Phys. J. A **52,** 268 (2016).

[43] E. C. Aschenauer, S. Fazio, J. H. Lee, H. Mantysaari, B. S. Page, B. Schenke, T. Ullrich, R. Venugopalan, and P. Zurita, The electron–ion collider: Assessing the energy dependence of key measurements, Rep. Prog. Phys. **82,** 024301 (2019).

[44] J. L. Abelleira Fernandez et al. (LHeC Study Group Collaboration), A large hadron electron collider at CERN: Report on the physics and design concepts for machine and detector, J. Phys. G **39,** 075001 (2012).

[45] X. Chen, A plan for electron ion collider in China, Proc. Sci. DIS2018 (**2018**) 170 [arXiv:1809.00448].

[46] H. J. Melosh, Quarks: Currents and constituents, Phys. Rev. D **9,** 1095 (1974).

[47] J. Hufner, Yu. P. Ivanov, B. Z. Kopeliovich, and A. V. Tarasov, Photoproduction of charmonia and total charmonium proton cross-sections, Phys. Rev. D **62,** 094022 (2000).

[48] H. Kowalski, L. Motyka, and G. Watt, Exclusive diffractive processes at HERA within the dipole picture, Phys. Rev. D **74,** 074016 (2006).

[49] Y. Hatta, B.-W. Xiao, and F. Yuan, Gluon tomography from deeply virtual Compton scattering at small-x, Phys. Rev. D **95,** 114026 (2017).

[50] A. G. Shuvaev, K. J. Golec-Biernat, A. D. Martin, and M. G. Ryskin, Off diagonal distributions fixed by diagonal partons at small x and xi, Phys. Rev. D **60,** 014015 (1999).

[51] H. Mäntysaari and B. Schenke, Evidence of Strong Proton Shape Fluctuations from Incoherent Diffraction, Phys. Rev. Lett. **117,** 052301 (2016).

[52] J. Cepila, J. G. Contreras, and J. D. Tapia Takaki, Energy dependence of dissociative J/ψ photoproduction as a signature of gluon saturation at the LHC, Phys. Lett. B **766,** 186 (2017).

[53] H. Mäntysaari and B. Schenke, Revealing proton shape fluctuations with incoherent diffraction at high energy, Phys. Rev. D **94,** 034042 (2016).

[54] M. C. Traini and J.-P. Blaizot, Diffractive incoherent vector meson production off protons: A quark model approach to gluon fluctuation effects, Eur. Phys. J. C **79,** 327 (2019).

[55] H. Mäntysaari, Review of proton and nuclear shape fluctuations at high energy, Rep. Prog. Phys. **83,** 082201 (2020).

[56] S. J. Brodsky, H.-C. Pauli, and S. S. Pinsky, Quantum chromodynamics and other field theories on the light cone, Phys. Rep. **301,** 299 (1998).

[57] Y. V. Kovchegov and E. Levin, Quantum chromodynamics at high energy, Cambridge Monogr. Part. Phys., Nucl. Phys., Cosmol. **33,** 1 (2012).

[58] G. P. Lepage and S. J. Brodsky, Exclusive processes in perturbative quantum chromodynamics, Phys. Rev. D **22,** 2157 (1980).

[59] H. G. Dosch, T. Gousset, G. Kulzinger, and H. J. Pirner, Vector meson leptoproduction and nonperturbative gluon fluctuations in QCD, Phys. Rev. D **55,** 2602 (1997).

[60] D. E. Soper, Infinite-momentum helicity states, Phys. Rev. D **5,** 1956 (1972).

[61] J. Jalilian-Marian, A. Kovner, L. D. McLerran, and H. Weigert, The intrinsic glue distribution at very small x, Phys. Rev. D **55,** 5414 (1997).

[62] J. Jalilian-Marian, A. Kovner, A. Leonidov, and H. Weigert, The BFKL equation from the Wilson renormalization group, Nucl. Phys. **B504,** 415 (1997).

[63] J. Jalilian-Marian, A. Kovner, A. Leonidov, and H. Weigert, The Wilson renormalization group for low x

physics: Towards the high density regime, Phys. Rev. D **59,** 014014 (1998).

[64] E. Iancu and L. D. McLerran, Saturation and universality in QCD at small *x*, Phys. Lett. B **510,** 145 (2001).

[65] E. Ferreiro, E. Iancu, A. Leonidov, and L. McLerran, Nonlinear gluon evolution in the color glass condensate. 2., Nucl. Phys. **A703,** 489 (2002).

[66] E. Iancu, A. Leonidov, and L. D. McLerran, The renormalization group equation for the color glass condensate, Phys. Lett. B **510,** 133 (2001).

[67] E. Iancu, A. Leonidov, and L. D. McLerran, Nonlinear gluon evolution in the color glass condensate. 1., Nucl. Phys. **A692,** 583 (2001).

[68] I. Balitsky, Operator expansion for high-energy scattering, Nucl. Phys. **B463,** 99 (1996).

[69] Y. V. Kovchegov, Small *x* F_2 structure function of a nucleus including multiple Pomeron exchanges, Phys. Rev. D **60,** 034008 (1999).

[70] J. L. Albacete, N. Armesto, J. G. Milhano, P. Quiroga-Arias, and C. A. Salgado, AAMQS: A non-linear QCD analysis of new HERA data at small-*x* including heavy quarks, Eur. Phys. J. C **71,** 1705 (2011).

[71] T. Lappi and H. Mantysaari, Forward dihadron correlations in deuteron-gold collisions with the Gaussian approximation of JIMWLK, Nucl. Phys. **A908,** 51 (2013).

[72] K. J. Golec-Biernat and A. M. Stasto, On solutions of the Balitsky-Kovchegov equation with impact parameter, Nucl. Phys. **B668,** 345 (2003).

[73] J. Berger and A. M. Stasto, Small x nonlinear evolution with impact parameter and the structure function data, Phys. Rev. D **84,** 094022 (2011).

[74] J. Berger and A. M. Stasto, Exclusive vector meson production and small-x evolution, J. High Energy Phys. 01 (2013) 001.

[75] H. Mäntysaari and B. Schenke, Confronting impact parameter dependent JIMWLK evolution with HERA data, Phys. Rev. D **98,** 034013 (2018).

[76] D. Bendova, J. Cepila, J. G. Contreras, and M. Matas, Solution to the Balitsky-Kovchegov equation with the collinearly improved kernel including impact-parameter dependence, Phys. Rev. D **100,** 054015 (2019).

[77] S. Schlichting and B. Schenke, The shape of the proton at high energies, Phys. Lett. B **739,** 313 (2014).

[78] H. Kowalski and D. Teaney, An impact parameter dipole saturation model, Phys. Rev. D **68,** 114005 (2003).

[79] V. N. Gribov and L. N. Lipatov, Deep inelastic *ep* scattering in perturbation theory, Yad. Fiz. **15,** 781 (1972) [Sov. J. Nucl. Phys. **15,** 438 (1972)].

[80] V. N. Gribov and L. N. Lipatov, e^+e^- pair annihilation and deep inelastic *ep* scattering in perturbation theory, Yad. Fiz. **15,** 1218 (1972) [Sov. J. Nucl. Phys. **15,** 675 (1972)].

[81] G. Altarelli and G. Parisi, Asymptotic freedom in parton language, Nucl. Phys. **B126,** 298 (1977).

[82] Y. L. Dokshitzer, Calculation of the structure functions for deep inelastic scattering and e+ e- annihilation by perturbation theory in quantum chromodynamics, Zh. Eksp. Teor. Fiz. **73,** 1216 (1977) [Sov. Phys. JETP **46,** 641 (1977)].

[83] F. D. Aaron *et al.* (H1 and ZEUS Collaborations), Combined measurement and QCD analysis of the inclusive $e^{\pm}p$

scattering cross sections at HERA, J. High Energy Phys. 01 (2010) 109.

[84] H. Abramowicz *et al.* (H1 and ZEUS Collaborations), Combination of measurements of inclusive deep inelastic $e^{\pm}p$ scattering cross sections and QCD analysis of HERA data, Eur. Phys. J. C **75,** 580 (2015).

[85] H. Abramowicz *et al.* (H1 and ZEUS Collaborations), Combination and QCD analysis of charm and beauty production cross-section measurements in deep inelastic *ep* scattering at HERA, Eur. Phys. J. C **78,** 473 (2018).

[86] H. Abramowicz *et al.* (H1 and ZEUS Collaborations), Combination and QCD analysis of charm production cross section measurements in deep-inelastic *ep* scattering at HERA, Eur. Phys. J. C **73,** 2311 (2013).

[87] H. Mäntysaari and P. Zurita, In depth analysis of the combined HERA data in the dipole models with and without saturation, Phys. Rev. D **98,** 036002 (2018).

[88] A. H. Rezaeian, M. Siddikov, M. Van de Klundert, and R. Venugopalan, Analysis of combined HERA data in the impact-parameter dependent saturation model, Phys. Rev. D **87,** 034002 (2013).

[89] G. T. Bodwin, E. Braaten, and G. P. Lepage, Rigorous QCD analysis of inclusive annihilation and production of heavy quarkonium, Phys. Rev. D **51,** 1125 (1995); **55,** 5853 (1997).

[90] V. V. Braguta, A. K. Likhoded, and A. V. Luchinsky, The study of leading twist light cone wave function of eta_c meson, Phys. Lett. B **646,** 80 (2007).

[91] V. V. Braguta, The study of leading twist light cone wave functions of J/ψ meson, Phys. Rev. D **75,** 094016 (2007).

[92] G. T. Bodwin, H. S. Chung, D. Kang, J. Lee, and C. Yu, Improved determination of color-singlet nonrelativistic QCD matrix elements for S-wave charmonium, Phys. Rev. D **77,** 094017 (2008).

[93] G. T. Bodwin, D. Kang, and J. Lee, Potential-model calculation of an order-v^2 NRQCD matrix element, Phys. Rev. D **74,** 014014 (2006).

[94] M. Escobedo and T. Lappi, Dipole picture and the non-relativistic expansion, Phys. Rev. D **101,** 034030 (2020).

[95] C. A. Flett, S. P. Jones, A. D. Martin, M. G. Ryskin, and T. Teubner, How to include exclusive J/ψ production data in global PDF analyses, Phys. Rev. D **101,** 094011 (2020).

[96] G. T. Bodwin, D. Kang, and J. Lee, Reconciling the light-cone and NRQCD approaches to calculating $e^+e^- \to$ J/ψ + η_c, Phys. Rev. D **74,** 114028 (2006).

[97] A. Krassnigg and H.-C. Pauli, On helicity and spin on the light cone, Nucl. Phys. B, Proc. Suppl. **108,** 251 (2002).

[98] M. Krelina, J. Nemchik, and R. Pasechnik, D-wave effects in diffractive electroproduction of heavy quarkonia from the photon-like $V \to Q\bar{Q}$ transition, Eur. Phys. J. C **80,** 92 (2020).

[99] J. Cepila, J. Nemchik, M. Krelina, and R. Pasechnik, Theoretical uncertainties in exclusive electroproduction of S-wave heavy quarkonia, Eur. Phys. J. C **79,** 495 (2019).

[100] M. Krelina, J. Nemchik, R. Pasechnik, and J. Cepila, Spin rotation effects in diffractive electroproduction of heavy quarkonia, Eur. Phys. J. C **79,** 154 (2019).

[101] R. Van Royen and V. F. Weisskopf, Hadron decay processes and the quark model, Nuovo Cimento A **50**, 617 (1967); Erratum, **51**, 583 (1967).

[102] M. Tanabashi *et al.* (Particle Data Group Collaboration), Review of particle physics, Phys. Rev. D **98**, 030001 (2018).

[103] J. P. Vary, H. Honkanen, J. Li, P. Maris, S. J. Brodsky, A. Harindranath, G. F. de Teramond, P. Sternberg, E. G. Ng, and C. Yang, Hamiltonian light-front field theory in a basis function approach, Phys. Rev. C **81**, 035205 (2010).

[104] H. Honkanen, P. Maris, J. P. Vary, and S. J. Brodsky, Electron in a Transverse Harmonic Cavity, Phys. Rev. Lett. **106**, 061603 (2011).

[105] X. Zhao, H. Honkanen, P. Maris, J. P. Vary, and S. J. Brodsky, Electron $g-2$ in light-front quantization, Phys. Lett. B **737**, 65 (2014).

[106] P. Wiecki, Y. Li, X. Zhao, P. Maris, and J. P. Vary, Basis light-front quantization approach to positronium, Phys. Rev. D **91**, 105009 (2015).

[107] L. Adhikari, Y. Li, X. Zhao, P. Maris, J. P. Vary, and A. Abd El-Hady, Form factors and generalized parton distributions in basis light-front quantization, Phys. Rev. C **93**, 055202 (2016).

[108] G. F. de Teramond and S. J. Brodsky, Light-Front Holography: A First Approximation to QCD, Phys. Rev. Lett. **102**, 081601 (2009).

[109] S. J. Brodsky, G. F. de Teramond, H. G. Dosch, and J. Erlich, Light-front holographic QCD and emerging confinement, Phys. Rep. **584**, 1 (2015).

[110] Y. Li, P. Maris, X. Zhao, and J. P. Vary, Heavy quarkonium in a holographic basis, Phys. Lett. B **758**, 118 (2016).

[111] Y. Li, P. Maris, and J. P. Vary, Quarkonium as a relativistic bound state on the light front, Phys. Rev. D **96**, 016022 (2017).

[112] G. Chen, Y. Li, P. Maris, K. Tuchin, and J. P. Vary, Diffractive charmonium spectrum in high energy collisions in the basis light-front quantization approach, Phys. Lett. B **769**, 477 (2017).

[113] G. Chen, Y. Li, K. Tuchin, and J. P. Vary, Heavy quarkonia production at energies available at the CERN Large Hadron Collider and future electron-ion colliding facilities using basis light-front quantization wave functions, Phys. Rev. C **100**, 025208 (2019).

[114] H. Mäntysaari and R. Venugopalan, Systematics of strong nuclear amplification of gluon saturation from exclusive vector meson production in high energy electron–nucleus collisions, Phys. Lett. B **781**, 664 (2018).

[115] R. Boussarie, A. V. Grabovsky, D. Yu. Ivanov, L. Szymanowski, and S. Wallon, Next-to-Leading Order Computation of Exclusive Diffractive Light Vector Meson Production in a Saturation Framework, Phys. Rev. Lett. **119**, 072002 (2017).

[116] M. Li, Y. Li, P. Maris, and J. P. Vary, Radiative transitions between 0^{-+} and 1^{--} heavy quarkonia on the light front, Phys. Rev. D **98**, 034024 (2018).
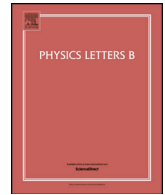
II

EXCLUSIVE HEAVY VECTOR MESON PRODUCTION AT NEXT-TO-LEADING ORDER IN THE DIPOLE PICTURE

by

Heikki Mäntysaari, Jani Penttala (2021)

Exclusive heavy vector meson production at next-to-leading order in the dipole picture

Heikki Mäntysaari [a,b], Jani Penttala [a,b,∗]

[a] *Department of Physics, University of Jyväskylä, P.O. Box 35, 40014 University of Jyväskylä, Finland*
[b] *Helsinki Institute of Physics, P.O. Box 64, 00014 University of Helsinki, Finland*

A B S T R A C T

We calculate exclusive production of a longitudinally polarized heavy vector meson at next-to-leading order in the dipole picture. The large quark mass allows us to separately include both the first QCD correction proportional to the coupling constant α_s, and the first relativistic correction suppressed by the quark velocity v^2. Both of these corrections are found to be numerically important in J/ψ production. The results obtained are directly suitable for phenomenological calculations. We also demonstrate how vector meson production provides complementary information to structure function analyses when one extracts the initial condition for the energy evolution of the proton small-x structure.

© 2021 The Author(s). Published by Elsevier B.V. This is an open access article under the CC BY license (http://creativecommons.org/licenses/by/4.0/). Funded by SCOAP³.

1. Introduction

Deep inelastic scattering (DIS) processes enable precision studies of proton and nuclear structure thanks to the pointlike structure of the electron probe. The vast amount of accurate measurements in electron-proton collisions at HERA has allowed for a detailed determination of the partonic structure of the proton. In particular, a rapid increase of the gluon density towards small momentum fraction x has been observed [1,2]. This rise can not continue indefinitely without violating unitarity, and nonlinear dynamics should eventually start to affect the proton or nuclear structure at small x.

In order to describe the hadron structure at high densities where nonlinear dynamics should be included, an effective theory of quantum chromodynamics known as the Color Glass Condensate (CGC) has been developed, see Refs. [3–5] for a review. Despite the success of the CGC framework in describing high-energy scattering measurements, there is no solid evidence that nonlinear saturation effects are visible at current collider energies. In order to access more pronounced nonlinear effects, there are concrete plans to construct an Electron-Ion Collider in the US [6–8] with similar longer term plans at CERN [9,10] and in China [11]. As the parton densities are enhanced by approximatively $A^{1/3}$ in heavy nuclei, the nonlinear dynamics should be more easily accessible by replacing the proton by a heavy nucleus in these future facilities.

Exclusive vector meson production is an especially powerful tool in probing hadron structure at small-x. In exclusive processes there cannot be a net color charge transfer in the process which, at leading order, requires an exchange of two gluons at the amplitude level. This renders the cross section to be approximatively sensitive to the squared gluon density [12], and nonlinear dynamics is expected to be pronounced in exclusive processes with heavy nuclear targets, see e.g. Ref. [13]. An additional benefit of exclusive processes is the fact that only in these events it is possible to measure the total momentum transfer to the target, which is the Fourier conjugate to the impact parameter. This enables studies of the Generalized Parton Distribution Functions (GPDs) [14,15] and the spatial structure of protons and nuclei with event-by-event fluctuations [16,17].

So far, almost all phenomenological applications in the CGC framework have been at leading order in the QCD coupling constant α_s, with the $\alpha_s \ln 1/x$ contributions resummed to all orders in terms of small-x evolution equations such as the Balitsky-Kovchegov (BK) equation [18,19]. Additionally, a subset of higher-order corrections to the evolution equation is included in terms of the running coupling corrections [20,21]. These applications include, for example, a successful description of the structure function [22,23] and vector meson production data [24–33] measured at HERA [34–36] and in Ultra Peripheral collisions [17,37] at the LHC [38–42]. In recent years, the theory has been developed towards next-to-leading order accuracy, including derivations of the next-to-leading order evolution equations [43–47] with perturbative corrections to initial conditions [48,49], and impact factors for structure functions [50–54], exclusive [55,56] and inclusive particle production [57–64].

---

* Corresponding author.
E-mail addresses: heikki.mantysaari@jyu.fi (H. Mäntysaari),
jani.j.penttala@student.jyu.fi (J. Penttala).

In this Letter we present the first calculation of the exclusive heavy vector meson production at next-to-leading order (NLO) in photon-proton collisions. The advantage of heavy mesons such as the J/ψ is that the mass scale renders the process perturbative even at low virtualities Q^2, enabling perturbative studies also in ultra peripheral collisions at RHIC and at the LHC where the photons are approximatively real. We include both the first QCD correction $\sim \alpha_s$, and the first nonrelativistic correction $\sim v^2$. We focus on J/ψ production, in which case both contributions can be expected to be parametrically important as for the charm quark velocity one can estimate $v^2 \sim \alpha_s$ [65]. These developments are crucial to enable precision studies of nonlinear dynamics in exclusive scattering processes in the CGC framework. In this work we consider the case where the photon is longitudinally polarized, but note that it will be possible to extend the results to the transverse photon case in the future.

2. Exclusive scattering at high energy

At high energies, it is convenient to describe exclusive vector meson production in the dipole picture in the frame where a highly energetic photon scatters off the target proton or nucleus and forms a vector meson. The exclusive nature of the process requires that there is no net color exchanged in the process. In this frame, the partonic Fock states of the virtual photon, e.g. $|q\bar{q}\rangle$ dipole and $|q\bar{q}g\rangle$ at NLO, have a long lifetime compared to the timescale of the interaction. These partons propagate eikonally through the color field of the target at fixed transverse coordinates $\mathbf{x}_i$ and pick up Wilson lines $V(\mathbf{x}_i)$ in the fundamental (quarks) or adjoint (gluons) representation. The scattering amplitude can be conveniently written as a convolution of the photon and vector meson wave functions Ψ_{γ^*} and Ψ_V, and Wilson line operators in the mixed longitudinal momentum fraction z_i, transverse coordinate $\mathbf{x}_i$ space. At high energies the imaginary part dominates, and the scattering amplitude at NLO in the case where the transverse momentum transfer to the target vanishes can be written as

$$-i\mathcal{A} = 2 \int_{\mathbf{x}_0 \mathbf{x}_1} \int \frac{\mathrm{d}z_0 \, \mathrm{d}z_1}{(4\pi)} \delta(z_0 + z_1 - 1) \Psi_V^{q\bar{q}*} \Psi_{\gamma^*}^{q\bar{q}} N_{01}$$
$$+ 2 \int_{\mathbf{x}_0 \mathbf{x}_1 \mathbf{x}_2} \int \frac{\mathrm{d}z_0 \, \mathrm{d}z_1 \, \mathrm{d}z_2}{(4\pi)^2} \delta(z_0 + z_1 + z_2 - 1) \Psi_V^{q\bar{q}g*} \Psi_{\gamma^*}^{q\bar{q}g} N_{012}.$$
(1)

Here $\mathbf{x}_0, \mathbf{x}_1$ and $\mathbf{x}_2$ are the quark, antiquark and gluon transverse coordinates respectively, and z_0, z_1 and z_2 are the fractions of the photon plus momentum carried by these partons. The calculations are done in the target rest frame where the photon plus momentum is chosen to be large. The wave functions depend implicitly on quark and gluon helicities, and a summation over the helicity states is also implicit. We consider coherent scattering processes, where the target proton remains in the same quantum state (i.e. no target breakup). The coherent vector meson production cross section reads

$$\frac{\mathrm{d}}{\mathrm{d}t} \sigma^{\gamma^* + A \to V + A} = \frac{1}{16\pi} |\mathcal{A}|^2.$$
(2)

The Wilson line operator describing the $q\bar{q}$ dipole-target scattering known as the dipole amplitude N_{01} is

$$1 - N_{01} = S_{01} = \mathrm{Re} \frac{1}{N_c} \left\langle V(\mathbf{x}_0) V^\dagger(\mathbf{x}_1) \right\rangle,$$
(3)

where $\mathbf{x}_0$ and $\mathbf{x}_1$ are the quark and antiquark transverse coordinates. Here the average $\langle \rangle$ refers to the average of the target color

charge configurations. Using the Fierz identity, the operator for the $q\bar{q}g$-target scattering can be written as (see e.g. Ref. [50])

$$1 - N_{012} = \frac{N_c}{2C_F} \left(S_{02} S_{12} - \frac{1}{N_c^2} S_{01} \right).$$
(4)

The transverse momentum transfer $|\mathbf{\Delta}| \approx \sqrt{-t}$ is the Fourier conjugate to the impact parameter. Consequently, an accurate calculation of the cross section differentially in $|t|$ would require a realistic description of the impact parameter dependence in the small-x evolution equation. Such equations exist and have been solved in the literature [29,66–68], but come with the price that one has to model confinement scale effects that suppress long range Coulomb tails. In this work, we want to perform a rigorous NLO calculation and limit our analysis to the $t = 0$ case in which the diffractive scattering amplitude is only sensitive to the dipole-target scattering amplitude integrated over the impact parameter, which we take to satisfy an impact parameter independent small-x evolution equation.

The necessary ingredients in the NLO calculation are the photon and vector meson wave functions and the dipole scattering amplitude, all at NLO level. The wave functions have been recently calculated in the literature, first in the massless quark limit in Refs. [50,51,55], and recently the heavy quark contributions have become available [54,56]. These wave functions are reviewed in Sec. 3. The dipole amplitude $N_{01} = N_{01}(Y)$ whose energy (or rapidity Y) dependence is given in terms of the BK equation is also available at NLO accuracy. The BK equation requires a non-perturbative input that can be taken to describe the dipole-target scattering amplitude at initial x, typically around $x \sim 0.01$. This perturbative evolution then predicts the dipole amplitude at smaller x (higher energies). In this work we use a BK evolved dipole scattering amplitude with the initial condition fitted to the HERA structure function data [1,2] at NLO accuracy in Ref. [69] (including only light quarks), using the public codes from Ref. [70].

3. Vector meson production at next to leading order

In order to calculate exclusive longitudinal quarkonium production at next-to-leading order accuracy, light front wave functions for the longitudinally polarized virtual photon Ψ_{γ^*} and vector meson Ψ_V are needed at this order in α_s (see also Ref. [71] for a discussion of negligibly small polarization changing contributions).

The virtual photon light front wave function at NLO accuracy in the case of massive quarks has recently been calculated in Ref. [54]. In our NLO calculation, we need the wave function describing the photon fluctuation to the $|q\bar{q}\rangle$ Fock state at NLO, $\Psi_{\gamma^*}^{q\bar{q}}$, and the tree level result for the formation of the $|q\bar{q}g\rangle$ state, $\Psi_{\gamma^*}^{q\bar{q}g}$. Detailed expressions can be found from Ref. [54], and we also explicitly show these results in supplementary Appendix A1, equations (A2) and (A3).

For the heavy quarkonium, a systematic method to include both the higher order QCD corrections and the relativistic corrections has been derived in Ref. [56]. In this approach, the quarkonium wave function is written in terms of the coefficients $C_{n \leftarrow m}^k$ defined as

$$\Psi_V^n = \sum_{m,k} C_{n \leftarrow m}^k \int_0^1 \frac{\mathrm{d}z'}{4\pi} \left(\frac{1}{m_q} \nabla \right)^k \phi^m(\mathbf{r} = 0, z'),$$
(5)

where $\nabla = (\partial_{r_1}, \partial_{r_2}, (z' - 1/2)2m_q i)$, M_V and $m_q = M_V/2$ are the meson and heavy quark masses, and ϕ^m is the leading order light front wave function which is generally nonrelativistic in the case of heavy quarkonium. The transverse separation between the quark and the antiquark is $\mathbf{r}$, and z' is the fraction of the meson plus

momentum carried by the quark. Here $k = (k_1, k_2, k_3)$ is to be understood as a multi-index, and the sum goes over all positive values of the single indices k_i, and $\left(\frac{1}{m_q}\nabla\right)^k = \frac{1}{m_q^{|k|}}\nabla_1^{k_1}\nabla_2^{k_2}\nabla_3^{k_3}$. As we neglect contributions $\sim \alpha_s v^2$, we need the quarkonium wave function Ψ_V^n at NLO in the nonrelativistic limit, which corresponds to the $|k| = k_1 + k_2 + k_3 = 0$ case. The $|k| > 0$ terms are suppressed by quark velocity, and are used to calculate relativistic corrections in Sec. 4. The variables m and n refer to the partonic Fock states, and at NLO in the nonrelativistic limit the non-zero coefficients are $C_{q\bar{q}\leftarrow q\bar{q}}^{(0,0,0)}$ and $C_{q\bar{q}g\leftarrow q\bar{q}}^{(0,0,0)}$. These have been calculated in Ref. [56] and are explicitly shown in supplementary Appendix A2 in Eqs. (A20) and (A21).

With $m = q\bar{q}$, the leading order wave function for the longitudinally polarized quarkonium is $\phi_{h'_0 h'_1}^{q\bar{q}}$ with the helicity structure given by $\delta_{h'_0, -h'_1}$. Here h'_0 and h'_1 are the quark and antiquark helicities. The coefficients $C_{n\leftarrow m}^k$ depend implicitly on the helicities of all the partons in state n, denoted by h_i, as well as on h'_0 and h'_1, and on parton colors as shown explicitly in supplementary Appendix A2. Summation over helicities and colors is implicit in Eq. (5). In particular, the helicity structure of the $\Psi_V^{q\bar{q}}$ wave function becomes $\delta_{h_0, -h_1}$ at lowest order in v, where h_0 and h_1 are the quark and antiquark helicities. The helicity flip contribution (where the quark helicities are the same) would only appear in the longitudinal quarkonium wave function $\Psi_V^{q\bar{q}}$ at the order v^4 [72] which is not included in our calculation. Consequently we can also drop the helicity flip component $\Psi_{h.f}$ from the longitudinal photon wave function at NLO.

Using the NLO wave functions available in the literature, we calculate longitudinally polarized exclusive heavy vector meson production amplitude $-i\mathcal{A}$ at next-to-leading order in the nonrelativistic limit. In this calculation there are both ultraviolet (UV) and infrared divergences that cancel at the level of the total NLO amplitude. First, both the real $q\bar{q}g$ and virtual $q\bar{q}$ contributions contain ultraviolet divergences that cancel in the sum. In practice, we use dimensional regularization and subtract this UV divergence from the real contribution, and add it to the virtual contribution which renders both terms finite. As the UV subtraction term can contain an arbitrary finite piece, division of the NLO contributions between the "real" and "virtual" parts is not unique. In this work, we follow the UV subtraction scheme developed in Refs. [50,54] which differs slightly from the one used in Ref. [56] and results in simpler expressions.

In addition to UV divergences, the NLO amplitude is singular in the infrared where the gluon plus momentum is very small. In order to cancel this divergence, we include two contributions as discussed in Ref. [56]. First, the leading order wave function $\phi_{h'_0 h'_1}^{q\bar{q}}$ is divergent at NLO, with the soft gluon divergence regulated by an infrared regulator α. The leptonic decay width $\Gamma(V \to e^- e^+)$, however, is finite and connects the wave function and the infrared regulator: [56]

$$\Gamma(V \to e^- e^+) = \frac{2N_c e_f^2 e^4}{3\pi M_V} \sum_{h'_0 h'_1} \left| \int \frac{dz'}{4\pi} \phi_{h'_0 h'_1}^{q\bar{q}} \right|^2$$
$$\times \left[1 + \frac{2\alpha_s C_F}{\pi} \left(\frac{1}{2\alpha} - 2 \right) \right]. \quad (6)$$

Here e is the elementary charge and e_f the fractional charge of the quark. In practice the wave function $\phi_{h'_0 h'_1}^{q\bar{q}}$ can be written in terms of the decay width and the infrared regulator, and the $1/\alpha$ divergence will cancel when combined with the virtual NLO contribution. Additionally, the real gluon emission contribution is also

singular in the soft gluon limit. This contribution can be absorbed in the target BK evolution.

The final result for the scattering amplitude at next-to-leading order reads

$$-i\mathcal{A}^L = -Q\sqrt{\Gamma(V \to e^- e^+)\frac{3M_V}{16\pi^2\alpha_{em}}} \int d^2\mathbf{x}_{01} \int d^2\mathbf{b}$$
$$\left\{ \mathcal{K}_{q\bar{q}}^{LO}(Y_0) + \frac{\alpha_s C_F}{2\pi}\mathcal{K}_{q\bar{q}}^{NLO}(Y_{dip}) \right.$$
$$\left. + \frac{\alpha_s C_F}{2\pi} \int d^2\mathbf{x}_{20} \int_{z_{min}}^{1/2} dz_2 \mathcal{K}_{q\bar{q}g}(Y_{qqg}) \right\}. \quad (7)$$

where $\mathcal{K}_{q\bar{q}}^{LO}(Y_0) = K_0(\zeta)N_{01}(Y_0)$, $\zeta = |\mathbf{x}_{01}|\sqrt{\frac{1}{4}Q^2 + m_q^2}$, $\mathbf{x}_{ij} = \mathbf{x}_i - \mathbf{x}_j$ and $\mathbf{b}$ is the impact parameter. Detailed expressions for the NLO contributions $\mathcal{K}_{q\bar{q}}^{NLO}$ and $\mathcal{K}_{q\bar{q}g}$ are shown in supplementary Appendix A3, Eqs. (A24) and (A26). This corresponds to the "unsubstracted scheme" discussed e.g. in Refs. [53,69]. Following the same terminology, we refer to the second term in Eq. (7) as the virtual "dipole" contribution (denoted by NLO_{dip} later), and the third term as the real contribution ($\text{NLO}_{q\bar{q}g}$). As discussed above, the division of the NLO corrections between these two terms is not unique. The dipole amplitudes are evaluated at evolution rapidities Y_0, Y_{dip} and $Y_{q\bar{q}g}$ that are discussed in detail below.

Evolution equations and rapidities

The integral of $\mathcal{K}_{q\bar{q}g}$ over z_2 in Eq. (7) is singular in the limit $z_{min} \to 0$. The singular part is related to the rapidity evolution of the dipole amplitude as can be seen by writing out the singularity explicitly:

$$\int d^2\mathbf{x}_{20} \int_{z_{min}}^{1/2} dz_2 \mathcal{K}_{q\bar{q}g} = \text{nonsingular term}$$
$$+ K_0(\zeta) \int d^2\mathbf{x}_{20} \int_{z_{min}}^{1/2} dz_2 \frac{2}{\pi z_2}\frac{\mathbf{x}_{01}^2}{\mathbf{x}_{20}^2\mathbf{x}_{21}^2}(S_{01} - S_{012}). \quad (8)$$

We can recognize from this the leading-order Balitsky-Kovchegov equation in integral form. It corresponds to the evolution over $\ln(\frac{1}{2z_{min}})$ units of projectile rapidity Y, defined as $Y = \ln k^+/P^+$. We recall that we work in the frame where the incoming photon has a large plus momentum q^+ and the gluon plus momentum reads $k^+ = z_2 q^+$. The target plus momentum P^+ is obtained as $P^+ = Q_0^2/(2P^-)$, where the transverse momentum scale of the target is taken to be $Q_0^2 = 1$ GeV^2 following [69]. The photon-proton center of mass energy squared is $W^2 = 2q^+ P^-$.

When the singular part in Eq. (8) is combined with the term $\mathcal{K}_{q\bar{q}}^{LO}(Y_0)$, one obtains the leading order contribution but with the dipole amplitude evolved from rapidity Y_0 to rapidity

$$Y_{dip} = Y_0 + \ln\frac{1}{2z_{min}} \quad (9)$$

using the LO BK equation at fixed coupling. This evolution is part of the actual leading order contribution, as the BK evolution resums $\alpha_s \ln 1/x$ contributions, that at high energy are of the order 1, to all orders. In this work we use the dipole amplitudes obtained as a result of the NLO fit to HERA structure function data [69]

where $Y_0 = 0$, and we also use the same running coupling prescription as in Ref. [69] in numerical analysis. We can write the leading order scattering amplitude as

$$-i\mathcal{A}_{\text{LO}}^L = -Q\sqrt{\Gamma(V \to e^-e^+)\frac{3M_V}{16\pi^2\alpha_{\text{em}}}}$$
$$\times \int d^2\mathbf{x}_{01} d^2\mathbf{b}\,\mathcal{K}_{q\bar{q}}^{\text{LO}}(Y_{\text{dip}}). \quad (10)$$

We note that what actually is the leading order contribution is not unique. One could as well define it as the sum of the lowest order contribution evaluated at Y_0 and the singular part of $\text{NLO}_{q\bar{q}g}$. These two definitions match at fixed coupling if no higher order corrections were included in the BK evolution [53]. In the NLO DIS fit of Ref. [69] applied in this work, modified versions of the BK equation that include the most important higher order corrections, in addition to the running coupling effects, were used and consequently Eq. (10) can not be obtained from Eq. (7). The definition of what is considered as the leading order contribution matters, because when calculating the cross sections an interference between the leading order and the genuine next-to-leading order contributions is needed, in which case the NLO correction is obtained as $-i\mathcal{A}^L - (-i)\mathcal{A}_{\text{LO}}^L$.

Let us then determine the lower limit of the z_2 integral $z_{\min}$ which controls the amount of small-x evolution. The applicability of the eikonal approximation requires that the invariant mass of the $q\bar{q}g$ system $M_{q\bar{q}g}$ satisfies $M_{q\bar{q}g}^2 \ll W^2$. There is some freedom in determining how strong ordering is required, and resulting differences at the cross section level will again formally be of higher order in α_s. In this work we use the same convention as in Ref. [69] and require $M_{q\bar{q}g}^2 < W^2$, which gives

$$z_2 > z_{\min} = \frac{P^+}{q^+} = \frac{Q_0^2}{W^2 + Q^2 - m_N^2}. \quad (11)$$

In the $\text{NLO}_{q\bar{q}g}$ term the rapidity at which the dipole amplitudes are evaluated depends on z_2, and using again $Y = z_2q^+/P^+$ we get

$$Y_{q\bar{q}g} = \ln z_2 + \ln \frac{W^2 + Q^2 - m_N^2}{Q_0^2}. \quad (12)$$

We note that the total evolution range probed in the NLO_{dip} contribution is exactly Y_{dip} discussed above.

For consistency, we choose to evaluate the dipole amplitude in the NLO_{dip} term at the same rapidity Y_{dip} as the leading order contribution. In Ref. [69] the virtual corrections to the structure functions were evaluated at $Y = \ln 1/x_{\text{bj}}$, which in our case would correspond to the rapidity $Y_{\text{dip}}^{\text{incl}} = \ln 1/x_{\mathbb{P}} \neq Y_{\text{dip}}$, where $x_{\mathbb{P}} \approx (M_V^2 + Q^2)/(W^2 + Q^2)$ is the fraction of the target longitudinal momentum transferred to the meson. Although it is not exactly consistent to use a different scheme to set the evolution rapidity in the structure function fit and in the application of these fit results in exclusive vector meson production, here we choose to apply the more natural choice for the evolution rapidity. The difference between these two choices is formally of higher order in α_s.

In Ref. [69] the fits are performed using initial conditions parametrized at both at $Y_{0,\text{BK}} = 0$ and at $Y_{0,\text{BK}} = 4.61$, in which case there is no evolution in the region $0 < Y < Y_{0,\text{BK}}$. The evolution equations that approximate the full NLO BK [43] in the fits are the so-called KCBK, ResumBK and TBK equations (following the terminology of Ref. [69]) derived in Refs. [73–76]. The "kinematically constrained BK equation" (KCBK) [75] is obtained by explicitly enforcing the required time ordering between the subsequent gluon emissions in the evolution. This procedure effectively resums

corrections that are enhanced by two large transverse logarithms $\sim \alpha_s \ln \frac{\mathbf{x}_{02}^2}{\mathbf{x}_{01}^2} \ln \frac{\mathbf{x}_{12}^2}{\mathbf{x}_{02}^2}$ in the evolution, and the same double logarithms are also resummed in Ref. [73]. When additional contributions enhanced by single transverse logarithms $\sim \alpha_s \ln 1/(\mathbf{x}_{ij}^2 Q_s^2)$ (where Q_s is the saturation scale of the target) are also resummed following Ref. [74] one obtains the evolution equation referred to as the ResumBK equation. The third evolution equation (TBK) refers to the BK equation where the evolution rapidity η ("target rapidity") is related to the fraction of the total longitudinal momentum of the target. When using the fit result that is written in terms of the target rapidity η in the impact factors written in terms of the (projectile) rapidity Y, we apply the same shift as in Ref. [69]: $\eta = Y + \ln(\min(1, \mathbf{x}_{01}^2 Q_0^2))$. For more details of the different evolution equations, we refer the reader to Ref. [69].

4. Relativistic corrections

As we have parametrically $\alpha_s \sim v^2$, it is also interesting to consider the first relativistic corrections of order v^2 at leading order in α_s. Using Eq. (5), we note that each term in the expansion corresponds to a correction of order $v^{|k|}$. The coefficient functions $C_{q\bar{q}\leftarrow q\bar{q}}^k$ are straightforward to calculate at leading order in α_s as then the wave function gets no loop corrections (and $C_{q\bar{q}g\leftarrow q\bar{q}}^k = 0$), and we can write

$$\Psi_V^{q\bar{q}}(\alpha_s = 0) = \sum_{k_1,k_2,k_3=0}^{\infty} C_{q\bar{q}\leftarrow q\bar{q}}^{(k_1,k_2,k_3)}\phi_{h_0'h_1'}^{q\bar{q}}(k_1,k_2,k_3), \quad (13)$$

where

$$C_{q\bar{q}\leftarrow q\bar{q}}^{(k_1,k_2,k_3)} = \frac{\delta_{\alpha_0\alpha_1}}{\sqrt{N_c}}\delta_{h_0h_0'}\delta_{h_1h_1'}\frac{1}{k_1!k_2!k_3!}(m_qr_1)^{k_1}(m_qr_2)^{k_2}$$
$$\times 4\pi\left(-\frac{1}{2i}\partial_z\right)^{k_3}\delta(z-1/2), \text{ and} \quad (14)$$

$$\phi_{h_0'h_1'}^{q\bar{q}}(k_1,k_2,k_3) := \int_0^1 \frac{dz'}{4\pi}\frac{1}{m_q^{k_1+k_2}}$$
$$\times \partial_1^{k_1}\partial_2^{k_2}\phi_{h_0'h_1'}^{q\bar{q}}(\mathbf{r}=0,z')[2i(z'-1/2)]^{k_3}. \quad (15)$$

Here $\mathbf{r} = (r_1, r_2)$ is the transverse separation of the two quarks and α_0, α_1 refer to the quark colors.

Calculating the production amplitude at order v^2 corresponds to keeping terms with $k_1 + k_2 + k_3 \leq 2$. The nonperturbative constants $\phi_{h_0'h_1'}^{q\bar{q}}(k_1,k_2,k_3)$ can be related to the derivatives of the leading-order rest frame wave function ϕ_{RF} at the origin as shown in Ref. [72]. This allows us to write (see discussion in supplementary Appendix A2 for more details)

$$\phi_{h_0'h_1'}^{q\bar{q}}(2,0,0) = \phi_{h_0'h_1'}^{q\bar{q}}(0,2,0) = \phi_{h_0'h_1'}^{q\bar{q}}(0,0,2)$$
$$= \frac{1}{\sqrt{2}}\delta_{h_0,-h_1}\frac{1}{\sqrt{m_q}}\frac{\nabla^2\phi_{\text{RF}}(0)}{6m_q^2}. \quad (16)$$

With this the order v^2 correction to the production amplitude is:

$$-i\mathcal{A}_{\text{rel}}^L = -\frac{ee_fQ\sqrt{N_c}}{2\pi\sqrt{2}}2\int d^2\mathbf{x}_{01}\int d^2\mathbf{b}\,N_{01}(Y_{\text{dip}})$$
$$\times \frac{\nabla^2\phi_{\text{RF}}(0)}{12m_q^2\sqrt{m_q}}\left[2K_0(\zeta) - \frac{Q^2\mathbf{x}_{01}^2}{4\zeta}K_1(\zeta) + m_q^2\mathbf{x}_{01}^2K_0(\zeta)\right]. \quad (17)$$
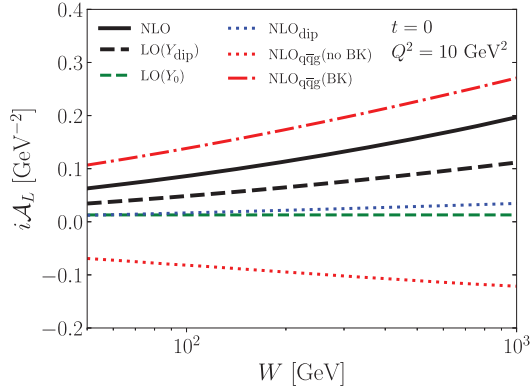
Fig. 1. Different contributions to the exclusive J/ψ production scattering amplitude as a function of center-of-mass energy W.
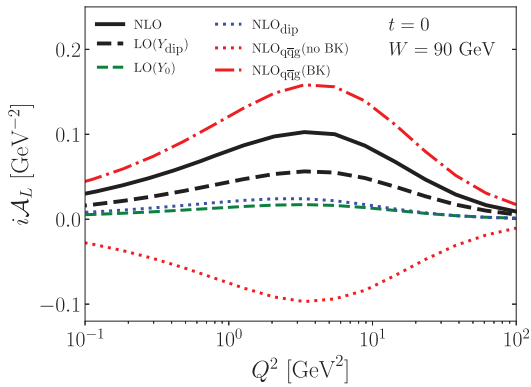

Fig. 2. Different contributions to the exclusive J/ψ production scattering amplitude as a function of photon virtuality Q^2.

The value for $\nabla^2 \phi_{\text{RF}}(0)$ for J/ψ can be determined using the non-relativistic QCD (NRQCD) matrix elements from [65]:

$$\nabla^2 \phi_{\text{RF}}(0) = -\sqrt{\frac{\langle \mathcal{O}_1 \rangle_V}{2N_c}} \langle \vec{q}^2 \rangle_V = -0.120 \pm 0.039 \text{ GeV}^{7/2}. \quad (18)$$

The long-distance matrix elements $\langle \mathcal{O}_1 \rangle_V$ and $\langle \vec{q}^2 \rangle_V$ are related to the J/ψ wave function and its derivative at the origin and explicitly defined in Ref. [65]. They are determined using $m_q = 1.4$ GeV for the charm mass. In this work, on the other hand, we use the nonrelativistic limit relation $m_q = M_V/2$ also when calculating the relativistic correction. This difference is of higher order in v, see also discussion in Ref. [72].

5. Numerical results

In this section we present numerical results for the exclusive J/ψ production at $t = 0$ in the kinematics covered by HERA and future EIC and LHeC/FCC-he measurements. Unless otherwise stated, we use the KCBK evolved dipole amplitude with the initial condition parametrized at $Y_{0,\text{BK}} = 4.61$ from Ref. [69]. The qualitative features do not depend on the actual dipole amplitude fit used.

The scattering amplitudes for exclusive J/ψ production at leading and next-to-leading order are shown in Figs. 1 and 2 as a function of center-of-mass energy W and photon virtuality Q^2. The total NLO amplitude is shown in Eq. (7), and should be compared to the leading-order result including the small-x BK evolution defined in Eq. (10) and denoted by LO(Y_{dip}) in the figures. Note that all results in Figs. 1 and 2 are obtained by using the same dipole amplitude N_{01} from Ref. [69]. The NLO corrections are found to be sizeable, of the order of $\sim 75\%$, and depend weakly on W and
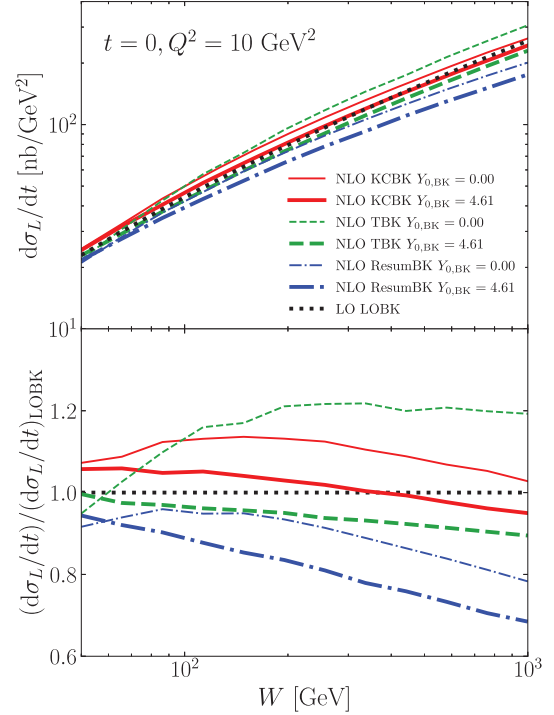
Fig. 3. Center-of-mass energy dependence of the exclusive J/ψ electroproduction cross section at NLO.

Q^2. Only at highest Q^2 values ~ 100 GeV^2 (where the high scale renders α_s smaller) the NLO corrections become slightly less important.

In Figs. 1 and 2 the different contributions to the NLO amplitude are also shown separately. First, the LO(Y_0) curve refers to the leading order result with no BK evolution. The virtual NLO correction NLO$_{\text{dip}}$ is found to be small and positive (by positive we mean that it has the same sign as the leading order result) at all W and Q^2. The real contribution NLO$_{q\bar{q}g}$ includes a leading order part in terms of the BK evolution. In the figures we show separately the contribution from the BK evolution shown in Eq. (8), and the genuine next-to-leading order correction to it due to the exact gluon emission kinematics included in the full NLO calculation. This NLO correction NLO$_{q\bar{q}g}$(no BK) = NLO$_{q\bar{q}g}$ − NLO$_{q\bar{q}g}$(BK) significantly suppresses the effect of the small-x BK evolution as expected. This systematics in the real and virtual corrections is similar to what is observed in case of structure function calculations at NLO in Ref. [53]. However, we emphasize that the division of the NLO corrections between the NLO$_{\text{dip}}$ and NLO$_{q\bar{q}g}$ terms is not unique, see the discussion in Sec. 3.

In Fig. 3 we show the energy dependence of the J/ψ electroproduction cross section at NLO using different dipole amplitude fits which describe the HERA structure function data approximatively equally well [69]. For comparison, the LO result using the fit with LO BK evolution and leading order impact factors from Ref. [23] is also shown. In the case of the LO BK evolved result the evolution rapidity is chosen as $Y = \ln 0.01/x_{\mathbb{P}}$, consistently with the leading-order fit procedure of Ref. [23].

Despite the fact that all dipole amplitudes result in almost identical descriptions of the HERA structure function data, we find that the resulting J/ψ production cross sections can differ by almost a factor of 2. This demonstrates that vector meson production provides complementary information for the extraction of the initial condition for the BK evolved dipole scattering amplitude, as it is sensitive to the dipole-target interaction at different distance scales (see also Ref. [29,30]) compared to total cross section measurements.
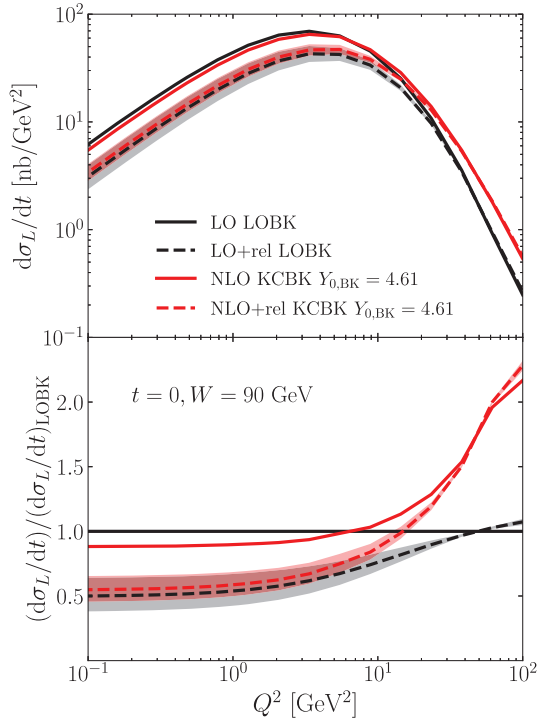
Fig. 4. The effect of the relativistic correction on J/ψ production at LO and at NLO as a function of photon virtuality Q^2. The bands show the uncertainties of the relativistic corrections.

It should be noted that the NLO results for the J/ψ production cross section are closer to the LO BK result than one might expect judging from Figs. 1 and 2. This can be understood by noting that the LO BK result in Fig. 3 is calculated using a LO dipole amplitude resulting from a leading-order fit, whereas in Figs. 1 and 2 the same NLO fit result was used for the dipole amplitude in all cases. In particular, the fit parameters obtained from the LO fit include an effective description of some of the higher-order effects. However, we still find that the NLO cross section generically evolves more slowly in W at high energies compared to LO results.

In Fig. 4 the effect of the relativistic corrections is shown. As previously discussed in Ref. [72], the relativistic corrections are significant and decrease the cross section up to $\sim 50\%$ at low photon virtualities, and become insignificant (but non-zero [77]) at large Q^2. At low virtualities the relativistic correction is more important than the next-to-leading order contribution. However, when comparing the relativistic $\sim v^2$ and NLO $\sim \alpha_s$ corrections one has to keep in mind that the leading order BK evolution effectively includes higher order corrections encoded in the fit parameters as discussed above. The relativistic correction is less important when it is added on top of the next-to-leading order result, $\sim 40\%$ at low Q^2, as we do not include corrections of the order $\alpha_s v^2$.

The next-to-leading order correction becomes large at high virtualities as can be seen from the lower panel of Fig. 4. We note that both LO and NLO fits provide a good description of the Q^2 dependence of the HERA structure function data at small x. The stronger virtuality dependence at leading order can be again understood to result from the fact that J/ψ production is sensitive to dipole scattering amplitude at smaller length scales compared to structure functions. The small dipole size region is also only weakly constrained by the structure function data when the initial condition for the BK evolution is fitted.

Technically, the dependence on the virtuality is related to the anomalous dimension γ which describes the behavior of the dipole amplitude at small dipole sizes: $N_{01} \sim (\mathbf{x}_{01}^2 Q_s^2)^\gamma$. At leading order the BK evolution results in $\gamma \sim 0.7$ at large rapidities,

but as $Y \sim \ln 1/x_{\mathbb{P}}$ in the LO fit, at high Q^2 one is actually sensitive to the dipole amplitude close to the initial condition where $\gamma \sim 1.2$ [22,23]. On the other hand, in our NLO setup there is a long evolution at high Q^2, see Eq. (12). However, the anomalous dimension at asymptotically small dipoles does not actually change when higher order corrections are resummed in the NLO fit. As the NLO fits also result in $\gamma \sim 1.2$ [69] at the initial rapidity, in principle we would expect to see comparable Q^2 evolution speeds in the exclusive J/ψ production. In practice one is not probing the dipole amplitude at asymptotically small dipoles but at $\mathbf{x}_{01}^2 \sim 1/Q^2$, and in the NLO fits γ decreases in the evolution at intermediate dipole sizes [69]. As a result, one finds that the NLO exclusive vector meson cross section decreases more slowly as a function of Q^2 than the leading order case at high virtualities.

6. Conclusions

We have calculated, for the first time, exclusive heavy vector meson production at next-to-leading order in the Color Glass Condensate framework. In the calculation we apply the recently derived wave functions for the virtual photon and vector meson including massive quarks. The main result of this work, the scattering amplitude for longitudinal vector meson production at NLO, is Eq. (7). We emphasize that this result is free from any ultraviolet or infrared divergences and suitable for phenomenological applications.

We have numerically evaluated the derived scattering amplitude, using dipole-proton scattering amplitudes recently obtained as a result of an NLO fit to HERA structure function data. We have presented the first numerical calculation of the exclusive J/ψ production cross section at NLO in the CGC framework. As the future Electron-Ion Collider and other nuclear DIS facilities will provide vast amounts of precise vector meson production data in the future, these developments that promote the CGC calculations to the precision level are extremely important.

We have shown that the next-to-leading order corrections to the J/ψ production cross section are significant, although these corrections can partially be captured in leading order calculations by the non-perturbative fit parameters. We also demonstrate that the vector meson production data provides complementary information compared to structure function measurements. A global analysis including both the reduced cross section and exclusive vector meson production data would be preferable in the future when extracting the initial condition for the Balitsky-Kovchegov evolution of the dipole scattering amplitude. Comparing the NLO $\sim \alpha_s$ correction to the relativistic $\sim v^2$ correction, we have observed that especially at low virtualities both corrections are numerically important, with the relativistic correction generically larger.

In the future, we will include the contribution from the transversely polarized virtual photons. This development will enable comparisons with the vector meson production data from HERA [34–36] and from the UPC physics program at the LHC [38, 39], as well as calculation of precise predictions for the EIC. Extending the calculation from protons to heavy nuclei will also enable precision studies of saturation phenomena in current [40–42] and future nuclear DIS experiments.

Declaration of competing interest

The authors declare that they have no known competing financial interests or personal relationships that could have appeared to influence the work reported in this paper.

Appendix A. Supplementary material

Supplementary material related to this article can be found online at https://doi.org/10.1016/j.physletb.2021.136723.

References

[1] H1, ZEUS collaborations, F.D. Aaron, et al., Combined measurement and QCD analysis of the inclusive $e^{\pm}p$ scattering cross sections at HERA, J. High Energy Phys. 01 (2010) 109, arXiv:0911.0884 [hep-ex].

[2] H1 ZEUS collaborations, H. Abramowicz, et al., Combination of measurements of inclusive deep inelastic $e^{\pm}p$ scattering cross sections and QCD analysis of HERA data, Eur. Phys. J. C 75 (12) (2015) 580, arXiv:1506.06042 [hep-ex].

[3] E. Iancu, R. Venugopalan, The color glass condensate and high-energy scattering in QCD, pp. 249–3363. 3, 2003, arXiv:hep-ph/0303204.

[4] F. Gelis, E. Iancu, J. Jalilian-Marian, R. Venugopalan, The color glass condensate, Annu. Rev. Nucl. Part. Sci. 60 (2010) 463, arXiv:1002.0333 [hep-ph].

[5] J.-P. Blaizot, High gluon densities in heavy ion collisions, Rep. Prog. Phys. 80 (3) (2017) 032301, arXiv:1607.04448 [hep-ph].

[6] A. Accardi, et al., Electron ion collider: the next QCD frontier: understanding the glue that binds us all, Eur. Phys. J. A 52 (9) (2016) 268, arXiv:1212.1701 [nucl-ex].

[7] E.C. Aschenauer, S. Fazio, J.H. Lee, H. Mäntysaari, B.S. Page, B. Schenke, T. Ullrich, R. Venugopalan, P. Zurita, The electron–ion collider: assessing the energy dependence of key measurements, Rep. Prog. Phys. 82 (2) (2019) 024301, arXiv:1708.01527 [nucl-ex].

[8] R. Abdul Khalek, et al., Science requirements and detector concepts for the electron-ion collider: EIC yellow report, arXiv:2103.05419 [physics.ins-det].

[9] LHeC Study Group collaboration, J.L. Abelleira Fernandez, et al., A large hadron electron collider at CERN: report on the physics and design concepts for machine and detector, J. Phys. G 39 (2012) 075001, arXiv:1206.2913 [physics.acc-ph].

[10] LHeC and FCC-he Study Group collaborations, P. Agostini, et al., The large hadron-electron collider at the HL-LHC, arXiv:2007.14491 [hep-ex].

[11] D.P. Anderle, et al., Electron-ion collider in China, Front. Phys. (Beijing) 16 (6) (2021) 64701, arXiv:2102.09222 [nucl-ex].

[12] M. Ryskin, Diffractive J/Ψ electroproduction in LLA QCD, Z. Phys. C 57 (1993) 89.

[13] H. Mäntysaari, R. Venugopalan, Systematics of strong nuclear amplification of gluon saturation from exclusive vector meson production in high energy electron–nucleus collisions, Phys. Lett. B 781 (2018) 664, arXiv:1712.02508 [nucl-th].

[14] K. Goeke, M.V. Polyakov, M. Vanderhaeghen, Hard exclusive reactions and the structure of hadrons, Prog. Part. Nucl. Phys. 47 (2001) 401, arXiv:hep-ph/0106012.

[15] A.V. Belitsky, A.V. Radyushkin, Unraveling hadron structure with generalized parton distributions, Phys. Rep. 418 (2005) 1, arXiv:hep-ph/0504030.

[16] H. Mäntysaari, Review of proton and nuclear shape fluctuations at high energy, Rep. Prog. Phys. 83 (8) (2020) 082201, arXiv:2001.10705 [hep-ph].

[17] S.R. Klein, H. Mäntysaari, Imaging the nucleus with high-energy photons, Nat. Rev. Phys. 1 (11) (2019) 662, arXiv:1910.10858 [hep-ex].

[18] Y.V. Kovchegov, Small-x F_2 structure function of a nucleus including multiple pomeron exchanges, Phys. Rev. D 60 (1999) 034008, arXiv:hep-ph/9901281 [hep-ph].

[19] I. Balitsky, Operator expansion for high-energy scattering, Nucl. Phys. B 463 (1996) 99, arXiv:hep-ph/9509348.

[20] I. Balitsky, Quark contribution to the small-x evolution of color dipole, Phys. Rev. D 75 (2007) 014001, arXiv:hep-ph/0609105.

[21] Y.V. Kovchegov, H. Weigert, Triumvirate of running couplings in small-x evolution, Nucl. Phys. A 784 (2007) 188, arXiv:hep-ph/0609090.

[22] J.L. Albacete, N. Armesto, J.G. Milhano, P. Quiroga-Arias, C.A. Salgado, AAMQS: a non-linear QCD analysis of new HERA data at small-x including heavy quarks, Eur. Phys. J. C 71 (2011) 1705, arXiv:1012.4408 [hep-ph].

[23] T. Lappi, H. Mäntysaari, Single inclusive particle production at high energy from HERA data to proton-nucleus collisions, Phys. Rev. D 88 (2013) 114020, arXiv:1309.6963 [hep-ph].

[24] H. Kowalski, L. Motyka, G. Watt, Exclusive diffractive processes at HERA within the dipole picture, Phys. Rev. D 74 (2006) 074016, arXiv:hep-ph/0606272.

[25] N. Armesto, A.H. Rezaeian, Exclusive vector meson production at high energies and gluon saturation, Phys. Rev. D 90 (5) (2014) 054003, arXiv:1402.4831 [hep-ph].

[26] V.P. Goncalves, M.V.T. Machado, The QCD pomeron in ultraperipheral heavy ion collisions. IV. Photonuclear production of vector mesons, Eur. Phys. J. C 40 (2005) 519, arXiv:hep-ph/0501099.

[27] J. Cepila, J.G. Contreras, M. Krelina, Coherent and incoherent J/ψ photonuclear production in an energy-dependent hot-spot model, Phys. Rev. C 97 (2) (2018) 024901, arXiv:1711.01855 [hep-ph].

[28] T. Lappi, H. Mäntysaari, J/ψ production in ultraperipheral Pb+Pb and p+Pb collisions at energies available at the CERN large hadron collider, Phys. Rev. C 87 (3) (2013) 032201, arXiv:1301.4095 [hep-ph].

[29] H. Mäntysaari, B. Schenke, Confronting impact parameter dependent JIMWLK evolution with HERA data, Phys. Rev. D 98 (3) (2018) 034013, arXiv:1806.06783 [hep-ph].

[30] H. Mäntysaari, P. Zurita, In depth analysis of the combined HERA data in the dipole models with and without saturation, Phys. Rev. D 98 (2018) 036002, arXiv:1804.05311 [hep-ph].

[31] H. Mäntysaari, B. Schenke, Revealing proton shape fluctuations with incoherent diffraction at high energy, Phys. Rev. D 94 (3) (2016) 034042, arXiv:1607.01711 [hep-ph].

[32] H. Mäntysaari, B. Schenke, Evidence of strong proton shape fluctuations from incoherent diffraction, Phys. Rev. Lett. 117 (5) (2016) 052301, arXiv:1603.04349 [hep-ph].

[33] H. Mäntysaari, B. Schenke, Probing subnucleon scale fluctuations in ultraperipheral heavy ion collisions, Phys. Lett. B 772 (2017) 832, arXiv:1703.09256 [hep-ph].

[34] ZEUS collaboration, S. Chekanov, et al., Exclusive photoproduction of J/ψ mesons at HERA, Eur. Phys. J. C 24 (2002) 345, arXiv:hep-ex/0201043.

[35] ZEUS collaboration, S. Chekanov, et al., Exclusive electroproduction of J/ψ mesons at HERA, Nucl. Phys. B 695 (2004) 3, arXiv:hep-ex/0404008.

[36] H1 collaboration, C. Alexa, et al., Elastic and proton-dissociative photoproduction of J/ψ mesons at HERA, Eur. Phys. J. C 73 (6) (2013) 2466, arXiv:1304.5162 [hep-ex].

[37] C.A. Bertulani, S.R. Klein, J. Nystrand, Physics of ultra-peripheral nuclear collisions, Annu. Rev. Nucl. Part. Sci. 55 (2005) 271, arXiv:nucl-ex/0502005.

[38] LHCb collaboration, R. Aaij, et al., Updated measurements of exclusive J/ψ and $\psi(2S)$ production cross-sections in pp collisions at $\sqrt{s} = 7$ TeV, J. Phys. G 41 (2014) 055002, arXiv:1401.3288 [hep-ex].

[39] ALICE collaboration, S. Acharya, et al., Energy dependence of exclusive J/ψ photoproduction off protons in ultra-peripheral p–Pb collisions at $\sqrt{s_{NN}} = 5.02$ TeV, Eur. Phys. J. C 79 (5) (2019) 402, arXiv:1809.03235 [nucl-ex].

[40] LHCb collaboration, H. Li, Z production in pPb collisions and charmonium production in PbPb ultra-peripheral collisions at LHCb, Nucl. Phys. A 1005 (2021) 121902, arXiv:2002.01863 [nucl-ex].

[41] CMS collaboration, V. Khachatryan, et al., Coherent J/ψ photoproduction in ultra-peripheral PbPb collisions at $\sqrt{s_{NN}} = 2.76$ TeV with the CMS experiment, Phys. Lett. B 772 (2017) 489, arXiv:1605.06966 [nucl-ex].

[42] ALICE collaboration, S. Acharya, et al., Coherent J/ψ photoproduction at forward rapidity in ultra-peripheral Pb-Pb collisions at $\sqrt{s_{NN}} = 5.02$ TeV, Phys. Lett. B 798 (2019) 134926, arXiv:1904.06272 [nucl-ex].

[43] I. Balitsky, G.A. Chirilli, Next-to-leading order evolution of color dipoles, Phys. Rev. D 77 (2008) 014019, arXiv:0710.4330 [hep-ph].

[44] A. Kovner, M. Lublinsky, Y. Mulian, Jalilian-Marian, Iancu, McLerran, Weigert, Leonidov, Kovner evolution at next to leading order, Phys. Rev. D 89 (6) (2014) 061704, arXiv:1310.0378 [hep-ph].

[45] I. Balitsky, G.A. Chirilli, Rapidity evolution of Wilson lines at the next-to-leading order, Phys. Rev. D 88 (2013) 111501, arXiv:1309.7644 [hep-ph].

[46] T. Lappi, H. Mäntysaari, Direct numerical solution of the coordinate space Balitsky-Kovchegov equation at next to leading order, Phys. Rev. D 91 (7) (2015) 074016, arXiv:1502.02400 [hep-ph].

[47] T. Lappi, H. Mäntysaari, Next-to-leading order Balitsky-Kovchegov equation with resummation, Phys. Rev. D 93 (9) (2016) 094004, arXiv:1601.06598 [hep-ph].

[48] A. Dumitru, R. Paatelainen, Sub-femtometer scale color charge fluctuations in a proton made of three quarks and a gluon, Phys. Rev. D 103 (3) (2021) 034026, arXiv:2010.11245 [hep-ph].

[49] A. Dumitru, H. Mäntysaari, R. Paatelainen, Color charge correlations in the proton at NLO: beyond geometry based intuition, Phys. Lett. B 820 (2021) 136560, arXiv:2103.11682 [hep-ph].

[50] H. Hänninen, T. Lappi, R. Paatelainen, One-loop corrections to light cone wave functions: the dipole picture DIS cross section, Ann. Phys. 393 (2018) 358, arXiv:1711.08207 [hep-ph].

[51] G. Beuf, Dipole factorization for DIS at NLO: loop correction to the $\gamma^*_{T,L} \to q\bar{q}$ light-front wave functions, Phys. Rev. D 94 (5) (2016) 054016, arXiv:1606.00777 [hep-ph].

[52] T. Lappi, R. Paatelainen, The one loop gluon emission light cone wave function, Ann. Phys. 379 (2017) 34, arXiv:1611.00497 [hep-ph].

[53] B. Ducloué, H. Hänninen, T. Lappi, Y. Zhu, Deep inelastic scattering in the dipole picture at next-to-leading order, Phys. Rev. D 96 (9) (2017) 094017, arXiv:1708.07328 [hep-ph].

[54] G. Beuf, T. Lappi, R. Paatelainen, Massive quarks in NLO dipole factorization for DIS: longitudinal photon, Phys. Rev. D 104 (5) (2021) 056032, arXiv:2103.14549 [hep-ph].

[55] R. Boussarie, A.V. Grabovsky, D.Y. Ivanov, L. Szymanowski, S. Wallon, Next-to-leading order computation of exclusive diffractive light vector meson production in a saturation framework, Phys. Rev. Lett. 119 (7) (2017) 072002, arXiv:1612.08026 [hep-ph].

[56] M.A. Escobedo, T. Lappi, Dipole picture and the nonrelativistic expansion, Phys. Rev. D 101 (3) (2020) 034030, arXiv:1911.01136 [hep-ph].

[57] B. Ducloué, E. Iancu, T. Lappi, A.H. Mueller, G. Soyez, D.N. Triantafyllopoulos, Y. Zhu, Use of a running coupling in the NLO calculation of forward hadron production, Phys. Rev. D 97 (5) (2018) 054020, arXiv:1712.07480 [hep-ph].

[58] B. Ducloué, T. Lappi, Y. Zhu, Single inclusive forward hadron production at next-to-leading order, Phys. Rev. D 93 (11) (2016) 114016, arXiv:1604.00225 [hep-ph].

[59] A.M. Stasto, B.-W. Xiao, D. Zaslavsky, Towards the test of saturation physics beyond leading logarithm, Phys. Rev. Lett. 112 (1) (2014) 012302, arXiv:1307.4057 [hep-ph].

[60] G.A. Chirilli, B.-W. Xiao, F. Yuan, One-loop factorization for inclusive hadron production in pA collisions in the saturation formalism, Phys. Rev. Lett. 108 (2012) 122301, arXiv:1112.1061 [hep-ph].

[61] G.A. Chirilli, B.-W. Xiao, F. Yuan, Inclusive hadron productions in pA collisions, Phys. Rev. D 86 (2012) 054005, arXiv:1203.6139 [hep-ph].

[62] T. Altinoluk, N. Armesto, G. Beuf, A. Kovner, M. Lublinsky, Single-inclusive particle production in proton-nucleus collisions at next-to-leading order in the hybrid formalism, Phys. Rev. D 91 (9) (2015) 094016, arXiv:1411.2869 [hep-ph].

[63] K. Watanabe, B.-W. Xiao, F. Yuan, D. Zaslavsky, Implementing the exact kinematical constraint in the saturation formalism, Phys. Rev. D 92 (3) (2015) 034026, arXiv:1505.05183 [hep-ph].

[64] E. Iancu, A.H. Mueller, D.N. Triantafyllopoulos, CGC factorization for forward particle production in proton-nucleus collisions at next-to-leading order, J. High Energy Phys. 12 (2016) 041, arXiv:1608.05293 [hep-ph].

[65] G.T. Bodwin, H.S. Chung, D. Kang, J. Lee, C. Yu, Improved determination of color-singlet nonrelativistic QCD matrix elements for S-wave charmonium, Phys. Rev. D 77 (2008) 094017, arXiv:0710.0994 [hep-ph].

[66] J. Berger, A.M. Stasto, Exclusive vector meson production and small-x evolution, J. High Energy Phys. 01 (2013) 001, arXiv:1205.2037 [hep-ph].

[67] J. Berger, A. Stasto, Numerical solution of the nonlinear evolution equation at small x with impact parameter and beyond the LL approximation, Phys. Rev. D 83 (2011) 034015, arXiv:1010.0671 [hep-ph].

[68] D. Bendova, J. Cepila, J.G. Contreras, M. Matas, Solution to the Balitsky-Kovchegov equation with the collinearly improved kernel including impact-parameter dependence, Phys. Rev. D 100 (5) (2019) 054015, arXiv:1907.12123 [hep-ph].

[69] G. Beuf, H. Hänninen, T. Lappi, H. Mäntysaari, Color glass condensate at next-to-leading order meets HERA data, Phys. Rev. D 102 (2020) 074028, arXiv:2007.01645 [hep-ph].

[70] G. Beuf, H. Hänninen, T. Lappi, H. Mäntysaari, Color glass condensate at next-to-leading order meets hera data (software), https://doi.org/10.5281/zenodo.4229269, 2020.

[71] H. Mäntysaari, K. Roy, F. Salazar, B. Schenke, Gluon imaging using azimuthal correlations in diffractive scattering at the electron-ion collider, Phys. Rev. D 103 (9) (2021) 094026, arXiv:2011.02464 [hep-ph].

[72] T. Lappi, H. Mäntysaari, J. Penttala, Relativistic corrections to the vector meson light front wave function, Phys. Rev. D 102 (5) (2020) 054020, arXiv:2006.02830 [hep-ph].

[73] E. Iancu, J.D. Madrigal, A.H. Mueller, G. Soyez, D.N. Triantafyllopoulos, Resumming double logarithms in the QCD evolution of color dipoles, Phys. Lett. B 744 (2015) 293, arXiv:1502.05642 [hep-ph].

[74] E. Iancu, J.D. Madrigal, A.H. Mueller, G. Soyez, D.N. Triantafyllopoulos, Collinearly-improved BK evolution meets the HERA data, Phys. Lett. B 750 (2015) 643, arXiv:1507.03651 [hep-ph].

[75] G. Beuf, Improving the kinematics for low-x QCD evolution equations in coordinate space, Phys. Rev. D 89 (7) (2014) 074039, arXiv:1401.0313 [hep-ph].

[76] B. Ducloué, E. Iancu, A.H. Mueller, G. Soyez, D.N. Triantafyllopoulos, Non-linear evolution in QCD at high-energy beyond leading order, J. High Energy Phys. 04 (2019) 081, arXiv:1902.06637 [hep-ph].

[77] P. Hoodbhoy, Wave function corrections and off forward gluon distributions in diffractive J/ψ electroproduction, Phys. Rev. D 56 (1997) 388, arXiv:hep-ph/9611207.

III

EXCLUSIVE PRODUCTION OF LIGHT VECTOR MESONS AT NEXT-TO-LEADING ORDER IN THE DIPOLE PICTURE

by

Heikki Mäntysaari, Jani Penttala (2022)

Exclusive production of light vector mesons at next-to-leading order in the dipole picture

Heikki Mäntysaari[*] and Jani Penttala[†]

*Department of Physics, University of Jyväskylä, P.O. Box 35, 40014 University of Jyväskylä, Finland
and Helsinki Institute of Physics, P.O. Box 64, 00014 University of Helsinki, Finland*

Exclusive production of light vector mesons in deep inelastic scattering is calculated at next-to-leading order in the dipole picture in the limit of high photon virtuality. The resulting expression is free of any divergences and suitable for numerical evaluations. The higher-order corrections are found to be numerically important, but they can be mostly captured by the nonperturbative fit parameters describing the initial condition for the small-x evolution of the dipole scattering amplitude. The vector meson production cross section is shown to depend only weakly on the meson distribution amplitude and the factorization scale. We also present phenomenological comparisons of our result to the existing exclusive ϕ and ρ production data from HERA and find an excellent agreement at high virtualities.

I. INTRODUCTION

Deep inelastic scattering (DIS) is a powerful tool to study the partonic structure of protons and nuclei at high energies. This process has been studied in detail in electron-proton collisions at HERA, where the vast amount of measured data has revealed a rapid increase in the density of gluons with small momentum fraction x [1,2]. The observed increase cannot continue indefinitely without violating unitarity, and as such the saturation effects are expected to dominate the small-x part of the hadron wave function. To describe QCD in this region of phase space where parton densities become of the same order as the inverse of the strong coupling, an effective field theory approach to QCD, called the color glass condensate (CGC), has been developed [3–5].

In CGC, the high density of small-x gluons gives rise to nonlinear dynamics that slows down the growth of the gluon density. Despite the success of the CGC-based calculations in describing various high-energy collider experiments [6], there has not been definitive experimental evidence of saturation. To get precise DIS data from the saturation region new experimental facilities have been proposed, such as the upcoming Electron-Ion Collider in the U.S. [7–9] and a similar collider at CERN [10].

These facilities would allow for DIS measurements with heavy nuclei where the saturation effects are amplified approximately by $A^{1/3}$. To meet the precision of these future experimental studies where nonlinear QCD dynamics is probed, it is necessary to promote the theory calculations in the CGC framework to higher-order accuracy.

One powerful process to probe gluon saturation is exclusive vector meson production as it requires an exchange of at least two gluons with the target. This renders the cross section roughly proportional to the gluon density squared [11] at leading order (but the situation is more complicated at next-to-leading order in a collinear factorization based approach, see Ref. [12]). Another advantage of it is that only in exclusive processes it is possible to measure the momentum transfer squared t in the process. The momentum transfer dependence can be related to the impact parameter dependence via a Fourier transform, providing access to the spatial distribution of nuclear matter in nuclei at high energy [13,14] and to the generalized parton distribution functions [15].

A convenient approach for describing exclusive vector meson production in DIS is the dipole picture where the process can be written in terms of the virtual photon and meson light-front wave functions along with the dipole-target scattering amplitude [16,17]. The dipole amplitude satisfies perturbative small-x evolution equations, such as the Balitsky-Kovchegov (BK) equation [18,19], which resums large logarithmic contributions $\sim \alpha_s \ln 1/x$. The photon wave function can be calculated perturbatively [20,21], but the meson wave function is instead nonperturbative and therefore requires additional modeling. For heavy vector mesons one can take advantage of the

[*]heikki.mantysaari@jyu.fi
[†]jani.j.penttala@jyu.fi

small relative velocity of the quark-antiquark pair in the meson and model it as a fully nonrelativistic bound state [11], with velocity corrections that can be linked to the nonrelativistic QCD (NRQCD) matrix elements [22]. Another possibility is to take the limit of high photon virtuality, $Q^2 \gg M_V^2$ (where M_V is the meson mass), where one can make a twist expansion for the process [23,24]. This corresponds to writing the meson wave function in terms of a nonperturbative distribution amplitude, on top of which higher-order corrections can be calculated perturbatively. This is especially suitable for light vector mesons and is a basic assumption in this paper.

The next-to-leading order (NLO) calculations in the dipole picture are starting to become available. First of all, the BK equation is available at NLO accuracy [25–28]. The NLO corrections to the virtual photon wave function have been calculated with both massless [29–31] and massive [32,33] quarks. These developments enable phenomenological studies of proton and nuclear structure functions at small x, and also make it possible to determine the nonperturbative initial condition for the small-x evolution of the dipole amplitude by performing fits to HERA data [34–37]. Another recently proposed approach to determine the initial condition is based on a perturbative calculation of the proton color charge correlators in terms of the nonperturbative proton valence quark wave function [38,39]. In order to calculate exclusive vector meson production at NLO accuracy, the additional ingredient required is the meson wave function at NLO. This wave function has been calculated in the nonrelativistic limit for heavy vector mesons in Ref. [40] and used for calculating longitudinal heavy vector meson production at NLO accuracy in Ref. [41] including also the first relativistic corrections [22]. Other recent developments towards the NLO accuracy in the CGC framework include, for example, studies of dijet production in DIS and hadronic collisions [42–44], and inclusive hadron production in proton-lead collisions [45–52].

The main focus of this work, light vector meson production in the high-Q^2 limit at NLO, has been calculated in Ref. [53] using covariant perturbation theory in momentum space including nonlinear QCD dynamics in the shockwave approach. In this paper, we calculate the NLO corrections using light cone perturbation theory [20] in mixed transverse coordinate, longitudinal momentum fraction space. The advantage of the light cone perturbation theory is that the calculation can be divided into the photon and meson wave functions that need to be combined only at the end. One can also directly take advantage of the recently calculated photon NLO wave function. The mixed coordinate space is convenient as the transverse coordinates of the partons do not change during the interaction with the target at high energies. Compared to Ref. [53] we also use a different scheme to subtract the rapidity divergence from the real gluon emission part. This scheme is developed in

Refs. [46,51,54,55] in order to avoid unphysical results in single hadron production and in proton structure function calculations at NLO accuracy. Our results are also straightforward to apply in phenomenological analyses using existing dipole amplitude fits as is demonstrated in this work.

The paper is structured as follows. In Sec. II we present the framework for vector meson production and explain the resummation of small-x gluons. In Sec. III, the photon and meson NLO wave functions are shown explicitly. The NLO corrections to the light vector meson wave function are calculated using light cone perturbation theory at leading twist. We then proceed to calculate the production amplitude in Sec. IV and present the result in the mixed space. In Sec. V, we show numerical calculations of the NLO production amplitude along with comparisons to the existing ρ and ϕ production data before presenting our conclusions in Sec. VI.

II. EXCLUSIVE SCATTERING AT HIGH ENERGY

A. High energy factorization

The scattering amplitude for exclusive vector meson production at high energy and in the zero squared momentum transfer $t = 0$ limit can be written in a factorized form

$$
\begin{aligned}
-i\mathcal{A} = \sum_f 2 \int & \mathrm{d}^{D-2}\mathbf{x}_0 \mathrm{d}^{D-2}\mathbf{x}_1 \\
\times \int & \frac{\mathrm{d}z_0 \mathrm{d}z_1}{(4\pi)^2} 4\pi\delta(z_0 + z_1 - 1)\Psi_f^{\gamma^* \to q\bar{q}}(\Psi_f^{V \to q\bar{q}})^* N_{01} \\
+ \sum_f 2 \int & \mathrm{d}^{D-2}\mathbf{x}_0 \mathrm{d}^{D-2}\mathbf{x}_1 \mathrm{d}^{D-2}\mathbf{x}_2 \\
\times \int & \frac{\mathrm{d}z_0 \mathrm{d}z_1 \mathrm{d}z_2}{(4\pi)^3} 4\pi\delta(z_0 + z_1 + z_2 - 1) \\
\times \Psi_f^{\gamma^* \to q\bar{q}g}(\Psi_f^{V \to q\bar{q}g})^* N_{012},
\end{aligned}
\tag{1}
$$

and the coherent vector meson V electroproduction cross section can now be obtained as

$$
\left. \frac{\mathrm{d}\sigma^{\gamma^*+p \to V+p}}{\mathrm{d}t} \right|_{t=0} = \frac{1}{16\pi}|\mathcal{A}|^2.
\tag{2}
$$

Here $\mathbf{x}_{0,1,2}$ are the quark, antiquark, and gluon transverse coordinates, and z_i denotes the fractions of the photon's plus momentum carried by these partons. This factorization is justified at high energy as the lifetimes of the virtual photon $q\bar{q}$ and $q\bar{q}g$ Fock states are much longer than the timescales related to the interactions with the target color field. We use the eikonal approximation and describe the interactions with the target in terms of Wilson line correlators. The Wilson line $V_{F,A}(\mathbf{x})$ describes a color rotation of a quark (fundamental representation F) or a gluon (adjoint representation A) when it propagates through the target, and the relevant correlators read

$$N_{01} = 1 - \frac{1}{N_c} \langle \text{Tr}\{V_F(\mathbf{x}_0)V_F^\dagger(\mathbf{x}_1)\} \rangle, \qquad (3)$$

$$N_{012} = 1 - \frac{1}{C_F N_c} \langle V_A^{ba}(\mathbf{x}_2)\text{Tr}\{t^b V_F(\mathbf{x}_0)t^a V_F^\dagger(\mathbf{x}_1)\} \rangle,$$

$$\approx 1 - \frac{N_c}{2C_F}\left(S_{02}S_{12} - \frac{1}{N_c{}^2}S_{01}\right), \qquad (4)$$

where $S_{01} = 1 - N_{01}$. Here we took the mean field limit where the average over the target color charge configurations denoted by $\langle \cdots \rangle$ factorizes. These correlators satisfy the BK evolution equation discussed in Sec. II C and depend implicitly on evolution rapidity, which we will specify later.

We only consider forward production in this work even though this framework can also be extended to calculate the momentum transfer dependent cross section. The momentum transfer is the Fourier conjugate to the impact parameter, and thus being able to calculate the cross section at finite momentum transfer is an advantage of exclusive processes as this can be used to do spatial imaging of the hadron structure [13]. On the other hand, this means that calculating vector meson production at $t \neq 0$ would require us to implement a model to describe the nonperturbative spatial structure of the proton. As the purpose of this work is to focus on a rigorous NLO calculation of a vector meson production cross section we choose not to employ any such modeling and limit our studies to $t = 0$ where only the dipole amplitude integrated over the impact parameter is required. The same quantity is also probed in structure function measurements that are used to constrain the initial condition for the BK evolution of the dipole scattering amplitude N_{01} [37].

B. Twist expansion

The meson light-front wave function is highly non-perturbative. For heavy vector mesons one can model the wave function based on the nonrelativistic nature of heavy quarks [22] but this simplification cannot be made for light mesons. On the other hand, the high-virtuality limit $Q^2 \gg M_V^2$, which is justified for light mesons, can be used to simplify the mathematical description of the process. In this limit transverse momentum scales on the meson side become corrections suppressed by powers of $1/Q^2$, leading to the twist expansion of the meson wave function [23,24]. The leading-twist term then does not depend on the transverse momentum scales of the meson, meaning that only the dependence on the longitudinal momenta remains.

The twist expansion can be explained formally using the virtual photon wave function. The photon wave function is exponentially suppressed in $Q^2\mathbf{r}^2$, where $\mathbf{r}$ is the dipole size, which renders the relevant dipole sizes to be $\mathbf{r}^2 \sim 1/Q^2$. We can then do a Taylor expansion

for the meson wave function $\Psi^V(\mathbf{r},z) = \Psi^V(0,z) + \frac{1}{6}\mathbf{r}^2\nabla_\mathbf{r}^2\Psi^V(0,z) + \ldots = \Psi^V(0,z) + \mathcal{O}(\frac{1}{Q^2})$ (see also Ref. [22]). Thus, only the dependence on the momentum fraction z remains at leading order in the twist expansion. The momentum space equivalent of this is a delta function in terms of the quark transverse momentum $\mathbf{k}$: $\Psi^V(\mathbf{k},z) = (2\pi)^2\delta^2(\mathbf{k})\Psi^V(\mathbf{r} = 0, z) + \mathcal{O}(\frac{1}{Q^2})$. This first term in the wave function corresponds to the twist-2 distribution amplitude $\phi(z)$ of the meson. In an NLO calculation the distribution amplitude has to be renormalized as we will demonstrate explicitly below, and the scale dependence of the renormalized distribution amplitude is described in terms of the Efremov-Radyushkin-Brodsky-Lepage (ERBL) evolution equation [20,56], which is discussed in more detail in Sec. IV C.

The twist expansion also guarantees that we need the nonperturbative part of the meson wave function only for the $q\bar{q}$ state. The nonperturbative part for other Fock states, such as $q\bar{q}g$, is higher order in twist and can therefore be neglected at high Q^2 [57,58]. This means that the meson wave function for the $q\bar{q}g$ state can be calculated perturbatively by considering gluon emission from the $q\bar{q}$ state, i.e., at high virtualities the Fock state $q\bar{q}g$ is created through the process $V \to q\bar{q} \to q\bar{q}g$ [see Figs. 1(f) and 1(g)].

Another consequence of the high virtuality is that we need to consider only the longitudinal polarization for both the photon and the meson. A polarization flip is highly suppressed in coherent vector meson production such that the meson and photon effectively have the same polarization [59] (see also Ref. [60]). In fact, in the limit of zero momentum exchange $t = 0$ the polarization flip contribution vanishes exactly in our calculation. In the case of transverse production the leading-twist distribution amplitude is twist 3 [23], meaning that transverse production is suppressed relative to longitudinal by $\sigma_T/\sigma_L \sim M_V^2/Q^2$ for high virtualities. Thus, total light vector meson production is given by the longitudinal cross section $\sigma(\gamma_L^* + A \to V_L + A)$ up to corrections of order $\mathcal{O}(\frac{M_V^2}{Q^2})$.

C. High-energy evolution

The dipole amplitude, given by the correlator $N_{01} = 1 - S_{01}$, satisfies the perturbative BK equation describing its energy dependence. At leading order the BK equation reads [18,19]

$$\frac{\partial}{\partial Y}S_{01} = \int d^2\mathbf{x}_2 K_{BK}(\mathbf{x}_0,\mathbf{x}_1,\mathbf{x}_2)[S_{02}S_{12} - S_{01}]. \quad (5)$$

This equation is written in terms of a rapidity variable Y, which is discussed in more detail shortly. The kernel K_{BK} describes the probability density for a dipole with transverse coordinates $\mathbf{x}_0$ and $\mathbf{x}_1$ to emit a gluon at the transverse coordinate $\mathbf{x}_2$. Including the running coupling corrections following Ref. [61], the kernel can be written as
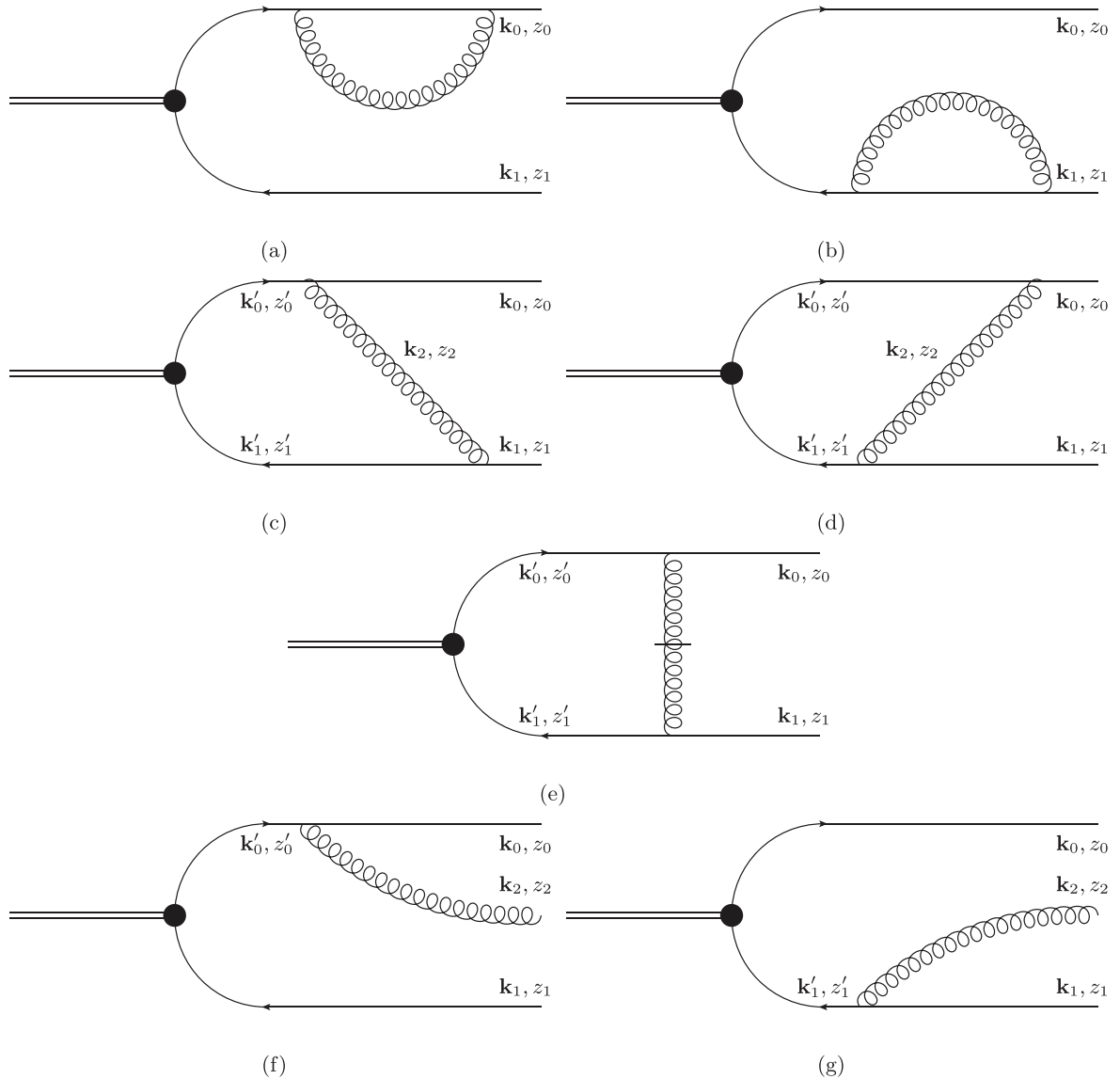
FIG. 1.   NLO corrections to the meson light-front wave function. (a) and (b) propagator corrections, (c) and (d) regular gluon exchange, (e) instantaneous gluon exchange, (f) and (g) perturbative generation of the $q\bar{q}g$ Fock state.

$$K_{\mathrm{BK}}(\mathbf{x}_0, \mathbf{x}_1, \mathbf{x}_2) = \frac{N_c \alpha_s(\mathbf{x}_{01}^2)}{2\pi^2} \left[\frac{\mathbf{x}_{01}^2}{\mathbf{x}_{21}^2 \mathbf{x}_{20}^2} + \frac{1}{\mathbf{x}_{20}^2} \left(\frac{\alpha_s(\mathbf{x}_{20}^2)}{\alpha_s(\mathbf{x}_{21}^2)} - 1 \right) \right.$$
$$\left. + \frac{1}{\mathbf{x}_{21}^2} \left(\frac{\alpha_s(\mathbf{x}_{21}^2)}{\alpha_s(\mathbf{x}_{20}^2)} - 1 \right) \right], \qquad (6)$$

where we use the notation $\mathbf{x}_{ij} = \mathbf{x}_i - \mathbf{x}_j$. The BK equation effectively resums the contributions $\alpha_s \ln 1/x \sim 1$ from small-x gluons, which is necessary for the stability of the perturbative calculations at high energy.

When higher-order corrections enhanced by large double transverse logarithms are resummed [62], the NLO BK equation [25] becomes stable and can in principle be used in phenomenological applications [27]. A usual and

numerically convenient approach, however, is to include resummations of the most important higher-order corrections to the leading-order BK equation. The leading-order BK equation with such resummations can be used to accurately approximate the full NLO BK equation [27,63]. Several resummation schemes exist, and in this work the following equations are used (we adopt the terminology used in Ref. [37]): KCBK [55], ResumBK [62,64], and TBK [65]. The nonperturbative initial conditions for these evolution equations have been determined in Ref. [37] by performing a fit to the HERA structure function data [1]. Of these, the evolution rapidity in the KCBK and ResumBK equations is the projectile rapidity $Y = \ln \frac{k^+}{P^+}$, where k^+ and P^+ are the gluon and target plus momenta. We work in the

frame where the photon plus momentum q^+ is large and the photon has no transverse momentum. The target plus momentum is obtained as $P^+ = Q_0^2/(2P^-)$, where the target transverse momentum scale is taken to be $Q_0^2 = 1$ GeV^2 (note that the photon-nucleon center-of-mass energy reads $W^2 = 2q^+P^-$).

Both KCBK ("kinematically constrained BK") and ResumBK ("resummed BK") involve a resummation of double transverse logarithms $\sim \alpha_s \ln \frac{|\mathbf{x}_{02}|}{|\mathbf{x}_{01}|} \ln \frac{|\mathbf{x}_{12}|}{|\mathbf{x}_{01}|}$, with ResumBK also resumming single transverse logarithms $\alpha_s \ln \frac{1}{\mathbf{x}_{ij}^2 Q_s^2}$ at all orders. In the KCBK equation the double logarithms are resummed by explicitly requiring a time ordering between the subsequent gluon emissions, which results in a nonlocal equation. The third evolution equation, TBK ("BK equation in target rapidity"), uses the target rapidity η as an evolution variable. This rapidity variable is related to the fraction of the target longitudinal momentum fraction transferred in the scattering process in the frame where the target has a large longitudinal momentum (see Ref. [65] for a detailed discussion). This evolution rapidity corresponds to

$$\eta = \ln \frac{1}{x_{\mathbb{P}}} = \ln \frac{W^2 + Q^2}{Q^2 + M_V^2}. \quad (7)$$

Consequently, the TBK evolution can be thought as evolution in $\ln 1/x_{\mathbb{P}}$ whereas the KCBK and ResumBK equations correspond to evolution in $\ln W^2$. In order to use dipole amplitudes as a function of the target rapidity η in the impact factors written in terms of the projectile rapidity Y, we use the same shift as in Ref. [37]:

$$\eta = Y - \ln \frac{1}{\min\{1, \mathbf{x}_{01}^2 Q_0^2\}}. \quad (8)$$

The BK equation contains a transverse-coordinate dependent coupling constant. We model the running of the coupling in the coordinate space following Ref. [37]:

$$\alpha_s(\mathbf{x}_{ij}^2) = \frac{4\pi}{\beta_0 \ln \left[\left(\frac{\mu_0^2}{\Lambda_{\text{QCD}}^2} \right)^{1/c} + \left(\frac{4C^2}{\mathbf{x}_{ij}^2 \Lambda_{\text{QCD}}^2} \right)^{1/c} \right]^c}. \quad (9)$$

This running coupling approaches a constant value in the infrared region $1/|\mathbf{x}_{ij}| \gtrsim \Lambda_{\text{QCD}}$, with the constants μ_0 and c controlling its behavior there. The values of these constants are chosen as in Ref. [37]. The constant C^2 is a fit parameter that describes the relation between momentum and coordinate spaces, $\mathbf{k}^2 = 4C^2/\mathbf{r}^2$, with the expected value $C^2 = e^{-2\gamma_E}$ from Fourier analysis [66,67]. The same coordinate space coupling constant is used when calculating the scattering amplitude, Eq. (1), where the coupling constant is included in the next-to-leading order photon and meson wave functions. As the running coupling prescription (6) can be seen to effectively choose the smallest of the three distance scales $\mathbf{x}_{01}^2, \mathbf{x}_{12}^2, \mathbf{x}_{02}^2$, when calculating the $q\bar{q}g$ contribution in Eq. (1) we choose to evaluate the coupling

at the scale set by the smallest of the daughter dipoles, as in Ref. [37]. When evaluating the $q\bar{q}$ term the scale choice is $\mathbf{x}_{01}$.

III. LIGHT-FRONT WAVE FUNCTIONS AT NEXT-TO-LEADING ORDER

The NLO corrections to exclusive vector meson production can be calculated in terms of the NLO wave functions for the photon and meson. In this section, we first list the relevant photon light-front wave functions at NLO accuracy calculated in Refs. [29–31]. Then, we proceed to calculate the light vector meson wave function at NLO in terms of the twist-2 distribution amplitude, and present the results Fourier transformed to mixed transverse coordinate, longitudinal momentum fraction space.

A. On the regularization scheme

The calculation will be done in two different regularization schemes. The first one is the conventional dimensional regularization (CDR) where the momenta and polarization vectors of all particles are continued to D dimensions. The second one is the four-dimensional helicity (FDH) scheme where the polarization vectors are kept in four dimensions [68,69]. In our case, this amounts to real gluons having two polarization states.

To do the calculations simultaneously in both schemes we follow the notation of Ref. [32]. The dimension arising from the gluon polarization vectors is denoted as D_s to distinguish it from the dimension D in the dimensional regularization. The CDR scheme corresponds to the case $D_s = D$, and for the FDH scheme we have $D_s = 4$. Sums over gluon helicities can be calculated as $\sum_\lambda \epsilon_\lambda^i \epsilon_\lambda^{j*} = \delta_{(D_s)}^{ij}$ where the subscript denotes that this Kronecker delta has $D_s - 2$ transverse dimensions. In the sums over spin and Lorenz indices we take $D_s \geq D$ so that the following relations for the Kronecker deltas hold:

$$\delta_{(D_s)}^{ij} \delta_{(D_s)}^{ij} = D_s - 2, \quad \delta_{(D)}^{ij} \delta_{(D)}^{ij} = D - 2, \quad \delta_{(D_s)}^{ij} \delta_{(D)}^{jk} = \delta_{(D)}^{ik}. \quad (10)$$

We will also make use of the following spinor identity [29]:

$$\bar{u}_{h'}(p - k)\not{\epsilon}_\lambda^*(k)u_h(p) = (\bar{v}_{h'}(p - k)\not{\epsilon}_\lambda(k)v_h(p))^*$$
$$= \frac{2p^+}{k^+}\sqrt{\frac{p^+}{p^+ - k^+}}\delta_{hh'}\epsilon_\lambda^{j*}$$
$$\times \left[\mathbf{k}^i - \frac{k^+}{p^+}\mathbf{p}^i \right] V_h^{ij}\left(\frac{k^+}{p^+} \right), \quad (11)$$

where $h = \pm 1$ is the quark helicity and

$$V_h^{ij}(z) = \left(1 - \frac{z}{2} \right)\delta_{(D_s)}^{ij} + ih\frac{z}{2}\epsilon_{(D_s)}^{ij}. \quad (12)$$

Here the D_s-dimensional Levi-Civita tensor has to be understood through the Fierz identity

$$\epsilon^{ij}_{(D_s)}\epsilon^{kl}_{(D_s)} = \delta^{ik}_{(D_s)}\delta^{jl}_{(D_s)} - \delta^{jk}_{(D_s)}\delta^{il}_{(D_s)}. \qquad (13)$$

This identity is valid in D_s dimensions if there are no more than two Levi-Civita tensors [29], which holds for the calculations considered in this paper.

B. Photon wave function

The photon light-front wave functions in the massless quark case have been calculated in Refs. [29–31] and are shown here for completeness. In our notation, an additional factor of $\frac{1}{2q^+}\prod_i \frac{1}{\sqrt{z_i}}$ appears in the wave functions. This additional factor follows from a different choice of the integration measure, which we choose to be $\prod_i \frac{d^2\mathbf{x}_i dz_i}{4\pi}$. With this choice the leading-order wave function for the virtual photon in the mixed transverse coordinate and plus momentum fraction space is

$$\Psi^{\gamma^* \to q\bar{q}}_{f,\text{LO}}(z_0, \mathbf{x}_{01}) = \frac{ee_f Q}{\pi}\delta_{\alpha_0\alpha_1}\delta_{h_0,-h_1}z_0(1-z_0)K_{\frac{D-4}{2}}(|\mathbf{x}_{01}|\overline{Q})$$
$$\times \left(\frac{\overline{Q}}{2\pi|\mathbf{x}_{01}|}\right)^{\frac{D-4}{2}}. \qquad (14)$$

We always work in the frame where the photon transverse momentum is zero. Here e_f is the fractional charge of the quark with flavor f, Q^2 is the virtuality of the photon, $z_i = k_i^+/q^+$ is the (anti)quark's fraction of the photon plus momentum, and α_i and h_i are the color and helicity indices. We also use the short-hand notation $\overline{Q}^2 = z_0(1-z_0)Q^2$. Quantities corresponding to the quark are denoted with $i = 0$ and antiquark with $i = 1$. We note that the last factor, which is equal to 1 at $D = 4$, is absent in Ref. [29] where the transverse momenta of the observed particles are kept in two dimensions. Here "observed" particles are those that appear as the final state in the wave function, not including soft or collinear particles. In this paper, we choose to evaluate the transverse momenta of the observed particles in $D - 2$ dimensions, as this is necessary for regularizing the NLO meson wave function. However, this term does not have any contribution to the final cross section where all $\frac{1}{D-4}$ divergences have been canceled. In principle, this factor multiplied by $K^{\gamma^*_L}$ contributes a finite logarithm term $\sim \ln|\mathbf{x}_{01}|$. It however cancels when we perform the UV subtraction in Sec. IV B.

The next-to-leading order correction to the photon wave function can be written as

$$\Psi^{\gamma^* \to q\bar{q}}_{f,\text{NLO}}(z_0, \mathbf{x}_{01}) = \frac{ee_f Q}{\pi}\delta_{\alpha_0\alpha_1}\delta_{h_0,-h_1}z_0(1-z_0)K_{\frac{D-4}{2}}(|\mathbf{x}_{01}|\overline{Q})\frac{\alpha_s C_F}{2\pi}K^{\gamma^*_L} \times \left(\frac{\overline{Q}}{2\pi|\mathbf{x}_{01}|}\right)^{\frac{D-4}{2}}, \qquad (15)$$

where

$$K^{\gamma^*_L} = \left[\frac{3}{2} + \ln\left(\frac{\alpha^2}{z_0(1-z_0)}\right)\right]\left[\frac{2}{4-D} + \gamma_E + \ln(\pi\mathbf{x}_{01}^2\mu^2)\right] + \frac{1}{2}\ln^2\left(\frac{z_0}{1-z_0}\right) - \frac{\pi^2}{6} + \frac{5}{2} + \frac{1}{2}\frac{D_s - 4}{D - 4}. \qquad (16)$$

Here α is the infrared cutoff for the gluon plus momentum fraction and μ is the mass scale for dimensional regularization, and the last term depends on the regularization scheme.

The virtual photon wave function for the Fock state $q\bar{q}g$ can be written as

$$\Psi^{\gamma^* \to q\bar{q}g}_f(z_i, \mathbf{x}_i) = 4ee_f Qgt^a_{\alpha_0\alpha_1}\delta_{h_0,-h_1}\frac{1}{\sqrt{z_2}}\epsilon^{j*}_{h_2}\left[z_1(1-z_1)V^{ij}_{h_0}\left(\frac{z_2}{z_0+z_2}\right)I^i_{(l)} - z_0(1-z_0)V^{ij}_{-h_0}\left(\frac{z_2}{z_1+z_2}\right)I^i_{(m)}\right], \qquad (17)$$

where

$$I^i_{(l)} = I^i(\mathbf{x}_{102}, \mathbf{x}_{20}, \overline{Q}^2_{(l)}, \omega_{(l)}), \qquad I^i_{(m)} = I^i(\mathbf{x}_{012}, \mathbf{x}_{21}, \overline{Q}^2_{(m)}, \omega_{(m)}),$$
$$\overline{Q}^2_{(l)} = z_1(1-z_1)Q^2, \qquad \overline{Q}^2_{(m)} = z_0(1-z_0)Q^2 = \overline{Q}^2,$$
$$\omega_{(l)} = \frac{z_0 z_2}{z_1(z_0+z_2)^2}, \qquad \omega_{(m)} = \frac{z_1 z_2}{z_0(z_1+z_2)^2},$$
$$\mathbf{x}_{ijk} = \mathbf{x}_{ij} - \frac{z_k}{z_j+z_k}\mathbf{x}_{kj}, \qquad (18)$$

and

$$I^i(\mathbf{b}, \mathbf{r}, \overline{Q}^2, \omega) = (4\pi^2\mu\mathbf{r}^2)^{\frac{4-D}{2}}\frac{i}{8\pi^2}\frac{\mathbf{r}^i}{\mathbf{r}^2}\int_0^\infty du\, u^{1-D/2}e^{-u\overline{Q}^2}e^{-\frac{\mathbf{b}^2}{4u}}\Gamma\left(1 + \frac{D-4}{2}, \frac{\omega\mathbf{r}^2}{4u}\right). \qquad (19)$$

Quantities with the subscript 2 correspond to the emitted gluon. The function I^i differs from the similar one in Ref. [29] by an additional power $\frac{4-D}{2}$ for the variable u, which has the same origin as the last factor in Eqs. (14) and (15).

C. Light vector meson wave function

In this section, we calculate the NLO corrections to the light vector meson light-front wave function. The calculation is done in the limit where the transverse coordinate dependence of the meson leading-order wave function can be neglected. As discussed in Sec. II, this follows from the large photon virtuality. This means that we can neglect all mass scales in the meson, allowing us to set the meson mass M_V to zero along with the transverse momenta $\mathbf{k}_i$ of the quark and the antiquark. We work in a frame where both the photon and the vector meson transverse momenta are zero, as we consider forward production. Consequently, at leading order the meson wave function is given by a delta function in the transverse plane:

$$\Psi_{f,\text{LO}}^{V\to q\bar{q}}(z_0, \mathbf{k}_0) = c_f \frac{\delta_{\alpha_0\alpha_1}}{\sqrt{N_c}} \delta_{h_0,-h_1} \frac{\pi f_V}{e_V\sqrt{N_c}} \phi_0(z_0)$$
$$\times (2\pi)^{D-2}\delta^{D-2}(\mathbf{k}_0). \tag{20}$$

Here $\phi_0(z)$ is the (bare) distribution amplitude of the meson that describes how the meson plus momentum is shared by the two quarks. This wave function is normalized in such a way that it gives the correct decay constant f_V given that the distribution amplitude is normalized as

$$\int_0^1 \mathrm{d}z\, \phi_0(z) = 1. \tag{21}$$

The decay constant f_V is related to the leptonic width by

$$\Gamma(V \to l^+l^-) = \frac{4\pi\alpha_{\text{em}}^2 f_V^2}{3M_V}. \tag{22}$$

The wave function (20) describes the probability of the meson to split into a quark-antiquark pair with the flavor f. Here c_f is a normalization factor needed for mesons that consist of a superposition of different flavored quark-antiquark states. For example, the ρ meson can be written at leading order as $|\rho\rangle = \frac{1}{\sqrt{2}}(|u\bar{u}\rangle - |d\bar{d}\rangle)$, giving us $c_u = \frac{1}{\sqrt{2}}$ and $c_d = -\frac{1}{\sqrt{2}}$. The normalization factors are also related to the effective charge fraction of the meson that is defined by $e_V = \sum_f c_f e_f$. We emphasize that in the high-Q^2 limit the dependence on the vector meson type is included in the nonperturbative distribution amplitude $\phi_0(z_0)$ (in addition to the normalization factors f_V, e_V, and c_f).

At next-to-leading order, we get perturbative corrections to the meson wave function from Feynman diagrams shown in Fig. 1. Of these, the Figs. 1(a) and 1(b), corresponding to the self-energy corrections of the quark and antiquark, evaluate to zero. This is a consequence of the dimensional regularization used in the calculation, as these diagrams give transverse integrals with no mass scales (in the high-Q^2 limit considered here where we neglect the quark and meson masses and the quark transverse momenta) such as $\int \frac{\mathrm{d}^{D-2}\mathbf{k}_0}{(2\pi)^{D-2}} \frac{1}{\mathbf{k}_0^2} = 0$.

To calculate the rest of the diagrams we use the Feynman rules of the light cone perturbation theory from Ref. [29]. For Fig. 1(c) this gives

$$\Psi_f^{1c} = \int \frac{\mathrm{d}^{D-2}\mathbf{k}_0' \mathrm{d}k_0'^+}{(2\pi)^{D-2}4\pi} \frac{1}{4k_2^+ k_0'^+ k_1'^+ (P^- - k_0^- - k_1^-)(P^- - k_0^- - k_1'^-)} \Psi_{\text{LO}}^{V\to q\bar{q}}(z_0', \mathbf{k}_0'; \alpha_0', \alpha_1', h_0', h_1') \sqrt{\frac{z'(1-z')}{z(1-z)}}$$
$$\times \mu^{4-D} g^2 t_{\alpha_0\alpha_0'}^{\alpha_2} t_{\alpha_1'\alpha_1}^{\alpha_2} \bar{u}(0)\slashed{\epsilon}_{h_2}^*(2)u(0')\bar{v}(1')\slashed{\epsilon}_{h_2}(2)v(1),$$
$$= -4\pi \frac{\alpha_s C_F}{2\pi} \frac{\mu^{4-D}}{\mathbf{k}_0^2} c_f \frac{\delta_{\alpha_0\alpha_1}}{\sqrt{N_c}} \delta_{h_0,-h_1} \frac{\pi f_V}{e_V\sqrt{N_c}}$$
$$\times \int_{z_0+\alpha}^1 \mathrm{d}z' \phi_0(z') \frac{z_0}{z'} \frac{1}{(z'-z_0)^2} \left[z'(1-z') + z_0(1-z_0) + \frac{D_s-4}{2}(z'-z_0)^2 \right], \tag{23}$$

where the identity (11) has been used to simplify the result. The square root factor in the first line comes from our choice for the integration measure, and the quark and antiquark transverse momenta after the gluon exchange are $\mathbf{k}_0$ and $\mathbf{k}_1 = -\mathbf{k}_0$. We use a notation $u(0) = u_{h_0}(k_0), v(1) = v_{h_1}(k_1)$ for the quark and antiquark spinors, and the primed quantities correspond to the intermediate quark and antiquark whose spins and helicities are summed over (see Fig. 1).

The contribution of Fig. 1(d) is similar to Fig. 1(c). An explicit calculation gives the result Eq. (23) with the substitutions $z_0 \to 1 - z_0$ and $z' \to 1 - z'$:

$$\Psi_f^{1\,d} = -4\pi \frac{\alpha_s C_F}{2\pi} \frac{\mu^{4-D}}{\mathbf{k}_0^2} c_f \frac{\delta_{\alpha_0\alpha_1}}{\sqrt{N_c}} \delta_{h_0,-h_1} \frac{\pi f_V}{e_V \sqrt{N_c}}$$

$$\times \int_0^{z_0-\alpha} \mathrm{d}z' \phi_0(z') \frac{1-z_0}{1-z'} \frac{1}{(z'-z_0)^2} \left[z'(1-z') + z_0(1-z_0) - \frac{D_s-4}{2}(z'-z_0)^2 \right]. \tag{24}$$

Here we used the symmetry condition $\phi(z') = \phi(1-z')$ that follows from the parity of the vector meson.

The final contribution to the NLO $q\bar{q}$ wave function comes from Fig. 1(e) describing an exchange of an instantaneous gluon between the quark and the antiquark. The contribution from this diagram can be evaluated to give

$$\Psi_f^{1\,e} = 8\pi \frac{\alpha_s C_F}{2\pi} \frac{\mu^{4-D}}{\mathbf{k}_0^2} c_f \frac{\delta_{\alpha_0\alpha_1}}{\sqrt{N_c}} \delta_{h_0,-h_1} \frac{\pi f_V}{e_V \sqrt{N_c}} \int_0^1 \mathrm{d}z' \phi_0(z') \frac{z_0(1-z_0)}{(z'-z_0)^2} [\theta(z'-z_0-\alpha) + \theta(z_0-z'-\alpha)]. \tag{25}$$

Summing these contributions together, we get the NLO correction to the meson $q\bar{q}$ wave function:

$$\Psi_{f,\mathrm{NLO}}^{V\to q\bar{q}}(z_0, \mathbf{k}_0) = c_f \frac{\delta_{\alpha_0\alpha_1}}{\sqrt{N_c}} \delta_{h_0,-h_1} \frac{\pi f_V}{e_V \sqrt{N_c}} \frac{\alpha_s C_F}{2\pi}$$

$$\times 4\pi \frac{\mu^{4-D}}{\mathbf{k}_0^2} \int_0^1 \mathrm{d}z' \phi_0(z') \left[\theta(z'-z_0-\alpha) \frac{z_0}{z'} \left(1 + \frac{1}{z'-z_0} \right) + \theta(z_0-z'-\alpha) \frac{1-z_0}{1-z'} \left(1 + \frac{1}{z_0-z'} \right) \right.$$

$$\left. + \frac{D_s-4}{2} \left(\frac{1-z_0}{1-z'} \theta(z_0-z') + \frac{z_0}{z'} \theta(z'-z_0) \right) \right]. \tag{26}$$

It should be noted that this NLO correction does not affect the normalization (21) of the distribution amplitude. The reason for this is that the decay constant is given by $f_V \sim \int \mathrm{d}z_0 \int \mathrm{d}^{D-2}\mathbf{k}_0 \Psi^{V\to q\bar{q}}(z_0, \mathbf{k}_0)$, and this integral vanishes for Eq. (26) in dimensional regularization.

We also need the wave function for the $q\bar{q}g$ state. This is simply given by the sum of Figs. 1(f) and 1(g), which evaluates to

$$\Psi_f^{V\to q\bar{q}g}(z_i, \mathbf{k}_i) = c_f \frac{\pi f_V}{e_V \sqrt{N_c}} \frac{2g t_{\alpha_0\alpha_1}^a}{\sqrt{N_c} z_2} \epsilon_{h_2}^{j*} \delta_{h_0,-h_1} \mu^{\frac{4-D}{2}} \frac{\mathbf{k}_2^i}{\mathbf{k}_2^2}$$

$$\times \left[(2\pi)^{D-2} \delta^{D-2}(\mathbf{k}_1) \phi_0(z_1) V_{h_0}^{ij} \left(\frac{z_2}{z_0+z_2} \right) - (2\pi)^{D-2} \delta^{D-2}(\mathbf{k}_0) \phi_0(z_0) V_{-h_0}^{ij} \left(\frac{z_2}{z_1+z_2} \right) \right]. \tag{27}$$

Note that the momentum conservation implies $z_0 + z_1 + z_2 = 1$ and $\mathbf{k}_0 + \mathbf{k}_1 + \mathbf{k}_2 = 0$.

These wave functions are presented in the momentum space. For the meson production calculation we need the mixed space wave functions, which can be calculated from the momentum space wave functions by a Fourier transform in the transverse plane. The leading-order wave function in the mixed space is given by

$$\Psi_{f,\mathrm{LO}}^{V\to q\bar{q}}(z_0, \mathbf{x}_{01}) = \int \frac{\mathrm{d}^{D-2}\mathbf{k}_0 \mathrm{d}^{D-2}\mathbf{k}_1}{(2\pi)^{2(D-2)}} e^{i(\mathbf{k}_0\cdot\mathbf{x}_0+\mathbf{k}_1\cdot\mathbf{x}_1)} (2\pi)^{D-2} \delta^{D-2}(\mathbf{k}_0+\mathbf{k}_1) \Psi_{\mathrm{LO}}^{V\to q\bar{q}}(z_0, \mathbf{k}_0),$$

$$= c_f \frac{\delta_{\alpha_0\alpha_1}}{\sqrt{N_c}} \delta_{h_0,-h_1} \frac{\pi f_V}{e_V \sqrt{N_c}} \phi_0(z_0). \tag{28}$$

The NLO correction to the $q\bar{q}$ wave function is given by

$$\Psi_{f,\mathrm{NLO}}^{V\to q\bar{q}}(z_0, \mathbf{x}_{01}) = \int \frac{\mathrm{d}^{D-2}\mathbf{k}_0 \mathrm{d}^{D-2}\mathbf{k}_1}{(2\pi)^{2(D-2)}} e^{i(\mathbf{k}_0\cdot\mathbf{x}_0+\mathbf{k}_1\cdot\mathbf{x}_1)} (2\pi)^{D-2} \delta^{D-2}(\mathbf{k}_0+\mathbf{k}_1) \Psi_{\mathrm{NLO}}^{V\to q\bar{q}}(z_0, \mathbf{k}_0),$$

$$= c_f \frac{\delta_{\alpha_0\alpha_1}}{\sqrt{N_c}} \delta_{h_0,-h_1} \frac{\pi f_V}{e_V \sqrt{N_c}} \frac{\alpha_s C_F}{2\pi} (\pi \mathbf{x}_{01}^2 \mu^2)^{\frac{4-D}{2}} \Gamma\left(\frac{D-4}{2} \right)$$

$$\times \int_0^1 \mathrm{d}z' \phi_0(z') \left[\theta(z'-z_0-\alpha) \frac{z_0}{z'} \left(1 + \frac{1}{z'-z_0} \right) + \theta(z_0-z'-\alpha) \frac{1-z_0}{1-z'} \left(1 + \frac{1}{z_0-z'} \right) \right.$$

$$\left. + \frac{D_s-4}{2} \left(\frac{1-z_0}{1-z'} \theta(z_0-z') + \frac{z_0}{z'} \theta(z'-z_0) \right) \right], \tag{29}$$

and the wave function for the $q\bar{q}g$ state is

$$
\begin{aligned}
\Psi_f^{V\to q\bar{q}g}(z_i, \mathbf{x}_i) &= \int \frac{\mathrm{d}^{D-2}\mathbf{k}_0 \mathrm{d}^{D-2}\mathbf{k}_1 \mathrm{d}^{D-2}\mathbf{k}_2}{(2\pi)^{3(D-2)}} e^{i(\mathbf{k}_0\cdot\mathbf{x}_0 + \mathbf{k}_1\cdot\mathbf{x}_1 + \mathbf{k}_2\cdot\mathbf{x}_2)} (2\pi)^{D-2}\delta^{D-2}(\mathbf{k}_0 + \mathbf{k}_1 + \mathbf{k}_2)\Psi^{V\to q\bar{q}g}(z_i, \mathbf{k}_i), \\
&= c_f \frac{\pi f_V}{e_V\sqrt{N_c}} \frac{2g t_{\alpha_0\alpha_1}^a}{\sqrt{N_c}z_2} \epsilon_{h_2}^{j*}\delta_{h_0,-h_1}\mu^{\frac{4-D}{2}} \int \frac{\mathrm{d}^{D-2}\mathbf{k}_2}{(2\pi)^{D-2}} \frac{\mathbf{k}_2^i}{\mathbf{k}_2^2} \\
&\quad \times \left[\phi_0(z_1)V_{h_0}^{ij}\left(\frac{z_2}{z_1+z_2}\right)e^{i\mathbf{k}_2\cdot\mathbf{x}_{20}} - \phi_0(z_0)V_{-h_0}^{ij}\left(\frac{z_2}{z_0+z_2}\right)e^{i\mathbf{k}_2\cdot\mathbf{x}_{21}} \right], \\
&= c_f \frac{\pi f_V}{e_V\sqrt{N_c}} \frac{2g t_{\alpha_0\alpha_1}^a}{\sqrt{N_c}z_2} \epsilon_{h_2}^{j*}\delta_{h_0,-h_1} \left[\phi_0(z_1)V_{h_0}^{ij}\left(\frac{z_2}{z_0+z_2}\right)J^i(\mathbf{x}_{20}) - \phi_0(z_0)V_{-h_0}^{ij}\left(\frac{z_2}{z_1+z_2}\right)J^i(\mathbf{x}_{21}) \right], \quad (30)
\end{aligned}
$$

where

$$
J^i(\mathbf{r}) = \frac{i}{2\pi}\frac{\mathbf{r}^i}{\mathbf{r}^2}(\pi\mu\mathbf{r}^2)^{\frac{4-D}{2}}\Gamma\left(1+\frac{D-4}{2}\right). \quad (31)
$$

IV. LIGHT VECTOR MESON PRODUCTION AT NEXT-TO-LEADING ORDER

A. Production amplitude

Having determined the NLO corrections to the meson wave function, we now have all the ingredients to calculate the exclusive light meson production amplitude. We substitute the photon wave functions for the $q\bar{q}$ [sum of Eqs. (14) and (15)] and $q\bar{q}g$ [Eq. (17)] states, along with the meson wave functions for the $q\bar{q}$ [sum of Eqs. (28) and (29)] and $q\bar{q}g$ [Eq. (30)] states, into Eq. (1) to obtain the production amplitude and keep terms up to $\mathcal{O}(\alpha_s)$. The production amplitude can then be divided into the dipole ($q\bar{q}$) and real emission ($q\bar{q}g$) parts. The dipole part contains the leading-order result

$$
-i\mathcal{A}_{\mathrm{LO}} = \frac{eQf_V}{\pi}\int_0^1 \mathrm{d}z_0 \int \mathrm{d}^{D-2}\mathbf{x}_{01} \int \mathrm{d}^{D-2}\mathbf{b} N_{01}z_0(1-z_0)K_{\frac{D-4}{2}}(|\mathbf{x}_{01}|\overline{Q})\phi_0(z_0) \times \left(\frac{\overline{Q}}{2\pi|\mathbf{x}_{01}|}\right)^{\frac{D-4}{2}}, \quad (32)
$$

and the NLO correction

$$
\begin{aligned}
-i\mathcal{A}_{\mathrm{NLO}}^{q\bar{q}} &= \frac{eQf_V}{\pi}\frac{\alpha_s C_F}{2\pi}\int_0^1 \mathrm{d}z_0 \int \mathrm{d}^{D-2}\mathbf{x}_{01} \int \mathrm{d}^{D-2}\mathbf{b} N_{01}z_0(1-z_0)K_{\frac{D-4}{2}}(\mathbf{x}_{01}\overline{Q}) \times \left(\frac{\overline{Q}}{2\pi|\mathbf{x}_{01}|}\right)^{\frac{D-4}{2}} \\
&\quad \times \left\{ (\pi\mathbf{x}_{01}^2\mu^2)^{\frac{4-D}{2}}\Gamma\left(\frac{D-4}{2}\right)\int_0^1 \mathrm{d}z'\phi_0(z')\left[\theta(z'-z_0-\alpha)\frac{z_0}{z'}\left(1+\frac{1}{z'-z_0}\right) + \theta(z_0-z'-\alpha)\frac{1-z_0}{1-z'}\left(1+\frac{1}{z_0-z'}\right)\right] \right. \\
&\quad \left. + \phi_0(z_0)K^{\gamma_L^*} + \frac{D_s-4}{D-4}\int_0^1 \mathrm{d}z'\phi_0(z')\left[\frac{1-z_0}{1-z'}\theta(z_0-z') + \frac{z_0}{z'}\theta(z'-z_0)\right] \right\}, \quad (33)
\end{aligned}
$$

where $\mathbf{b} = (\mathbf{x}_0 + \mathbf{x}_1)/2$. The real emission part reads

$$
\begin{aligned}
-i\mathcal{A}^{q\bar{q}g} &= \frac{eQf_V}{\pi}\frac{\alpha_s C_F}{2\pi}\int_0^1 \mathrm{d}z_0 \int \mathrm{d}^{D-2}\mathbf{x}_{01} \int \mathrm{d}^{D-2}\mathbf{b} \int_\alpha^{1-z_0} \mathrm{d}z_2 \int \mathrm{d}^{D-2}\mathbf{x}_{20}N_{012} \\
&\quad \times \frac{-8\pi^2}{z_2}\left\{ \phi_0(z_1)J^i(\mathbf{x}_{20})\frac{1}{1-z_1}[z_1(z_0^2+(1-z_1)^2)I_{(l)}^i - z_0(z_0(1-z_0)+z_1(1-z_1))I_{(m)}^i] \right. \\
&\quad + \phi_0(z_0)J^i(\mathbf{x}_{21})\frac{1}{1-z_0}[z_0(z_1^2+(1-z_0)^2)I_{(m)}^i - z_1(z_0(1-z_0)+z_1(1-z_1))I_{(l)}^i] \\
&\quad \left. + \frac{D_s-4}{2}z_2^2\left[\phi_0(z_1)\frac{z_1}{1-z_1}J^i(\mathbf{x}_{20})I_{(l)}^i + \phi_0(z_0)\frac{z_0}{1-z_0}J^i(\mathbf{x}_{21})I_{(m)}^i\right] \right\}, \quad (34)
\end{aligned}
$$

where $\mathbf{b} = z_0\mathbf{x}_0 + z_1\mathbf{x}_1 + z_2\mathbf{x}_2$. These choices for the impact parameter $\mathbf{b}$ follow Ref. [37], but we note that in the $t=0$ case the weighting of the coordinates by the momentum fractions z_i in the definition of $\mathbf{b}$ does not affect the results.

The coherent vector meson V electroproduction cross section (2) can now be evaluated using the scattering amplitude

$$i\mathcal{A} = i\mathcal{A}_{\text{LO}}^{q\bar{q}} + i\mathcal{A}_{\text{NLO}}^{q\bar{q}} + i\mathcal{A}^{q\bar{q}g}. \qquad (35)$$

When squaring the amplitude, we keep terms up to $\mathcal{O}(\alpha_s)$. However, the $i\mathcal{A}^{q\bar{q}g}$ amplitude also contains a large contribution enhanced by a large logarithm $\ln 1/z_2 \sim 1/\alpha_s$, and as such this contribution has to be considered as being part of the leading order amplitude. This is in practice done by

taking into account the BK evolution as we will discuss in more detail in Secs. IV D and V.

B. UV subtraction

The dipole $(-i\mathcal{A}_{\text{NLO}}^{q\bar{q}})$ and real emission $(-i\mathcal{A}^{q\bar{q}g})$ parts of the amplitude are separately UV divergent. However, most of the divergences cancel in their sum. Therefore it is useful to subtract the UV divergent part of the real emission and combine it with the dipole part. The subtracted term is chosen to be

$$-i\mathcal{A}_{\text{UV}}^{q\bar{q}g} = \frac{eQf_V}{\pi}\frac{\alpha_s C_F}{2\pi}\int_0^1 dz_0 \int d^{D-2}\mathbf{x}_{01} \int d^{D-2}\mathbf{b} \int_\alpha^{1-z_0} dz_2 \int d^{D-2}\mathbf{x}_{20} N_{01}$$
$$\times \frac{-8\pi^2}{z_2}\left\{ \phi_0(z_1)J^i(\mathbf{x}_{20})I_{\text{UV}}^i(\mathbf{x}_{20}, z_1(1-z_1)Q^2)\frac{z_1}{1-z_1}(z_0^2 + (1-z_1)^2) \right.$$
$$+ \phi_0(z_0)J^i(\mathbf{x}_{21})I_{\text{UV}}^i(\mathbf{x}_{21}, z_0(1-z_0)Q^2)\frac{z_0}{1-z_0}(z_1^2 + (1-z_0)^2)$$
$$\left. + \frac{D_s-4}{2}z_2^2\left[\phi_0(z_1)\frac{z_1}{1-z_1}J^i(\mathbf{x}_{20})I_{(l)}^i + \phi_0(z_0)\frac{z_0}{1-z_0}J^i(\mathbf{x}_{21})I_{(m)}^i \right] \right\}, \qquad (36)$$

where

$$I_{\text{UV}}^i(\mathbf{r}, \overline{Q}^2) = \frac{i}{4\pi^2}(\pi\mu\mathbf{r}^2)^{\frac{4-D}{2}}\frac{\mathbf{r}^i}{\mathbf{r}^2}\Gamma\left(1 + \frac{D-4}{2}\right)e^{-\frac{\mathbf{r}^2}{\mathbf{x}_{01}^2 e^{\gamma_E}}}K_{\frac{D-4}{2}}(|\mathbf{x}_{01}|\overline{Q}) \times \left(\frac{\overline{Q}}{2\pi|\mathbf{x}_{01}|}\right)^{\frac{D-4}{2}}. \qquad (37)$$

This choice for the UV subtraction term is analogous to the one in Ref. [29] and also what is used when considering heavy vector meson production in Ref. [41]. Unlike in Ref. [29], we choose to include the additional factor $\left(\frac{\overline{Q}}{2\pi|\mathbf{x}_{01}|}\right)^{\frac{D-4}{2}}$ to the UV subtraction to cancel the same factor in the dipole part.

The integrals over $\mathbf{x}_{20}$ and z_2 can be done analytically, which simplifies the UV subtraction term to

$$-i\mathcal{A}_{\text{UV}}^{q\bar{q}g} = -\frac{eQf_V}{\pi}\frac{\alpha_s C_F}{2\pi}\int_0^1 dz_0 \int d^{D-2}\mathbf{x}_{01} \int d^{D-2}\mathbf{b} N_{01}\phi_0(z_0)z_0(1-z_0)K_{\frac{D-4}{2}}(\mathbf{x}_{01}\overline{Q}) \times \left(\frac{\overline{Q}}{2\pi|\mathbf{x}_{01}|}\right)^{\frac{D-4}{2}}$$
$$\times \left\{ \Gamma\left(1 + \frac{D-4}{2}\right)\Gamma\left(\frac{4-D}{2}\right)(\pi\mu^2\mathbf{x}_{01}^2 e^{\gamma_E})^{\frac{4-D}{2}}\left[3 + 2\ln\left(\frac{\alpha^2}{z_0(1-z_0)}\right)\right] + \frac{D_s-4}{D-4} \right\}. \qquad (38)$$

We then add this to the dipole part, which gives us

$$-i\mathcal{A}_{\text{sub}}^{q\bar{q}} = \frac{eQf_V}{\pi}\int_0^1 dz_0 \int d^{D-2}\mathbf{x}_{01} \int d^{D-2}\mathbf{b} N_{01}z_0(1-z_0)K_{\frac{D-4}{2}}(\mathbf{x}_{01}\overline{Q}) \times \left(\frac{\overline{Q}}{2\pi|\mathbf{x}_{01}|}\right)^{\frac{D-4}{2}}$$
$$\times \int_0^1 dz'\phi_0(z')\left\{ \delta(z_0 - z') \right.$$
$$+ \frac{\alpha_s C_F}{2\pi}\left[K(z_0, z')\left(\frac{2}{D-4} - \ln(\pi\mu^2\mathbf{x}_{01}^2 e^{\gamma_E})\right) + \delta(z_0 - z')\left(\frac{1}{2}\ln^2\left(\frac{z_0}{1-z_0}\right) - \frac{\pi^2}{6} + \frac{5}{2}\right) \right]$$
$$\left. + \frac{\alpha_s C_F}{2\pi}\frac{D_s-4}{D-4}\left[-\frac{1}{2}\delta(z_0 - z') + \frac{1-z_0}{1-z'}\theta(z_0 - z') + \frac{z_0}{z'}\theta(z' - z_0) \right] \right\}. \qquad (39)$$

Here $K(z, z')$ is the kernel of the ERBL equation [20,56], which describes the scale dependence of the distribution amplitude as we will discuss in Sec. IV C:

$$K(z, z') = \frac{z}{z'}\left(1 + \frac{1}{z' - z}\right)\theta(z' - z - \alpha) + \frac{1 - z}{1 - z'}\left(1 + \frac{1}{z - z'}\right)\theta(z - z' - \alpha) + \left(\frac{3}{2} + \ln\left(\frac{\alpha^2}{z(1 - z)}\right)\right)\delta(z' - z). \quad (40)$$

This form for the ERBL kernel is equivalent to the usual one written in terms of the plus distributions in the limit $\alpha \to 0$.

After the UV subtraction, the real emission part becomes finite and reads:

$$-i\mathcal{A}_{\text{sub}}^{q\bar{q}g} = \frac{eQf_V}{\pi}\frac{\alpha_s C_F}{2\pi}\int_0^1 dz_0 \int d^2\mathbf{x}_{01} \int d^2\mathbf{b}\int_\alpha^{1-z_0} dz_2 \int d^2\mathbf{x}_{20}\frac{2}{\pi z_2}\phi_0(z_0)$$

$$\times\left\{N_{012}K_0(RQ)\frac{1}{1-z_0}\left[z_0((1 - z_0 - z_2)^2 + (1 - z_0)^2)\frac{1}{\mathbf{x}_{21}^2} - (1 - z_0 - z_2)(z_0(1 - z_0))\right.\right.$$

$$\left.+ (1 - z_0 - z_2)(z_0 + z_2))\frac{\mathbf{x}_{20}\cdot\mathbf{x}_{21}}{\mathbf{x}_{20}^2\mathbf{x}_{21}^2}\right] - N_{01}\frac{z_0}{1 - z_0}((1 - z_0 - z_2)^2 + (1 - z_0)^2)\frac{1}{\mathbf{x}_{21}^2}e^{-\frac{\mathbf{x}_{21}^2}{\mathbf{x}_{01}^2 e^{\gamma_E}}}K_0(\mathbf{x}_{01}\bar{Q})\right\}, \quad (41)$$

where $R^2 = z_0 z_1\mathbf{x}_{01}^2 + z_1 z_2\mathbf{x}_{21}^2 + z_0 z_2\mathbf{x}_{20}^2$.

C. ERBL evolution and the renormalized distribution amplitude

The dipole part $-i\mathcal{A}_{\text{sub}}^{q\bar{q}}$, Eq. (39), still contains a divergence of the form $\frac{1}{D-4}$, which is canceled when the distribution amplitude is renormalized. We define the renormalized distribution amplitude $\phi(z, \mu_F)$ as

$$\phi(z, \mu_F) = \phi_0(z) + \frac{\alpha_s C_F}{2\pi}\int_0^1 dz' K(z, z')\phi_0(z')$$

$$\times\left(\frac{2}{D-4} + \gamma_E - \ln(4\pi) + \ln\left(\frac{\mu_F^2}{\mu^2}\right)\right), \quad (42)$$

where μ_F is the factorization scale. This choice for the finite terms in the subtraction corresponds to the $\overline{\text{MS}}$ scheme. We note that the distribution amplitude depends on the regularization scheme (FDH or CDR), as in practice it has to be determined from some experimental process for which an NLO calculation also depends on the same scheme choice. In principle the scheme-dependent term $\sim (D_s - 4)/(D - 4)$ in Eq. (39) could be also included in the definition

of the renormalized distribution amplitude (42). However, in this work we choose to keep the scheme dependence explicitly visible in the dipole term, Eq. (39). This allows us to straightforwardly quantify the scheme dependence which is shown in the Appendix to be negligible.

The renormalized distribution amplitude satisfies the ERBL evolution equation [20,56]

$$\frac{\partial\phi(z, \mu_F)}{\partial\ln\mu_F^2} = \frac{\alpha_s C_F}{2\pi}\int_0^1 dz' K(z, z')\phi(z', \mu_F), \quad (43)$$

where the kernel $K(z, z')$ is given in Eq. (40). We note that this renormalization does not change Eq. (21) for the normalization of the distribution amplitude as the z integral over the ERBL kernel vanishes: $\int_0^1 dz K(z, z') = 0$.

Next we use Eq. (42) to write the bare distribution amplitude $\phi_0(z)$ in $-i\mathcal{A}_{\text{sub}}^{q\bar{q}}$, Eq. (39), in terms of the renormalized distribution amplitude. We also choose to use the scale dependent renormalized distribution amplitude instead of the bare distribution in the NLO part, as their difference is now formally higher order in α_s. This results in the finite expression

$$-i\mathcal{A}_{\text{fin}}^{q\bar{q}} = \frac{eQf_V}{\pi}\int_0^1 dz_0 \int d^2\mathbf{x}_{01} \int d^2\mathbf{b}N_{01}z_0(1 - z_0)K_0(\mathbf{x}_{01}\overline{Q})$$

$$\times\int_0^1 dz'\phi(z', \mu_F)\left\{\delta(z_0 - z') + \frac{\alpha_s C_F}{2\pi}\left[-K(z_0, z')\ln\left(\frac{\mu_F^2\mathbf{x}_{01}^2 e^{2\gamma_E}}{4}\right) + \delta(z_0 - z')\left(\frac{1}{2}\ln^2\left(\frac{z_0}{1 - z_0}\right) - \frac{\pi^2}{6} + \frac{5}{2}\right)\right]\right.$$

$$\left.+ \frac{\alpha_s C_F}{2\pi}\frac{D_s - 4}{D - 4}\left[-\frac{1}{2}\delta(z_0 - z') + \frac{1 - z_0}{1 - z'}\theta(z_0 - z') + \frac{z_0}{z'}\theta(z' - z_0)\right]\right\}. \quad (44)$$

Similarly we can replace $\phi_0(z)$ by $\phi(z, \mu_F)$ in the real emission part (41).

Let us briefly consider the evolution of the renormalized distribution amplitude. It is useful to write the distribution amplitude in terms of the eigenfunctions $f_n(z)$ of the ERBL kernel

$$\int_0^1 dz' K(z, z')f_n(z') = \lambda_n f_n(z). \quad (45)$$

The eigenfunctions can be written in terms of the Gegenbauer polynomials $C_n^{(\frac{3}{2})}$ as $f_n(z) = 6z(1 - z)C_n^{(\frac{3}{2})}(2z - 1)$, and the corresponding eigenvalues are given by [20]

$$\lambda_n = -\frac{1}{2} + \frac{1}{(n+1)(n+2)} - 2\sum_{k=2}^{n+1}\frac{1}{k}. \tag{46}$$

Writing the distribution amplitude as a sum of the eigenfunctions, the ERBL equation then tells us that the coefficients in the sum depend on the factorization scale:

$$\phi(z,\mu_F) = \sum_{n=0}^{\infty} a_n(\mu_F)f_n(z). \tag{47}$$

Taking into account the running of the coupling constant as $\alpha_s(\mu_F^2) = \frac{4\pi}{\beta\ln(\mu_F^2/\Lambda_{\text{QCD}}^2)}$, we can solve the evolution of the coefficients a_n explicitly [20]:

$$a_n(\mu_F) = a_n \ln\left(\frac{\mu_F^2}{\Lambda_{\text{QCD}}^2}\right)^{\frac{2C_F}{\beta}\lambda_n}. \tag{48}$$

Here $\Lambda_{\text{QCD}} = 0.241\,\text{GeV}$ and $\beta = (11N_c - 2N_f)/3$ with $N_f = 3$. Values for the coefficients a_n at an initial scale are a nonperturbative input for the calculation. These coefficients also depend on the considered vector meson, and should be determined from experimental data. It should be noted that the eigenvalue λ_n is zero for the term $n = 0$ and negative for the $n > 0$ terms. This means that the first term is actually constant in μ_F, and the higher-order terms become suppressed as μ_F increases. In the asymptotic limit $\mu_F \to \infty$ only the first term contributes, and the distribution amplitude then simplifies to $\phi(z, \mu_F = \infty) = 6z(1-z)$. Here we have also used the fact that the coefficient a_0 of the first term is actually determined by the normalization condition Eq. (21), as the orthogonality of the Gegenbauer polynomials guarantees that only the first term contributes to the normalization, giving us $a_0 = 1$. It should also be noted that parity conservation demands that the distribution amplitude is invariant under the substitution $z \leftrightarrow 1 - z$, meaning that all terms with $n = $ odd are zero in the sum.

We point out that Eq. (48) is divergent for $\mu_F = \Lambda_{\text{QCD}}$. In practice, we avoid this singularity by introducing an infrared (IR) cutoff μ_{F0} for the ERBL evolution and freeze the distribution amplitude below this scale: $\phi(z,\mu_F) = \phi(z,\mu_{F0})$ for $\mu_F < \mu_{F0}$. We choose the value of the IR cutoff to be $\mu_{F0} = 1$ GeV. The dependence on the IR cutoff is quantified in the Appendix.

D. Soft gluon divergence

The real emission part still has an IR divergence from the lower limit α of the z_2 integral. This is related to the emission of soft gluons from the dipole, and to the rapidity evolution of the dipole amplitude. This can be seen by noting that the singular part of the real emission can be written as

$$-i\mathcal{A}_{\text{sing}}^{q\bar{q}g} = \frac{eQf_V}{\pi}\int_0^1 dz_0 \int d^2\mathbf{x}_{01} \int d^2\mathbf{b}\phi(z_0,\mu_F)z_0(1-z_0)$$
$$\times K_0(|\mathbf{x}_{01}|\overline{Q})\frac{\alpha_s C_F}{2\pi}\int_{z_{\text{min}}}^{1-z_0} dz_2 \int d^2\mathbf{x}_{20}\frac{2}{\pi z_2}$$
$$\times [N_{012} - N_{01}]\frac{\mathbf{x}_{01}^2}{\mathbf{x}_{20}^2\mathbf{x}_{21}^2}, \tag{49}$$

where the identity [29]

$$\int d^2\mathbf{x}_2 \left[\frac{\mathbf{x}_{01}^2}{\mathbf{x}_{20}^2\mathbf{x}_{21}^2} - \frac{1}{\mathbf{x}_{20}^2}e^{-\mathbf{x}_{20}^2/(\mathbf{x}_{01}^2 e^{\gamma_E})} - \frac{1}{\mathbf{x}_{21}^2}e^{-\mathbf{x}_{21}^2/(\mathbf{x}_{01}^2 e^{\gamma_E})}\right] = 0 \tag{50}$$

has been used. Note that as we do not have an explicit dependence on the infrared cutoff α in the integrands anymore, from now on the lower limit of the z_2 integral is denoted by z_{min} whose value will be discussed shortly. We can recognize the integrand in Eq. (49) as the kernel of the (fixed coupling leading order) BK equation (5). This can then be combined with the leading-order term [α_s^0 part of Eq. (44)], and the sum of these two contributions corresponds to using in the leading-order term a dipole amplitude evolved from the initial rapidity Y_0 to the rapidity

$$Y_{\text{dip}} = Y_0 + \ln\frac{1-z_0}{z_{\text{min}}}. \tag{51}$$

At finite center-of-mass energy the lower limit z_{min} of the z_2 integral should not be taken to zero. In particular, the invariant mass of the $q\bar{q}g$ system should be much less than W^2 in order to justify the usage of the eikonal approximation, which imposes the lower limit z_{min}. We follow Refs. [37,41] and choose

$$z_{\text{min}} = \min\left(e^{Y_0}\frac{Q_0^2}{W^2 + Q^2 - m_N^2}, 1 - z_0\right). \tag{52}$$

Here the minimum comes from the kinematic constraint $z_0 + z_2 \le 1$, which guarantees that the dipole does not evolve backwards in rapidity. As we are interested in the high (but finite) energy limit, the minimum is only needed in a small subset of the integration region and in practice the evolved rapidity is

$$Y_{\text{dip}} = \ln\left((1-z_0)\frac{W^2 + Q^2 - m_N^2}{Q_0^2}\right). \tag{53}$$

For the α_s-suppressed terms the dependence on the evolution rapidity is formally of higher order in the coupling constant. Following again Refs. [37,41] we choose to use the same evolution rapidity Y_{dip} when evaluating the next-to-leading order terms in the dipole part, Eq. (44). The z_2-dependent evolution rapidity used with real gluon emission term is obtained from the definition $Y = \ln\frac{k^+}{P^+}$ and can be written as [41]

$$Y_{q\bar{q}g} = \ln z_2 + \ln\frac{W^2 + Q^2 - m_N^2}{Q_0^2}. \tag{54}$$

E. Full result

We can now write the scattering amplitude for light meson electroproduction in its full form. It reads

$$
-i\mathcal{A} = \frac{eQf_V}{\pi} \int d^2\mathbf{x}_{01} \int d^2\mathbf{b} \int_0^1 dz_0 \left\{ \mathcal{K}_{q\bar{q}}^{\mathrm{LO}}(Y_0) + \frac{\alpha_s C_F}{2\pi} \mathcal{K}_{q\bar{q}}^{\mathrm{NLO}}(Y_{\mathrm{dip}}) + \int d^2\mathbf{x}_{20} \int_{z_{\min}}^{1-z_0} dz_2 \frac{\alpha_s C_F}{2\pi} \mathcal{K}_{q\bar{q}g}(Y_{q\bar{q}g}) \right\}, \quad (55)
$$

where the LO part is

$$
\mathcal{K}_{q\bar{q}}^{\mathrm{LO}}(Y_0) = N_{01}(Y_0) z_0 (1-z_0) K_0(|\mathbf{x}_{01}|\overline{Q}) \phi(z_0, \mu_F), \quad (56)
$$

and the NLO corrections are

$$
\begin{aligned}
\mathcal{K}_{q\bar{q}}^{\mathrm{NLO}}(Y_{\mathrm{dip}}) = {}& N_{01}(Y_{\mathrm{dip}}) z_0 (1-z_0) K_0(|\mathbf{x}_{01}|\overline{Q}) \Bigg\{ \phi(z_0, \mu_F) \left(\frac{1}{2} \ln^2\left(\frac{z_0}{1-z_0}\right) - \frac{\pi^2}{6} + \frac{5}{2} \right) \\
& - \ln\left(\frac{\mu_F^2 \mathbf{x}_{01}^2 e^{2\gamma_E}}{4} \right) \int_0^1 dz' K(z_0, z') \phi(z', \mu_F) \\
& + \frac{D_s - 4}{D - 4} \int_0^1 dz' \phi(z', \mu_F) \left[-\frac{1}{2} \delta(z_0 - z') + \frac{1 - z_0}{1 - z'} \theta(z_0 - z') + \frac{z_0}{z'} \theta(z' - z_0) \right] \Bigg\}
\end{aligned} \quad (57)
$$

for the dipole part and

$$
\begin{aligned}
\mathcal{K}_{q\bar{q}g}(Y_{q\bar{q}g}) = {}& \frac{2}{\pi z_2} \phi(z_0, \mu_F) \Bigg\{ N_{012}(Y_{q\bar{q}g}) K_0(RQ) \frac{1}{1-z_0} \left[z_0 ((1-z_0-z_2)^2 + (1-z_0)^2) \frac{1}{\mathbf{x}_{21}^2} \right. \\
& \left. - (1-z_0-z_2)(z_0(1-z_0) + (1-z_0-z_2)(z_0+z_2)) \frac{\mathbf{x}_{20} \cdot \mathbf{x}_{21}}{\mathbf{x}_{20}^2 \mathbf{x}_{21}^2} \right] \\
& - N_{01}(Y_{q\bar{q}g}) \frac{z_0}{1-z_0} ((1-z_0-z_2)^2 + (1-z_0)^2) \frac{1}{\mathbf{x}_{21}^2} e^{-\frac{\mathbf{x}_{21}^2}{\mathbf{x}_{01}^2 e^{\gamma_E}}} K_0(\mathbf{x}_{01}\overline{Q}) \Bigg\}
\end{aligned} \quad (58)
$$

for the real emission. The lower limit for the z_2 integral is given by Eq. (52). This expression is finite and suitable for numerical evaluation. The rapidity scales at which the different dipole amplitudes are evaluated, Y_0, Y_{dip}, and $Y_{q\bar{q}g}$, are shown explicitly. In numerical calculations we follow Ref. [37] and take $Y_0 = 0$.

The NLO correction to the dipole part has a dependence on the regularization scheme given by a term proportional to

$$
\frac{D_s - 4}{D - 4} = \begin{cases} 1 \text{ for CDR} \\ 0 \text{ for FDH} \end{cases}. \quad (59)
$$

This regularization scheme dependence is in principle canceled by the regularization scheme dependence of the distribution amplitude at the given order in α_s. The distribution amplitude is a nonperturbative quantity that has to be determined from some process where the same regularization scheme dependence should also appear. In this paper, we choose to use the CDR regularization scheme when we show numerical results in Sec. V. However, it will turn out that the regularization scheme dependence is very small even if the same distribution amplitude is used in both

schemes, which is a consequence of the fact that for the first term in the Gegenbauer expansion (47) of the distribution amplitude this regularization scheme dependent term vanishes. The regularization scheme dependence of the cross section will be discussed quantitatively in the Appendix.

The dependence on the factorization scale μ_F is of higher order in α_s, as can be verified by taking into account the ERBL equation. However, as we are keeping terms only to the order α_s, the results do have a dependence on the factorization scale. The value of μ_F can be chosen in different ways. Equation (44) suggests the choice $\mu_F^2 = 4e^{-2\gamma_E}/\mathbf{x}_{01}^2$, as with this choice the logarithm multiplying the ERBL kernel $K(z, z')$ vanishes (we will refer to this term as the "ERBL term"). Note that the factor $4e^{-2\gamma_E}$ is the same one that appears in the Fourier analysis of the coordinate space running coupling [66,67]. This choice for the factorization scale will be referred to as the r scheme to emphasize its dependence on the dipole size. In the $q\bar{q}g$ term we choose to use the smallest dipole size $\min\{|\mathbf{x}_{01}|, |\mathbf{x}_{20}|, |\mathbf{x}_{21}|\}$ for the factorization scale, in accordance with the running of the coupling constant α_s. Another possible choice for the factorization scale is to use $\mu_F = Q$, which is supported by the fact that the relevant length scales

for meson production are $Q \sim 1/|\mathbf{x}_{01}|$, meaning that the logarithm $\ln(Q^2 \mathbf{x}_{01}^2)$ of the ERBL term in Eq. (44) should also be small in this scheme. This will be referred to as the Q scheme, and its main advantage is that the hard scale does not depend on the integration variable. In this paper, we will use the r scheme in our calculations as then the ERBL term vanishes completely. In the Q scheme, there can in practice be a large contribution from the ERBL term as the dipole amplitude amplifies the contribution of larger dipoles that can have a numerically significant contribution even at moderately large virtualities [70,71]. This scheme dependence is studied in more detail in the Appendix, where it is shown that the factorization scale dependence at the cross section level is a few percent.

The result (55) can be compared to the previously calculated NLO light vector meson production from Ref. [53]. In that paper the production amplitude is presented in the momentum space as opposed to the mixed space used in this paper. Comparing these results is nontrivial, as one has to perform complicated Fourier transforms from momentum space to coordinate space to match the results. We have only been able to make comparisons for the dipole part of the amplitude, finding that the result of Ref. [53] matches our result in the CDR scheme apart from differences in the UV subtraction procedure. The real gluon emission part is much more complicated, and so far we have not been able to make actual comparisons of the results.

V. NUMERICAL RESULTS

In this section, we present numerical results for coherent light vector meson electroproduction at next-to-leading order, calculated using Eq. (55). As our default setup, we use the CDR scheme for regularization and r scheme for the factorization scale μ_F. For the distribution amplitude, we choose to keep only the first two terms in the Gegenbauer expansion (47). The reason for this is that the

exact values for the higher-order terms are not well known but estimated to be small [72]. For the ρ meson, the coefficient of the second term has been extracted in many different ways, with relatively large uncertainties [73]. We choose to use the value $a_2(\mu_F = 1 \text{ GeV}) = 0.1$, which is in agreement with most of the values tabulated in Ref. [73]. We also choose to use this same value for the ϕ meson, as current analyses suggest that they are of the same order of magnitude [57,72]. As we then use the same distribution amplitude for both mesons, the only difference between ρ and ϕ production is the decay constant f_V, which appears as an overall coefficient in Eq. (55). These decay constants can be calculated from the experimental values for the leptonic widths [74] using Eq. (22).

The numerical results are calculated using the dipole amplitude fits from Refs. [37,75] for the different schemes of the BK evolution equation discussed in Sec. II C. We use the fits where the "Balitsky + smallest dipole" running coupling scheme is used, and use both fits with initial evolution rapidities $Y_{0,\text{BK}}, \eta_{0,\text{BK}} = 0$ and $Y_{0,\text{BK}}, \eta_{0,\text{BK}} = 4.61$ (in which case the dipole amplitude is frozen in the region $Y_0 = 0 < Y < Y_{0,\text{BK}}$ or $\eta_0 = 0 < \eta < \eta_{0,\text{BK}}$). In these fits the impact parameter dependence is assumed to factorize and one can replace $\int d^2\mathbf{b} \to \sigma_0/2$, and the proton transverse area $\sigma_0/2$ is a fit parameter which is also determined in Ref. [37].

In Fig. 2, we show different contributions to the exclusive ρ production amplitude at NLO as a function of the center-of-mass energy W [Fig. 2(a)] and photon virtuality Q^2 [Fig. 2(b)]. The same dipole amplitude, corresponding to the KCBK equation with the initial rapidity $Y_{0,\text{BK}} = 4.61$ for the BK evolution [37], is used in these figures. Here the leading-order result is denoted by $\text{LO}(Y_{\text{dip}})$, which is calculated from the leading-order part of Eq. (55) with the dipole amplitude evaluated at rapidity Y_{dip}. Using the evolved rapidity Y_{dip} means that the $\text{LO}(Y_{\text{dip}})$ contains the resummation of large logarithms $\sim \alpha_s \ln 1/x$ included in the BK evolution. The result $\text{LO}(Y_0)$
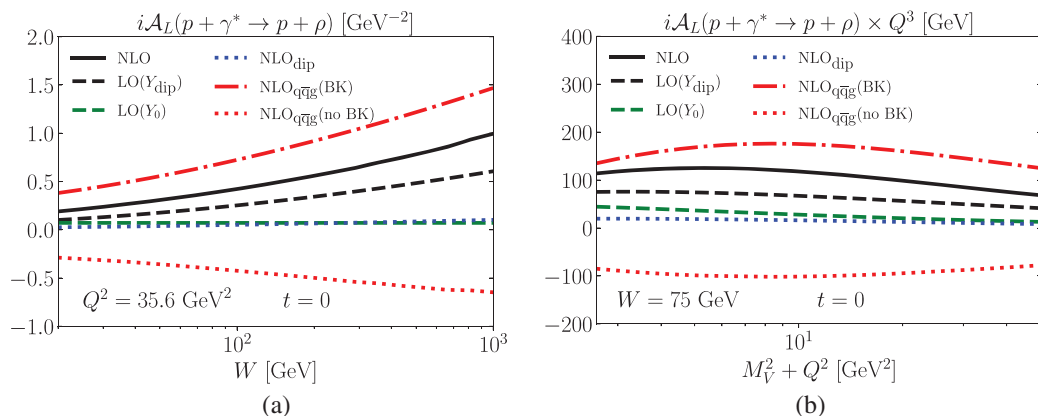

FIG. 2. Different parts of the longitudinal NLO amplitude for exclusive ρ production. (a) Dependence on the center-of-mass energy of the $\gamma^* - p$ system. (b) Dependence on the photon virtuality Q^2. The amplitude has been scaled by Q^3 for easier readability.

is the leading-order term of Eq. (55) at the initial rapidity Y_0, and $\mathrm{NLO_{dip}}$ is the NLO correction to the dipole term corresponding to Eq. (57). The contribution from the $q\bar{q}g$ term, Eq. (58), has been divided into two parts: the result $\mathrm{NLO_{q\bar{q}g}}(\mathrm{BK})$ contains only the part corresponding to the BK equation, Eq. (49), and $\mathrm{NLO_{q\bar{q}g}}(\mathrm{no\ BK})$ is Eq. (58) from which the BK contribution has been subtracted. The total NLO result is then the sum

$$\mathrm{NLO} = \mathrm{LO}(Y_0) + \mathrm{NLO_{dip}} + \mathrm{NLO_{q\bar{q}g}}(\mathrm{BK}) + \mathrm{NLO_{q\bar{q}g}}(\mathrm{no\ BK}). \tag{60}$$

From these plots we see that the contributions from the LO result at the initial rapidity and from the NLO dipole term are small. Both $q\bar{q}g$ contributions are large, but they mainly cancel each other. These findings are similar to what has been observed in the case of heavy vector meson production [41]. The total NLO correction, the difference between NLO and $\mathrm{LO}(Y_{\mathrm{dip}})$, is large and positive. However, we point out that in these plots the same NLO fitted dipole amplitude was used to calculate all of the results. Consequently, these results only quantify the largeness of the NLO correction terms in Eq. (55) and not the actual difference between the NLO and LO results where the corresponding dipole amplitude fits should be used.

We also note that at fixed coupling the identification $\mathrm{LO}(Y_{\mathrm{dip}}) = \mathrm{LO}(Y_0) + \mathrm{NLO_{q\bar{q}g}}(\mathrm{BK})$ would be exact if the dipole amplitude satisfied the leading-order fixed coupling BK equation. In that case there would be no ambiguity in defining the leading-order amplitude. In our setup this is not the case, and consequently the leading-order amplitude is not uniquely defined. In this work we choose it to be $\mathrm{LO}(Y_{\mathrm{dip}})$ following Ref. [41], as this is the most natural choice when using a dipole amplitude that satisfies a resummed BK evolution equation. Identifying $\mathrm{LO}(Y_0) + \mathrm{NLO_{q\bar{q}g}}(\mathrm{BK})$ as a leading order term instead would have maximally a $\sim 20\%$ effect on the calculated cross sections discussed below.

Next we show numerical comparisons to the existing coherent vector meson production data for ρ and ϕ mesons at (moderately) large Q^2. The H1 data is from Ref. [59], and the ZEUS data is from Ref. [76] for ϕ and Ref. [77] for ρ. The results are shown with various different dipole amplitude fits that all give a good description of the HERA structure function data. As discussed above, the NLO results use fits from Ref. [37]. For the leading order, the dipole amplitude used is the "MV^e" fit from Ref. [35]. In the leading-order calculation the evolution rapidity is chosen as $Y = \ln\frac{1}{x_{\mathbb{P}}} = \ln\frac{W^2+Q^2}{Q^2+M_V^2}$, consistently with the fit. The differential cross section is proportional to the square of the production amplitude as given by Eq. (2). When calculating the cross section at NLO, we drop the higher-order terms proportional to α_s^2 so that we only keep the genuine NLO correction at the cross section level.

In Fig. 3, we show the differential cross section for the longitudinal ϕ and ρ production at $t = 0$. Here the experimental data is for the total production, which is the sum of the longitudinal and transverse channels. However, the longitudinal production dominates at $Q^2 \gg M_V^2$, and therefore it is expected that for high virtualities these data points accurately correspond to the longitudinal case.

In general, we see that both the LO and NLO results describe the H1 data well. The difference between the LO and NLO results is smaller than one would expect based on Fig. 2, as in the leading-order fit the nonperturbative parameters describing the initial condition of the dipole amplitude effectively capture part of the higher-order effects. This difference becomes small at high virtualities, where our approach is expected to be most reliable.
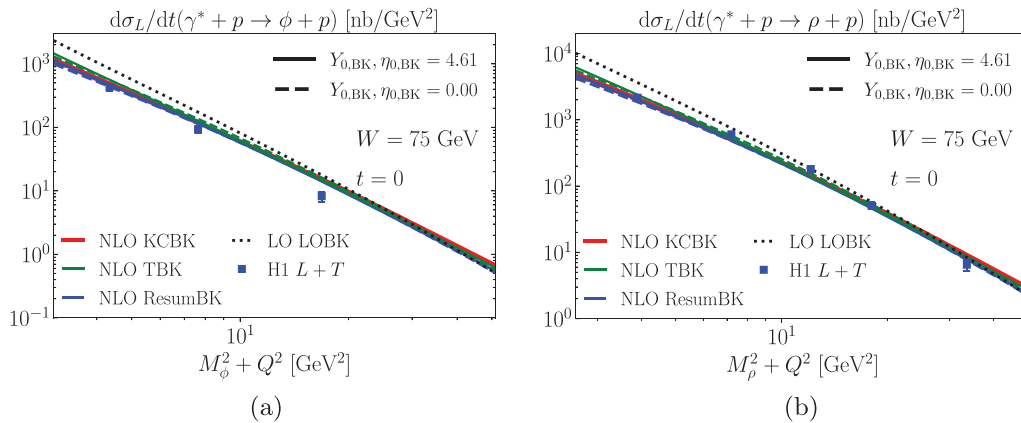

FIG. 3. Photon virtuality dependence of the longitudinal cross section at $t = 0$ for various different dipole amplitude fits, compared to the H1 data for the sum of longitudinal and transverse productions [59]. (a) Cross section for ϕ production. (b) Cross section for ρ production.
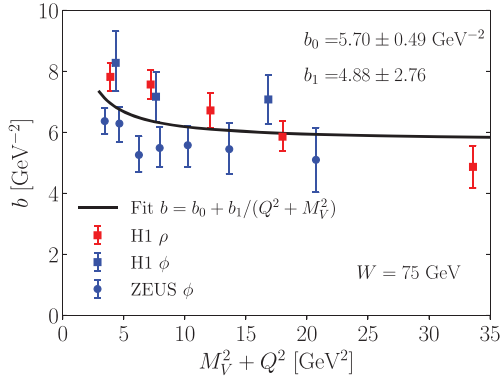
FIG. 4. The measured slope parameter b for ρ and ϕ production as a function of photon virtuality [59,76,77] and a fit to this data.

The NLO results also give a surprisingly accurate description of the data for smaller values of the photon virtuality where the framework cannot be trusted (we have assumed that $Q^2 \gg M_V^2$). We consider this agreement to be accidental for two reasons. First, we have only calculated the longitudinal cross section, leaving out the transverse contribution which is significant at small Q^2. Second, we neglect any dependence on the dipole size in the meson wave function, keeping only the $\mathbf{r} = 0$ case which corresponds to the distribution amplitude. In general, the wave function is expected to be a decreasing function of $|\mathbf{r}|$, meaning that this approximation overestimates the results. These two corrections, which may have significant numerical contributions at small virtualities, affect the result in opposite ways and therefore their total contribution at least partially cancels.

Next we will consider the t-integrated cross sections for which more data exists. To avoid additional modeling for the impact parameter dependence of the dipole amplitude, we evaluate the t integral by using the following experimental parametrization for the t dependence of the cross section:
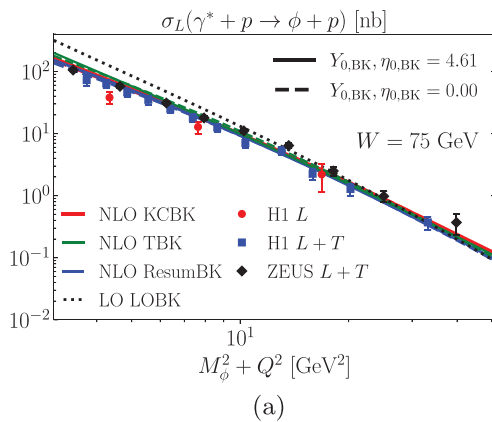
$$\frac{d\sigma}{dt} = e^{-b|t|} \times \frac{d\sigma}{dt}(t = 0). \tag{61}$$

Here b is the slope parameter that in general depends on Q^2 and W. It has been measured for both ϕ and ρ [59,76,77] at different values of the virtuality at $W = 75$ GeV. The slope parameter can be thought of as the effective transverse area of the meson-target system, and we model its dependence on virtuality and center-of-mass energy by assuming the parametrization

$$b = b_0 + \frac{b_1}{Q^2 + M_V^2} + 4\alpha' \ln \frac{W}{W_0}. \tag{62}$$

The W dependence determined from HERA data [59] gives $\alpha' = 0.12 \pm 0.04$. The model for the virtuality dependence is chosen for its simplicity and that it approaches a constant value at high Q^2. Also, the dependence on the virtuality and the center-of-mass energy does not seem to be correlated [59]. We fit the parameters b_0 and b_1 to H1 and ZEUS data at $W_0 = 75$ GeV, with the fit shown in Fig. 4, and note that the errors on these fitted parameters are significant, which results in $\sim$10% uncertainty in the calculated total cross sections.

The virtuality dependence of the coherent ϕ and ρ production cross sections is shown in Figs. 5 and 6. In Fig. 5, the results are calculated using different dipole amplitudes fitted to the HERA structure function data in Ref. [37], using fits with both choices for the initial evolution rapidities $Y_{0,\mathrm{BK}}$ ($\eta_{0,\mathrm{BK}}$ in the case of TBK evolution). The H1 collaboration has measured, in addition to the total production cross section, the longitudinally polarized ρ production, which exactly corresponds to the presented theory calculations. In general we find an excellent agreement with the H1 and ZEUS data [59,76,77], except that the ϕ production cross section is overestimated at low virtualities where our approximations are not justified.
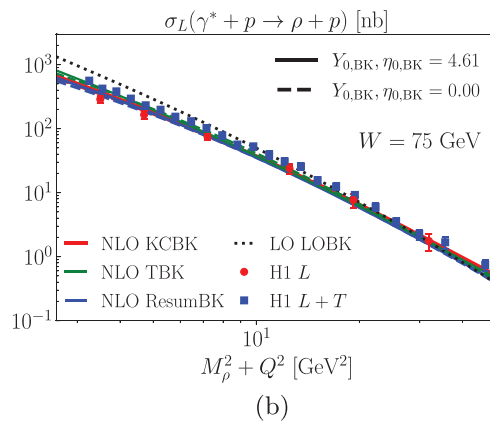
FIG. 5. Photon virtuality dependence of the integrated longitudinal cross section for various different dipole amplitude fits, compared to the HERA data [59,76,77]. (a) Cross section for ϕ production. (b) Cross section for ρ production.
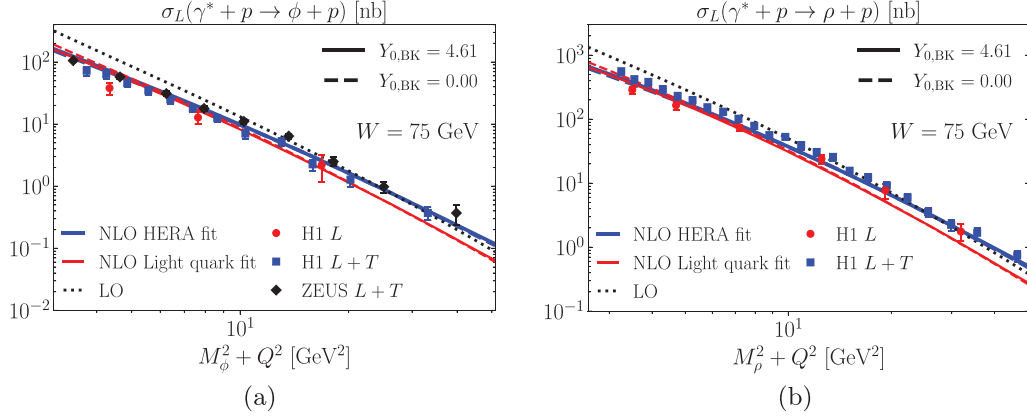
FIG. 6. Photon virtuality dependence of the integrated cross section for longitudinal production, with dipole amplitudes fitted to HERA structure function data and pseudodata consisting of only light quark production. (a) Cross section for ϕ production. (b) Cross section for ρ production.

In Fig. 6, we show results obtained using the dipole amplitudes fitted to the structure function pseudodata generated in Ref. [37] such that it includes only the approximative light quark contribution. For comparison, the results calculated with the dipole amplitudes fitted to the full HERA structure function data are also shown. In the fit process of Ref. [37] only the light quark contribution is calculated, and as such the fit to light quark pseudodata is in principle better motivated than the fit to the full HERA structure function data. On the other hand, the light-quark-only data contains a larger nonperturbative contribution, and the determined parametrizations describing the initial condition of the dipole amplitude are not physically as well motivated. Here we use these light quark fits with the KCBK evolution equation, but different schemes for the BK evolution result in very similar cross sections at all Q^2.

We see that the results calculated with dipole amplitudes fitted to the light quark pseudodata also show a relatively good agreement with the virtuality dependence of the H1 and ZEUS light meson production data. However, the cross

sections at large virtualities are somewhat underestimated. This difference in Q^2 dependence between the two fit setups is expected, as the light-quark-only pseudodata is close to the full structure function data at low Q^2 where similar results for other observables are also expected. On the other hand, at high Q^2 the charm contribution on structure functions is significant, and consequently the light quark fit should result in smaller cross sections in this kinematical region, which is exactly what we observe in Fig. 6.

In Figs. 7 and 8, we show the dependence of the integrated cross section on the photon-proton center-of-mass energy W. Again, Fig. 7 shows results obtained with the dipole amplitudes fitted to the HERA data, and Fig. 8 shows results calculated with dipole amplitudes fitted to the light quark pseudodata for comparison. The center-of-mass energy dependence of the results agrees with the data, although the results with the light quark fit seem to underestimate the data by a constant factor as already seen in Fig. 6. The differences in the results with different schemes for the BK evolution start growing at larger W, as
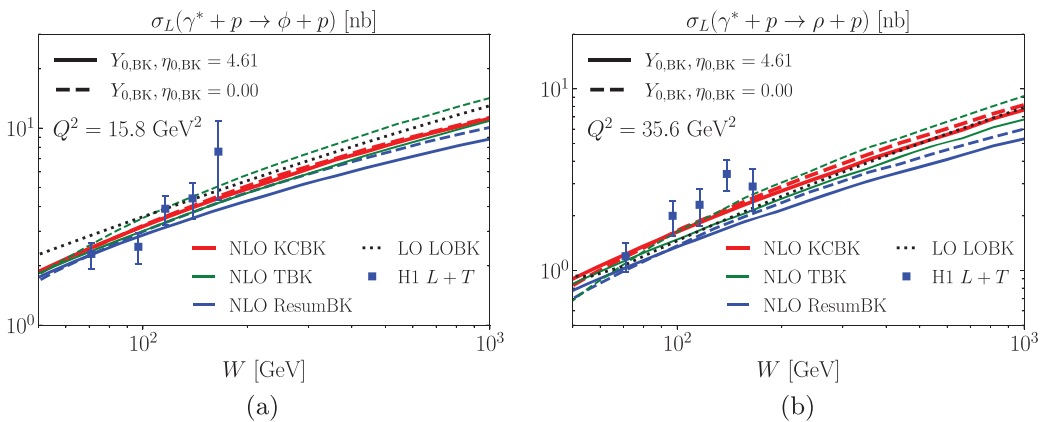
FIG. 7. Center-of-mass dependence of the integrated longitudinal cross section compared to the H1 data [59]. (a) Cross section for ϕ production. (b) Cross section for ρ production.
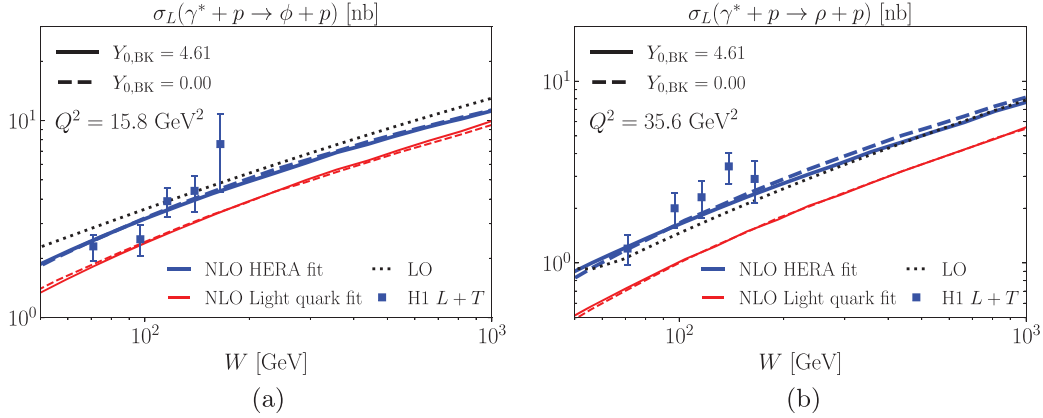
FIG. 8.   Center-of-mass dependence of the integrated longitudinal cross section, with dipole amplitudes fitted to HERA structure function data and pseudodata consisting of only light quark production. (a) Cross section for ϕ production. (b) Cross section for ρ production.

at high W one starts to be sensitive to the region not constrained by the structure function data. This suggests that light meson production data can provide additional constraints when the nonperturbative initial condition for the BK evolution is extracted from experimental data. The dependence on the center-of-mass energy is similar for the HERA and light quark fitted dipole amplitudes.

In Fig. 9(a), we show the dependence of the cross section on the distribution amplitude. We have normalized the results by the cross section calculated using the asymptotic form for the distribution amplitude that corresponds to the case where the higher-order terms in the Gegenbauer expansion (47) vanish, i.e., $a_n = 0$ for $n > 0$. The case $a_2(1 \text{ GeV}) = 0.1$ corresponds to our default setup, and the cases $a_2(1 \text{ GeV}) = \pm 0.2$ are estimates for the upper and lower bounds for the coefficient, chosen based on Ref. [73]. The final setup shown has the coefficients $a_2(1 \text{ GeV}) = -0.054$ and $a_4(1 \text{ GeV}) = -0.022$ chosen such that the

distribution amplitude matches the boosted Gaussian wave function parametrization for the ρ meson from Ref. [16] at $\mathbf{r} = 0$, where the higher Gegenbauer terms are neglected. The reason for this choice is that the distribution amplitude should roughly correspond to the wave function at $\mathbf{r} = 0$, and the boosted Gaussian is a phenomenological wave function that describes well vector meson production at leading order [16]. We see that the dependence on the distribution amplitude is moderate, and maximally $\sim 30\%$ in the considered kinematical domain.

The different distribution amplitudes are illustrated in Fig. 9(b), both at the initial scale $\mu_F^2 = 1 \text{ GeV}^2$ and after the ERBL evolution up to $\mu_F^2 = 50 \text{ GeV}^2$ using the extreme values for a_2. While the form of the distribution amplitude depends considerably on the value of a_2, the effect on the cross section in Fig. 9(a) is small. In Fig. 9(b), we also see that as the factorization scale μ_F increases the distribution amplitude approaches the asymptotic form, but there is still
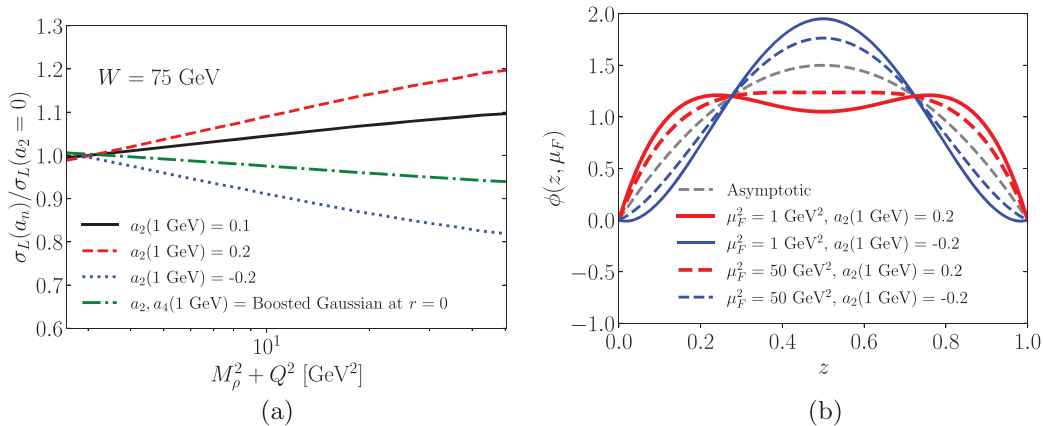
FIG. 9.   Dependence of the cross section on the distribution amplitude. (a) Ratio of the cross section with varied coefficients in the Gegenbauer expansion to the default setup. (b) Distribution amplitude with different coefficients a_2 and the effect of the ERBL evolution. The asymptotic form with $a_{n>0} = 0$ is also shown.

a significant deviation from the asymptotic shape at $\mu_F^2 = 50$ GeV^2.

VI. CONCLUSIONS

In this paper, we have presented a next-to-leading order calculation of exclusive light vector meson production in the dipole picture using the light cone perturbation theory. The main result of this work is the scattering amplitude for longitudinally polarized light vector meson production at high Q^2 given in Eq. (55). This amplitude is finite and directly suitable for numerical evaluations. In particular the $\frac{1}{D-4}$ divergences have been canceled between the real and virtual diagrams after the ERBL evolution of the renormalized distribution amplitude is also taken into account. The apparent soft gluon divergence is shown to be factorizable into the small-x Balitsky-Kovchegov evolution of the dipole amplitude. While a similar calculation has already been done in the momentum space [53] (using also a different scheme to subtract the rapidity divergence), the results presented in this paper are in the mixed transverse coordinate-longitudinal momentum fraction space where the numerical calculations using existing results for the dipole-target scattering amplitude are straightforward. Comparing the results in the different spaces is cumbersome due to the requirement of calculating complicated Fourier transforms, and thus an explicit comparison of the two results has been made only partially.

We have also calculated numerically exclusive light meson production at NLO and compared the results to the existing HERA data for ρ and ϕ mesons. The NLO corrections are numerically important, but their effect can be partially captured when the initial condition for the small-x evolution of the dipole amplitude is fitted to the structure function data. Consequently, the differences between LO and NLO results are moderate in the high virtuality region $Q^2 \gg M_V^2$ where our framework is valid. The different schemes used to capture higher-order effects in the small-x evolution result in similar cross sections for vector meson production. Some deviations can be seen in the center-of-mass energy W dependence, which means that the exclusive vector meson production data can further constrain the nonperturbative initial condition for the small-x evolution. Both the Q^2 and W dependencies of the production cross section are in excellent agreement with the HERA data. If a dipole amplitude with an initial condition fitted to the structure function pseudodata that only includes a light quark contribution is used, the experimental cross sections are underestimated at high Q^2. We also note that there is some overall normalization uncertainty due to, e.g., modeling the t dependence of the vector meson production cross section. We additionally left out the commonly used phenomenological corrections (see, e.g., [16]) whose role should be further clarified.

Our result for the analytic expression of the production amplitude is presented in two different schemes for regularization in the transverse plane: the CDR and FDH schemes. The regularization scheme dependence is shown to be very small. The results also depend on the choice for the factorization scale μ_F, for which we present two different choices, taking this scale to be either a function of the dipole size or of the photon virtuality. The dependence on the factorization scale is also relatively small. Both of these scheme dependencies have numerically small effects because the distribution amplitudes for the ρ and ϕ mesons are close to the asymptotic form, and the dependence on regularization scheme and factorization scale vanishes in the $Q^2 \to \infty$ limit. The dependence on the exact form of the distribution amplitude, on the other hand, is somewhat larger with effects of up to $\sim 30\%$ in the HERA kinematics at the cross section level for realistic values of the higher-order terms in the Gegenbauer expansion.

The results in this paper are calculated at zero momentum transfer $t = 0$. Calculating the t dependence of exclusive vector meson production is also interesting as it allows access to the spatial distribution of the target color field including its event-by-event fluctuations [14,78,79]. This requires additional nonperturbative modeling of the dipole amplitude that we wanted to avoid in this paper. We also note that the dipole amplitudes used in numerical calculations in this paper were fitted to HERA data using only massless quarks, while there is a significant contribution from the massive c quark to the structure functions in HERA kinematics. As the NLO photon wave functions with massive quarks are becoming available [32,33], it will be possible to make a new NLO fit for the dipole amplitude to the HERA data including heavy quark contributions. This is needed for accurate phenomenological comparisons with the HERA data. The results of this work can then be used for predicting exclusive light vector meson production in the future Electron-Ion Collider which will also produce data for DIS off heavy nuclei, allowing for precision studies of saturation phenomena.

ACKNOWLEDGMENTS

APPENDIX: SCHEME DEPENDENCE

In this appendix, we quantify the dependence of the light vector meson production cross section on the choices for regularization and factorization schemes. The cross sections have been calculated as described in Sec. V, and our default setup is the same. The dipole amplitude used in this appendix is the KCBK evolved one from Ref. [37] with the initial rapidity $Y_{0,\text{BK}} = 4.61$.

First, we show the dependence of the cross section on the regularization scheme in the transverse plane. The cross section has been calculated in both the CDR and FDH schemes and their ratio is shown in Fig. 10. This ratio depends on the distribution amplitude, and it is equal to unity in the asymptotic limit $\mu_F^2 \to \infty$, where only the first term in the Gegenbauer expansion (47) contributes. For this reason we show the ratio with two different distribution amplitudes: one with $a_2(1~\text{GeV}) = 0.1$ (our standard setup), and one with $a_2(1~\text{GeV}) = 0$, $a_4(1~\text{GeV}) = 0.1$. Higher-order terms are set to zero. We see that the dependence on the regularization scheme is very small in both cases, of the order 0.2% at most. Small scheme dependence is expected, as the first dominant term in the Gegenbauer expansion vanishes when one calculates the scheme dependent term in Eq. (44). It should be noted that the ratio does not seem to approach the asymptotic limit in the considered kinematics. This is a consequence of the ERBL evolution with running coupling being extremely slow, and the scheme dependence vanishes if we go to even higher values of virtuality.

The cross section depends on the factorization scale μ_F at which the distribution amplitudes are evaluated as discussed in Sec. IV C. In Fig. 11, the cross sections have been calculated evaluating the distribution amplitude in both the r and Q schemes using our default choice for the distribution amplitude with $a_2(1~\text{GeV}) = 0.1$. The factorization scale has also been scaled by factors of 0.5 and 2. These results have been normalized by our default setup
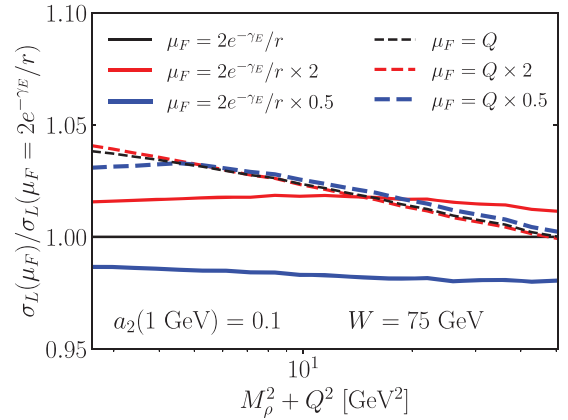

FIG. 11. Ratio of the cross section with different choices for the factorization scale μ_F to the default setup.

(r scheme with $\mu_F = 2e^{-\gamma_E}/r$). In the Q scheme, varying the factorization scale by a factor of 2 has a very small effect. For the r scheme the cross section varies somewhat more, but the variation is still only ~2%. The difference between the r and Q schemes is also only a few percent at most, meaning that the dependence on the factorization scale is small. This follows from the fact that the distribution amplitude receives only a small correction from the second scale-dependent Gegenbauer term, and the dominant term is factorization scale independent.

Finally, we show the dependence on the infrared cutoff μ_{F0} in Fig. 12 using our default setup [r scheme and $a_2(1~\text{GeV}) = 0.1$]. There is some dependence on the IR cutoff, almost 5% at most with our choice for a_2. The reason for the cutoff dependence is that the dipole amplitude amplifies the contribution of large dipoles, meaning that dipoles of size $1/r \sim 1~\text{GeV}$ may have a numerically significant contribution even when $Q^2 \gg 1~\text{GeV}^2$. The dependence on the IR cutoff vanishes exactly in the limit $Q^2 \to \infty$.

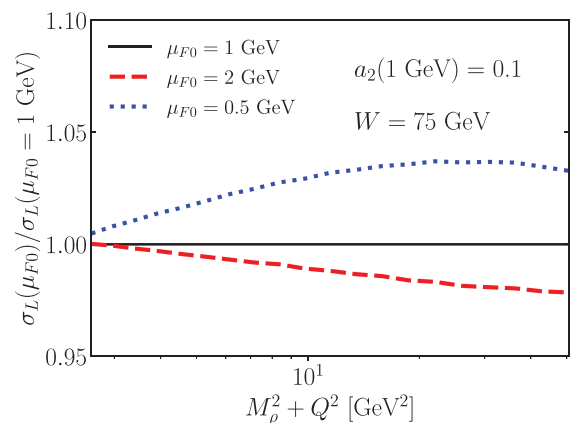FIG. 10. Ratio of the ρ production cross sections calculated in FDH and CDR regularization schemes.

FIG. 12. Ratio of the cross section with different IR cutoffs μ_{F0} for the ERBL evolution to the default setup.

[1] F. D. Aaron *et al.* (H1 and ZEUS Collaborations), Combined measurement and QCD analysis of the inclusive $e^{\pm}p$ scattering cross sections at HERA, J. High Energy Phys. 01 (2010) 109.

[2] H. Abramowicz *et al.* (H1 and ZEUS Collaborations), Combination of measurements of inclusive deep inelastic $e^{\pm}p$ scattering cross sections and QCD analysis of HERA data, Eur. Phys. J. C **75**, 580 (2015).

[3] E. Iancu and R. Venugopalan, The color glass condensate and high-energy scattering in QCD, *Quark Gluon Plasma 3* (World Scientific, Singapore, 2004), pp. 249–363, 10.1142/9789812795533_0005.

[4] F. Gelis, E. Iancu, J. Jalilian-Marian, and R. Venugopalan, The color glass condensate, Annu. Rev. Nucl. Part. Sci. **60**, 463 (2010).

[5] J.-P. Blaizot, High gluon densities in heavy ion collisions, Rep. Prog. Phys. **80**, 032301 (2017).

[6] A. Morreale and F. Salazar, Mining for gluon saturation at colliders, Universe **7**, 312 (2021).

[7] A. Accardi *et al.*, Electron Ion Collider: The next QCD frontier: Understanding the glue that binds us all, Eur. Phys. J. A **52**, 268 (2016).

[8] E. C. Aschenauer, S. Fazio, J. H. Lee, H. Mantysaari, B. S. Page, B. Schenke, T. Ullrich, R. Venugopalan, and P. Zurita, The Electron–Ion Collider: Assessing the energy dependence of key measurements, Rep. Prog. Phys. **82**, 024301 (2019).

[9] R. Abdul Khalek *et al.*, Science requirements and detector concepts for the Electron-Ion Collider: EIC Yellow Report, arXiv:2103.05419.

[10] P. Agostini *et al.* (LHeC and FCC-he Study Group Collaborations), The Large Hadron–Electron Collider at the HL-LHC, J. Phys. G **48**, 110501 (2021).

[11] M. G. Ryskin, Diffractive J/ψ electroproduction in LLA QCD, Z. Phys. C **57**, 89 (1993).

[12] K. J. Eskola, C. A. Flett, V. Guzey, T. Löytäinen, and H. Paukkunen, Exclusive J/ψ photoproduction in ultraperipheral Pb + Pb collisions at the LHC to next-to-leading order perturbative QCD, arXiv:2203.11613.

[13] S. R. Klein and H. Mäntysaari, Imaging the nucleus with high-energy photons, Nat. Rev. Phys. **1**, 662 (2019).

[14] H. Mäntysaari, Review of proton and nuclear shape fluctuations at high energy, Rep. Prog. Phys. **83**, 082201 (2020).

[15] A. V. Belitsky and A. V. Radyushkin, Unraveling hadron structure with generalized parton distributions, Phys. Rep. **418**, 1 (2005).

[16] H. Kowalski, L. Motyka, and G. Watt, Exclusive diffractive processes at HERA within the dipole picture, Phys. Rev. D **74**, 074016 (2006).

[17] C. Marquet, R. B. Peschanski, and G. Soyez, Exclusive vector meson production at HERA from QCD with saturation, Phys. Rev. D **76**, 034011 (2007).

[18] I. Balitsky, Operator expansion for high-energy scattering, Nucl. Phys. **B463**, 99 (1996).

[19] Y. V. Kovchegov, Small-x F_2 structure function of a nucleus including multiple pomeron exchanges, Phys. Rev. D **60**, 034008 (1999).

[20] G. P. Lepage and S. J. Brodsky, Exclusive processes in perturbative quantum chromodynamics, Phys. Rev. D **22**, 2157 (1980).

[21] H. G. Dosch, T. Gousset, G. Kulzinger, and H. J. Pirner, Vector meson leptoproduction and nonperturbative gluon fluctuations in QCD, Phys. Rev. D **55**, 2602 (1997).

[22] T. Lappi, H. Mäntysaari, and J. Penttala, Relativistic corrections to the vector meson light front wave function, Phys. Rev. D **102**, 054020 (2020).

[23] V. L. Chernyak and A. R. Zhitnitsky, Asymptotic behavior of exclusive processes in QCD, Phys. Rep. **112**, 173 (1984).

[24] J. C. Collins, L. Frankfurt, and M. Strikman, Factorization for hard exclusive electroproduction of mesons in QCD, Phys. Rev. D **56**, 2982 (1997).

[25] I. Balitsky and G. A. Chirilli, Next-to-leading order evolution of color dipoles, Phys. Rev. D **77**, 014019 (2008).

[26] T. Lappi and H. Mäntysaari, Direct numerical solution of the coordinate space Balitsky-Kovchegov equation at next to leading order, Phys. Rev. D **91**, 074016 (2015).

[27] T. Lappi and H. Mäntysaari, Next-to-leading order Balitsky-Kovchegov equation with resummation, Phys. Rev. D **93**, 094004 (2016).

[28] T. Lappi, H. Mäntysaari, and A. Ramnath, Next-to-leading order Balitsky-Kovchegov equation beyond large N_c, Phys. Rev. D **102**, 074027 (2020).

[29] H. Hänninen, T. Lappi, and R. Paatelainen, One-loop corrections to light cone wave functions: The dipole picture DIS cross section, Ann. Phys. (Amsterdam) **393**, 358 (2018).

[30] G. Beuf, Dipole factorization for DIS at NLO: Loop correction to the $\gamma^*_{T,L} \to q\bar{q}$ light-front wave functions, Phys. Rev. D **94**, 054016 (2016).

[31] G. Beuf, Dipole factorization for DIS at NLO: Combining the $q\bar{q}$ and $q\bar{q}g$ contributions, Phys. Rev. D **96**, 074033 (2017).

[32] G. Beuf, T. Lappi, and R. Paatelainen, Massive quarks in NLO dipole factorization for DIS: Longitudinal photon, Phys. Rev. D **104**, 056032 (2021).

[33] G. Beuf, T. Lappi, and R. Paatelainen, Massive quarks at one loop in the dipole picture of Deep Inelastic Scattering, arXiv:2112.03158.

[34] J. L. Albacete, N. Armesto, J. G. Milhano, P. Quiroga-Arias, and C. A. Salgado, AAMQS: A non-linear QCD analysis of new HERA data at small-x including heavy quarks, Eur. Phys. J. C **71**, 1705 (2011).

[35] T. Lappi and H. Mäntysaari, Single inclusive particle production at high energy from HERA data to proton-nucleus collisions, Phys. Rev. D **88**, 114020 (2013).

[36] B. Ducloué, E. Iancu, G. Soyez, and D. N. Triantafyllopoulos, HERA data and collinearly-improved BK dynamics, Phys. Lett. B **803**, 135305 (2020).

[37] G. Beuf, H. Hänninen, T. Lappi, and H. Mäntysaari, Color Glass Condensate at next-to-leading order meets HERA data, Phys. Rev. D **102**, 074028 (2020).

[38] A. Dumitru and R. Paatelainen, Sub-femtometer scale color charge fluctuations in a proton made of three quarks and a gluon, Phys. Rev. D **103**, 034026 (2021).

[39] A. Dumitru, H. Mäntysaari, and R. Paatelainen, Color charge correlations in the proton at NLO: Beyond geometry based intuition, Phys. Lett. B **820**, 136560 (2021).

[40] M. A. Escobedo and T. Lappi, Dipole picture and the nonrelativistic expansion, Phys. Rev. D **101**, 034030 (2020).

[41] H. Mäntysaari and J. Penttala, Exclusive heavy vector meson production at next-to-leading order in the dipole picture, Phys. Lett. B **823**, 136723 (2021).

[42] P. Caucal, F. Salazar, and R. Venugopalan, Dijet impact factor in DIS at next-to-leading order in the color glass condensate, J. High Energy Phys. 11 (2021) 222.

[43] E. Iancu and Y. Mulian, Forward dijets in proton-nucleus collisions at next-to-leading order: The real corrections, J. High Energy Phys. 03 (2021) 005.

[44] R. Boussarie, A. V. Grabovsky, L. Szymanowski, and S. Wallon, On the one loop $\gamma^{(*)} \to q\bar{q}$ impact factor and the exclusive diffractive cross sections for the production of two or three jets, J. High Energy Phys. 11 (2016) 149

[45] B. Ducloué, E. Iancu, T. Lappi, A. H. Mueller, G. Soyez, D. N. Triantafyllopoulos, and Y. Zhu, Use of a running coupling in the NLO calculation of forward hadron production, Phys. Rev. D **97**, 054020 (2018).

[46] B. Ducloué, T. Lappi, and Y. Zhu, Implementation of NLO high energy factorization in single inclusive forward hadron production, Phys. Rev. D **95**, 114007 (2017).

[47] B. Ducloué, T. Lappi, and Y. Zhu, Single inclusive forward hadron production at next-to-leading order, Phys. Rev. D **93**, 114016 (2016).

[48] A. M. Stasto, B.-W. Xiao, and D. Zaslavsky, Towards the Test of Saturation Physics Beyond Leading Logarithm, Phys. Rev. Lett. **112**, 012302 (2014).

[49] T. Altinoluk, N. Armesto, G. Beuf, A. Kovner, and M. Lublinsky, Single-inclusive particle production in proton-nucleus collisions at next-to-leading order in the hybrid formalism, Phys. Rev. D **91**, 094016 (2015).

[50] K. Watanabe, B.-W. Xiao, F. Yuan, and D. Zaslavsky, Implementing the exact kinematical constraint in the saturation formalism, Phys. Rev. D **92**, 034026 (2015).

[51] E. Iancu, A. H. Mueller, and D. N. Triantafyllopoulos, CGC factorization for forward particle production in proton-nucleus collisions at next-to-leading order, J. High Energy Phys. 12 (2016) 041.

[52] G. A. Chirilli, B.-W. Xiao, and F. Yuan, Inclusive hadron productions in pA collisions, Phys. Rev. D **86**, 054005 (2012).

[53] R. Boussarie, A. V. Grabovsky, D. Y. Ivanov, L. Szymanowski, and S. Wallon, Next-to-Leading Order Computation of Exclusive Diffractive Light Vector Meson Production in a Saturation Framework, Phys. Rev. Lett. **119**, 072002 (2017).

[54] B. Ducloué, H. Hänninen, T. Lappi, and Y. Zhu, Deep inelastic scattering in the dipole picture at next-to-leading order, Phys. Rev. D **96**, 094017 (2017).

[55] G. Beuf, Improving the kinematics for low-x QCD evolution equations in coordinate space, Phys. Rev. D **89**, 074039 (2014).

[56] A. V. Efremov and A. V. Radyushkin, Factorization and asymptotical behavior of pion form-factor in QCD, Phys. Lett. B **94**, 245 (1980).

[57] P. Ball, V. M. Braun, Y. Koike, and K. Tanaka, Higher twist distribution amplitudes of vector mesons in QCD: Formalism and twist—Three distributions, Nucl. Phys. **B529**, 323 (1998).

[58] V. M. Braun and I. E. Filyanov, Conformal invariance and pion wave functions of nonleading twist, Z. Phys. C **48**, 239 (1990).

[59] F. D. Aaron et al. (H1 Collaboration), Diffractive electroproduction of ρ and ϕ mesons at HERA, J. High Energy Phys. 05 (2010) 032.

[60] H. Mäntysaari, K. Roy, F. Salazar, and B. Schenke, Gluon imaging using azimuthal correlations in diffractive scattering at the Electron-Ion Collider, Phys. Rev. D **103**, 094026 (2021).

[61] I. Balitsky, Quark contribution to the small-x evolution of color dipole, Phys. Rev. D **75**, 014001 (2007).

[62] E. Iancu, J. D. Madrigal, A. H. Mueller, G. Soyez, and D. N. Triantafyllopoulos, Resumming double logarithms in the QCD evolution of color dipoles, Phys. Lett. B **744**, 293 (2015).

[63] H. Hänninen, Deep inelastic scattering in the dipole picture at next-to-leading order, Ph.D. thesis, University of Jyväskylä, JYU Dissertations 444, 2021, arXiv:2112.08818.

[64] E. Iancu, J. D. Madrigal, A. H. Mueller, G. Soyez, and D. N. Triantafyllopoulos, Collinearly-improved BK evolution meets the HERA data, Phys. Lett. B **750**, 643 (2015).

[65] B. Ducloué, E. Iancu, A. H. Mueller, G. Soyez, and D. N. Triantafyllopoulos, Non-linear evolution in QCD at high-energy beyond leading order, J. High Energy Phys. 04 (2019) 081.

[66] Y. V. Kovchegov and H. Weigert, Triumvirate of running couplings in small-x evolution, Nucl. Phys. **A784**, 188 (2007).

[67] T. Lappi and H. Mäntysaari, On the running coupling in the JIMWLK equation, Eur. Phys. J. C **73**, 2307 (2013).

[68] Z. Bern and D. A. Kosower, The computation of loop amplitudes in gauge theories, Nucl. Phys. **B379**, 451 (1992).

[69] Z. Bern, A. De Freitas, L. J. Dixon, and H. L. Wong, Supersymmetric regularization, two loop QCD amplitudes and coupling shifts, Phys. Rev. D **66**, 085002 (2002).

[70] H. Mäntysaari and B. Schenke, Confronting impact parameter dependent JIMWLK evolution with HERA data, Phys. Rev. D **98**, 034013 (2018).

[71] H. Mäntysaari and P. Zurita, In depth analysis of the combined HERA data in the dipole models with and without saturation, Phys. Rev. D **98**, 036002 (2018).

[72] F. Gao, L. Chang, Y.-X. Liu, C. D. Roberts, and S. M. Schmidt, Parton distribution amplitudes of light vector mesons, Phys. Rev. D **90**, 014011 (2014).

[73] M. V. Polyakov and H.-D. Son, Second Gegenbauer moment of a ρ-meson distribution amplitude, Phys. Rev. D **102**, 114005 (2020).

[74] P. A. Zyla et al. (Particle Data Group), Review of particle physics, Prog. Theor. Exp. Phys. **2020**, 083C01 (2020).

[75] G. Beuf, H. Hänninen, T. Lappi, and H. Mäntysaari, Color glass condensate at next-to-leading order meets HERA data (software), 10.5281/zenodo.4229269 (2020).

[76] S. Chekanov et al. (ZEUS Collaboration), Exclusive electroproduction of ϕ mesons at HERA, Nucl. Phys. **B718**, 3 (2005).

[77] J. Breitweg et al. (ZEUS Collaboration), Exclusive electroproduction of ρ^0 and J/ψ mesons at HERA, Eur. Phys. J. C **6**, 603 (1999).

[78] H. Mäntysaari and B. Schenke, Revealing proton shape fluctuations with incoherent diffraction at high energy, Phys. Rev. D **94**, 034042 (2016).

[79] H. Mäntysaari and B. Schenke, Evidence of Strong Proton Shape Fluctuations from Incoherent Diffraction, Phys. Rev. Lett. **117**, 052301 (2016).

Correction: Equations (24) and (25) contained errors and have been fixed. Text indicating validity was added after Eq. (13). The fourth sentence of the last paragraph in Sec. IV contained an error and has been set right.

IV

COMPLETE CALCULATION OF EXCLUSIVE HEAVY VECTOR MESON PRODUCTION AT NEXT-TO-LEADING ORDER IN THE DIPOLE PICTURE

by

Heikki Mäntysaari, Jani Penttala (2022)

Complete calculation of exclusive heavy vector meson production at next-to-leading order in the dipole picture

Heikki Mäntysaari and Jani Penttala

Department of Physics, University of Jyväskylä,
P.O. Box 35, 40014 Jyväskylä, Finland

Helsinki Institute of Physics, University of Helsinki,
P.O. Box 64, 00014 Helsinki, Finland

E-mail: heikki.mantysaari@jyu.fi, jani.j.penttala@jyu.fi

ABSTRACT: Exclusive production of transversely polarized heavy vector mesons in deep inelastic scattering at high energy is calculated at next-to-leading order accuracy in the Color Glass Condensate framework. In addition to the first QCD correction proportional to the strong coupling constant α_s, we systematically also include the first relativistic correction proportional to the heavy quark velocity squared v^2. When combined with our previously published results for longitudinal vector meson production at next-to-leading order accuracy, these results make phenomenological calculations of heavy vector meson production possible at the order $\mathcal{O}(\alpha_s v^0, \alpha_s^0 v^2)$. When applied to J/ψ and Υ production at HERA and at the LHC, a good agreement between the next-to-leading order calculations and experimental data is found. Additionally, we demonstrate that vector meson production can provide additional constraints compared to structure function analyses when the nonperturbative initial condition for the Balitsky-Kovchegov evolution equation is extracted.

Contents

1 Introduction

In Quantum Chromodynamics (QCD), emission of small momentum fraction x gluons is preferred, which renders parton densities very large when probed at small momentum fraction x in high-energy collider experiments [1, 2]. Consequently, parton densities eventually become so large that the smallness of the QCD coupling α_s is compensated by the gluon density, and non-linear dynamics starts to dominate in the hadron wave function [3].

An especially powerful probe of non-linear QCD dynamics is given by exclusive vector meson production in deep inelastic scattering (DIS) experiments. The exclusivity of the process requires that, at leading order, two gluons are exchanged with the target hadron at the amplitude level. Thus the cross section approximately scales as gluon density squared [4] (at next-to-leading order in collinear factorization the relationship is less direct, see ref. [5]) An additional advantage is that only in exclusive scattering processes it is possible to determine the total transverse momentum transfer $\boldsymbol{\Delta}$, which is a Fourier conjugate to the

impact parameter, and as such the spectra are sensitive to the spatial distribution of color charge in the target color field [6].

Exclusive production of heavy vector mesons, in particular J/ψ, has been studied in detail in electron-proton DIS experiments at HERA [7–14]. Recently, it has also become possible to access even higher center-of-mass energies and scattering off nuclear targets in ultra-peripheral collisions (UPCs) at RHIC [15–17] and at the LHC [18–29]. In these events the impact parameter is larger than the sum of the radii of the colliding nuclei, which suppresses strong interactions and these events are effectively real photon-nucleus scattering processes [30].

In the next decade, the Electron-Ion Collider in the US [31, 32] and other potential nuclear DIS facilities [33, 34] will provide vast amounts of precise data on exclusive vector meson production over a wide kinematical domain. To take advantage of these recent and future developments that provide a unique access to non-linear QCD dynamics at small x, it is important to develop theoretical calculations to the comparable level of accuracy.

To describe QCD in the high energy (and density) regime, we employ the Color Glass Condensate (CGC) effective field theory approach [35, 36]. In this formulation the color field of the target is written in terms of Wilson lines that describe an eikonal propagation of partons in the color field, resumming multiple interactions. The purpose of this work is to present the first next-to-leading order (NLO) calculation of transversely polarized exclusive heavy vector meson production cross section at high energy within the CGC framework.

Exclusive vector meson production has been studied extensively within the CGC framework at leading order in the QCD coupling, see for example refs. [37–41] related to J/ψ production in $\gamma^* + p$ scattering and [42–50] in $\gamma^* + A$ scattering (e.g. in UPCs where the photon is real). Note also that in these leading-order calculations the small-x evolution equations such as the Balitsky-Kovchegov (BK) equation [51, 52] (or phenomenological parametrizations modeling the small-x evolution) resum contributions $\sim \alpha_s \ln 1/x$ to all orders, and running coupling corrections [53, 54] also resum a subset of higher-order contributions.

At high energy the scattering process is conveniently described in the dipole picture where the (virtual) photon splits into a quark-antiquark dipole long before the interaction with the target (see discussion in section 2). The dipole then interacts with the target and eventually forms the bound state. In order to develop the CGC calculations to NLO accuracy, all ingredients (the virtual photon and heavy vector meson wave functions, and the dipole-target scattering amplitude) are needed at this order in perturbation theory. In recent years there has been a rapid progress in the field to achieve this. The evolution equations at NLO, describing the center-of-mass energy dependence of the dipole-target scattering amplitude, are derived and solved in refs. [55–60] (and a subset of higher-order corrections are resummed in [61–65]). The initial condition for the perturbative evolution is fitted to HERA structure function data at NLO accuracy in ref. [66] (see also refs. [67, 68] for an NLO calculation of the proton color charge correlations at moderate x that can potentially be used to initialize the evolution). The NLO light-front wave function for a virtual photon was first derived in the massless quark limit in refs. [69–72] and recently the results with finite quark masses have also become available [73–75]. The NLO wave functions exist also for heavy [76] and light [77, 78] vector mesons. In addition to structure

functions and exclusive processes, NLO calculations for dijet production in DIS and hadronic collisions [79–82], and inclusive particle production in proton-nucleus collisions [83–91] are becoming available.

The present paper completes the calculation of exclusive heavy vector meson production at next-to-leading order that we initialized in previous publications. First, the relativistic corrections suppressed by the squared quark velocity $\sim v^2 \alpha_{\rm s}^0$ were determined in ref. [92]. Later, in ref. [93] we calculated the next-to-leading order corrections $\sim v^0 \alpha_{\rm s}$ to longitudinally polarized heavy vector meson production. This paper presents the calculation of transversely polarized heavy vector meson in virtual photon-target scattering at the order $\alpha_{\rm s} v^0$, and demonstrates how the NLO corrections and the relativistic corrections can both be included consistently. This development enables us to present the first calculation of exclusive J/ψ production at the order $\mathcal{O}(\alpha_{\rm s} v^0, \alpha_{\rm s}^0 v^2)$, and comparisons with the HERA and LHC data are presented in this paper.

This manuscript is structured as follows. The exclusive vector meson production process in the dipole picture is first presented in section 2. The next-to-leading order QCD corrections for the transverse heavy vector meson production are calculated in section 3. The implementation of relativistic (velocity) corrections is discussed in section 4 before presenting numerical results in section 5 and conclusions in section 6.

2 High-energy scattering in the dipole picture

2.1 Exclusive vector meson production

The high-energy limit allows us to describe exclusive scattering in a factorized form where different parts of the process can be written independently. We work in a frame where the photon plus momentum q^+ is very large and it has no transverse momentum. The splitting of the virtual photon and the vector meson formation are described by the (boost invariant) light-front wave functions of the photon (Ψ_{γ^*}) and meson (Ψ_V). At leading order the only contribution comes from the photon splitting into a quark-antiquark dipole. Additional Fock states have to be introduced at higher orders in $\alpha_{\rm s}$, and at next-to-leading order one has to include a contribution from the photon splitting into a $q\bar{q}g$ state. The corresponding NLO scattering amplitude for vector meson production at $t \approx -\mathbf{\Delta}^2 = 0$ can be written as

$$
\begin{aligned}
-i\mathcal{A} = {} & 2 \int \mathrm{d}^2\mathbf{x}_0 \, \mathrm{d}^2\mathbf{x}_1 \int \frac{\mathrm{d}z_0 \, \mathrm{d}z_1}{(4\pi)^2} 4\pi \delta(z_0 + z_1 - 1) \Psi_{\gamma^*}^{q\bar{q}} \Psi_V^{q\bar{q}*} N_{01} \\
& + 2 \int \mathrm{d}^2\mathbf{x}_0 \, \mathrm{d}^2\mathbf{x}_1 \, \mathrm{d}^2\mathbf{x}_2 \int \frac{\mathrm{d}z_0 \, \mathrm{d}z_1 \, \mathrm{d}z_2}{(4\pi)^3} 4\pi \delta(z_0 + z_1 + z_2 - 1) \Psi_{\gamma^*}^{q\bar{q}g} \Psi_V^{q\bar{q}g*} N_{012}.
\end{aligned} \tag{2.1}
$$

Here $\mathbf{x}_i$ are the transverse coordinates of the quark ($i = 0$), the antiquark ($i = 1$) and the gluon ($i = 2$), and z_i are the corresponding fractions of the photon plus momentum. The different helicity and color components of the wave functions are summed over implicitly. The coherent vector meson production cross section then reads [94]

$$
\left. \frac{\mathrm{d}\sigma}{\mathrm{d}t} \right|_{t=0} = \frac{1}{16\pi} \left| \langle \mathcal{A} \rangle \right|^2 . \tag{2.2}
$$

The action of the Wilson lines $V(\mathbf{x}_i)$ on the quark-antiquark dipole is given by the dipole amplitude N_{01}:

$$1 - N_{01} = \operatorname{Re} \frac{1}{N_c} \left\langle \operatorname{Tr} V(\mathbf{x}_0) V^\dagger(\mathbf{x}_1) \right\rangle. \tag{2.3}$$

The dipole-target scattering amplitude N_{01} depends on the transverse separation $\mathbf{x}_{01} = \mathbf{x}_0 - \mathbf{x}_1$, impact parameter $\mathbf{b} = (\mathbf{x}_0 + \mathbf{x}_1)/2$ and projectile evolution rapidity Y. The evolution rapidity depends on the photon-nucleon system center-of-mass energy W as discussed in section 2.2. The notation $\langle \cdots \rangle$ corresponds to the average of the target color charge configurations, which is done at the amplitude level in eq. (2.2) when calculating coherent (i.e. no target dissociation) vector meson production [94] (see also e.g. refs. [41, 45, 95] related to incoherent diffraction and discussion about the averaging procedure). Similarly, interaction of the $q\bar{q}g$ system with the target is given in terms of the dipole amplitude N_{012} which in the mean field limit can be written as [96]

$$1 - N_{012} = \frac{N_c}{2C_F} \left(S_{02} S_{12} - \frac{1}{N_c^2} S_{01} \right), \tag{2.4}$$

where $S_{ij} = 1 - N_{ij}$.

As the impact parameter is conjugate to the momentum transfer in the process, the impact parameter dependence of the dipole amplitudes can be connected to the t-dependence of the production amplitude. However, the impact parameter dependence of the dipole amplitude requires additional modeling and an effective description of confinement effects (see e.g. [39, 97–99]), and for simplicity we choose to study only the case $t = 0$ given by eq. (2.1) where only the impact parameter integrated dipole amplitude constrained by structure function measurements [66] contributes.

In general, the production amplitude depends on both the polarization of the photon λ_γ and the vector meson λ_V. The polarization mixing $\lambda_\gamma \neq \lambda_V$ is heavily suppressed and consequently it is sufficient to consider only the case $\lambda_\gamma = \lambda_V$ [100]. Vector meson production can then be divided into longitudinal and transverse production, of which longitudinal channel has already been calculated at NLO by us in ref. [93]. In this paper we complete the NLO production calculation by computing the transverse production case, allowing us to consider total vector meson production.

2.2 High-energy evolution

The center-of-mass energy or, equivalently, Bjorken-x dependence of the Wilson lines can be obtained by solving the perturbative JIMWLK [101–107] evolution equation. In the large-N_c limit one can derive from it the BK equation describing the energy (evolution rapidity Y) dependence of the dipole amplitude N_{01}:

$$\frac{\partial S_{01}}{\partial Y} = \int \mathrm{d}^2 \mathbf{x}_2 K_{\mathrm{BK}}(\mathbf{x}_0, \mathbf{x}_1, \mathbf{x}_2)[S_{02} S_{12} - S_{01}]. \tag{2.5}$$

The kernel K_{BK} describes the probability to emit a gluon at the transverse position $\mathbf{x}_2$ from the quark-antiquark dipole at the coordinates $\mathbf{x}_0$ and $\mathbf{x}_1$. Including the running-coupling

corrections following [53], the kernel reads

$$K_{\mathrm{BK}}(\mathbf{x}_0, \mathbf{x}_1, \mathbf{x}_2) = \frac{N_c \alpha_{\mathrm{s}}(\mathbf{x}_{01}^2)}{2\pi^2} \left[\frac{\mathbf{x}_{01}^2}{\mathbf{x}_{21}^2 \mathbf{x}_{20}^2} + \frac{1}{\mathbf{x}_{20}^2} \left(\frac{\alpha_{\mathrm{s}}(\mathbf{x}_{20}^2)}{\alpha_{\mathrm{s}}(\mathbf{x}_{21}^2)} - 1 \right) + \frac{1}{\mathbf{x}_{21}^2} \left(\frac{\alpha_{\mathrm{s}}(\mathbf{x}_{21}^2)}{\alpha_{\mathrm{s}}(\mathbf{x}_{20}^2)} - 1 \right) \right], \quad (2.6)$$

where $\mathbf{x}_{ij} = \mathbf{x}_i - \mathbf{x}_j$.

The BK equation at next-to-leading order, and a numerical solution to it, are available [55, 58–60] (as well as the NLO JIMWLK equation [56, 57]). In principle it would be consistent to use the full NLO evolution equation when calculating vector meson production at this order in α_{s}. However, the NLO BK equation is numerically demanding due to an extra transverse integral, which is also the reason why there is no initial condition to it fitted to experimental data. In this work we follow ref. [66] and use the leading-order BK evolution equation combined with different implementations of a resummation of the most important higher-order contributions. These resummations are known to approximate the full NLO BK equation well as shown in refs. [59, 108]. The initial conditions for these evolutions are determined in ref. [66] by performing a fit to HERA structure function data [1, 2]. In our numerical analysis we use the fit results from publicly available codes [109]. The running strong coupling constant in coordinate space is evaluated using the same parametrization as in the corresponding dipole amplitude fits in ref. [66]. The explicit expression for the running coupling is

$$\alpha_{\mathrm{s}}(\mathbf{x}_{ij}^2) = \frac{4\pi}{\beta_0 \ln \left[\left(\frac{\mu_0^2}{\Lambda_{\mathrm{QCD}}^2} \right)^{1/c} + \left(\frac{4C^2}{\mathbf{x}_{ij}^2 \Lambda_{\mathrm{QCD}}^2} \right)^{1/c} \right]^c} \quad (2.7)$$

with $\Lambda_{\mathrm{QCD}} = 0.241 \, \mathrm{GeV}$, $c = 0.2$, $\mu_0/\Lambda_{\mathrm{QCD}} = 2.5$, $\beta_0 = (11 N_c - 2N_F)/3$ and $N_F = 3$, and C^2 is a fit parameter determined when the initial condition for the BK evolution is fitted to the HERA data.

The three different schemes to include resummation of higher-order corrections into the BK equation used in this work are, following the terminology of ref. [66], *KCBK* [110], *ResumBK* [63, 64] and *TBK* [61]. The evolution rapidity in the KCBK and ResumBK equations is related the fraction of the projectile (photon) plus momentum carrried by the gluon:

$$Y = \ln \frac{k^+}{P^+}, \quad (2.8)$$

where $k^+ = z_2 q^+$ is the gluon plus momentum and P is the target momentum. The evolution rapidity in the TBK equation is related to the target longitudinal momentum fraction as we will discuss shortly.

The KCBK ("kinematically constrained BK equation") is derived in ref. [110] by requiring the necessary time ordering between the subsequent gluon emissions. This procedure effectively resums corrections that are enhanced by double transverse logarithm $\sim \alpha_{\mathrm{s}} \ln \frac{\mathbf{x}_{02}}{\mathbf{x}_{01}} \ln \frac{\mathbf{x}_{12}}{\mathbf{x}_{01}}$. The same logarithms are included in the ResumBK ("resummed BK") equation, with the difference that in ref. [63] a form of the evolution equation which is local in rapidity Y is derived. Additionally, the ResumBK evolution equation further includes a resummation of single transverse logarithms [64] $\sim \alpha_{\mathrm{s}} \ln \frac{1}{\mathbf{x}_{ij}^2 Q_{\mathrm{s}}^2}$ to all orders. For explicit expressions for these evolution equations, see ref. [66].

The third evolution equation used in this work is the TBK equation ("BK equation in target rapidity"), where the evolution rapidity η is expressed in terms of the fraction of the target longitudinal (minus) momentum transferred in the process $x_{\mathbb{P}}$ (see detailed discussion in ref. [61]):

$$x_{\mathbb{P}} \approx \frac{M_V^2 + Q^2}{W^2 + Q^2}, \tag{2.9}$$

where M_V is the meson mass. Consequently the TBK evolution can be thought of as evolution in $\ln 1/x_{\mathbb{P}}$, whereas the KCBK and ResumBK evolutions written in terms of the projectile rapidity Y are evolutions in $\ln W^2$ [61, 66].

When using a solution to the TBK evolution, written in terms of the target rapidity η, in the NLO impact factors calculated in this work that are written in terms of projectile rapidity Y we use the same shift as in ref. [66]:

$$\eta = Y - \ln \frac{1}{\min\{1, \mathbf{x}_{01}^2 Q_0^2\}}, \tag{2.10}$$

where the target transverse momentum scale is set to $Q_0^2 = 1\,\mathrm{GeV}^2$.

Initial conditions for all these three evolution equations are obtained in ref. [66] by parametrizing the initial condition and fitting the free parameters to the HERA reduced cross section data. In this work we use the fit results obtained using the "Balitsky + smallest dipole" running coupling scheme. We note that in ref. [66] only the light quark contribution is included in the NLO structure function calculations. On the other hand, in this work we consider heavy vector meson production, and as such it is not fully consistent to use the fit results from ref. [66]. However, the main purpose of this work is to derive the cross section at NLO accuracy, and detailed phenomenological comparisons to experimental data should be done later when the initial condition for the BK evolution is determined including the effect of quark masses.

3   Vector meson production at next-to-leading order

Next-to-leading order corrections to exclusive vector meson production consist of corrections from perturbative gluons. These can be included by calculating the virtual photon and meson wave functions at proper order in α_s such that we have all the corrections at the order α_s at the amplitude level. This means that we have to include the $\mathcal{O}(\alpha_s)$ loop corrections to the light-cone wave functions $\Psi_\gamma^{q\bar{q}}$ and $\Psi_V^{q\bar{q}}$, and also take into account the contribution from the $q\bar{q}g$ state with the wave functions $\Psi_\gamma^{q\bar{q}g}$ and $\Psi_V^{q\bar{q}g}$. The NLO wave function for the transverse photon with massive quarks has been calculated in refs. [74, 75], and the NLO heavy vector meson wave function in the nonrelativistic limit is evaluated in ref. [76]. These results are applied in this work.

For completeness, we present here the next-to-leading order wave functions that enter our calculations. Our notation follows mostly refs. [74, 75] with the exception that the integration measure is chosen to be $\prod_i \frac{\mathrm{d}^2 \mathbf{x}_i \mathrm{d} z_i}{4\pi}$ where i goes over the partons of the Fock state corresponding to the wave function. This introduces additional normalization factors $\frac{1}{2q^+} \prod_i \frac{1}{\sqrt{z_i}}$ compared to the photon wave functions presented in [74, 75]. Also, we choose to

use the conventional dimensional regularization (CDR) scheme for our calculations, which corresponds to the case $D_s = D$ in refs. [74, 75].

The wave functions contain divergences that need to be regularized. Ultraviolet (UV) divergences are regularized using dimensional regularization in $D - 2$ dimensions for the transverse coordinates. Infrared (IR) divergences originating from gluons with zero plus momenta are removed by introducing a cut-off α for the gluon plus momenta, $k_2^+ > \alpha q^+$ where $\alpha > 0$ and q^+ is the plus momentum of the photon. The divergences will cancel in the calculation, and at the end we will take the limit $D \to 4$ and $\alpha \to 0$.

3.1 Virtual photon wave function at next-to-leading order

With these conventions, the LO transverse photon wave function for the $q\bar{q}$ state (at zero photon transverse momentum, $\mathbf{q} = 0$) is [75]

$$
\Psi_{\mathrm{LO}}^{\gamma^* \to q\bar{q}} = -\frac{1}{2q^+\sqrt{z_0(1-z_0)}} \frac{ee_f}{2\pi} \left(\frac{\kappa_z}{2\pi|\mathbf{x}_{01}|}\right)^{(D-4)/2} \epsilon_{\lambda_\gamma}^j \delta_{\alpha_0\alpha_1}
$$
$$
\times \left\{ \bar{u}(0)\left[(2z_0-1)\delta^{ij}\gamma^+ + \frac{1}{2}\gamma^+\left[\gamma^i,\gamma^j\right]\right]v(1)i\kappa_z\frac{\mathbf{x}_{01}^i}{|\mathbf{x}_{01}|}K_{(D-4)/2+1}\left(|\mathbf{x}_{01}|\kappa_z\right)\right.
$$
$$
\left. - m_q\bar{u}(0)\gamma^+\gamma^j v(1)K_{(D-4)/2}\left(|\mathbf{x}_{01}|\kappa_z\right)\right\}
\tag{3.1}
$$

where $u(0)$ and $v(1)$ are spinors corresponding to the quark and antiquark, m_q is the heavy quark mass, $\kappa_v = \sqrt{v(1-v)Q^2 + m_q^2}$ where Q^2 is the photon virtuality, and α_0, α_1 are the color indices of the quark and antiquark. The fraction of the photon plus momentum carried by the quark is z_0. Repeated indices in the Latin alphabet are summed over in $D - 2$ transverse dimensions. The functions K_ν are modified Bessel functions of the second kind. The NLO correction to the $q\bar{q}$ wave function is [74, 75]

$$
\Psi_{\mathrm{NLO}}^{\gamma^* \to q\bar{q}} = -\frac{1}{2q^+\sqrt{z_0(1-z_0)}} \frac{ee_f}{2\pi} \left(\frac{\alpha_s C_F}{2\pi}\right) \epsilon_{\lambda_\gamma}^j \delta_{\alpha_0\alpha_1}
$$
$$
\times \left\{ \bar{u}(0)\left[(2z_0-1)\delta^{ij}\gamma^+ + \frac{1}{2}\gamma^+\left[\gamma^i,\gamma^j\right]\right]v(1)\mathcal{F}[\mathbf{P}^i\mathcal{V}^T]\right.
$$
$$
+ \bar{u}(0)\gamma^+ v(1)\mathcal{F}[\mathbf{P}^j\mathcal{N}^T] + m_q\bar{u}(0)\gamma^+\gamma^i v(1)\mathcal{F}\left[\left(\frac{\mathbf{P}^i\mathbf{P}^j}{\mathbf{P}^2} - \frac{1}{2}\delta^{ij}\right)\mathcal{S}^T\right]
$$
$$
\left. - m_q\bar{u}(0)\gamma^+\gamma^j v(1)\mathcal{F}\left[\mathcal{M}^T + \mathcal{V}^T - \frac{1}{2}\mathcal{S}^T\right]\right\},
\tag{3.2}
$$

where the wave function is written in terms of different form factors. It will turn out that we do not need to know the explicit expressions for all of these form factors, which follows from the fact that at leading order in α_s and v the vector meson spin structure is very simple, picking up only parts with an odd number of transverse gamma matrices. In addition to this, the traceless part $\frac{\mathbf{P}^i\mathbf{P}^j}{\mathbf{P}^2} - \frac{1}{2}\delta^{ij}$ also vanishes as after taking the gamma matrix traces one gets $\epsilon_{\lambda_\gamma}^j \epsilon_{\lambda_V}^{i*}\left(\frac{\mathbf{P}^i\mathbf{P}^j}{\mathbf{P}^2} - \frac{1}{2}\delta^{ij}\right) = 0$ which is valid for $\lambda_\gamma = \lambda_V$ in 2 transverse dimensions.

In the polarization mixing case, $\lambda_\gamma \neq \lambda_V$, there would be a non-zero contribution from this term. Thus, only the last term in eq. (3.2) contributes to vector meson production in the nonrelativistic limit, and the required combination of the form factors reads

$$
\mathcal{F}\left[\mathcal{M}^T + \mathcal{V}^T - \frac{1}{2}\mathcal{S}^T\right] = \left(\frac{\kappa_z}{2\pi|\mathbf{x}_{01}|}\right)^{(D-4)/2} K_{(D-4)/2}\left(|\mathbf{x}_{01}|\kappa_z\right)\left\{\frac{1}{2}\right.
$$
$$
+ \left[\frac{3}{2} + \ln\left(\frac{\alpha}{z_0}\right) + \ln\left(\frac{\alpha}{1-z_0}\right)\right]\left[\frac{2\,(4\pi)^{(4-D)/2}}{4-D}\Gamma\left(1+\frac{4-D}{2}\right) + \ln\left(\frac{\mathbf{x}_{01}^2\mu^2}{4}\right) + 2\gamma_E\right]\right\}
$$
$$
+ K_0\left(|\mathbf{x}_{01}|\kappa_z\right)\left\{\Omega_\mathcal{V}^T(\gamma;z_0) + L(\gamma;z_0) - \frac{\pi^2}{3} + \ln^2\left(\frac{z_0}{1-z_0}\right) + 3\right\}
$$
$$
+ \widetilde{I}_{\mathcal{VMS}}^T(|\mathbf{x}_{01}|, z_0). \tag{3.3}
$$

Here μ is the mass scale coming from dimensional regularization. The functions $\Omega_\mathcal{V}^T$ and L are defined as

$$
\Omega_\mathcal{V}^T(\gamma;z) = \left(1 + \frac{1}{2z}\right)\left[\ln(1-z) + \gamma\ln\left(\frac{1+\gamma}{1+\gamma-2z}\right)\right]
$$
$$
- \frac{1}{2z}\left[\left(z+\frac{1}{2}\right)(1-\gamma) + \frac{m_q^2}{Q^2}\right]\ln\left(\frac{\kappa_z^2}{m_q^2}\right) \tag{3.4}
$$
$$
+ (z \leftrightarrow 1-z),
$$

and

$$
L(\gamma;z) = \sum_{\sigma=\pm 1}\left[\mathrm{Li}_2\left(\frac{1}{1-\frac{1}{2z}(1+\sigma\gamma)}\right) + \mathrm{Li}_2\left(\frac{1}{1-\frac{1}{2(1-z)}(1+\sigma\gamma)}\right)\right] \tag{3.5}
$$

where Li_2 is the dilogarithm function and

$$
\gamma = \sqrt{1 + \frac{4m_q^2}{Q^2}}. \tag{3.6}
$$

The function $\widetilde{I}_{\mathcal{VMS}}^T(r,z)$ can be written in the form

$$
\widetilde{I}_{\mathcal{VMS}}^T(r,z) =
$$
$$
\int_0^1 d\xi\left\{\frac{1}{\xi}\left[\frac{2\ln\xi}{1-\xi} - \frac{1+\xi}{2}\right]\left[K_0\left(r\sqrt{\kappa_z^2 + \frac{\xi(1-z)}{1-\xi}m_q^2}\right) - K_0\left(r\kappa_z\right)\right]\right.
$$
$$
\left.+ \left[-\frac{3(1-z)}{2(1-\xi)} + \frac{1-z}{2}\right]K_0\left(r\sqrt{\kappa_z^2 + \frac{\xi(1-z)}{1-\xi}m_q^2}\right)\right\}
$$
$$
+ \int_0^z d\chi\int_0^\infty du\left\{\frac{1}{1-\chi}\frac{1}{(u+1)^2}\left[-z - \frac{u}{1+u}\frac{z+u\chi}{z}(\chi-(1-z))\right]K_0\left(r\sqrt{\kappa_z^2 + u\frac{1-z}{1-\chi}\kappa_\chi^2}\right)\right.
$$
$$
+ \frac{1}{(u+1)^3}\left[\frac{\kappa_z^2}{\kappa_\chi^2}\left(1 + u\frac{\chi(1-\chi)}{z(1-z)}\right) - \frac{m_q^2}{\kappa_\chi^2}\frac{\chi}{1-\chi}\left(2\frac{(1+u)^2}{u} + \frac{u}{z(1-z)}(z-\chi)^2\right)\right]
$$
$$
\left.\times\left[K_0\left(r\sqrt{\kappa_z^2 + u\frac{1-z}{1-\chi}\kappa_\chi^2}\right) - K_0\left(r\kappa_z\right)\right]\right\}
$$
$$
+ (z \leftrightarrow 1-z), \tag{3.7}
$$

where the substitution $(z \leftrightarrow 1-z)$ corresponds to the whole expression.

In addition to the $q\bar{q}$ wave function of the photon, we also need the light-front wave function for the $q\bar{q}g$ state (again for the photon with zero transverse momentum). This can written as [75]

$$\psi^{\gamma^* \to q\bar{q}g} = \frac{1}{2q^+\sqrt{z_0 z_1 z_2}} t^a_{\alpha_0 \alpha_1} e e_f g \epsilon^l_{\lambda_\gamma} \epsilon^{*j}_\sigma \left(\Sigma^{lj} + \Sigma^{lj}_m \right),$$ (3.8)

where σ is the gluon helicity and

$$\begin{aligned}
\Sigma^{lj} = &-\frac{1}{(z_0 + z_2)} \bar{u}(0)\gamma^+ \left[(2z_0 + z_2)\delta^{ij} - \frac{z_2}{2} \left[\gamma^i, \gamma^j\right] \right] \\
&\times \left[(2z_1 - 1)\delta^{kl} - \frac{1}{2}\left[\gamma^k, \gamma^l\right] \right] v(1)\mathcal{I}^{ik}_{(j)} \\
&- \frac{1}{(z_1 + z_2)}\bar{u}(0)\gamma^+ \left[(2z_0 - 1)\delta^{kl} + \frac{1}{2}\left[\gamma^k, \gamma^l\right] \right] \\
&\times \left[(2z_1 + z_2)\delta^{ij} + \frac{z_2}{2}\left[\gamma^i, \gamma^j\right] \right] v(1)\mathcal{I}^{ik}_{(k)} \\
&+ \frac{z_2 z_0}{(z_0 + z_2)^2}\bar{u}(0)\gamma^+\gamma^j\gamma^l v(1)\mathcal{J}_{(l)} - \frac{z_2 z_1}{(z_1 + z_2)^2}\bar{u}(0)\gamma^+\gamma^l\gamma^j v(1)\mathcal{J}_{(m)}
\end{aligned}$$ (3.9)

and

$$\begin{aligned}
\Sigma^{lj}_m = &-m_q \frac{1}{(z_0 + z_2)}\bar{u}(0)\gamma^+ \left[(2z_0 + z_2)\delta^{ij} - \frac{z_2}{2}\left[\gamma^i, \gamma^j\right] \right] \gamma^l v(1)\mathcal{I}^i_{(j)} \\
&+ m_q \frac{z_2^2}{(z_0 + z_2)^2}\bar{u}(0)\gamma^+\gamma^j \left[(2z_1 - 1)\delta^{kl} - \frac{1}{2}\left[\gamma^k, \gamma^l\right] \right] v(1)\hat{\mathcal{I}}^k_{(j)} \\
&+ m_q^2 \frac{z_2^2}{(z_0 + z_2)^2}\bar{u}(0)\gamma^+\gamma^j\gamma^l v(1)\mathcal{I}_{(j)} \\
&+ m_q \frac{1}{(z_1 + z_2)}\bar{u}(0)\gamma^+\gamma^l \left[(2z_1 + z_2)\delta^{ij} + \frac{z_2}{2}\left[\gamma^i, \gamma^j\right] \right] v(1)\mathcal{I}^i_{(k)} \\
&+ m_q \frac{z_2^2}{(z_1 + z_2)^2}\bar{u}(0)\gamma^+ \left[(2z_0 - 1)\delta^{kl} + \frac{1}{2}\left[\gamma^k, \gamma^l\right] \right] \gamma^j v(1)\hat{\mathcal{I}}^k_{(k)} \\
&- m_q^2 \frac{z_2^2}{(z_1 + z_2)^2}\bar{u}(0)\gamma^+\gamma^l\gamma^j v(1)\mathcal{I}_{(k)}.
\end{aligned}$$ (3.10)

The special functions use the following labeling for the subindices

$$\mathcal{I}_{(j)} = \mathcal{I}(\mathbf{x}_{0+2;1}, \mathbf{x}_{20}, \overline{Q}^2_{(j)}, \omega_{(j)}, \lambda_{(j)}) \qquad \mathcal{I}_{(k)} = \mathcal{I}(\mathbf{x}_{0;1+2}, \mathbf{x}_{21}, \overline{Q}^2_{(k)}, \omega_{(k)}, \lambda_{(k)}) \qquad (3.11)$$

$$\hat{\mathcal{I}}_{(j)} = \hat{\mathcal{I}}(\mathbf{x}_{0+2;1}, \mathbf{x}_{20}, \overline{Q}^2_{(j)}, \omega_{(j)}, \lambda_{(j)}) \qquad \hat{\mathcal{I}}_{(k)} = \hat{\mathcal{I}}(\mathbf{x}_{0;1+2}, \mathbf{x}_{21}, \overline{Q}^2_{(k)}, \omega_{(k)}, \lambda_{(k)}) \qquad (3.12)$$

$$\mathcal{J}_{(l)} = \mathcal{J}(\mathbf{x}_{0+2;1}, \mathbf{x}_{20}, \overline{Q}^2_{(j)}, \omega_{(j)}, \lambda_{(j)}) \qquad \mathcal{J}_{(m)} = \mathcal{J}(\mathbf{x}_{0;1+2}, \mathbf{x}_{21}, \overline{Q}^2_{(k)}, \omega_{(k)}, \lambda_{(k)}) \qquad (3.13)$$

(and analogously for the special functions with transverse indices), where

$$\begin{aligned}
\omega_{(j)} &= \frac{z_0 z_2}{z_1(z_0 + z_2)^2}, & \omega_{(k)} &= \frac{z_1 z_2}{z_0(z_1 + z_2)^2}, \\
\overline{Q}^2_{(j)} &= z_1(1 - z_1)Q^2, & \overline{Q}^2_{(k)} &= z_0(1 - z_0)Q^2, \\
\lambda_{(j)} &= \frac{z_1 z_2}{z_0}, & \lambda_{(k)} &= \frac{z_0 z_2}{z_1},
\end{aligned}$$ (3.14)

$$\mathbf{x}_{n+m;p} = -\mathbf{x}_{p;n+m} = \frac{z_n \mathbf{x}_n + z_m \mathbf{x}_m}{z_n + z_m} - \mathbf{x}_p.$$ (3.15)

The special functions $\mathcal{I}$ are defined as:

$$\mathcal{I}^{ij}(\mathbf{b},\mathbf{r},\overline{Q}^2,\omega,\lambda) =$$
$$-\frac{\mu^{(4-D)/2}}{4(4\pi)^{D-2}}\mathbf{b}^i\mathbf{r}^j\int_0^\infty \mathrm{d}u\, u^{-D/2}e^{-u(\overline{Q}^2+m_q^2)}e^{-\mathbf{b}^2/(4u)}\int_0^{u/\omega}\mathrm{d}t\, t^{-D/2}e^{-t\omega\lambda m_q^2}e^{-\mathbf{r}^2/(4t)}, \quad (3.16)$$

$$\mathcal{I}^i(\mathbf{b},\mathbf{r},\overline{Q}^2,\omega,\lambda) =$$
$$\frac{i\mu^{(4-D)/2}}{2(4\pi)^{D-2}}\mathbf{r}^i\int_0^\infty \mathrm{d}u\, u^{1-D/2}e^{-u(\overline{Q}^2+m_q^2)}e^{-\mathbf{b}^2/(4u)}\int_0^{u/\omega}\mathrm{d}t\, t^{-D/2}e^{-t\omega\lambda m_q^2}e^{-\mathbf{r}^2/(4t)}, \quad (3.17)$$

$$\hat{\mathcal{I}}^i(\mathbf{b},\mathbf{r},\overline{Q}^2,\omega,\lambda) =$$
$$\frac{i\mu^{(4-D)/2}}{2(4\pi)^{D-2}}\mathbf{b}^i\int_0^\infty \mathrm{d}u\, u^{-D/2}e^{-u(\overline{Q}^2+m_q^2)}e^{-\mathbf{b}^2/(4u)}\int_0^{u/\omega}\mathrm{d}t\, t^{1-D/2}e^{-t\omega\lambda m_q^2}e^{-\mathbf{r}^2/(4t)}, \quad (3.18)$$

$$\mathcal{I}(\mathbf{b},\mathbf{r},\overline{Q}^2,\omega,\lambda) =$$
$$\frac{\mu^{(4-D)/2}}{(4\pi)^{D-2}}\int_0^\infty \mathrm{d}u\, u^{1-D/2}e^{-u(\overline{Q}^2+m_q^2)}e^{-\mathbf{b}^2/(4u)}\int_0^{u/\omega}\mathrm{d}t\, t^{1-D/2}e^{-t\omega\lambda m_q^2}e^{-\mathbf{r}^2/(4t)}, \quad (3.19)$$

$$\mathcal{J}(\mathbf{b},\mathbf{r},\overline{Q}^2,\omega,\lambda) =$$
$$(2\pi)^{2-D}\left(\frac{\mu}{\omega}\right)^{\frac{4-D}{2}}\left(\sqrt{\frac{\overline{Q}^2+m_q^2+\lambda m_q^2}{\mathbf{b}^2+\omega\mathbf{r}^2}}\right)^{D-3}K_{D-3}\left(\sqrt{\overline{Q}^2+m_q^2+\lambda m_q^2}\sqrt{\mathbf{b}^2+\omega\mathbf{r}^2}\right). \quad (3.20)$$

3.2 Meson wave function at next-to-leading order

For the heavy vector meson wave function we can use the nonrelativistic expansion developed in ref. [76]. In this expansion, corrections in α_s are included in factors multiplying the leading-order wave function, and corrections suppressed by the heavy quark velocity v appear as derivatives of the leading-order wave function. For a general Fock state n we write this in the following form:

$$\Psi_V^n = \sum_{m,k}C_{n\leftarrow m}^k\int_0^1\frac{\mathrm{d}z'}{4\pi}\left(\frac{1}{m_q}\nabla\right)^k\phi^m(\mathbf{r}=0,z'), \quad (3.21)$$

where ϕ^m is the leading-order wave function (LOWF) for the Fock state m and the sum goes over all Fock states m. The case $m = q\bar{q}$, $n = q\bar{q}$ is shown schematically in figure 1, where the primed indices $0'$, $1'$ correspond to the nonrelativistic quark and antiquark in the LOWF and the non-primed indices 0, 1 correspond to the quark and antiquark in the wave function $\Psi^{q\bar{q}}$. It should be noted that the coefficient functions $C_{n\leftarrow m}^k$ depend on colors and helicities of the particles in Fock states n and m, and the sum over these is left implicit. The derivative ∇ is defined in the mixed space as $\nabla = (\partial_{r_1},\partial_{r_2},(z'-1/2)2m_qi)$, where r_i are the components of the transverse separation $\mathbf{r}$, and $k = (k_1,k_2,k_3)$ is to be understood as a multi-index: $\left(\frac{1}{m_q}\nabla\right)^k = \frac{1}{m_q^{|k|}}\nabla_1^{k_1}\nabla_2^{k_2}\nabla_3^{k_3}$ where $|k| = k_1 + k_2 + k_3$.
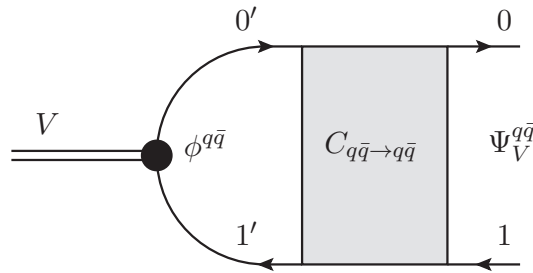
(a) Contribution of the leading-order wave function $\phi^{q\bar{q}}$ to the total vector meson wave function.
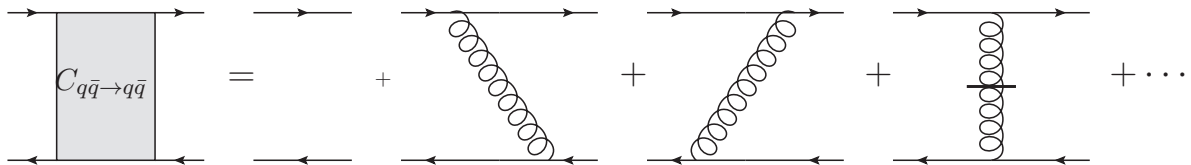
(b) The coefficient function $C_{q\bar{q}\leftarrow q\bar{q}}$ in terms of Feynman diagrams. The self-energy corrections are not shown.

Figure 1. Perturbative corrections to the meson light-front wave function $\Psi_V^{q\bar{q}}$.

The strength of this expansion is that it is now straightforward to include corrections at a given order in α_s and v. Higher-order corrections in α_s can be calculated perturbatively from Feynman diagrams, and they are defined as parts of the coefficient functions $C_{n\leftarrow m}^k$. Relativistic corrections in v can be read from the derivatives which amount to a suppression of $v^{|k|}$.

At next-to-leading order in the nonrelativistic limit, we need the following wave functions [76]:

$$\Psi_V^{q\bar{q}} = C_{q\bar{q}\leftarrow q\bar{q}}^{(0,0,0)} \int_0^1 \frac{\mathrm{d}z'}{4\pi} \phi_{h_0' h_1'}^{q\bar{q}}(\mathbf{r}=0, z'), \tag{3.22}$$

$$\Psi_V^{q\bar{q}g} = C_{q\bar{q}g\leftarrow q\bar{q}}^{(0,0,0)} \int_0^1 \frac{\mathrm{d}z'}{4\pi} \phi_{h_0' h_1'}^{q\bar{q}}(\mathbf{r}=0, z'). \tag{3.23}$$

Here $C_{q\bar{q}\leftarrow q\bar{q}}^{(0,0,0)}$ is calculated to the order $\mathcal{O}(g^2)$ and $C_{q\bar{q}g\leftarrow q\bar{q}}^{(0,0,0)}$ to the order $\mathcal{O}(g)$ in the strong coupling constant. Only the LOWF for the dominating Fock state $q\bar{q}$ contributes at this order in the expansion, as soft gluons in the LOWF Fock state would bring additional suppression in velocity (see also discussion in ref. [76]). Relativistic corrections at leading order in α_s are discussed in more detail in section 4.

As the functions $C_{n\leftarrow m}^{(0,0,0)}$ are fully perturbative (and calculated at NLO accuracy in ref. [76]), the nonperturbative physics is contained in the constants $\int \frac{\mathrm{d}z'}{4\pi} \phi_{h_0' h_1'}^{q\bar{q}}(\mathbf{r}=0, z')$ where h_0' and h_1' are the helicities of the quark and antiquark in the LOWF. The nonrelativistic limit requires that the helicity structure of LOWF is simply $\delta_{(h_0'+h_1')/2, \lambda_V}$ where λ_V is the polarization of the vector meson. To write the expressions in a more compact form we extract the helicity and color structure from the LOWF in the coefficients $\widetilde{C}_{n\leftarrow q\bar{q}}^k$:

$$\widetilde{C}_{n\leftarrow q\bar{q}}^{(0,0,0)} = \frac{1}{\sqrt{N_c}} \delta_{\alpha_0 \alpha_1} \frac{-1}{m_q 2\sqrt{2}} \bar{u}(0') \not{\epsilon}_{\lambda_V} v(1') C_{n\leftarrow q\bar{q}}^{(0,0,0)} \tag{3.24}$$

and write the spin-independent part of the LOWF as $\int \frac{dz'}{4\pi} \phi^{q\bar{q}}(\mathbf{r}=0, z')$. The spinors $u(0'), v(1')$ correspond to the nonrelativistic quark and antiquark in the LOWF with $z_{0'} = z_{1'} = \frac{1}{2}$. The perturbative coefficients required for the transverse NLO calculation in the nonrelativistic limit are then

$$
\widetilde{C}_{q\bar{q} \leftarrow q\bar{q}}^{(0,0,0)} = \frac{1}{\sqrt{N_c}} \delta_{\alpha_0 \alpha_1} \frac{1}{4\sqrt{k_0^+ k_1^+ k_{0'}^+ k_{1'}^+}} \bar{u}(0)\gamma^+ u(0')\bar{v}(1')\gamma^+ v(1)\epsilon_{\lambda_V}^j
$$

$$
\times \left\{ 4\pi\delta(z-1/2)(1+\delta Z)\frac{1}{m_q 2\sqrt{2}}\bar{u}(0')\gamma^j v(1') \right.
$$

$$
+ \frac{\alpha_s C_F}{2\pi} \frac{16\pi z_0(1-z_0)}{(z_0-1/2)^2} \frac{1}{m_q 2\sqrt{2}}\bar{u}(0')\gamma^j v(1') \left[\theta\left(z_0-\frac{1}{2}-\alpha\right) + \theta\left(\frac{1}{2}-z_0-\alpha\right) \right]
$$

$$
\times \left[K_0(\tau) - \frac{1}{2z_0(1-z_0)}\left(\theta\left(z_0-\frac{1}{2}\right)(1-z_0) + \theta\left(\frac{1}{2}-z_0\right)z_0\right)\left(K_0(\tau) - \frac{\tau}{2}K_1(\tau)\right) \right]
$$

$$
- \frac{\alpha_s C_F}{2\pi} 8\pi i K_0(\tau)\left(\theta\left(z_0-\frac{1}{2}-\alpha\right)(1-z_0) + \theta\left(\frac{1}{2}-z_0-\alpha\right)z_0\right)
$$

$$
\left. \times \frac{2m_q}{\sqrt{2}q^+}\mathbf{x}_{01}^i \bar{u}(0')\left[\delta^{ij}\gamma^+(2z_0-1) + \frac{1}{2}\gamma^+\left[\gamma^i, \gamma^j\right]\right]v(1') \right\} \tag{3.25}
$$

and

$$
\widetilde{C}_{q\bar{q}g \leftarrow q\bar{q}}^{(0,0,0)} = \frac{1}{\sqrt{N_c}} t_{\alpha_0\alpha_1}^a \frac{g}{2\pi} \frac{1}{(q^+)^2}\epsilon_\sigma^{j*}\bar{u}(0')\gamma^k \epsilon_{\lambda_V}^k v(1')\bar{v}(1')\gamma^+ v(1)
$$

$$
\times \left(\frac{m_q z_2}{\pi|\mathbf{x}_{20}|\mu}\right)^{(D-4)/2}\sqrt{\frac{2z_2}{1-2z_2}} \cdot 4\pi\delta(z_1-1/2)
$$

$$
\times \left\{ -i(1-z_2)\frac{\mathbf{x}_{20}^i}{|\mathbf{x}_{20}|}K_{D/2-1}(2m_q z_2|\mathbf{x}_{02}|)\bar{u}(0)\left[\delta^{ij} - \frac{z_2}{2(1-z_2)}[\gamma^i, \gamma^j]\right]\gamma^+ u(0') \right.
$$

$$
\left. + z_2 K_{D/2-2}(2m_q z_2|\mathbf{x}_{20}|)\bar{u}(0)\gamma^j \gamma^+ u(0') \right\}
$$

+ gluon emission from antiquark, \tag{3.26}

with

$$
\tau = 2m_q|\mathbf{x}_{01}|\left|z_0 - \frac{1}{2}\right|. \tag{3.27}
$$

The wave function renormalization factor δZ is calculated in the pole-mass scheme and is given by

$$
\delta Z = -\frac{\alpha_s C_F}{2\pi}\left[\frac{1}{D-4}(4\ln(2\alpha)+3) + 2\ln(2\alpha)\left(\ln\left(\frac{m_q^2}{4\pi\mu^2}\right) + 1 + \ln(2\alpha)\right) \right.
$$

$$
\left. + (4\ln(2\alpha)+3)\frac{\gamma_E}{2} + \frac{3}{2}\ln\left(\frac{m_q^2}{4\pi\mu^2}\right) - 2\right]. \tag{3.28}
$$

The contribution from an antiquark emitting the gluon is left implicit in eq. (3.26). Its contribution to the final expression is equal to the quark emitting the gluon, meaning that we can include its contribution by multiplying the result from the quark contribution by two.

3.3 Calculation of the next-to-leading order production

The next-to-leading order amplitude (2.1) has contributions from two terms: the quark-antiquark dipole contribution $2\int_{\mathbf{x}_0\mathbf{x}_1}\int\frac{\mathrm{d}z_0\mathrm{d}z_1}{(4\pi)^2}4\pi\delta(z_0+z_1-1)\Psi_{\gamma^*}^{q\bar{q}}\Psi_V^{q\bar{q}*}N_{01}$ and real gluon emission $2\int_{\mathbf{x}_0\mathbf{x}_1\mathbf{x}_2}\int\frac{\mathrm{d}z_0\mathrm{d}z_1\mathrm{d}z_2}{(4\pi)^3}4\pi\delta(z_0+z_1+z_2-1)\Psi_{\gamma^*}^{q\bar{q}g}\Psi_V^{q\bar{q}g*}N_{012}$. The next-to-leading order corrections to the dipole term come from virtual gluon loops. Using the above expressions for the photon and meson wave functions it is possible to calculate these two contributions.

The evaluation of the dipole term yields

$$
\begin{aligned}
2&\int_{\mathbf{x}_0\mathbf{x}_1}\int\frac{\mathrm{d}z_0\,\mathrm{d}z_1}{(4\pi)^2}4\pi\delta(z_0+z_1-1)\Psi_{\gamma^*}^{q\bar{q}}\Psi_V^{q\bar{q}*}N_{01} \\
&=\int_0^1\frac{\mathrm{d}z'}{4\pi}\phi^{q\bar{q}}(\mathbf{r}=0,z')\int\mathrm{d}^{D-2}\mathbf{x}_{01}\,\mathrm{d}^2\mathbf{b}\,N_{01}(\mathbf{r},\mathbf{b})\sqrt{\frac{N_c}{2}}\frac{2ee_fm_q}{\pi}\bigg\{K_0(\zeta) \\
&\quad+\frac{\alpha_sC_F}{2\pi}\bigg\{-\frac{2}{D-4}\left[4\ln(2\alpha)+3\right]K_{(D-4)/2}(\zeta)+\widetilde{I}_{\mathcal{VMS}}^T\left(\frac{1}{2},\mathbf{x}_{01}\right)+\mathcal{K}^T \\
&\quad+K_0(\zeta)\bigg[\Omega_\mathcal{V}^T\left(\gamma;\frac{1}{2}\right)+L\left(\gamma;\frac{1}{2}\right)-\frac{\pi^2}{3}+\frac{7}{2} \\
&\quad+\frac{1}{\alpha}+4\ln(2\alpha)\ln\left(\frac{2\pi^2|\mathbf{x}_{01}|^4\mu^2e^{\gamma_E}}{\zeta}\right)+3\ln\left(\frac{4\pi^2|\mathbf{x}_{01}|^3\mu^2}{m_q\zeta}\right)\bigg]\bigg\}\bigg\}
\end{aligned}
\tag{3.29}
$$

where $\zeta=|\mathbf{x}_{01}|\sqrt{\frac{1}{4}Q^2+m_q^2}$, $\mathbf{b}=\frac{1}{2}(\mathbf{x}_0+\mathbf{x}_1)$ and

$$
\begin{aligned}
\mathcal{K}^T=\int_0^{1/2}\mathrm{d}z&\bigg\{4z|\mathbf{x}_{01}|\kappa_zK_1\left(|\mathbf{x}_{01}|\kappa_z\right)K_0(\tau)\left[1+(1-2z)^2\right] \\
&+\frac{1}{(z-1/2)^2}\bigg\{8z(1-z)K_0\left(|\mathbf{x}_{01}|\kappa_z\right)\left[K_0(\tau)-\frac{1}{2(1-z)}\left(K_0(\tau)-\frac{\tau}{2}K_1(\tau)\right)\right] \\
&\quad-2K_0(\zeta)\left[\frac{1}{2}+(z-1/2)\left(1+2\gamma_E+2\ln\left(\frac{\tau}{2}\right)\right)\right]\bigg\}\bigg\}.
\end{aligned}
\tag{3.30}
$$

For simplicity, we have chosen the LOWF to be real. The real emission contribution is

$$
2 \int_{\mathbf{x}_0 \mathbf{x}_1 \mathbf{x}_2} \int \frac{\mathrm{d}z_0 \, \mathrm{d}z_1 \, \mathrm{d}z_2}{(4\pi)^3} 4\pi \delta(z_0 + z_1 + z_2 - 1) \Psi_{\gamma^*}^{q\bar{q}g} \Psi_V^{q\bar{q}g*} N_{012}
$$
$$
= \int_0^1 \frac{\mathrm{d}z'}{4\pi} \phi^{q\bar{q}}(\mathbf{r} = 0, z') \int \mathrm{d}^{D-2}\mathbf{x}_{01} \, \mathrm{d}^{D-2}\mathbf{x}_{20} \, \mathrm{d}^2\mathbf{b} \int_\alpha^{1/2} \mathrm{d}z_2
$$
$$
\times N_{012} \sqrt{\frac{N_c}{2}} \frac{2 e e_f m_q}{\pi} \frac{\alpha_s C_F}{2\pi} 4\pi \left(\frac{m_q z_2}{\pi |\mathbf{x}_{20}| \mu} \right)^{\frac{D-4}{2}}
$$
$$
\times \left\{ 8 K_{(D-2)/2}(2 m_q z_2 |\mathbf{x}_{20}|) \frac{i \mathbf{x}_{20}^i}{|\mathbf{x}_{20}|} m_q \left[-\mathcal{I}_{(j)}^i \left((D-2) z_2^2 - 2 z_2 + 1 \right) - z_2^2 \hat{\mathcal{I}}_{(j)}^i (2 z_2 - 1) \right. \right.
$$
$$
\left. + \mathcal{I}_{(k)}^i \frac{1}{2 z_2 + 1} + z_2^2 \hat{\mathcal{I}}_{(k)}^i \frac{1}{(2 z_2 + 1)^2} \left(4 z_2^2 - 4 z_2 + 1 \right) \right]
$$
$$
+ 8 z_2 K_0 \left(2 m_q z_2 |\mathbf{x}_{20}| \right) \left[\frac{1}{2} \mathcal{I}_{(j)}^{ii} (-1 + 2 z_2) + \frac{1}{2(1 + 2 z_2)} \mathcal{I}_{(k)}^{ii} \left(4 z_2^2 + 4 z_2 + 1 \right) \right.
$$
$$
\left. \left. - 2 \left((1 - 2 z_2) z_2 \mathcal{J}_{(l)} + 2 m_q^2 z_2^2 \mathcal{I}_{(j)} \right) \right] \right\},
\tag{3.31}
$$

where we have set $D \to 4$ wherever possible and $\mathbf{b} = z_0 \mathbf{x}_0 + z_1 \mathbf{x}_1 + z_2 \mathbf{x}_2$. Both the dipole term (3.29) and real gluon emission contributions (3.31) have divergences in the $D \to 4$ (UV) and $\alpha \to 0$ (IR) limits. However, the UV divergences cancel in their sum. Therefore it is useful to subtract the UV divergent part of the real correction and add it to the dipole term. Note that now the division of the NLO contributions between the two terms is not unique but depends on the chosen UV subtraction scheme. We choose to do this subtraction following the scheme presented in ref. [96] and used in refs. [74, 93]. In our case, this means that we write:

$$
N_{012} \mathbf{x}_{20}^i \mathcal{I}_{(j)}^i K_{(D-2)/2}(2 m_q z_2 |\mathbf{x}_{20}|) =
$$
$$
\left\{ N_{012} \mathbf{x}_{20}^i \mathcal{I}_{(j)}^i K_{(D-2)/2}(2 m_q z_2 |\mathbf{x}_{20}|) - N_{01} \mathcal{I}_{\mathrm{UV}}^{q\bar{q}g} \right\} + N_{01} \mathcal{I}_{\mathrm{UV}}^{q\bar{q}g}
\tag{3.32}
$$

where

$$
\mathcal{I}_{\mathrm{UV}}^{q\bar{q}g} = (m_q z_2 |\mathbf{x}_{20}|)^{-D/2+1} \Gamma(D/2 - 1)^2
$$
$$
\times \frac{i \mu^{2-D/2}}{8 \pi^{D/2}} |\mathbf{x}_{20}|^{4-D} \left(\frac{\zeta}{2\pi |\mathbf{x}_{01}|^2} \right)^{(D-4)/2} K_{(D-4)/2}(\zeta) e^{-|\mathbf{x}_{20}|^2 / (|\mathbf{x}_{01}|^2 e^{\gamma_E})}.
\tag{3.33}
$$

Although the subtraction procedure is not unique, this particular choice has the correct behavior at $\mathbf{x}_{20} \to 0$ and results in relatively simple expressions. With the subtraction of

eq. (3.32) we can perform the $\mathbf{x}_{20}$ and z_2 integrals before adding it to the dipole part:

$$\left[2\int_{\mathbf{x}_0\mathbf{x}_1\mathbf{x}_2}\int\frac{\mathrm{d}z_0\,\mathrm{d}z_1\,\mathrm{d}z_2}{(4\pi)^3}4\pi\delta(z_0+z_1+z_2-1)\Psi_{\gamma^*}^{q\bar{q}g}\Psi_V^{q\bar{q}g*}N_{012}\right]_{\text{UV subtraction}}$$

$$=\int_0^1\frac{\mathrm{d}z'}{4\pi}\phi^{q\bar{q}}(\mathbf{r}=0,z')\int\mathrm{d}^{D-2}\mathbf{x}_{01}\,\mathrm{d}^{D-2}\mathbf{x}_{20}\,\mathrm{d}^2\mathbf{b}\int_\alpha^{1/2}\mathrm{d}z_2$$

$$\times N_{01}\sqrt{\frac{N_c}{2}}\frac{2ee_fm_q}{\pi}\frac{\alpha_sC_F}{2\pi}4\pi\left(\frac{mz_2}{\pi|\mathbf{x}_{20}|\mu}\right)^{(D-4)/2}\frac{-8im_q}{|\mathbf{x}_{20}|}\left[(D-2)z_2^2-2z_2+1\right]\mathcal{I}_{\text{UV}}^{q\bar{q}g}$$

$$=\int_0^1\frac{\mathrm{d}z'}{4\pi}\phi^{q\bar{q}}(\mathbf{r}=0,z')\int\mathrm{d}^{D-2}\mathbf{x}_{01}\,\mathrm{d}^2\mathbf{b}\,N_{01}\sqrt{\frac{N_c}{2}}\frac{2ee_fm_q}{\pi}\frac{\alpha_sC_F}{2\pi}K_{(D-4)/2}(\zeta)$$

$$\times\left\{(4\ln(2\alpha)+3)\left[\frac{2}{D-4}+\ln\left(\frac{\zeta}{2\pi^2|\mathbf{x}_{01}|^4\mu^2e^{\gamma_E}}\right)\right]-1\right\}. \tag{3.34}$$

Adding this to the dipole term we get

$$-i\mathcal{A}_{q\bar{q}}=2\int_0^1\frac{\mathrm{d}z'}{4\pi}\phi^{q\bar{q}}(\mathbf{r}=0,z')\int\mathrm{d}^2\mathbf{x}_{01}\,\mathrm{d}^2\mathbf{b}\,N_{01}(\mathbf{r},\mathbf{b})\sqrt{\frac{N_c}{2}}\frac{ee_fm_q}{\pi}\left\{K_0(\zeta)\right.$$

$$+\frac{\alpha_sC_F}{2\pi}\left\{\widetilde{I}_{\mathcal{VMS}}^T\left(\frac{1}{2},\mathbf{x}_{01}\right)+\mathcal{K}^T+K_0(\zeta)\left[\Omega_{\mathcal{V}}^T\left(\gamma;\frac{1}{2}\right)+L\left(\gamma;\frac{1}{2}\right)-\frac{\pi^2}{3}+\frac{5}{2}\right.\right.$$

$$\left.\left.\left.+\frac{1}{\alpha}-3\ln\left(\frac{m_q|\mathbf{x}_{01}|}{2}\right)-3\gamma_E\right]\right\}\right\}. \tag{3.35}$$

Note that this expression is now UV finite, allowing us to take the limit $D\to 4$. The UV subtraction also cancelled the dependence on the scale μ introduced by dimensional regularization.

For the real correction, the UV subtracted form is

$$-i\mathcal{A}_{q\bar{q}g}=2\int_0^1\frac{\mathrm{d}z'}{4\pi}\phi^{q\bar{q}}(\mathbf{r}=0,z')\sqrt{\frac{N_c}{2}}\frac{ee_fm_q}{\pi}\int\mathrm{d}^2\mathbf{x}_{01}\,\mathrm{d}^2\mathbf{b}\,\mathrm{d}^2\mathbf{x}_{20}\int_\alpha^{1/2}\mathrm{d}z_2\,\frac{\alpha_sC_F}{2\pi}\mathcal{K}_{q\bar{q}g}$$

$$\tag{3.36}$$

where

$$\mathcal{K}_{q\bar{q}g}=32\pi m_q\left\{K_1(2m_qz_2|\mathbf{x}_{20}|)\frac{i\mathbf{x}_{20}^i}{|\mathbf{x}_{20}|}\left[-\mathcal{I}_{(j)}^i\left((1-z_2)^2+z_2^2\right)-z_2^2\left(2z_2-1\right)\hat{\mathcal{I}}_{(j)}^i\right.\right.$$

$$\left.+\mathcal{I}_{(k)}^i\frac{1}{2z_2+1}+\hat{\mathcal{I}}_{(k)}^i\frac{z_2^2(2z_2-1)^2}{(2z_2+1)^2}\right]N_{012}$$

$$+\frac{z_2}{m_q}K_0\left(2m_qz_2|\mathbf{x}_{20}|\right)\left[\frac{-1+2z_2}{2}\mathcal{I}_{(j)}^{ii}+\frac{1+2z_2}{2}\mathcal{I}_{(k)}^{ii}-2(1-2z_2)z_2\mathcal{J}_{(l)}-4m_q^2z_2^2\mathcal{I}_{(j)}\right]N_{012}$$

$$\left.-\left((1-z_2)^2+z_2^2\right)\frac{1}{8\pi^2m_qz_2|\mathbf{x}_{20}|^2}K_0\left(\zeta\right)e^{-\mathbf{x}_{20}^2/(\mathbf{x}_{01}^2e^{\gamma_E})}N_{01}\right\}. \tag{3.37}$$

This expression is also UV finite and does not depend on the renormalization scale μ.

The dipole term (3.35) still has an apparent IR divergence coming from the $\frac{1}{\alpha}$ term. This is related to the fact that the LOWF is also divergent and has to be renormalized. This can be seen explicitly in the NLO equation for the leptonic width which in the nonrelativistic limit is given by [76]

$$\Gamma(V \to e^- e^+) = \frac{2N_c e_f^2 e^4}{3\pi M_V} \left| \int \frac{\mathrm{d}z'}{4\pi} \phi^{q\bar{q}}(\mathbf{r} = 0, z') \right|^2 \left[1 + \frac{\alpha_s C_F}{\pi} \left(\frac{1}{\alpha} - 4 \right) \right]. \tag{3.38}$$

As the leptonic width has to be finite, the LOWF has to have an IR divergent part that cancels the $\frac{1}{\alpha}$ divergence appearing in this equation. One way to account for this IR divergence of the LOWF is to invert eq. (3.38) and solve the integrated LOWF directly from it, which gives at the order $\mathcal{O}(\alpha_s)$

$$\int \frac{\mathrm{d}z'}{4\pi} \phi^{q\bar{q}}(\mathbf{r} = 0, z') = \sqrt{\Gamma(V \to e^- e^+) \frac{3\pi M_V}{2e_f^2 e^4 N_c}} \left[1 + \frac{\alpha_s C_F}{2\pi} \left(4 - \frac{1}{\alpha} \right) \right]. \tag{3.39}$$

This expression can then used in eqs. (3.35) and (3.36) to cancel the IR divergence in the dipole term and to connect the nonperturbative integral over LOWF to the leptonic width for which one can use the experimental value in numerical calculations. The dipole part of the amplitude is then

$$-i\mathcal{A}_{q\bar{q}} = \sqrt{\Gamma(V \to e^- e^+) \frac{3\pi M_V}{2N_c e_f^2 e^4}} \sqrt{\frac{N_c}{2}} \frac{e e_f m_q}{\pi} 2 \int \mathrm{d}^2\mathbf{x}_{01} \int \mathrm{d}^2\mathbf{b} \left\{ \mathcal{K}_{q\bar{q}}^{\mathrm{LO}} + \frac{\alpha_s C_F}{2\pi} \mathcal{K}_{q\bar{q},\Gamma}^{\mathrm{NLO}} \right\} \tag{3.40}$$

where the LO part is

$$\mathcal{K}_{q\bar{q}}^{\mathrm{LO}} = K_0(\zeta) N_{01}, \tag{3.41}$$

and the NLO part, which contains the corrections from virtual gluon loops, is defined as

$$\mathcal{K}_{q\bar{q},\Gamma}^{\mathrm{NLO}} = \left\{ \widetilde{I}_{\mathcal{V}\mathcal{MS}}^T \left(\frac{1}{2}, \mathbf{x}_{01} \right) + \mathcal{K}^T \right.$$
$$\left. + K_0(\zeta) \left[\Omega_{\mathcal{V}}^T \left(\gamma; \frac{1}{2} \right) + L \left(\gamma; \frac{1}{2} \right) - \frac{\pi^2}{3} + \frac{5}{2} + 4 - 3\ln\left(\frac{m_q |\mathbf{x}_{01}|}{2} \right) - 3\gamma_E \right] \right\} N_{01}. \tag{3.42}$$

We define this way of renormalizing the LOWF to be the *decay width* scheme. Note that this renormalization scheme adds the term $\frac{\alpha_s C_F}{2\pi} \times 4$ from the equation of the leptonic width to the virtual correction $\mathcal{K}_{q\bar{q},\Gamma}^{\mathrm{NLO}}$.

We can also renormalize the LOWF in a different way where such an additional term does not appear. This is done by connecting the LOWF $\phi^{q\bar{q}}$ in our regularization scheme to the dimensionally regularized one $\phi_{\mathrm{DR}}^{q\bar{q}}$ following ref. [76]:

$$\int \frac{\mathrm{d}z'}{4\pi} \phi^{q\bar{q}} = \int \frac{\mathrm{d}z'}{4\pi} \phi_{\mathrm{DR}}^{q\bar{q}} \times \left[1 - \frac{\alpha_s C_F}{2\pi} \frac{1}{\alpha} \right]. \tag{3.43}$$

This also cancels the IR divergence in the virtual correction. Now the dipole part of the amplitude can be written as

$$-i\mathcal{A}_{q\bar{q}} = \int \frac{\mathrm{d}z'}{4\pi} \phi_{\mathrm{DR}}^{q\bar{q}} \times \sqrt{\frac{N_c}{2}} \frac{e e_f m_q}{\pi} 2 \int \mathrm{d}^2\mathbf{x}_{01} \int \mathrm{d}^2\mathbf{b} \left\{ \mathcal{K}_{q\bar{q}}^{\mathrm{LO}} + \frac{\alpha_s C_F}{2\pi} \mathcal{K}_{q\bar{q},\Psi}^{\mathrm{NLO}} \right\} \tag{3.44}$$

where the LO part is still given by eq. (3.41) but the NLO correction is slightly different:

$$\mathcal{K}_{q\bar{q},\Psi}^{\mathrm{NLO}} = \left\{ \widetilde{I}_{\mathcal{V}\mathcal{MS}}^T \left(\frac{1}{2}, \mathbf{x}_{01} \right) + \mathcal{K}^T \right.$$

$$\left. + K_0(\zeta) \left[\Omega_{\mathcal{V}}^T \left(\gamma; \frac{1}{2} \right) + L \left(\gamma; \frac{1}{2} \right) - \frac{\pi^2}{3} + \frac{5}{2} - 3\ln \left(\frac{m_q |\mathbf{x}_{01}|}{2} \right) - 3\gamma_E \right] \right\} N_{01}. \quad (3.45)$$

We will refer to this renormalization scheme of the LOWF as the *wave function* scheme. Here one still has to determine the value of the dimensionally regularized LOWF for numerical calculations. This can likewise be done with the leptonic width, from which we can solve the dimensionally regularized LOWF in the nonrelativistic limit as

$$\int \frac{\mathrm{d}z'}{4\pi} \phi_{\mathrm{DR}}^{q\bar{q}} = \sqrt{\Gamma(V \to e^-e^+) \frac{3\pi M_V}{2e_f^2 e^4 N_c}} \left[1 + \frac{\alpha_s C_F}{2\pi} \times 4 \right]. \quad (3.46)$$

Note that when the relativistic corrections are taken into account in section 4 the relation (3.46) will be modified. The difference between the decay width and wave function schemes boils down to the location of the NLO correction $\frac{\alpha_s C_F}{2\pi} \times 4$ from the equation for the leptonic width, i.e., whether the correction appears in the equation for the virtual correction or as an overall coefficient when solving the LOWF. The difference between the schemes is parametrically of the order $\mathcal{O}(\alpha_s^2)$ which is of higher order than considered here. This difference is also numerically small in realistic kinematics as we will demonstrate in appendix A.

When choosing the scheme one also has to take into account the running of the coupling constant α_s. In the decay width scheme we use the running coupling in the coordinate space $\alpha_s(\mathbf{x}_{ij})$, eq. (2.7), whereas in the wave function scheme the coupling constant is evaluated at the momentum scale of the decay process. Following ref. [111], we take this to be the vector meson mass so that the coupling constant in eq. (3.46) is chosen to be $\alpha_s(M_V)$.

3.4 Rapidity divergence and the leading-order result

The real correction (3.36) is still IR divergent as can be verified by taking the $\alpha \to 0$ limit for the lower bound of the z_2 integral. This divergence is actually related to the rapidity evolution of the dipole amplitude. The divergent part of the real correction (3.37) is

$$\frac{\alpha_s C_F}{2\pi} \mathcal{K}_{q\bar{q}g}^{\mathrm{sing}} = \frac{\alpha_s C_F}{\pi^2} \frac{1}{z_2} K_0(\zeta) \frac{\mathbf{x}_{01}^2}{\mathbf{x}_{20}^2 \mathbf{x}_{21}^2} [N_{012} - N_{01}] \quad (3.47)$$

from which we recognize, using eq. (2.4), the leading-order BK equation (2.5) if the running of the coupling is neglected. Thus at fixed coupling it is possible to combine this divergent part with the leading-order part (3.41) of the production amplitude by taking into account the rapidity evolution of the dipole amplitude.

The amount of BK evolution is controlled by the lower limit of the z_2 integral (recall that $Y = \ln(z_2 q^+/P^+)$ as discussed in section 2.2). In practice one should not take here the $\alpha \to 0$ limit. Instead, the lower limit has to be set to a finite value. The reason is the following: as the invariant mass $M_{q\bar{q}g}$ of the $q\bar{q}g$ system goes like $M_{q\bar{q}g}^2 \sim 1/z_2$ at small

z_2, in the limit $z_2 \to 0$ we would have $M_{q\bar{q}g} \to \infty$. However, in the calculation we employ the eikonal approximation which assumes that $M_{q\bar{q}g}^2 \ll W^2$ where W is the center-of-mass energy of the photon-proton system. Therefore we should set the lower limit, denoted by $z_{\min}$ from now on, such that the eikonal limit is satisfied. We follow ref. [66] and choose $z_{\min} = P^+/q^+$.

The target plus momentum is given by $P^+ = Q_0^2/(2P^-)$ where Q_0^2 is again the transverse momentum scale of the target which we have taken to be $Q_0^2 = 1\,\text{GeV}^2$ following [66]. The center-of-mass energy of the photon-proton system is then given by $W^2 = 2q^+P^- - Q^2 + m_N^2$. Using these expressions we get the following condition for z_2:

$$z_2 > z_{\min} = \frac{P^+}{q^+} = \frac{Q_0^2}{2P^-q^+} = \frac{Q_0^2}{W^2 + Q^2 - m_N^2}. \tag{3.48}$$

Using this integration limit we find that the z_2 integral of the $\mathcal{K}_{q\bar{q}g}^{\text{sing}}$ part corresponds to the evolution of the dipole amplitude from the initial rapidity $Y_0 = 0$ to the rapidity

$$Y_{\text{dip}} = \ln \frac{\frac{1}{2}}{z_{\min}} = \ln \frac{W^2 + Q^2 - m_N^2}{2Q_0^2} \tag{3.49}$$

using the leading order BK equation.

Evaluating the dipole amplitude at this rapidity corresponds to a resummation of large logarithms $\alpha_s \ln W^2$. As parametrically $\alpha_s \ln W^2 \sim 1$, the actual leading-order part of the production amplitude corresponds to the term $\mathcal{K}_{q\bar{q}}^{\text{LO}}(Y_{\text{dip}})$ where we use the rapidity Y_{dip} to evaluate the dipole amplitude:

$$-i\mathcal{A}_{\text{LO}}^T = \int \frac{\mathrm{d}z'}{4\pi}\phi_{\text{DR}}^{q\bar{q}} \times \sqrt{\frac{N_c}{2}}\frac{ee_f m}{\pi}2\int \mathrm{d}^2\mathbf{x}_{01}\int \mathrm{d}^2\mathbf{b}\,\mathcal{K}_{q\bar{q}}^{\text{LO}}(Y_{\text{dip}}). \tag{3.50}$$

Note that the IR divergent part (3.47) combined with the lowest order part in (3.41) results in eq. (3.50) (which corresponds to the *subtracted* scheme of ref. [70]) exactly only at fixed coupling. As discussed in section 2.2, in this work we use dipole amplitudes that are evolved using running coupling BK equations that include a resummation of most important higher order corrections to all orders and as such approximate the full next-to-leading order BK equation accurately. Consequently the definition of the leading order scattering amplitude is not unique, but we use the definition (3.50) as it naturally includes also the parametrically large resummation effects included in the used BK equations.

At next-to-leading order, we choose to evaluate the leading-order part at the initial rapidity Y_0 and let the $q\bar{q}g$ part take care of the rapidity evolution. This corresponds to the *unsubtracted* scheme used also in ref. [66]. For the virtual correction $\mathcal{K}_{q\bar{q}}^{\text{NLO}}$ we choose to evaluate the dipole amplitudes at the evolved rapidity Y_{dip} which corresponds to the total evolution range as discussed above (but note that the dependence on the evolution rapidity is formally of higher order in α_s). For the term $\mathcal{K}_{q\bar{q}g}$ in eq. (3.37) we use the definition $Y = \ln k_2^+/P^+$ and evaluate the dipole scattering amplitude at the rapidity:

$$Y_{\text{q}\bar{\text{q}}\text{g}} = \ln \frac{z_2 q^+}{P^+} = \ln z_2 + \ln \frac{W^2 + Q^2 - m_N^2}{Q_0^2} \tag{3.51}$$

Taking the rapidity dependence of the dipole amplitudes into account we can write the final scattering amplitude for the next-to-leading order production amplitude of transversely polarized vector meson in the form

$$
-i\mathcal{A}^T = \int \frac{\mathrm{d}z'}{4\pi} \phi_{\mathrm{DR}}^{q\bar{q}} \times \sqrt{\frac{N_c}{2}} \frac{ee_f m_q}{\pi} 2 \int \mathrm{d}^2\mathbf{x}_{01} \int \mathrm{d}^2\mathbf{b} \left\{ \mathcal{K}_{q\bar{q}}^{\mathrm{LO}}(Y_0) \right.
$$
$$
\left. + \frac{\alpha_s C_F}{2\pi} \mathcal{K}_{q\bar{q},\Psi}^{\mathrm{NLO}}(Y_{\mathrm{dip}}) + \int \mathrm{d}^2\mathbf{x}_{20} \int_{z_{\mathrm{min}}}^{1/2} \mathrm{d}z_2 \frac{\alpha_s C_F}{2\pi} \mathcal{K}_{q\bar{q}g}(Y_{q\bar{q}g}) \right\}. \quad (3.52)
$$

Here $\mathcal{K}_{q\bar{q}}^{\mathrm{LO}}$, $\mathcal{K}_{q\bar{q},\Psi}^{\mathrm{NLO}}$ and $\mathcal{K}_{q\bar{q}g}$ are given by eqs. (3.41), (3.45) and (3.37), and the rapidity values in parentheses correspond to the rapidities at which the dipole amplitudes are evaluated. An analogous result can also be written in the decay width scheme. The initial rapidity is chosen to be $Y_0 = 0$ following ref. [66]. The strong coupling constant is evaluated at the distance scale set by the parent dipole, $|\mathbf{x}_{01}|^2$, in the first two terms and by the smallest dipole $\min\{|\mathbf{x}_{01}|^2, |\mathbf{x}_{20}|^2, |\mathbf{x}_{21}|^2\}$ in the last term, consistently with the NLO fit of ref. [66].

We note that in ref. [66] the virtual contribution $\mathcal{K}_{q\bar{q}}^{\mathrm{NLO}}$ is evaluated at the rapidity $Y = \ln 1/x_{\mathrm{bj}}$ which in our case would correspond to $Y^{\mathrm{incl}} = \ln 1/x_{\mathbb{P}} \neq Y_{\mathrm{dip}}$. It is not entirely consistent to use a different evolution rapidity in our NLO calculation of vector meson production and in the fit procedure used to determine the dipole-proton amplitude. However, as in ref. [93] we choose to use the more natural choice for the evolution rapidity and note that the difference between the usage of the two rapidities is formally of higher order in α_s.

4 Relativistic corrections at leading order

We can use the nonrelativistic expansion (3.21) to include the first relativistic corrections of order v^2. At leading order in α_s, the nonrelativistic expansion reduces to a distributional identity

$$
\Psi_{\mathrm{LO}}^{V\to q\bar{q}} = \phi_{h_0 h_1}^{q\bar{q}}(\mathbf{r}, z) = \sum_k \frac{1}{k_1! k_2! k_3!} (m_q r_1)^{k_1} (m_q r_2)^{k_2} 4\pi \left(-\frac{1}{2i}\partial_z \right)^{k_3} \delta\left(z - 1/2\right)
$$
$$
\times \int_0^1 \frac{\mathrm{d}z'}{4\pi} \frac{1}{m_q^{k_1+k_2}} \partial_{r_1}^{k_1} \partial_{r_2}^{k_2} \phi_{h_0 h_1}^{q\bar{q}}(\mathbf{r} = 0, z')[2i(z' - 1/2)]^{k_3} \quad (4.1)
$$

from which it is easy to read off the coefficients $C_{q\bar{q}\leftarrow q\bar{q}}^k$. In general, including terms of order v^2 corresponds to including the terms with $|k| = k_1 + k_2 + k_3 \leq 2$. From now on, we will focus on the case where the meson polarization is $\lambda_V = +1$. The final result, eq. (4.10), will be the same for both transverse polarizations $\lambda_V = \pm 1$. We can then write the relativistic correction at the order v^2 as

$$
-i\mathcal{A}_{\mathrm{rel}}^{\lambda_V=+1} = \sqrt{\frac{N_c}{2}} \frac{ee_f m_q}{\pi} 2 \int \mathrm{d}^2\mathbf{x}_{01} \int \mathrm{d}^2\mathbf{b}\, N_{01}
$$
$$
\times \left\{ K_0(\zeta)\frac{m_q^2}{2} \left[r_1^2 \phi_{++}^{q\bar{q}}(2,0,0) + r_2^2 \phi_{++}^{q\bar{q}}(0,2,0) \right] - \frac{r^2 Q^2}{8\zeta} K_1(\zeta)\phi_{++}^{q\bar{q}}(0,0,2) \right.
$$
$$
- K_1(\zeta)\frac{i\zeta(r_1 - ir_2)}{2r^2}\Big[r_1 \left(\phi_{+-}^{q\bar{q}}(1,0,0) - \phi_{-+}^{q\bar{q}}(1,0,0) \right)
$$
$$
\left. + r_2 \left(\phi_{+-}^{q\bar{q}}(0,1,0) - \phi_{-+}^{q\bar{q}}(0,1,0) \right) \Big] \right\} \quad (4.2)
$$

– 19 –

where we introduced a simplifying notation

$$\phi^{q\bar{q}}_{h_0 h_1}(k_1, k_2, k_3) := \int_0^1 \frac{dz'}{4\pi} \frac{1}{m_q^{k_1+k_2}} \partial_{r_1}^{k_1} \partial_{r_2}^{k_2} \phi^{q\bar{q}}_{h_0 h_1}(\mathbf{r} = 0, z')[2i(z' - 1/2)]^{k_3} \qquad (4.3)$$

and $r_i = (\mathbf{x}_{01})_i$. Strictly speaking, it is the complex conjugate of eq. (4.2) that corresponds to vector meson production, but as this quantity is real we have chosen to write it in this form to get rid of the complex conjugates on the meson wave function. Note that we do not have here terms like $\phi^{q\bar{q}}_{+-}(1, 0, 1)$ or $\phi^{q\bar{q}}_{--}(2, 0, 0)$. The reason for this is that non-dominant spin components also bring additional velocity suppression, giving a total velocity suppression of $v^{|k|+|\frac{1}{2}(h'_0+h'_1)-\lambda_V|}$. This is because in momentum space the meson wave function must have angle-dependence given by $(p_x \pm ip_y)^{|\frac{1}{2}(h'_0+h'_1)-\lambda_V|}$ which then has to be coupled with similar terms when combined with the photon wave function. This explains why the non-dominant spin terms have to go like $p_T^{2|\frac{1}{2}(h'_0+h'_1)-\lambda_V|} \sim v^{|h'_0+h'_1-2\lambda_V|}$, meaning that there is an additional velocity suppression of $v^{|\frac{1}{2}(h'_0+h'_1)-\lambda_V|}$. This can be seen explicitly in ref. [92] where $\phi^{\lambda_V=+1}_{+-}(1, 0, 0) \sim v^2$ and $\phi^{\lambda_V=+1}_{--}(2, 0, 0) = 0$ at $\mathcal{O}(v^2)$.

We can simplify eq. (4.2) by using the spin-parity $J^{PC} = 1^{--}$ of the vector meson. Although parity is only a dynamical symmetry in the light-front, one can still use it to derive symmetry relations of the light-front wave function using similar properties such as the so-called mirror parity (see the discussion in ref. [112] and the references therein). The spin of the meson allows us to write the dependence on the azimuthal angle $\varphi_\perp$ as $\phi^{\lambda_V}_{h_0 h_1}(\mathbf{r}, z) = e^{im_l\varphi_\perp}\bar{\phi}^{\lambda_V}_{h_0 h_1}(|\mathbf{r}|, z)$ where $m_l = \lambda_V - (h_0 + h_1)/2$ is the magnetic quantum number and the part $\bar{\phi}$ does not depend on the angle $\varphi_\perp$. The C- and P-parities give the requirements $\phi^{\lambda_V}_{h_0 h_1}(\mathbf{r}, z) = C(-1)^{1+m_l}\phi^{\lambda_V}_{h_1 h_0}(\mathbf{r}, 1-z)$ and $\phi^{\lambda_V}_{h_0 h_1}(\mathbf{r}, z) = P(-1)^{m_l+J}e^{im_l\varphi_\perp}\bar{\phi}^{-\lambda_V}_{-h_0,-h_1}(|\mathbf{r}|, z)$. Using these, the relativistic corrections can be simplified as

$$-i\mathcal{A}^{\lambda_V=+1}_{\text{rel}} = \sqrt{\frac{N_c}{2}} \frac{ee_f m_q}{\pi} 2 \int d^2\mathbf{x}_{01} \int d^2\mathbf{b}\, N_{01}$$

$$\times \left\{ \frac{1}{2}m^2\mathbf{x}_{01}^2 K_0(\zeta)\phi^{q\bar{q}}_{++}(2, 0, 0) - \frac{r^2 Q^2}{8\zeta} K_1(\zeta)\phi^{q\bar{q}}_{++}(0, 0, 2) - \zeta K_1(\zeta)\left[i\phi^{q\bar{q}}_{+-}(1, 0, 0)\right] \right\}.$$
$$(4.4)$$

In ref. [93] where longitudinal production is calculated at NLO, the decay width scheme is used throughout the paper to renormalize the LOWF. This is possible for the longitudinal production even with the relativistic corrections, as it turns out that the leptonic width for a longitudinally polarized vector meson depends only on the fully nonrelativistic part of the LOWF. For transverse production it is no longer possible to use the decay width scheme with the relativistic corrections as then the leptonic width (at leading order in α_s) has the form

$$\Gamma(V(\lambda_V = +1) \to e^- e^+) = \frac{2N_c e_f^2 e^4}{3\pi M_V} \left[\int \frac{dz'}{4\pi} \frac{1}{2M_V z'(1-z')} \right.$$

$$\left. \times \left\{ m_q\phi^{q\bar{q}}_{++}(\mathbf{r}, z') + i(\partial_{\mathbf{r}_1} - i\partial_{\mathbf{r}_2})\left(-z'\phi^{q\bar{q}}_{+-}(\mathbf{r}, z') + (1-z')\phi^{q\bar{q}}_{-+}(\mathbf{r}, z')\right) \right\}_{\mathbf{r}=0} \right]^2$$
$$(4.5)$$

which also has contributions from relativistic components of the wave function. The leptonic width (4.5) can be calculated using the light-cone perturbation theory (see e.g. ref. [113]), and eq. (4.5) is the form one gets without making any assumptions about the meson wave function. In the nonrelativistic limit $\phi_{++}^{q\bar{q}} \sim \delta(z' - \frac{1}{2})$, $M_V = 2m_q$, eq. (4.5) reduces to eq. (3.38) at LO.

For consistency, one should use the same scheme when combining NLO results of transverse and longitudinal production. We choose to use the wave function scheme throughout this paper as then it is possible to quantify the significance of the relativistic corrections without additional complications coming from the scheme dependence. The previously derived longitudinal cross section is presented in the wave function scheme in appendix B.

Using eqs. (3.52) and (4.4) requires that we know the nonperturbative constants related to the LOWF. Note that when relativistic corrections are included we cannot use eq. (3.43) to directly express dimensionally regularized wave function in terms of the leptonic decay width, as in the case of transverse polarization the relativistic corrections contribute to the decay width as can be seen from eq. (4.5). We instead calculate these constants using the heavy vector meson wave function from ref. [92] that includes relativistic corrections of order v^2. This is a convenient choice as this wave function connects the nonperturbative constants in eq. (3.52) and (4.4) to the universal NRQCD matrix elements at order v^2. Using this wave function allows us to write

$$\phi_{\mathrm{DR}}^{q\bar{q}} = \phi_{++}^{q\bar{q}}(0,0,0) = \frac{1}{\sqrt{4m_q}}\left[\phi_{\mathrm{RF}}(0) + \frac{7}{12m_q^2}\vec{\nabla}^2\phi_{\mathrm{RF}}(0)\right], \qquad (4.6)$$

$$\phi_{++}^{q\bar{q}}(2,0,0) = \phi_{++}^{q\bar{q}}(0,0,2) = 2[i\phi_{+-}^{q\bar{q}}(1,0,0)] = \frac{1}{6\sqrt{m_q}}\frac{1}{m_q^2}\vec{\nabla}^2\phi_{\mathrm{RF}}(0) \qquad (4.7)$$

where $\phi_{\mathrm{RF}}(\vec{r})$ is the value of the *rest-frame* wave function in the position space (see ref. [92] for the corresponding light-front wave function). One advantage of using this particular choice of the wave function is that it results in the same leptonic width for both the longitudinal and transverse polarizations at the order $\mathcal{O}(v^2)$, which follows from the spherical symmetry of the wave function in the rest frame.

The rest-frame wave function can be connected to the NRQCD matrix elements by [111]

$$\phi_{\mathrm{RF}}(0) = \frac{1}{\sqrt{2N_c}}\sqrt{\langle\mathcal{O}_1\rangle_V}\left[1 + \mathcal{O}\left(v^4\right)\right], \qquad (4.8)$$

$$\vec{\nabla}^2\phi_{\mathrm{RF}}(0) = -\langle\vec{q}^2\rangle_V\phi_{\mathrm{RF}}(0)\left[1 + \mathcal{O}\left(v^2\right)\right] = -\langle\vec{q}^2\rangle_V\frac{1}{\sqrt{2N_c}}\sqrt{\langle\mathcal{O}_1\rangle_V}\left[1 + \mathcal{O}\left(v^2\right)\right]. \qquad (4.9)$$

Numerical values for the NRQCD matrix elements can be obtained from the decay width data. For J/ψ production, we use the values for $\langle\mathcal{O}_1\rangle_V$ and $\langle\vec{q}^2\rangle_V$ (with their correlated uncertainties) from ref. [111]. Similarly, for Υ production the matrix elements from ref. [114] are used. We note that the matrix elements for J/ψ in ref. [111] are determined using a charm mass $m_c = 1.4\,\mathrm{GeV}$. On the other hand, in our calculation we use the non-relativistic value $m_c = M_V/2$, where M_V is the J/ψ mass, effectively neglecting the quark momentum contribution to the meson invariant mass (similarly the b quark mass is taken to be half of the Υ mass). Consequently, the different mass values result in a difference which is of higher order in quark velocity v, see also the discussion in ref. [92].

The relativistic corrections to the production amplitude can then be written as

$$-i\mathcal{A}_{\mathrm{rel}}^T = \sqrt{\frac{N_c}{2}} \frac{e e_f m_q}{\pi} 2 \int \mathrm{d}^2\mathbf{x}_{01} \int \mathrm{d}^2\mathbf{b}\, N_{01}$$

$$\times \frac{1}{6\sqrt{m_q}} \frac{1}{m_q^2} \vec{\nabla}^2 \phi_{\mathrm{RF}}(0) \left\{ \frac{1}{2} m_q^2 \mathbf{x}_{01}^2 K_0(\zeta) - \frac{\mathbf{x}_{01}^2 Q^2}{8\zeta} K_1(\zeta) - \frac{1}{2}\zeta K_1(\zeta) \right\}. \quad (4.10)$$

The main result of this work, the exclusive heavy vector meson production cross section at the order $\mathcal{O}(\alpha_s v^0, \alpha_s^0 v^2)$ is then eq. (3.52), to which eq. (4.10) is added.

5 Numerical results

We show numerical results for the transverse vector meson production amplitude and for the total (longitudinal and transverse) coherent vector meson production cross section in $\gamma^* + p$ scattering at next-to-leading order. We consider separately the fully nonrelativistic limit $\mathcal{O}(\alpha_s v^0)$, and the case where first relativistic corrections are included, $\mathcal{O}(\alpha_s v^0, \alpha_s^0 v^2)$. The longitudinal vector meson production is calculated using the results of ref. [93] included for completeness in appendix B.

The numerical calculations are done in the wave function scheme for the renormalization of the LOWF. We note that it would be possible to use the decay width scheme in the nonrelativistic limit, but this would introduce additional scheme dependence when comparing to the case with the relativistic corrections included. The difference between the two wave function renormalization schemes is studied numerically in detail in appendix A.

5.1 Transverse vector meson production amplitude

First we study in detail different contributions to the forward ($t = 0$) transverse J/ψ production amplitude, eq. (3.52), in the nonrelativistic limit. This equation is finite and can be directly evaluated numerically. We limit ourselves to the forward production case as we do not want to specify any specific form of impact parameter dependence for the dipole-proton scattering amplitude, and at $t = 0$ only the dipole-proton amplitude integrated over the impact parameter appears. The dipole-proton amplitude is obtained from ref. [66] where the assumption is that the impact parameter $\mathbf{b}$ integral only results in a constant factor $\sigma_0/2$ interpreted as the proton transverse area, also determined from the fit to HERA structure function data.

Different contributions to the scattering amplitude as a function of center-of-mass energy W and photon virtuality Q^2 are shown in figure 2. In these calculations we have chosen to use as the dipole amplitude the fit performed with the KCBK evolution and using an initial evolution rapidity $Y_{0,\mathrm{BK}} = 4.61$ in ref. [66]. Note that in ref. [66] two different initial rapidities for the BK evolution are used ($Y_{0,\mathrm{BK}} = 4.61$ and $Y_{0,\mathrm{BK}} = 0$), and the dipole amplitude is frozen in the region $Y_0 < Y < Y_{0,\mathrm{BK}}$. Results using both of these initial evolution rapidities are shown later in this section.

The different contributions to the scattering amplitude shown in figure 2 are labeled as follows. First, NLO corresponds to the full NLO level scattering amplitude of eq. (3.52).
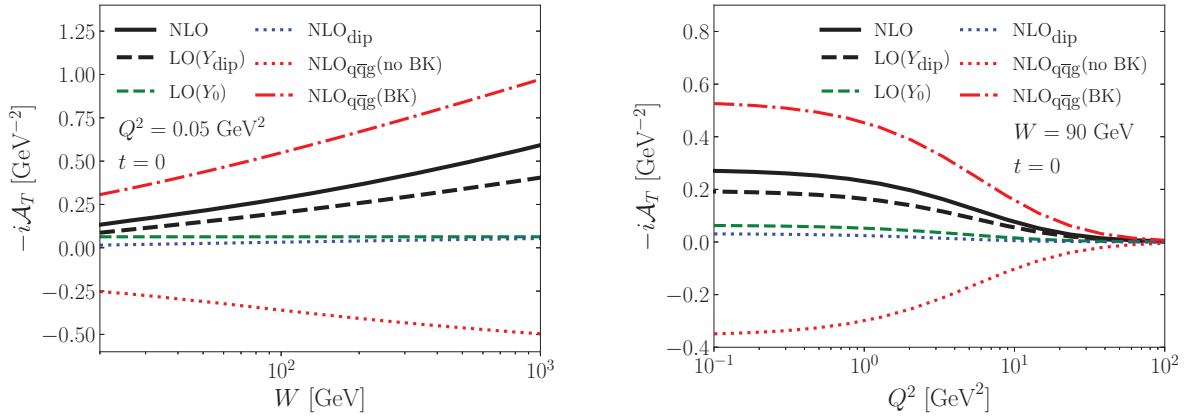
(a) Amplitude as a function of the center-of-mass energy W.

(b) Amplitude as a function of the photon virtuality Q^2.

Figure 2. Different contributions to the transverse exclusive J/ψ production scattering amplitude at next-to-leading order.

The leading-order result, obtained using a BK-evolved dipole amplitude evaluated at the rapidity $Y = Y_{\rm dip}$ is labeled as $\rm LO(Y_{\rm dip})$ and shown in eq. (3.50), and $\rm LO(Y_0)$ corresponds to the $\sim \alpha_s^0$ part (first line of eq. (3.52)) where the dipole amplitude is evaluated at the initial rapidity. The virtual NLO contribution is denoted by $\rm NLO_{\rm dip}$, but we emphasize that an UV divergence has been cancelled between the real and virtual contributions and as such the division of NLO corrections into the real and virtual parts is not unique. The real gluon emission correction obtained using the UV subtraction scheme used in this work, eq. (3.36), is shown as $\rm NLO_{q\bar{q}g}(BK)$ and $\rm NLO_{q\bar{q}g}(no\ BK)$. The $\rm NLO_{q\bar{q}g}(BK)$ term refers to the singular part of the gluon emission contribution (see eq. (3.47)) which can be included in the BK evolution, and $\rm NLO_{q\bar{q}g}(no\ BK)$ corresponds to the remaining pure NLO correction. In this notation the total NLO amplitude can be expressed as

$$\rm NLO = LO(Y_0) + NLO_{\rm dip} + NLO_{q\bar{q}g}(BK) + NLO_{q\bar{q}g}(no\ BK). \qquad (5.1)$$

The real gluon emission contribution ($\rm NLO_{q\bar{q}g}$ terms) has a large contribution, which is expected as the BK evolution resumming terms $\sim \alpha_s \ln 1/x \sim 1$ to all orders should be considered to be part of the leading order result. However, we also find a significant negative NLO correction $\rm NLO_{q\bar{q}g}(no\ BK)$ to the BK evolution from the actual NLO calculation where the exact gluon emission kinematics is included. In our UV subtraction scheme the virtual NLO contribution $\rm NLO_{\rm dip}$ is very small. The total NLO correction is significant, about $\sim 50\%$ of the (BK-evolved) LO contribution. These conclusions are valid at all W and Q^2.

In the longitudinal production case presented in ref. [93], the NLO corrections were found to be even more significant ($\sim 75\%$ of the LO result); however, these results cannot be directly compared as the longitudinal calculation used the decay width scheme for the renormalization of the LOWF as opposed to the wave function scheme. In the decay width scheme the NLO corrections are larger because of the larger scheme-dependent constant in $\mathcal{K}_{\rm NLO}^{q\bar{q}}$, which is true for both longitudinal and transverse production. It should be noted that this difference in

the NLO corrections is compensated by the overall LOWF-related constant in the amplitude which is smaller in the decay width scheme, bringing the numerical values of the full NLO result in the two schemes closer to each other and thus reducing the scheme dependence.

The term $\mathrm{NLO}_{q\bar{q}g}(\mathrm{BK})$ corresponds to the (leading order) BK evolution, and as such one could also take the leading order scattering amplitude to be $\mathrm{LO}(Y_0) + \mathrm{NLO}_{q\bar{q}g}(\mathrm{BK})$. As can be seen in figure 2, this differs from $\mathrm{LO}(Y_{\mathrm{dip}})$ by roughly a factor of 2. As discussed in section 3.4 this difference would vanish at fixed coupling if the dipole amplitude satisfied the leading order BK equation, but in this work where we use resummed BK evolution equations to approximate the full NLO BK equation it is more natural to use $\mathrm{LO}(Y_{\mathrm{dip}})$ as a leading order amplitude. This choice includes most of the parametrically large resummation corrections to the leading order amplitude and renders the NLO corrections moderate. On the other hand, if one used $\mathrm{LO}(Y_0) + \mathrm{NLO}_{q\bar{q}g}(\mathrm{BK})$ as a leading order amplitude, the NLO corrections would be dominant and even render the cross section negative at high Q^2.

5.2 Differential cross section at $t = 0$

Next we calculate the coherent transverse J/ψ production cross section at $t = 0$. When squaring the scattering amplitude only the genuine NLO corrections are kept, and NNLO contributions proportional to α_s^2 are dropped out. In practice, eq. (3.50) is used as the leading-order amplitude, and when squaring the amplitude its interference with genuine NLO contributions is needed. This NLO correction is obtained from eq. (3.52) by subtracting the leading-order amplitude (3.50). Similarly, when including relativistic corrections we do not keep the square of the relativistic correction that would be proportional to v^4 (but note that such contribution was included in the numerical results reported in ref. [93]). Instead, when relativistic corrections are included we add the interference term between the leading-order amplitude, eq. (3.50), and the v^2 suppressed part of the amplitude, eq. (4.10).

The differential J/ψ production cross section at $t = 0$ is shown in figure 3(a) as a function of the center-of-mass energy W, using different fits for the dipole-proton scattering amplitude from ref. [66]. Results obtained using fits where the initial evolution rapidity is $Y_{0,\mathrm{BK}} = 4.61$ (or $\eta_{0,\mathrm{BK}} = 4.61$ in the case of TBK evolution) are shown as solid lines, and dashed lines correspond to calculations where fits with the initial rapidity $Y_{0,\mathrm{BK}} = 0$ ($\eta_{0,\mathrm{BK}} = 0$) are used. The LO result is "LO LOBK" which uses the leading-order dipole-proton amplitude from ref. [42] (we use the fit referred to as "MV^e" in [42]) at the rapidity $Y = \ln 1/x_{\mathbb{P}}$ as this is the rapidity scale used in the LO fit.

We see that the NLO corrections reduce the cross section slightly. This is in contrast to what is seen in figure 2, and can be explained by the fact that in figure 2 the same NLO-fitted dipole amplitude was used for both the LO and NLO results. When nonperturbative parameters describing the initial condition for the BK evolution are determined in leading-order fits such as in refs. [42, 115], they effectively absorb a part of the higher-order contributions.

These results are in line with what has been obtained for longitudinal vector meson production at NLO [93]. The NLO corrections generally change the center-of-mass energy dependence (faster evolution at low W compared to LO, slower or similar to LO at high W). We also find some deviations between the results with different NLO dipole amplitudes,

$$p + \gamma^* \to p + \mathrm{J}/\psi$$

$$p + \gamma^* \to p + \mathrm{J}/\psi$$
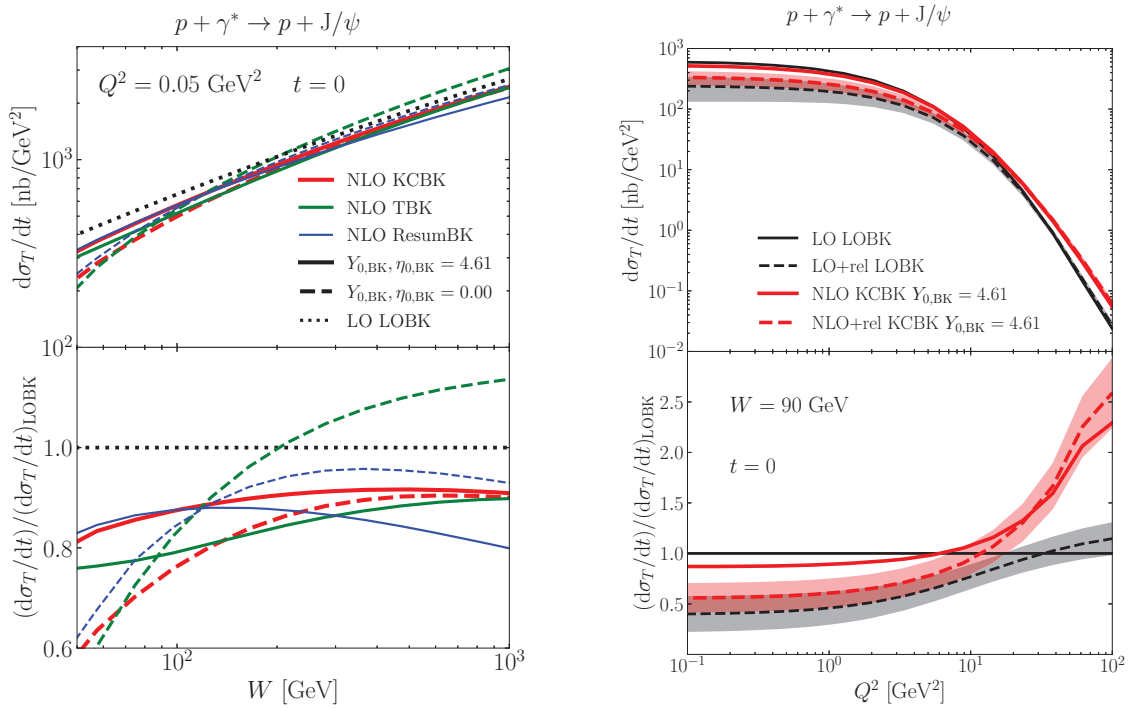
(a) Comparison of results with different dipole amplitudes.

(b) Comparison of the relativistic and next-to-leading order corrections.

**Figure 3.** Differential cross section for transverse J/ψ production at next-to-leading order. In the case of TBK evolution the rapidity values correspond to the target rapidity η. The uncertainty bands are obtained by taking into account the uncertainties of the NRQCD matrix elements.

similarly to the longitudinal J/ψ production case [93]. As all of these dipole amplitudes were fitted to the same HERA structure function data, this deviation shows that vector meson production gives us complementary information to structure function analyses. This will be discussed more in section 5.3.

In figure 3(b), we show the effect of relativistic corrections at LO and NLO. At small Q^2, the relativistic corrections reduce the cross section by $\sim 60\%$ at LO and $\sim 40\%$ at NLO and are numerically more important than the next-to-leading order QCD corrections, that in turn have a much larger effect at large Q^2. The relativistic corrections have a smaller relative effect at NLO than at LO because of the sizable NLO corrections (recall that we do not include $\mathcal{O}(\alpha_\mathrm{s} v^2)$ corrections). It should be noted that the relativistic corrections do not vanish at high Q^2, which is in contrast with longitudinal production where the relativistic corrections are negligible for high photon virtualities [93, 116].

5.3 Total vector meson production cross section

The transverse vector meson production can be combined with longitudinal production to calculate the total vector meson production cross section $\sigma_\mathrm{tot} = \sigma_L + \sigma_T$. This is a phenomenologically more interesting quantity as most exclusive vector meson production data is measured in terms of the total production cross section.
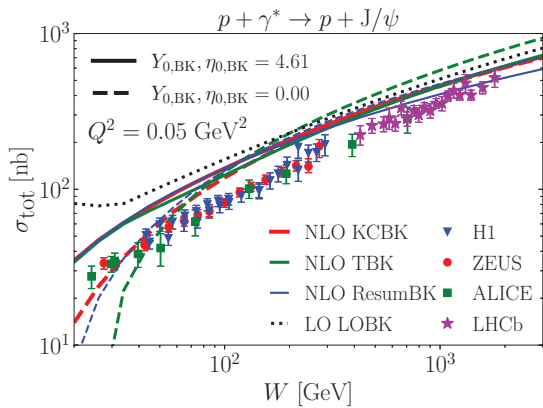
(a) Cross section at the nonrelativistic limit as a function of the center-of-mass energy W.
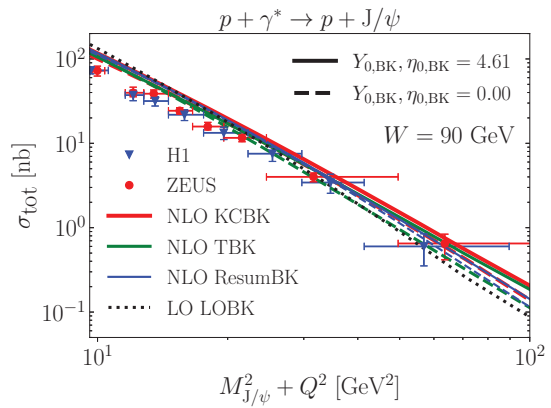
(b) Cross section at the nonrelativistic limit as a function of the photon virtuality Q^2.
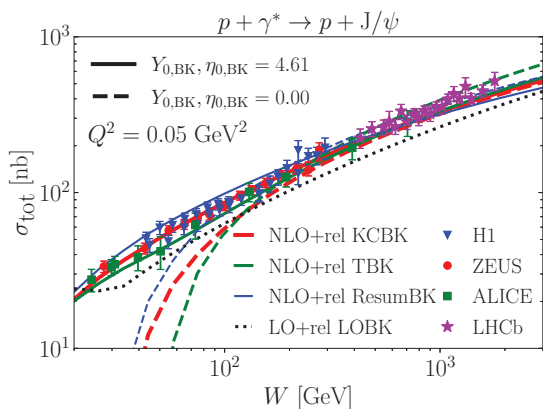
(c) Cross section with v^2 corrections as a function of the center-of-mass energy W.
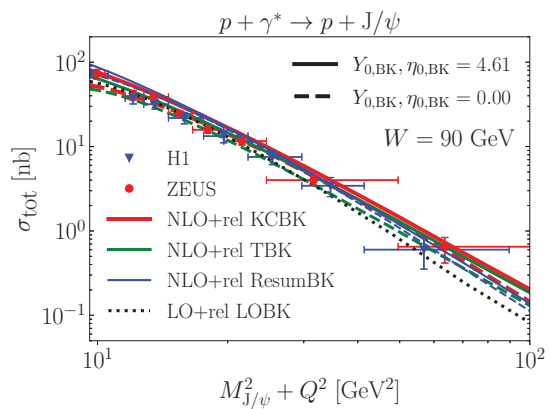
(d) Cross section with v^2 corrections as a function of the photon virtuality Q^2.

Figure 4. Total exclusive J/ψ production at next-to-leading order, with HERA data from [7–9, 14], ALICE data from [19, 20], and LHCb data from [22, 23].

As discussed above, we only calculate vector meson production at $t = 0$ (see eq. (2.1)) as we do not want to specify any particular model for the proton impact parameter profile. In order to obtain results that can be compared with experimental t-integrated cross section measurements, we use the experimentally measured t slopes that allow us to write the $\gamma^* + p \to V + p$ cross section as

$$\frac{\mathrm{d}\sigma}{\mathrm{d}t} = e^{-b|t|} \times \frac{\mathrm{d}\sigma}{\mathrm{d}t}(t = 0). \tag{5.2}$$

For the J/ψ production the slope b can be written as $b = b_0 + 4\alpha' \ln(W/(90\,\mathrm{GeV}))$, where the experimentally measured values for the J/ψ production are $b_0 = 4.15\,\mathrm{GeV}^{-2}$ and $\alpha' = 0.116\,\mathrm{GeV}^{-2}$ [8]. This allows us to calculate the total t-integrated vector meson production.

The results are shown in figure 4 separately for the nonrelativistic case and with the v^2 relativistic corrections, and they are compared to the experimental data measured by

H1 [9, 14], ZEUS [7, 8], ALICE [19, 20], and LHCb [22, 23] collaborations. However, we emphasize again that the phenomenological analysis here is not fully consistent as we are using the dipole amplitudes extracted from a fit to structure function data where only the light quark contribution is included [66], and a fully consistent setup would require a heavy quark contribution to be included in the structure function calculations also. Consequently, strong conclusions cannot be drawn from these data comparisons.

Keeping this uncertainty in mind, we find that both the W and Q^2 dependence of the experimental data is described reasonably well, especially when the relativistic corrections are included. For the virtuality dependence, the relativistic corrections are important at low Q^2 and the next-to-leading order corrections also modify the dependence on Q^2 slightly, however both LO and NLO results are compatible with the HERA data. Generally, we again find that both the relativistic and NLO corrections can be numerically important and need to be included when considering the J/ψ production.

At $W \lesssim 100\,\text{GeV}$ the calculations using dipole amplitudes from BK fits where the evolution starts at the smallest possible evolution rapidity $Y_{0,\text{BK}} = 0$ (or $\eta_{0,\text{BK}} = 0$ in the case of TBK evolution) result in W slope which is not compatible with the data. The next-to-leading order corrections also become extremely large, even rendering the cross section negative. As we will demonstrate in appendix A, the results obtained with $Y_{0,\text{BK}} = 0$ ($\eta_{0,\text{BK}} = 0$) in the low-W region are also sensitive to the wave function renormalization scheme, but this is not the case for the fits with $Y_{0,\text{BK}} = 4.61$ ($\eta_{0,\text{BK}} = 4.61$). We consider this behavior in the low-energy region to be an artifact of the unphysical initial condition obtained in the BK evolution fits in ref. [66] when the evolution is started at $Y_{0,\text{BK}} = 0$, in which case there is a long evolution before one enters in the region probed by small-x structure function data. In that case the fit results in unphysical parameters, and especially the anomalous dimension γ is very large at the initial condition.[1] As heavy vector meson production is sensitive to smaller size dipoles than the structure function fitted in [66], similar unrealistically large NLO corrections were not observed in the NLO fit of ref. [66]. Consequently, we consider the results obtained with $Y_{0,\text{BK}} = 4.61$ to be our main numerical results and emphasize that heavy vector meson production data provides additional constraints for the determination of the nonperturbative initial condition for the small-x evolution.

The leading-order result is constant at $W < 31\,\text{GeV}$ which corresponds to $x_{\mathbb{P}} > 0.01$. This is because in the leading-order calculation the dipole amplitude is evaluated at $Y = \ln 1/x_{\mathbb{P}}$ and no BK evolution is included in the region $Y < \ln\frac{1}{0.01}$ in the leading order fit [118] used in this work.

Next we study the longitudinal-to-transverse J/ψ production cross section ratio where e.g. the normalization uncertainty cancels. This is plotted in figure 5 where we show the results for the nonrelativistic case (figure 5(a)) and with the relativistic corrections (figure 5(b)), compared to the HERA data [7, 9]. Excluding the TBK $\eta_{0,\text{BK}} = 0.00$ dipole, the NLO corrections have only a modest effect on this ratio, slightly increasing it in general.

---

[1]The dipole amplitude behaves as $N_{01} \sim (\mathbf{x}_{01}^2 Q_s^2)^\gamma$ in the dilute region, and large γ corresponds to e.g. negative unintegrated gluon distribution [117].

(a) Ratio in the nonrelativistic limit.
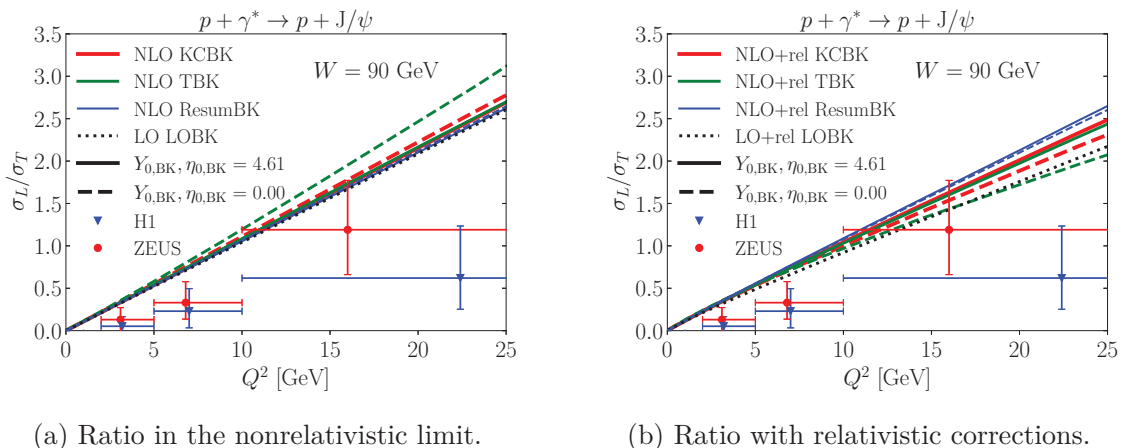
(b) Ratio with relativistic corrections.

Figure 5. Longitudinal J/ψ production cross section divided by the transverse cross section compared to H1 [9] and ZEUS [7] data at $W = 90$ GeV.
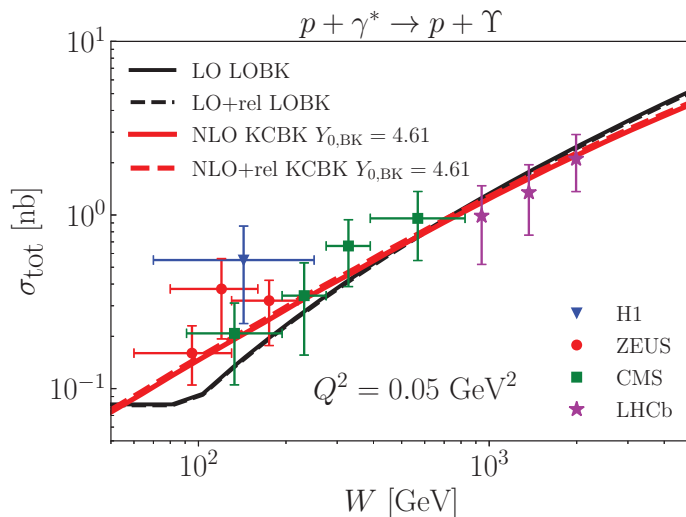

Figure 6. Exclusive Υ photoproduction cross section as a function of center-of-mass energy W compared with HERA [119–121] and LHC [122, 123] data. Results are obtained using the KCBK evolution equation with initial evolution rapidity $Y_{0,\mathrm{BK}} = 4.61$.

In the nonrelativistic limit the differences between the different dipole amplitude fits having initial evolution rapidity $Y_{0,\mathrm{BK}} = 4.61$ (or $\eta_{0,\mathrm{BK}} = 4.61$) are negligible, whereas with $Y_{0,\mathrm{BK}} = 0$ ($\eta_{0,\mathrm{BK}} = 0$) there is some variation. Including the relativistic corrections increases this variation in both cases. The agreement with the experimental data is similar for both the LO and NLO results, and in both cases the ratio seems to be somewhat overestimated. This ratio is sensitive to the form of the wave function (see e.g. ref. [92]), and in particular including the relativistic corrections improves the agreement with the HERA data slightly.

Finally, we consider exclusive Υ photoproduction. As Υ is much heavier than the J/ψ studied above, relativistic corrections become very small and it can be expected to be more sensitive to the next-to-leading order QCD corrections. The Υ photoproduction cross section as a function of the center-of-mass energy W is shown in figure 6 and compared with

HERA [119–121], CMS [122] and LHCb [123] data. The t-integration of the analytic result is done using eq. (5.2) with the experimentally measured W-independent slope parameter $b = 4.3\,\mathrm{GeV}^{-2}$ [124]. The relativistic corrections, calculated using the NRQCD matrix elements from ref. [114], are indeed small at $\sim 3\%$ level at all W. The next-to-leading order contributions are larger, and result in a slower W dependence compared to leading-order results. Results obtained at leading and next-to-leading order are both compatible with the available data. Again the leading-order result is constant at $W < 95\,\mathrm{GeV}$ where $x_{\mathbb{P}} > 0.01$.

6 Conclusions

We have presented the first calculation for transversely polarized exclusive heavy vector meson production at next-to-leading order accuracy in the Color Glass Condensate framework. The main result of this work is eq. (3.52), which is the scattering amplitude for the transverse vector meson production at NLO in the nonrelativistic limit. We have also presented how relativistic corrections, which are generally as important numerically as the NLO QCD corrections (in the case of J/ψ production), can be consistently included in the NLO calculation. The corresponding part of the scattering amplitude is given in eq. (4.10). Combined with the NLO calculation for the longitudinal production presented in ref. [93], the results of this paper allow for phenomenological studies of heavy vector meson production at next-to-leading order accuracy.

The NLO corrections are numerically significant for both the transverse and longitudinal production amplitude. This is largely compensated by the smaller dipole amplitude in the NLO calculation, making the NLO results mostly in line with the LO production and rendering the NLO corrections generally moderate. When the first relativistic corrections are added the agreement of the coherent J/ψ production cross section with the HERA and LHC data is improved, especially at small photon virtualities where the relativistic corrections are larger than the NLO corrections.

If the NLO cross sections are calculated using dipole amplitude fits from ref. [66] where there is a long evolution before one enters the region constrained by the small-x structure function data ($Y_{0,\mathrm{BK}} = 0$ or $\eta_{0,\mathrm{BK}} = 0$ fits), the NLO corrections become very large at small center-of-mass energies and even result in negative cross sections. However, we also note that the nonperturbative parameters describing the initial condition in these fits are not physically well motivated. Large NLO corrections observed in this case illustrate how heavy particle production is sensitive to different length scales than structure function calculations and can provide additional constraints when the nonperturbative initial condition for the Balitsky-Kovchegov equation is determined.

Now that the results for both longitudinal and transverse [73–75] photon wave functions with massive quarks are available, it will be possible to extend the dipole amplitude fits of ref. [66] to the massive quark case. This will allow for a consistent phenomenological study of NLO vector meson production at $t = 0$, which was not possible in this paper. Furthermore, as the impact parameter dependence of the gluon structure is directly related to the t dependence of vector meson production, it would be especially interesting to study t-dependent vector meson production amplitudes. This requires additional modeling for

the impact parameter dependence of the dipole amplitude, which is the reason it was not considered in this work.

With these possible future developments in mind, the results presented in this paper can be used for extensive comparisons with heavy vector meson production data from HERA [7, 8, 14] and from the UPC physics program at the LHC [20, 22, 23], along with making predictions for the future EIC. The results can also be extended from proton targets to heavy nuclei by changing the dipole-target scattering amplitude, which enables studies of non-linear QCD dynamics in heavy nuclei at small-x. This is especially interesting given the existing and future data from ultra-peripheral Pb+Pb collisions at the LHC [24–29] and possibilities at the future nuclear DIS experiments.

Acknowledgments

A   Dependence on the wave function renormalization scheme

As discussed in section 4, the renormalization of the LOWF can be done in different ways. In this paper we consider two different renormalization schemes, called the *decay width* scheme (eq. (3.39)) and the *wave function* scheme (eq. (3.43)). The reason for the different schemes is that the decay width scheme is convenient in the nonrelativistic case as then one can use the same running coupling constant (2.7) as in the rest of the calculation when renormalizing the meson wave function. On the other hand the wave function scheme is necessary when considering the relativistic corrections as in that case the decay width scheme is not possible for transverse production. This makes the NLO cross section dependent on the choice of the wave function renormalization scheme. The choice of the scheme appears parametrically at α_s^2, and is thus of higher order than we consider here, but it can still have an effect on the numerical results. This is what we will study in this appendix.

In the nonrelativistic case we can choose to use either of these two schemes. The decay width scheme is used as described by eq. (3.39). For the wave function scheme, we can calculate the dimensionally regularized LOWF in eq. (3.43) from the nonrelativistic limit of the leptonic width using eq. (3.46). In that case one has to choose the scale at which to calculate the coupling constant. A natural choice is the mass of the vector meson which in the case of J/ψ evaluates to $\alpha_s(M_{J/\psi}) \approx 0.25$ [111] (for Υ this is $\alpha_s(M_\Upsilon) \approx 0.18$ [114]). The difference between the decay width and wave function schemes is then where the NLO contribution
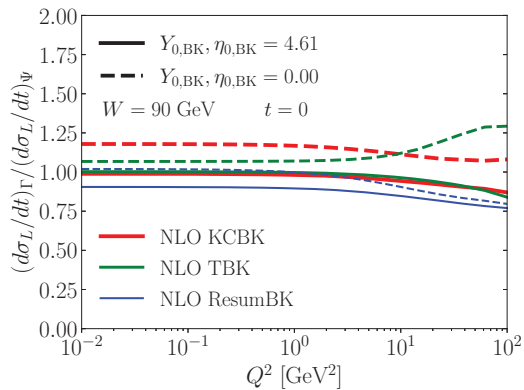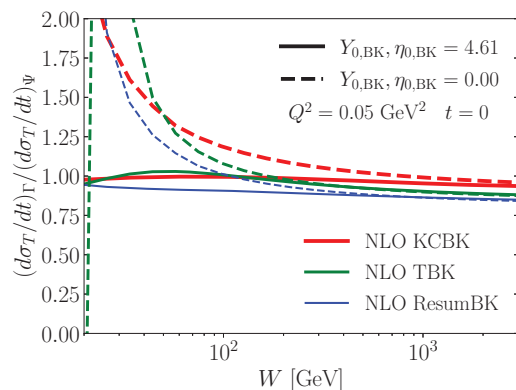
(a) Longitudinal production as a function of virtuality.
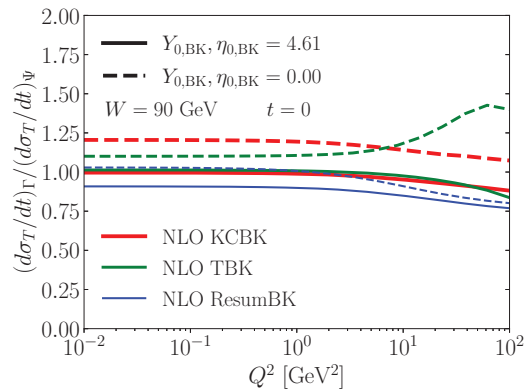
(b) Transverse production as a function of virtuality.
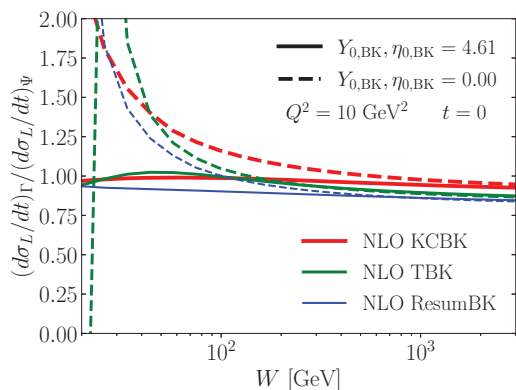
(c) Longitudinal production as a function of center-of-mass energy.

(d) Transverse production as a function of center-of-mass energy.

Figure 7. Scheme dependence of the differential J/ψ production cross section at NLO illustrated as a ratio of the cross sections calculated in the decay width (Γ) and wave function (Ψ) schemes in the nonrelativistic limit.

to the decay width appears when calculating the NLO production amplitude. In the decay width scheme it is calculated as part of the virtual correction $\mathcal{K}_{q\bar{q}}^{\mathrm{NLO}}$; in the wave function scheme it appears when we calculate the value of the dimensionally regularized LOWF.

To quantify the effects of the scheme choice, we have evaluated the NLO differential cross section for exclusive J/ψ production as a function of Q^2 and W in the nonrelativistic case using the two different schemes. The ratio of these cross sections is shown in figure 7 for both longitudinal and transverse production. We see that in the calculations where a BK evolution starting at rapidity $Y_{0,\mathrm{BK}} = 4.61$ (or $\eta_{0,\mathrm{BK}} = 4.61$ in the case of TBK evolution) is used there is only a small dependence on the scheme, of the order 10%. On the other hand, if the BK evolution starts at initial rapidity 0 the differences between the two schemes become very large at small center-of-mass energies W. However, we note that as discussed in section 5 the initial conditions for evolutions starting at rapidity $Y_{0,\mathrm{BK}} = 0$ have unphysical features that do not strongly affect the structure function calculations and the fit process of ref. [66], but have a large effect here as heavy vector meson production is

sensitive to smaller dipole sizes.

B Longitudinal vector meson production at next-to-leading order

For completeness, we list here the expressions for longitudinal vector meson production at NLO from ref. [93]. The NLO production amplitude can be divided into similar parts as in the case of transverse production. In the decay width scheme, the production amplitude can be written as

$$
-i\mathcal{A}^L = -\sqrt{\Gamma(V \to e^-e^+)\frac{3\pi M_V}{2N_c e_f^2 e^4}}\sqrt{\frac{N_c}{2}}\frac{ee_f Q}{2\pi}2\int \mathrm{d}^2\mathbf{x}_{01}\int \mathrm{d}^2\mathbf{b}\left\{\mathcal{K}_{q\bar{q}}^{\mathrm{LO}}(Y_0)\right.
$$
$$
\left. +\frac{\alpha_s C_F}{2\pi}\mathcal{K}_{q\bar{q},\Gamma}^{\mathrm{NLO},L}(Y_{\mathrm{dip}})+\frac{\alpha_s C_F}{2\pi}\int \mathrm{d}^2\mathbf{x}_{20}\int_{z_{\min}}^{1/2}\mathrm{d}z_2\,\mathcal{K}_{q\bar{q}g}^L(Y_{\mathrm{qqg}})\right\} \quad \text{(B.1)}
$$

where $\mathcal{K}_{q\bar{q}}^{\mathrm{LO}}$ is defined in eq. (3.41),

$$
\mathcal{K}_{q\bar{q},\Gamma}^{\mathrm{NLO},L}(Y_{\mathrm{dip}})=N_{01}(Y_{\mathrm{dip}})\times\left[\tilde{\mathcal{I}}_\nu\left(\frac{1}{2},\mathbf{x}_{01}\right)+\mathcal{K}^L\right.
$$
$$
\left. +K_0(\zeta)\left(\Omega_{\mathcal{V}}^L\left(\gamma;\frac{1}{2}\right)+L\left(\gamma;\frac{1}{2}\right)-\frac{\pi^2}{3}+2+4-3\ln\left(\frac{|\mathbf{x}_{01}|m_q}{2}\right)-3\gamma_E\right)\right]
$$
$$
\text{(B.2)}
$$

and

$$
\mathcal{K}_{q\bar{q}g}^L(Y_{\mathrm{qqg}})=-32\pi m_q\left\{\frac{i\mathbf{x}_{20}^i}{|\mathbf{x}_{20}|}K_1(2m_q z_2|\mathbf{x}_{20}|)\right.
$$
$$
\times\left[\left((1-z_2)^2+z_2^2\right)\mathcal{I}_{(j)}^i+(2z_2^2-1)(1-2z_2)\mathcal{I}_{(k)}^i\right]N_{012}(Y_{\mathrm{qqg}})
$$
$$
+4m_q z_2^3 K_0(2m_q z_2|\mathbf{x}_{20}|)\left[\mathcal{I}_{(j)}-\frac{1-2z_2}{1+2z_2}\mathcal{I}_{(k)}\right]N_{012}(Y_{\mathrm{qqg}})
$$
$$
\left. +\frac{1}{8\pi^2}\left((1-z_2)^2+z_2^2\right)\frac{1}{m_q z_2|\mathbf{x}_{20}|^2}K_0(\zeta)e^{-\mathbf{x}_{20}^2/(\mathbf{x}_{01}^2 e^{\gamma_E})}N_{01}(Y_{\mathrm{qqg}})\right\}. \quad \text{(B.3)}
$$

The special functions $L(\gamma,z)$, $\mathcal{I}_{(j)}$, $\mathcal{I}_{(k)}$, $\mathcal{I}_{(j)}^i$ and $\mathcal{I}_{(k)}^i$ are defined in section 3.1. The terms $\mathcal{K}^L$ and $\Omega_{\mathcal{V}}^L$ can be written as

$$
\mathcal{K}^L=\int_0^{1/2}\mathrm{d}z\left\{16z(1-z)K_0\left(|\mathbf{x}_{01}|\sqrt{\overline{Q}^2+m_q^2}\right)2z[K_0(\tau)-\tau K_1(\tau)]\right.
$$
$$
+\frac{1}{(z-1/2)^2}\left\{16z(1-z)K_0\left(|\mathbf{x}_{01}|\sqrt{\overline{Q}^2+m_q^2}\right)\left[2z(1-z)K_0(\tau)-z\left(K_0(\tau)-\frac{\tau}{2}K_1(\tau)\right)\right]\right.
$$
$$
\left.\left.-K_0(\zeta)\left[1+2\left(z-\frac{1}{2}\right)\left[1+2\gamma_E+2\ln(m_q|\mathbf{x}_{01}|)+2\ln\left(\frac{1}{2}-z\right)\right]\right]\right\}\right\} \quad \text{(B.4)}
$$

– 32 –

and

$$\Omega_{\mathcal{V}}^L(\gamma; z) = \frac{1}{2z} \left[\ln(1-z) + \gamma \ln\left(\frac{1+\gamma}{1+\gamma-2z} \right) \right]$$
$$+ \frac{1}{2(1-z)} \left[\ln(z) + \gamma \ln\left(\frac{1+\gamma}{1+\gamma-2(1-z)} \right) \right]$$
$$+ \frac{1}{4z(1-z)} (\gamma-1) \ln\left(\frac{\overline{Q}^2 + m_q^2}{m_q^2} \right) + \frac{m_q^2}{2\overline{Q}^2} \ln\left(\frac{\overline{Q}^2 + m_q^2}{m_q^2} \right). \qquad \text{(B.5)}$$

Finally, the special function $\tilde{\mathcal{I}}_{\mathcal{V}}(z, \mathbf{x}_{01})$ is given by

$$\tilde{\mathcal{I}}_{\mathcal{V}}(z, \mathbf{x}_{01}) = \tilde{\mathcal{I}}_{\mathcal{V}_{(a)+(b)}}(z, \mathbf{x}_{01}) + \tilde{\mathcal{I}}_{\mathcal{V}_{(c)+(d)}}(z, \mathbf{x}_{01}), \qquad \text{(B.6)}$$

with

$$\tilde{\mathcal{I}}_{\mathcal{V}_{(a)+(b)}}(z, \mathbf{x}_{01}) = \int_0^1 \frac{\mathrm{d}\xi}{\xi} \left(-\frac{2\ln\xi}{1-\xi} + \frac{1+\xi}{2} \right)$$
$$\times \left[2K_0\left(|\mathbf{x}_{01}| \sqrt{\overline{Q}^2 + m_q^2} \right) - K_0\left(|\mathbf{x}_{01}| \sqrt{\overline{Q}^2 + m_q^2 + \frac{(1-z)\xi}{1-\xi} m_q^2} \right) \right.$$
$$\left. - K_0\left(|\mathbf{x}_{01}| \sqrt{\overline{Q}^2 + m_q^2 + \frac{z\xi}{1-\xi} m_q^2} \right) \right] \qquad \text{(B.7)}$$

and

$$\tilde{\mathcal{I}}_{\mathcal{V}_{(c)+(d)}}(z, \mathbf{x}_{01}) = m_q^2 \int_0^1 \mathrm{d}\xi \int_0^1 \mathrm{d}x$$
$$\times \left\{ \left[K_0\left(|\mathbf{x}_{01}| \sqrt{\overline{Q}^2 + m_q^2} \right) - K_0\left(|\mathbf{x}_{01}| \sqrt{\frac{\overline{Q}^2 + m_q^2}{1-x} + \kappa} \right) \right] \right.$$
$$\times \frac{C_m^L}{(1-\xi)(1-x)\left[x(1-\xi) + \frac{\xi}{1-z} \right] \left[\frac{x(\overline{Q}^2 + m_q^2)}{1-x} + \kappa \right]}$$
$$\left. + (z \to 1-z) \right\}. \qquad \text{(B.8)}$$

The coefficient C_m^L in the above expression reads

$$C_m^L = \frac{z^2(1-\xi)}{1-z} \left[-\xi^2 + x(1-\xi) \frac{1 + (1-\xi)\left(1 + \frac{z\xi}{1-z} \right)}{x(1-\xi) + \frac{\xi}{1-z}} \right], \qquad \text{(B.9)}$$

and

$$\kappa = \frac{\xi m_q^2}{(1-\xi)(1-x)\left[x(1-\xi) + \frac{\xi}{1-z} \right]} \left[\xi(1-x) + x\left(1 - \frac{z(1-\xi)}{1-z} \right) \right]. \qquad \text{(B.10)}$$

– 33 –

When considering relativistic corrections, one can no longer use the decay width scheme for transverse production. It is then more consistent to use the wave function scheme which works also with the relativistic corrections. In the wave function scheme, the longitudinal production amplitude can be written as

$$-i\mathcal{A}^L = -\int \frac{\mathrm{d}z'}{4\pi}\phi_{\mathrm{DR}}^{q\bar{q},L} \times \sqrt{\frac{N_c}{2}}\frac{ee_f Q}{2\pi}2\int \mathrm{d}^2\mathbf{x}_{01}\int \mathrm{d}^2\mathbf{b}\left\{\mathcal{K}_{q\bar{q}}^{\mathrm{LO}}(Y_0)\right.$$
$$\left.+\frac{\alpha_s C_F}{2\pi}\mathcal{K}_{q\bar{q},\Psi}^{\mathrm{NLO},L}(Y_{\mathrm{dip}}) + \frac{\alpha_s C_F}{2\pi}\int \mathrm{d}^2\mathbf{x}_{20}\int_{z_{\min}}^{1/2}\mathrm{d}z_2\,\mathcal{K}_{q\bar{q}g}^L(Y_{q\bar{q}g})\right\} \quad \text{(B.11)}$$

where the LOWF $\phi_{\mathrm{DR}}^{q\bar{q},L}$ is now the dimensionally regularized one from eq. (3.43), and the virtual correction becomes

$$\mathcal{K}_{q\bar{q},\Psi}^{\mathrm{NLO},L}(Y_{\mathrm{dip}}) = N_{01}(Y_{\mathrm{dip}}) \times \left[\tilde{\mathcal{I}}_\nu\left(\frac{1}{2},\mathbf{x}_{01}\right)+\mathcal{K}^L\right.$$
$$\left.+K_0(\zeta)\left(\Omega_{\mathcal{V}}^L\left(\gamma;\frac{1}{2}\right)+L\left(\gamma;\frac{1}{2}\right)-\frac{\pi^2}{3}+2-3\ln\left(\frac{|\mathbf{x}_{01}|m}{2}\right)-3\gamma_E\right)\right] \quad \text{(B.12)}$$

instead of $\mathcal{K}_{q\bar{q},\Gamma}^{\mathrm{NLO}}(Y_{\mathrm{dip}})$. The relativistic corrections to longitudinal production can be written as

$$-i\mathcal{A}_{\mathrm{rel}}^L = -\frac{ee_f Q\sqrt{N_c}}{2\pi}2\int \mathrm{d}^2\mathbf{x}_{01}\,N_{01}(Y_{\mathrm{dip}})$$
$$\times\frac{1}{4}\left\{\left(\phi_{+-}^{q\bar{q},L}(0,0,2)+\phi_{-+}^{q\bar{q},L}(0,0,2)\right)\left[2K_0(\zeta)-\frac{Q^2\mathbf{x}_{01}^2}{4\zeta}K_1(\zeta)\right]\right.$$
$$\left.+\left(\phi_{+-}^{q\bar{q},L}(2,0,0)+\phi_{-+}^{q\bar{q},L}(2,0,0)+\phi_{+-}^{q\bar{q},L}(0,2,0)+\phi_{-+}^{q\bar{q},L}(0,2,0)\right)\frac{m^2\mathbf{x}_{01}^2}{2}K_0(\zeta)\right\}$$
$$=-\frac{ee_f Q\sqrt{N_c}}{2\pi}2\int \mathrm{d}^2\mathbf{x}_{01}\,N_{01}(Y_{\mathrm{dip}})$$
$$\times\frac{1}{2}\left\{\phi_{+-}^{q\bar{q},L}(0,0,2)\left[2K_0(\zeta)-\frac{Q^2 r^2}{4\zeta}K_1(\zeta)\right]+\phi_{+-}^{q\bar{q},L}(2,0,0)m^2\mathbf{x}_{01}^2 K_0(\zeta)\right\}. \quad \text{(B.13)}$$

where the expression was simplified using the identity $\phi_{+-}^{q\bar{q},L}(\mathbf{r},z')=\phi_{-+}^{q\bar{q},L}(\mathbf{r},z')$ that follows from the spin-parity of the vector meson as discussed in section 4.

The nonperturbative constants related to the LOWF can be written in terms of the rest-frame wave function $\phi_{\mathrm{RF}}(\vec{r})$ [92], giving us

$$\int \frac{\mathrm{d}z'}{4\pi}\phi_{\mathrm{DR}}^{q\bar{q},L} = \sqrt{2}\phi_{+-}^{q\bar{q},L}(0,0,0) = \frac{1}{\sqrt{4m_q}}\left[\phi_{\mathrm{RF}}(0)+\frac{5}{12m_q^2}\vec{\nabla}^2\phi_{\mathrm{RF}}(0)\right] \quad \text{(B.14)}$$

$$\phi_{+-}^{q\bar{q},L}(2,0,0) = \phi_{-+}^{q\bar{q},L}(0,0,2) = \frac{1}{6\sqrt{2m_q}}\frac{1}{m_q^2}\vec{\nabla}^2\phi_{\mathrm{RF}}(0). \quad \text{(B.15)}$$

– 34 –

This allows us to write the v^2 relativistic correction in the compact form

$$-i\mathcal{A}_{\mathrm{rel}}^L = -\frac{ee_f Q\sqrt{N_c}}{2\pi\sqrt{2}} 2 \int \mathrm{d}^2\mathbf{x}_{01} \int \mathrm{d}^2\mathbf{b}\, N_{01}(Y_{\mathrm{dip}})$$
$$\times \frac{\nabla^2\phi_{\mathrm{RF}}(0)}{12m_q^2\sqrt{m_q}} \left[2K_0(\zeta) - \frac{Q^2\mathbf{x}_{01}^2}{4\zeta}K_1(\zeta) + m_q^2\mathbf{x}_{01}^2 K_0(\zeta) \right]. \quad \text{(B.16)}$$

The value of the rest-frame wave function and its derivatives can be related to NRQCD matrix elements as described in section 4.

Open Access. This article is distributed under the terms of the Creative Commons Attribution License ([CC-BY 4.0](#)), which permits any use, distribution and reproduction in any medium, provided the original author(s) and source are credited. SCOAP³ supports the goals of the International Year of Basic Sciences for Sustainable Development.

References

[1] H1 and ZEUS collaborations, *Combined Measurement and QCD Analysis of the Inclusive $e^{\pm}p$ Scattering Cross Sections at HERA*, *JHEP* **01** (2010) 109 [arXiv:0911.0884] [INSPIRE].

[2] H1 and ZEUS collaborations, *Combination of measurements of inclusive deep inelastic $e^{\pm}p$ scattering cross sections and QCD analysis of HERA data*, *Eur. Phys. J. C* **75** (2015) 580 [arXiv:1506.06042] [INSPIRE].

[3] A. Morreale and F. Salazar, *Mining for Gluon Saturation at Colliders*, *Universe* **7** (2021) 312 [arXiv:2108.08254] [INSPIRE].

[4] M.G. Ryskin, *Diffractive J/ψ electroproduction in LLA QCD*, *Z. Phys. C* **57** (1993) 89 [INSPIRE].

[5] K.J. Eskola, C.A. Flett, V. Guzey, T. Löytäinen and H. Paukkunen, *Exclusive J/ψ photoproduction in ultraperipheral Pb+Pb collisions at the LHC to next-to-leading order perturbative QCD*, arXiv:2203.11613 [INSPIRE].

[6] S.R. Klein and H. Mäntysaari, *Imaging the nucleus with high-energy photons*, *Nature Rev. Phys.* **1** (2019) 662 [arXiv:1910.10858] [INSPIRE].

[7] ZEUS collaboration, *Exclusive electroproduction of J/ψ mesons at HERA*, *Nucl. Phys. B* **695** (2004) 3 [hep-ex/0404008] [INSPIRE].

[8] ZEUS collaboration, *Exclusive photoproduction of J/ψ mesons at HERA*, *Eur. Phys. J. C* **24** (2002) 345 [hep-ex/0201043] [INSPIRE].

[9] H1 collaboration, *Elastic J/ψ production at HERA*, *Eur. Phys. J. C* **46** (2006) 585 [hep-ex/0510016] [INSPIRE].

[10] ZEUS collaboration, *Measurement of J/ψ photoproduction at large momentum transfer at HERA*, *JHEP* **05** (2010) 085 [arXiv:0910.1235] [INSPIRE].

[11] ZEUS collaboration, *Measurement of diffractive photoproduction of vector mesons at large momentum transfer at HERA*, *Eur. Phys. J. C* **14** (2000) 213 [hep-ex/9910038] [INSPIRE].

[12] ZEUS collaboration, *Measurement of proton dissociative diffractive photoproduction of vector mesons at large momentum transfer at HERA*, *Eur. Phys. J. C* **26** (2003) 389 [hep-ex/0205081] [INSPIRE].

[13] H1 collaboration, *Diffractive photoproduction of J/ψ mesons with large momentum transfer at HERA*, *Phys. Lett. B* **568** (2003) 205 [hep-ex/0306013] [INSPIRE].

[14] H1 collaboration, *Elastic and Proton-Dissociative Photoproduction of J/ψ Mesons at HERA*, *Eur. Phys. J. C* **73** (2013) 2466 [arXiv:1304.5162] [INSPIRE].

[15] STAR collaboration, *Coherent J/ψ photoproduction in ultra-peripheral collisions at STAR*, *PoS* **DIS2019** (2019) 042 [INSPIRE].

[16] PHENIX collaboration, *Photoproduction of J/ψ and of high mass e^+e^- in ultra-peripheral Au+Au collisions at $\sqrt{s} = 200\ GeV$*, *Phys. Lett. B* **679** (2009) 321 [arXiv:0903.2041] [INSPIRE].

[17] STAR collaboration, *Probing the Gluonic Structure of the Deuteron with J/ψ Photoproduction in d+Au Ultraperipheral Collisions*, *Phys. Rev. Lett.* **128** (2022) 122303 [arXiv:2109.07625] [INSPIRE].

[18] ALICE collaboration, *First measurement of the |t|-dependence of coherent J/ψ photonuclear production*, *Phys. Lett. B* **817** (2021) 136280 [arXiv:2101.04623] [INSPIRE].

[19] ALICE collaboration, *Exclusive J/ψ photoproduction off protons in ultra-peripheral p-Pb collisions at $\sqrt{s_{NN}} = 5.02\ TeV$*, *Phys. Rev. Lett.* **113** (2014) 232504 [arXiv:1406.7819] [INSPIRE].

[20] ALICE collaboration, *Energy dependence of exclusive J/ψ photoproduction off protons in ultra-peripheral p-Pb collisions at $\sqrt{s_{NN}} = 5.02\ TeV$*, *Eur. Phys. J. C* **79** (2019) 402 [arXiv:1809.03235] [INSPIRE].

[21] LHCb collaboration, *Exclusive J/ψ and ψ(2S) production in pp collisions at $\sqrt{s} = 7\ TeV$*, *J. Phys. G* **40** (2013) 045001 [arXiv:1301.7084] [INSPIRE].

[22] LHCb collaboration, *Updated measurements of exclusive J/ψ and ψ(2S) production cross-sections in pp collisions at $\sqrt{s} = 7\ TeV$*, *J. Phys. G* **41** (2014) 055002 [arXiv:1401.3288] [INSPIRE].

[23] LHCb collaboration, *Central exclusive production of J/ψ and ψ(2S) mesons in pp collisions at $\sqrt{s} = 13\ TeV$*, *JHEP* **10** (2018) 167 [arXiv:1806.04079] [INSPIRE].

[24] ALICE collaboration, *Coherent J/ψ photoproduction at forward rapidity in ultra-peripheral Pb-Pb collisions at $\sqrt{s_{NN}} = 5.02\ TeV$*, *Phys. Lett. B* **798** (2019) 134926 [arXiv:1904.06272] [INSPIRE].

[25] ALICE collaboration, *Charmonium and e^+e^- pair photoproduction at mid-rapidity in ultra-peripheral Pb-Pb collisions at $\sqrt{s_{NN}} = 2.76\ TeV$*, *Eur. Phys. J. C* **73** (2013) 2617 [arXiv:1305.1467] [INSPIRE].

[26] ALICE collaboration, *Coherent J/ψ photoproduction in ultra-peripheral Pb-Pb collisions at $\sqrt{s_{NN}} = 2.76\ TeV$*, *Phys. Lett. B* **718** (2013) 1273 [arXiv:1209.3715] [INSPIRE].

[27] ALICE collaboration, *Coherent J/ψ and ψ' photoproduction at midrapidity in ultra-peripheral Pb-Pb collisions at $\sqrt{s_{NN}} = 5.02\ TeV$*, *Eur. Phys. J. C* **81** (2021) 712 [arXiv:2101.04577] [INSPIRE].

[28] CMS collaboration, *Coherent J/ψ photoproduction in ultra-peripheral PbPb collisions at $\sqrt{s_{NN}} = 2.76\ TeV$ with the CMS experiment*, *Phys. Lett. B* **772** (2017) 489 [arXiv:1605.06966] [INSPIRE].

[29] LHCb collaboration, *Study of coherent J/ψ production in lead-lead collisions at* $\sqrt{s_{NN}} = 5$ *TeV*, *JHEP* **07** (2022) 117 [arXiv:2107.03223] [INSPIRE].

[30] C.A. Bertulani, S.R. Klein and J. Nystrand, *Physics of ultra-peripheral nuclear collisions*, *Ann. Rev. Nucl. Part. Sci.* **55** (2005) 271 [nucl-ex/0502005] [INSPIRE].

[31] E.C. Aschenauer et al., *The electron-ion collider: assessing the energy dependence of key measurements*, *Rept. Prog. Phys.* **82** (2019) 024301 [arXiv:1708.01527] [INSPIRE].

[32] R. Abdul Khalek et al., *Science Requirements and Detector Concepts for the Electron-Ion Collider: EIC Yellow Report*, arXiv:2103.05419 [INSPIRE].

[33] LHeC and FCC-he Study Group collaborations, *The Large Hadron-Electron Collider at the HL-LHC*, *J. Phys. G* **48** (2021) 110501 [arXiv:2007.14491] [INSPIRE].

[34] D.P. Anderle et al., *Electron-ion collider in China*, *Front. Phys. (Beijing)* **16** (2021) 64701 [arXiv:2102.09222] [INSPIRE].

[35] E. Iancu and R. Venugopalan, *The Color glass condensate and high-energy scattering in QCD*, in *Quark-gluon plasma 4*, R.C. Hwa and X.-N. Wang eds., pp. 249–3363 (2003) [DOI] [hep-ph/0303204] [INSPIRE].

[36] F. Gelis, E. Iancu, J. Jalilian-Marian and R. Venugopalan, *The Color Glass Condensate*, *Ann. Rev. Nucl. Part. Sci.* **60** (2010) 463 [arXiv:1002.0333] [INSPIRE].

[37] H. Kowalski, L. Motyka and G. Watt, *Exclusive diffractive processes at HERA within the dipole picture*, *Phys. Rev. D* **74** (2006) 074016 [hep-ph/0606272] [INSPIRE].

[38] N. Armesto and A.H. Rezaeian, *Exclusive vector meson production at high energies and gluon saturation*, *Phys. Rev. D* **90** (2014) 054003 [arXiv:1402.4831] [INSPIRE].

[39] H. Mäntysaari and B. Schenke, *Confronting impact parameter dependent JIMWLK evolution with HERA data*, *Phys. Rev. D* **98** (2018) 034013 [arXiv:1806.06783] [INSPIRE].

[40] H. Mäntysaari and B. Schenke, *Revealing proton shape fluctuations with incoherent diffraction at high energy*, *Phys. Rev. D* **94** (2016) 034042 [arXiv:1607.01711] [INSPIRE].

[41] H. Mäntysaari and B. Schenke, *Evidence of strong proton shape fluctuations from incoherent diffraction*, *Phys. Rev. Lett.* **117** (2016) 052301 [arXiv:1603.04349] [INSPIRE].

[42] T. Lappi and H. Mäntysaari, J/ψ *production in ultraperipheral Pb+Pb and p+Pb collisions at energies available at the CERN Large Hadron Collider*, *Phys. Rev. C* **87** (2013) 032201 [arXiv:1301.4095] [INSPIRE].

[43] T. Lappi and H. Mäntysaari, *Incoherent diffractive* J/ψ *production in high energy nuclear DIS*, *Phys. Rev. C* **83** (2011) 065202 [arXiv:1011.1988] [INSPIRE].

[44] T. Toll and T. Ullrich, *Exclusive diffractive processes in electron-ion collisions*, *Phys. Rev. C* **87** (2013) 024913 [arXiv:1211.3048] [INSPIRE].

[45] A. Caldwell and H. Kowalski, *The* J/ψ *Way to Nuclear Structure*, in *13th International Conference on Elastic and Diffractive Scattering (Blois Workshop): Moving Forward into the LHC Era*, pp. 190–192 (2009) [arXiv:0909.1254] [INSPIRE].

[46] B. Sambasivam, T. Toll and T. Ullrich, *Investigating saturation effects in ultraperipheral collisions at the LHC with the color dipole model*, *Phys. Lett. B* **803** (2020) 135277 [arXiv:1910.02899] [INSPIRE].

[47] H. Mäntysaari and R. Venugopalan, *Systematics of strong nuclear amplification of gluon saturation from exclusive vector meson production in high energy electron-nucleus collisions*, *Phys. Lett. B* **781** (2018) 664 [`arXiv:1712.02508`] [InSPIRE].

[48] H. Mäntysaari and B. Schenke, *Probing subnucleon scale fluctuations in ultraperipheral heavy ion collisions*, *Phys. Lett. B* **772** (2017) 832 [`arXiv:1703.09256`] [InSPIRE].

[49] V.P. Goncalves and M.V.T. Machado, *The QCD Pomeron in ultraperipheral heavy ion collisions. IV. Photonuclear production of vector mesons*, *Eur. Phys. J. C* **40** (2005) 519 [`hep-ph/0501099`] [InSPIRE].

[50] D. Bendova, J. Cepila, J.G. Contreras and M. Matas, *Photonuclear J/ψ production at the LHC: Proton-based versus nuclear dipole scattering amplitudes*, *Phys. Lett. B* **817** (2021) 136306 [`arXiv:2006.12980`] [InSPIRE].

[51] I. Balitsky, *Operator expansion for high-energy scattering*, *Nucl. Phys. B* **463** (1996) 99 [`hep-ph/9509348`] [InSPIRE].

[52] Y.V. Kovchegov, *Small x F_2 structure function of a nucleus including multiple Pomeron exchanges*, *Phys. Rev. D* **60** (1999) 034008 [`hep-ph/9901281`] [InSPIRE].

[53] I. Balitsky, *Quark contribution to the small-x evolution of color dipole*, *Phys. Rev. D* **75** (2007) 014001 [`hep-ph/0609105`] [InSPIRE].

[54] Y.V. Kovchegov and H. Weigert, *Triumvirate of Running Couplings in Small-x Evolution*, *Nucl. Phys. A* **784** (2007) 188 [`hep-ph/0609090`] [InSPIRE].

[55] I. Balitsky and G.A. Chirilli, *Next-to-leading order evolution of color dipoles*, *Phys. Rev. D* **77** (2008) 014019 [`arXiv:0710.4330`] [InSPIRE].

[56] I. Balitsky and G.A. Chirilli, *Rapidity evolution of Wilson lines at the next-to-leading order*, *Phys. Rev. D* **88** (2013) 111501 [`arXiv:1309.7644`] [InSPIRE].

[57] A. Kovner, M. Lublinsky and Y. Mulian, *Jalilian-Marian, Iancu, McLerran, Weigert, Leonidov, Kovner evolution at next to leading order*, *Phys. Rev. D* **89** (2014) 061704 [`arXiv:1310.0378`] [InSPIRE].

[58] T. Lappi, H. Mäntysaari and A. Ramnath, *Next-to-leading order Balitsky-Kovchegov equation beyond large N_c*, *Phys. Rev. D* **102** (2020) 074027 [`arXiv:2007.00751`] [InSPIRE].

[59] T. Lappi and H. Mäntysaari, *Next-to-leading order Balitsky-Kovchegov equation with resummation*, *Phys. Rev. D* **93** (2016) 094004 [`arXiv:1601.06598`] [InSPIRE].

[60] T. Lappi and H. Mäntysaari, *Direct numerical solution of the coordinate space Balitsky-Kovchegov equation at next to leading order*, *Phys. Rev. D* **91** (2015) 074016 [`arXiv:1502.02400`] [InSPIRE].

[61] B. Ducloué, E. Iancu, A.H. Mueller, G. Soyez and D.N. Triantafyllopoulos, *Non-linear evolution in QCD at high-energy beyond leading order*, *JHEP* **04** (2019) 081 [`arXiv:1902.06637`] [InSPIRE].

[62] B. Ducloué, E. Iancu, G. Soyez and D.N. Triantafyllopoulos, *HERA data and collinearly-improved BK dynamics*, *Phys. Lett. B* **803** (2020) 135305 [`arXiv:1912.09196`] [InSPIRE].

[63] E. Iancu, J.D. Madrigal, A.H. Mueller, G. Soyez and D.N. Triantafyllopoulos, *Resumming double logarithms in the QCD evolution of color dipoles*, *Phys. Lett. B* **744** (2015) 293 [`arXiv:1502.05642`] [InSPIRE].

[64] E. Iancu, J.D. Madrigal, A.H. Mueller, G. Soyez and D.N. Triantafyllopoulos, *Collinearly-improved BK evolution meets the HERA data*, *Phys. Lett. B* **750** (2015) 643 [arXiv:1507.03651] [InSPIRE].

[65] Y. Hatta and E. Iancu, *Collinearly improved JIMWLK evolution in Langevin form*, *JHEP* **08** (2016) 083 [arXiv:1606.03269] [InSPIRE].

[66] G. Beuf, H. Hänninen, T. Lappi and H. Mäntysaari, *Color Glass Condensate at next-to-leading order meets HERA data*, *Phys. Rev. D* **102** (2020) 074028 [arXiv:2007.01645] [InSPIRE].

[67] A. Dumitru, H. Mäntysaari and R. Paatelainen, *Color charge correlations in the proton at NLO: Beyond geometry based intuition*, *Phys. Lett. B* **820** (2021) 136560 [arXiv:2103.11682] [InSPIRE].

[68] A. Dumitru and R. Paatelainen, *Sub-femtometer scale color charge fluctuations in a proton made of three quarks and a gluon*, *Phys. Rev. D* **103** (2021) 034026 [arXiv:2010.11245] [InSPIRE].

[69] G. Beuf, *Dipole factorization for DIS at NLO: Combining the $q\bar{q}$ and $q\bar{q}g$ contributions*, *Phys. Rev. D* **96** (2017) 074033 [arXiv:1708.06557] [InSPIRE].

[70] B. Ducloué, H. Hänninen, T. Lappi and Y. Zhu, *Deep inelastic scattering in the dipole picture at next-to-leading order*, *Phys. Rev. D* **96** (2017) 094017 [arXiv:1708.07328] [InSPIRE].

[71] G. Beuf, *Dipole factorization for DIS at NLO: Loop correction to the $\gamma^*_{T,L} \to q\bar{q}$ light-front wave functions*, *Phys. Rev. D* **94** (2016) 054016 [arXiv:1606.00777] [InSPIRE].

[72] I. Balitsky and G.A. Chirilli, *Photon impact factor in the next-to-leading order*, *Phys. Rev. D* **83** (2011) 031502 [arXiv:1009.4729] [InSPIRE].

[73] G. Beuf, T. Lappi and R. Paatelainen, *Massive quarks in NLO dipole factorization for DIS: Longitudinal photon*, *Phys. Rev. D* **104** (2021) 056032 [arXiv:2103.14549] [InSPIRE].

[74] G. Beuf, T. Lappi and R. Paatelainen, *Massive Quarks at One Loop in the Dipole Picture of Deep Inelastic Scattering*, *Phys. Rev. Lett.* **129** (2022) 072001 [arXiv:2112.03158] [InSPIRE].

[75] G. Beuf, T. Lappi and R. Paatelainen, *Massive quarks in NLO dipole factorization for DIS: Transverse photon*, *Phys. Rev. D* **106** (2022) 034013 [arXiv:2204.02486] [InSPIRE].

[76] M.A. Escobedo and T. Lappi, *Dipole picture and the nonrelativistic expansion*, *Phys. Rev. D* **101** (2020) 034030 [arXiv:1911.01136] [InSPIRE].

[77] R. Boussarie, A.V. Grabovsky, D.Y. Ivanov, L. Szymanowski and S. Wallon, *Next-to-Leading Order Computation of Exclusive Diffractive Light Vector Meson Production in a Saturation Framework*, *Phys. Rev. Lett.* **119** (2017) 072002 [arXiv:1612.08026] [InSPIRE].

[78] H. Mäntysaari and J. Penttala, *Exclusive production of light vector mesons at next-to-leading order in the dipole picture*, *Phys. Rev. D* **105** (2022) 114038 [arXiv:2203.16911] [InSPIRE].

[79] P. Taels, T. Altinoluk, G. Beuf and C. Marquet, *Dijet photoproduction at low x at next-to-leading order and its back-to-back limit*, arXiv:2204.11650 [InSPIRE].

[80] P. Caucal, F. Salazar and R. Venugopalan, *Dijet impact factor in DIS at next-to-leading order in the Color Glass Condensate*, *JHEP* **11** (2021) 222 [arXiv:2108.06347] [InSPIRE].

[81] E. Iancu and Y. Mulian, *Forward dijets in proton-nucleus collisions at next-to-leading order: the real corrections*, *JHEP* **03** (2021) 005 [arXiv:2009.11930] [InSPIRE].

[82] R. Boussarie, A.V. Grabovsky, L. Szymanowski and S. Wallon, *On the one loop $\gamma^{(*)} \to q\bar{q}$ impact factor and the exclusive diffractive cross sections for the production of two or three jets*, *JHEP* **11** (2016) 149 [arXiv:1606.00419] [INSPIRE].

[83] B. Ducloué et al., *Use of a running coupling in the NLO calculation of forward hadron production*, *Phys. Rev. D* **97** (2018) 054020 [arXiv:1712.07480] [INSPIRE].

[84] B. Ducloué, T. Lappi and Y. Zhu, *Single inclusive forward hadron production at next-to-leading order*, *Phys. Rev. D* **93** (2016) 114016 [arXiv:1604.00225] [INSPIRE].

[85] A.M. Stasto, B.-W. Xiao and D. Zaslavsky, *Towards the Test of Saturation Physics Beyond Leading Logarithm*, *Phys. Rev. Lett.* **112** (2014) 012302 [arXiv:1307.4057] [INSPIRE].

[86] T. Altinoluk, N. Armesto, G. Beuf, A. Kovner and M. Lublinsky, *Single-inclusive particle production in proton-nucleus collisions at next-to-leading order in the hybrid formalism*, *Phys. Rev. D* **91** (2015) 094016 [arXiv:1411.2869] [INSPIRE].

[87] K. Watanabe, B.-W. Xiao, F. Yuan and D. Zaslavsky, *Implementing the exact kinematical constraint in the saturation formalism*, *Phys. Rev. D* **92** (2015) 034026 [arXiv:1505.05183] [INSPIRE].

[88] E. Iancu, A.H. Mueller and D.N. Triantafyllopoulos, *CGC factorization for forward particle production in proton-nucleus collisions at next-to-leading order*, *JHEP* **12** (2016) 041 [arXiv:1608.05293] [INSPIRE].

[89] G.A. Chirilli, B.-W. Xiao and F. Yuan, *Inclusive Hadron Productions in pA Collisions*, *Phys. Rev. D* **86** (2012) 054005 [arXiv:1203.6139] [INSPIRE].

[90] H.-Y. Liu, Z.-B. Kang and X. Liu, *Threshold resummation for hadron production in the small-x region*, *Phys. Rev. D* **102** (2020) 051502 [arXiv:2004.11990] [INSPIRE].

[91] H.-y. Liu, K. Xie, Z. Kang and X. Liu, *Single inclusive jet production in pA collisions at NLO in the small-x regime*, *JHEP* **07** (2022) 041 [arXiv:2204.03026] [INSPIRE].

[92] T. Lappi, H. Mäntysaari and J. Penttala, *Relativistic corrections to the vector meson light front wave function*, *Phys. Rev. D* **102** (2020) 054020 [arXiv:2006.02830] [INSPIRE].

[93] H. Mäntysaari and J. Penttala, *Exclusive heavy vector meson production at next-to-leading order in the dipole picture*, *Phys. Lett. B* **823** (2021) 136723 [arXiv:2104.02349] [INSPIRE].

[94] M.L. Good and W.D. Walker, *Diffraction disssociation of beam particles*, *Phys. Rev.* **120** (1960) 1857 [INSPIRE].

[95] H. Mäntysaari, *Review of proton and nuclear shape fluctuations at high energy*, *Rept. Prog. Phys.* **83** (2020) 082201 [arXiv:2001.10705] [INSPIRE].

[96] H. Hänninen, T. Lappi and R. Paatelainen, *One-loop corrections to light cone wave functions: the dipole picture DIS cross section*, *Annals Phys.* **393** (2018) 358 [arXiv:1711.08207] [INSPIRE].

[97] J. Berger and A.M. Stasto, *Exclusive vector meson production and small-x evolution*, *JHEP* **01** (2013) 001 [arXiv:1205.2037] [INSPIRE].

[98] J. Berger and A.M. Stasto, *Small x nonlinear evolution with impact parameter and the structure function data*, *Phys. Rev. D* **84** (2011) 094022 [arXiv:1106.5740] [INSPIRE].

[99] J. Berger and A. Stasto, *Numerical solution of the nonlinear evolution equation at small x with impact parameter and beyond the LL approximation*, *Phys. Rev. D* **83** (2011) 034015 [arXiv:1010.0671] [INSPIRE].

[100] H. Mäntysaari, K. Roy, F. Salazar and B. Schenke, *Gluon imaging using azimuthal correlations in diffractive scattering at the Electron-Ion Collider*, *Phys. Rev. D* **103** (2021) 094026 [arXiv:2011.02464] [InSPIRE].

[101] J. Jalilian-Marian, A. Kovner, L.D. McLerran and H. Weigert, *The Intrinsic glue distribution at very small x*, *Phys. Rev. D* **55** (1997) 5414 [hep-ph/9606337] [InSPIRE].

[102] J. Jalilian-Marian, A. Kovner, A. Leonidov and H. Weigert, *The BFKL equation from the Wilson renormalization group*, *Nucl. Phys. B* **504** (1997) 415 [hep-ph/9701284] [InSPIRE].

[103] J. Jalilian-Marian, A. Kovner, A. Leonidov and H. Weigert, *The Wilson renormalization group for low x physics: Towards the high density regime*, *Phys. Rev. D* **59** (1998) 014014 [hep-ph/9706377] [InSPIRE].

[104] E. Iancu and L.D. McLerran, *Saturation and universality in QCD at small x*, *Phys. Lett. B* **510** (2001) 145 [hep-ph/0103032] [InSPIRE].

[105] E. Iancu, A. Leonidov and L.D. McLerran, *The Renormalization group equation for the color glass condensate*, *Phys. Lett. B* **510** (2001) 133 [hep-ph/0102009] [InSPIRE].

[106] E. Ferreiro, E. Iancu, A. Leonidov and L. McLerran, *Nonlinear gluon evolution in the color glass condensate. 2*, *Nucl. Phys. A* **703** (2002) 489 [hep-ph/0109115] [InSPIRE].

[107] E. Iancu, A. Leonidov and L.D. McLerran, *Nonlinear gluon evolution in the color glass condensate. 1*, *Nucl. Phys. A* **692** (2001) 583 [hep-ph/0011241] [InSPIRE].

[108] H. Hänninen, *Deep Inelastic Scattering in the Dipole Picture at Next-to-Leading Order*, Ph.D. Thesis, University of Jyväskylä (2021) [arXiv:2112.08818 [InSPIRE].

[109] G. Beuf, H. Hänninen, T. Lappi and H. Mäntysaari, *Color glass condensate at next-to-leading order meets hera data (software)*, https://doi.org/10.5281/zenodo.4229269 (2020).

[110] G. Beuf, *Improving the kinematics for low-x QCD evolution equations in coordinate space*, *Phys. Rev. D* **89** (2014) 074039 [arXiv:1401.0313] [InSPIRE].

[111] G.T. Bodwin, H.S. Chung, D. Kang, J. Lee and C. Yu, *Improved determination of color-singlet nonrelativistic QCD matrix elements for S-wave charmonium*, *Phys. Rev. D* **77** (2008) 094017 [arXiv:0710.0994] [InSPIRE].

[112] Y. Li, P. Maris and J.P. Vary, *Quarkonium as a relativistic bound state on the light front*, *Phys. Rev. D* **96** (2017) 016022 [arXiv:1704.06968] [InSPIRE].

[113] H.G. Dosch, T. Gousset, G. Kulzinger and H.J. Pirner, *Vector meson leptoproduction and nonperturbative gluon fluctuations in QCD*, *Phys. Rev. D* **55** (1997) 2602 [hep-ph/9608203] [InSPIRE].

[114] H.S. Chung, J. Lee and C. Yu, *NRQCD matrix elements for S-wave bottomonia and $\Gamma[\eta_b(nS) \to \gamma\gamma]$ with relativistic corrections*, *Phys. Lett. B* **697** (2011) 48 [arXiv:1011.1554] [InSPIRE].

[115] J.L. Albacete, N. Armesto, J.G. Milhano, P. Quiroga-Arias and C.A. Salgado, *AAMQS: A non-linear QCD analysis of new HERA data at small-x including heavy quarks*, *Eur. Phys. J. C* **71** (2011) 1705 [arXiv:1012.4408] [InSPIRE].

[116] P. Hoodbhoy, *Wave function corrections and off forward gluon distributions in diffractive J/ψ electroproduction*, *Phys. Rev. D* **56** (1997) 388 [hep-ph/9611207] [InSPIRE].

[117] B.G. Giraud and R. Peschanski, *Fourier-positivity constraints on QCD dipole models*, *Phys. Lett. B* **760** (2016) 26 [arXiv:1604.01932] [InSPIRE].

[118] T. Lappi and H. Mäntysaari, *Single inclusive particle production at high energy from HERA data to proton-nucleus collisions*, *Phys. Rev. D* **88** (2013) 114020 [arXiv:1309.6963] [INSPIRE].

[119] H1 collaboration, *Elastic photoproduction of* J/ψ *and* Υ *mesons at HERA*, *Phys. Lett. B* **483** (2000) 23 [hep-ex/0003020] [INSPIRE].

[120] ZEUS collaboration, *Measurement of elastic Upsilon photoproduction at HERA*, *Phys. Lett. B* **437** (1998) 432 [hep-ex/9807020] [INSPIRE].

[121] ZEUS collaboration, *Exclusive photoproduction of upsilon mesons at HERA*, *Phys. Lett. B* **680** (2009) 4 [arXiv:0903.4205] [INSPIRE].

[122] CMS collaboration, *Measurement of exclusive* Υ *photoproduction from protons in pPb collisions at* $\sqrt{s_{\mathrm{NN}}} = 5.02$ *TeV*, *Eur. Phys. J. C* **79** (2019) 277 [*Erratum ibid.* **82** (2022) 343] [arXiv:1809.11080] [INSPIRE].

[123] LHCb collaboration, *Measurement of the exclusive* Υ *production cross-section in pp collisions at* $\sqrt{s} = 7$ *TeV and 8 TeV*, *JHEP* **09** (2015) 084 [arXiv:1505.08139] [INSPIRE].

[124] ZEUS collaboration, *Measurement of the t dependence in exclusive photoproduction of* Υ(1S) *mesons at HERA*, *Phys. Lett. B* **708** (2012) 14 [arXiv:1111.2133] [INSPIRE].

V

PROTON STRUCTURE FUNCTIONS AT NLO IN THE DIPOLE PICTURE WITH MASSIVE QUARKS

by

Henri Hänninen, Heikki Mäntysaari, Risto Paatelainen, Jani Penttala (2023)

Proton Structure Functions at Next-to-Leading Order in the Dipole Picture with Massive Quarks

Henri Hänninen,[1,2,3,*] Heikki Mäntysaari[2,3,†] Risto Paatelainen[3,4,‡] and Jani Penttala[2,3,§]

[1]*Department of Mathematics and Statistics, University of Jyväskylä, P.O. Box 35, 40014 University of Jyväskylä, Finland*
[2]*Department of Physics, University of Jyväskylä, P.O. Box 35, 40014 University of Jyväskylä, Finland*
[3]*Helsinki Institute of Physics, University of Helsinki, P.O. Box 64, 00014 University of Helsinki, Finland*
[4]*Department of Physics, University of Helsinki, P.O. Box 64, 00014 University of Helsinki, Finland*

We predict heavy quark production cross sections in deep inelastic scattering at high energy by applying the color glass condensate effective theory. We demonstrate that, when the calculation is performed consistently at next-to-leading order accuracy with massive quarks, it becomes possible, for the first time in the dipole picture with perturbatively calculated center-of-mass energy evolution, to simultaneously describe both the light and heavy quark production data at small x_{Bj}. Furthermore, we show how the heavy quark cross section data provides additional strong constraints on the extracted nonperturbative initial condition for the small-x_{Bj} evolution equations.

Introduction.—Probing the properties of the nonlinearly behaving gluonic matter in protons and nuclei at high energies is a major science goal of the future Electron-Ion Collider (EIC) [1–3]. Measuring the total and heavy quark production cross sections in deep inelastic scattering (DIS) off nuclei is especially intriguing, as nonlinear saturation effects are enhanced in heavy nuclei [4]. The EIC will be able to perform very precise total cross section measurements over a relatively wide kinematical domain characterized by the gluon longitudinal momentum fraction x_{Bj} and the photon virtuality Q^2.

Nonlinear gluon saturation effects are expected to have a modest effect on structure functions in the EIC kinematics (see, e.g., [5–7]). To unambiguously determine the existence of nonlinear QCD dynamics at collider energies and to quantify its role on the small-x_{Bj} structure of protons and nuclei, it is likely necessary to perform a global analysis of the future proton and nuclear DIS data at small x_{Bj}. In particular, it will be important to include both the inclusive and heavy quark production data that have different sensitivities on saturation effects in order to extract in detail the properties of the QCD matter at extremely large parton densities. Charm production is an especially powerful process as the charm mass is large enough to suppress nonperturbative effects, but simultaneously light enough to allow one to access QCD dynamics in the nonlinear regime.

To describe QCD dynamics at high energies, where parton densities are very large and emergent nonlinear phenomena dominate, it is convenient to use the color glass condensate (CGC) [8,9] effective field theory framework. The DIS process is then naturally described in the dipole picture [10,11], where the photon splits into a quark-antiquark pair long before the interaction with the target. The interaction of the quark dipole with the target is then taken to be eikonal, i.e., the transverse coordinates of the partons do not change when they traverse through the target color field. In this picture, leading-order (LO) calculations including a resummation of the high-energy logarithms $\alpha_s \ln 1/x$ to all orders (where α_s is the strong coupling) within the CGC framework have been successful in describing the precise proton structure function data from HERA [12–14]. This suggests that the HERA data is compatible with the hypothesis that gluon saturation is manifest at HERA energies. In addition, calculations based on collinear factorization have also found the resummation of the high-energy logarithms to be important in order to describe the details of the HERA data [15].

The structure function data is used to constrain the nonperturbative initial condition for the small-x_{Bj} evolution equations. Therefore, a good description of the total cross section data is crucial when applying the CGC framework to describe any other scattering process (e.g., proton-nucleus collisions at the LHC [13,16–20]). Compatibility with the available cross section data is also required when developing a realistic description for the early stages of heavy-ion collisions [21], needed to extract the fundamental properties of the quark-gluon plasma.

In this Letter, we present predictions for heavy quark production cross sections in DIS using the nonperturbative

initial condition for the perturbative Balitsky-Kovchegov (BK) small-x_{Bj} evolution equation [22,23], determined from the fits to total DIS cross section data in [24]. The predicted heavy quark cross sections are shown to be in excellent agreement with the HERA data [25]. This is the first time in the CGC framework that a simultaneous description of total and heavy quark production data is achieved in calculations where the energy dependence is obtained by solving the small-x_{Bj} evolution equation. A crucial ingredient, here, is the next-to-leading order (NLO) accuracy in α_s recently achieved for the massive impact factors from first-principle light-cone perturbation theory calculations [26–28]. We also demonstrate how the heavy quark production data can provide additional constraints for the extracted nonperturbative initial condition of the BK evolution.

The results presented here are from the first-ever numerical calculation of the heavy quark structure functions in the dipole picture at NLO. The successful description of the HERA data demonstrates that future global analyses are feasible and can be applied to probe in detail gluon saturation at the LHC and future EIC, where nuclear targets with larger saturation scales are available.

Structure functions at high energy.—Using the optical theorem, the total virtual photon (γ^*)—proton (p) cross section can be obtained from the forward elastic $\gamma^* + p \to \gamma^* + p$ scattering amplitude. In the dipole picture, the $\gamma^* + p$ scattering is described in terms of eikonal interactions between the partonic Fock states of the photon and the target color field, and perturbatively calculable impact factors describing the photon fluctuations to the given partonic states. Eikonal interactions with the target are encoded in the Wilson lines, which are the scattering matrix elements for bare partons propagating through the target color field.

At NLO, the contributing photon Fock states are the quark-antiquark $|q\bar{q}\rangle$ and quark-antiquark-gluon $|q\bar{q}g\rangle$ states. Therefore, at NLO, the total virtual photon cross section can be schematically decomposed into two parts. The first contribution [illustrated in Fig. 1(a)] corresponds to the case where the $q\bar{q}g$ system crosses the shockwave

$$\sigma^{\gamma^*}_{q\bar{q}g} = K_{q\bar{q}g} \otimes N_{012}. \tag{1}$$

(a) $q\bar{q}g$ (b) $q\bar{q}$

FIG. 1. Example diagrams contributing to the elastic $\gamma^* p$ amplitude at NLO. The blue band represents the dipole–shockwave interaction.

The second contribution [illustrated in Fig. 1(b)], which includes the lowest-order part (interaction with an unevolved target) and the one-gluon-loop QCD corrections to it, reads

$$\sigma^{\gamma^*}_{q\bar{q}} = K_{q\bar{q}} \otimes N_{01}. \tag{2}$$

Here, $K_{q\bar{q}}$ and $K_{q\bar{q}g}$ refer to the perturbatively computed NLO impact factors obtained with massive quarks in [26–28] and in the massless quark limit in [29–31]. In addition, the notation $\otimes$ refers to an integral over the parton transverse coordinates $\mathbf{x}_i$ and longitudinal momentum fractions in the mixed space. Additionally, N_{01} and N_{012} are correlators of two or three Wilson lines, where the subscripts 0,1,2 refer to the transverse coordinates of the quark, antiquark, and the gluon. In terms of the Wilson lines, $V(\mathbf{x})$ in the fundamental representation, these correlators read

$$S_{01} = \frac{1}{N_c} \langle \mathrm{Tr}\{V(\mathbf{x}_0)V^\dagger(\mathbf{x}_1)\}\rangle, \tag{3}$$

$$S_{012} = \frac{N_c}{2C_F}\left(S_{02}S_{21} - \frac{1}{N_c^2}S_{01}\right). \tag{4}$$

Here, $\langle\cdots\rangle$ refers to the average over the target color charge configurations, N_c is the number of colors, $C_F = (N_c^2 - 1)/(2N_c)$, $S_{ij} = 1 - N_{ij}$, and $S_{ijk} = 1 - N_{ijk}$. In addition, we have used the mean-field limit (which is a precise approximation [32]) to factorize the expectation value of the product to a product of expectation values.

The Wilson lines and their correlators satisfy small-x_{Bj} evolution equations describing their dependency on the center-of-mass energy (see Ref. [33] for a detailed discussion of the evolution variable). The dipole amplitude N_{01} satisfies the BK equation [22,23] and via Eq. (4) N_{012} also depends on the center-of-mass energy. The evolution rapidity depends on the lower limit of the emitted gluon longitudinal momentum fraction [24,34]. The integration over the emitted gluon phase space in Eq. (1) contributes a large logarithm of energy that modifies the scattering amplitude of the original dipole N_{01}. These logarithms are resummed into the BK equation [34]. The BK equation and a numerical solution to it are known at NLO [35–37]. We use the initial condition fitted to the HERA data in [24] including only massless quarks, where the full (numerically heavy) NLO BK equation has been approximated by evolution equations that use different schemes to resum the most important higher-order corrections. The same evolution equations, ResumBK [38,39], KCBK [40], and TBK [33], referring to different resummation schemes, are used in this Letter as in [24].

The structure functions are written in terms of the total virtual photon-target cross sections as $F_2 = (Q^2/4\pi^2\alpha_{\mathrm{em}})\times(\sigma^{\gamma^*}_T + \sigma^{\gamma^*}_L)$, and $F_L = (Q^2/4\pi^2\alpha_{\mathrm{em}})\sigma^{\gamma^*}_L$. Here, the subscripts T and L refer to the transverse and longitudinal

virtual photon polarization, respectively, and $\sigma_{T,L}^{\gamma^*}$ correspond to a sum of $q\bar{q}$ and $q\bar{q}g$ contributions. The experimental data is reported in terms of the reduced cross section

$$\sigma_r(y, x, Q^2) = F_2(x, Q^2) - \frac{y^2}{1 + (1-y)^2} F_L(x, Q^2), \quad (5)$$

where $y = Q^2/(sx)$ is the inelasticity and $\sqrt{s}$ is the lepton-nucleon center-of-mass energy.

Results.—We calculate the proton reduced cross section σ_r and the charm and bottom contributions to it ($\sigma_{r,c}$ and $\sigma_{r,b}$). We use the NLO dipole-proton scattering amplitudes determined in [24], available at [41]. In particular, we use the "light quark" fits of [24] where only the massless u, d, and s quarks are included and the nonperturbative initial condition is fitted to the light quark contribution of the reduced cross section data measured at HERA [42]. This contribution is determined in [24] by subtracting interpolated charm and bottom quark contributions from the total cross section data. We do not include the fits to the inclusive HERA data as they use the massless quark cross sections to fit the inclusive data containing a substantial heavy quark contribution.

In [24], multiple different fits are reported, corresponding to different choices for the initial evolution rapidity $Y_{0,\mathrm{BK}}$ and different schemes for the coordinate space running coupling and resummations of particular higher-order corrections. In total, there are 12 fits reported for massless quarks. All different fits result in an approximately equally good description of the light quark contribution to the HERA structure function data.

We calculate predictions for the charm production cross section in the region $x_{\mathrm{Bj}} < 0.01, 2.5\,\mathrm{GeV}^2 \le Q^2 < 50\,\mathrm{GeV}^2$ using all the different fits from [24], and compare the result to the HERA data from [25] in order to find which fits (if any) are allowed by the heavy quark production data. The charm mass (in the pole mass scheme used in the calculation of [27]) is allowed to vary within $1.1\,\mathrm{GeV} < m_c < 1.6\,\mathrm{GeV}$. We consider a fit to be compatible with the HERA charm production data if one obtains $\chi_c^2/N \lesssim 2.5$ with the optimal charm mass. We find that predictions calculated by using three of the 12 fits are in excellent agreement with the charm production data. This is illustrated in Fig. 2, where a comparison to the HERA reduced cross section data in a few selected Q^2 bins is shown. The H1 and ZEUS collaborations have also measured inclusive b quark production [25], but due to the larger uncertainties and more limited kinematical coverage, we do not use this dataset to determine which NLO fits from [24] are allowed. However, we note that, using each of the three fits discussed above, an excellent description of the b quark production data is obtained. In each case, we find $\chi_b^2/N \lesssim 1.6$ when the b quark mass is also fitted to this data.

The excellent agreement with the predicted heavy quark production cross sections and the HERA measurements
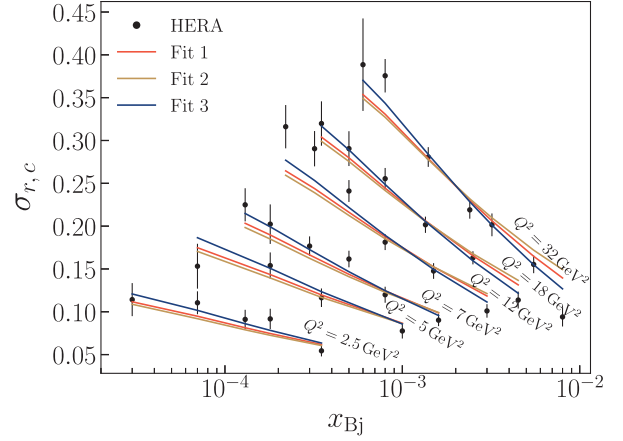

FIG. 2. Charm reduced cross section predictions calculated using the different NLO fits from [24] for the dipole amplitude that result in a good description of the charm data. The results are compared to the combined HERA data from [25].

shows that, at NLO, it is possible to simultaneously describe all small-x_{Bj} proton structure function data. The results also demonstrate that the inclusion of the heavy quark production data to the extraction of the nonperturbative initial condition for the high-energy evolution equation provides additional tight constraints. Similar conclusions have also been made in calculations of exclusive heavy quarkonium production [43,44]. The advantage of the charm reduced cross section studied in this Letter is that one does not need to introduce an additional model uncertainty related to the nonperturbative vector meson structure.

The fits that are found to be compatible with the charm quark production data are summarized in Table I along with the determined optimal heavy quark masses. The fact that the heavy quark data provides additional strong constraints for the determination of the initial condition for the BK evolution is expected. The heavy quark cross section is sensitive to much smaller dipoles than the inclusive one which can not discriminate fits that differ only at small dipole sizes. We note that the heavy quark production data

TABLE I. Fitted initial conditions for the small-x_{Bj} evolution at NLO from [24] that are compatible with the heavy quark production data from HERA. The corresponding charm and bottom masses are also shown. The terminology used to specify the resummation scheme and the running coupling prescription follows that of [24], and the abbreviation PD refers to parent dipole and BSD to Balitsky + smallest dipole [45] running coupling.

#	Resummation scheme	α_s	$Y_{0,\mathrm{BK}}$	m_c (GeV)	χ_c^2/N	m_b (GeV)	χ_b^2/N	χ_{tot}^2/N
1	ResumBK	PD	0	1.42	1.86	4.83	1.37	1.25
2	KCBK	PD	0	1.49	2.55	4.96	1.58	1.23
3	TBK	BSD	0	1.29	1.02	5.04	1.12	1.83

only allows fits where the BK evolution is started at initial rapidity $Y_{0,\mathrm{BK}} = 0$. In the second class of fits considered in [24], the dipole is frozen in the low-energy region $0 < Y < Y_{0,\mathrm{BK}} = \ln(1/0.01)$ where Y is the evolution rapidity. This is not completely consistent as the $q\bar{q}g$ production cross section (1) in the soft gluon limit results in a (leading order) BK evolution for the dipole. Additionally, we note that (in the case of ResumBK and KCBK evolutions formulated in terms of the projectile rapidity) the parent dipole prescription for the running coupling is preferred. We interpret that these physical constraints from the heavy-quark production data are because charm and bottom production probe dipole amplitudes in the perturbative region, and contribution from large dipoles dominating in light quark production with $N \sim 1$, is suppressed, see, e.g., [6]. Based on the observations above, we argue that the fits summarized in Table I are the ones that should be used in all NLO CGC calculations. The potential deviation between the predictions is then a measure of the model uncertainty after the nonperturbative input is constrained by all HERA structure function data.

To more clearly illustrate the compatibility of the NLO CGC calculation with the most recent precise HERA data from [46], we show, in Fig. 3, the total reduced cross sections computed using the dipole amplitude fits allowed by the charm data. We emphasize that this is the first time in the CGC framework that a simultaneous description of both the total and heavy quark production cross section is obtained when a perturbative small-x_{Bj} evolution equation is used to describe the center-of-mass energy dependence.

Previous LO analyses have found it impossible to perform such a global fit to the HERA data without introducing, for example, additional parameters that render the proton probed by a charm quark dipole different from the proton probed by a light quark dipole [12]. A similar approximative NLO evolution equation as in this Letter

was used in [14] but coupled to the LO impact factor. In that case, it was also found impossible to simultaneously describe the inclusive and heavy quark production data.

When the computation is promoted to full NLO accuracy, the mass dependence is modified for two reasons. First, after including higher-order corrections to the BK equation (in projectile rapidity), the dipole amplitude no longer evolves toward an asymptotic shape with an anomalous dimension $\gamma < 1$ (at small dipole sizes r, the amplitude behaves as $N \sim r^{2\gamma}$) [47]. Instead, the anomalous dimension (which is $\gamma \gtrsim 1$ in the fits reported in [24]) remains approximatively constant suppressing the dipole amplitudes at small dipoles [24,37]. Hence, the heavy quark production cross section is suppressed relative to light quark production. Second, adding the NLO corrections to the massive impact factor enhances the heavy quark production. With TBK evolution, we have opposite systematics: a small γ is developed and the impact factor suppresses heavy quark production. The net effect of these two competing NLO corrections is such that the mass dependence of the cross section matches that of the HERA data when the three fits identified in this Letter are used.

Finally, we illustrate the remaining theory uncertainty when performing NLO CGC calculations. We calculate predictions for the proton longitudinal structure function F_L, and for the charm and bottom quark contributions to it, in the EIC kinematics. We take $x_{\mathrm{Bj}} = 2 \times 10^{-3}$, and show, in Fig. 4, the structure functions as a function of Q^2 calculated using the three fits determined above. For the bottom structure function, the different fits result in almost identical predictions for the EIC, whereas for charm production, the predictions begin to differ at $Q^2 \gtrsim 20~\mathrm{GeV}^2$. On the other hand, in the total longitudinal cross section a significant difference up to 20% is seen at all Q^2. Therefore, an inclusion of the future F_L data in the global analysis will
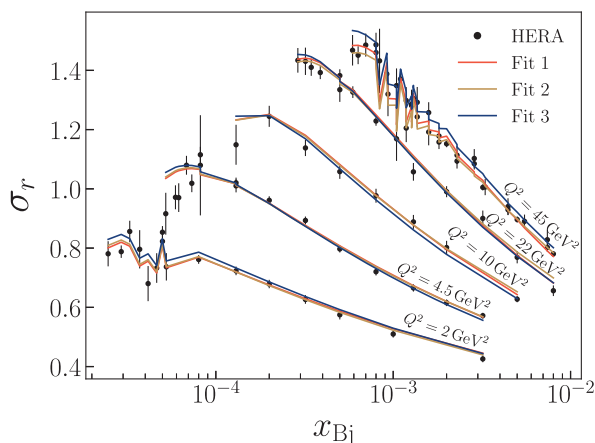

FIG. 3. Total reduced cross section calculated using the dipole amplitude fits allowed by the heavy quark production data. Note that, as the σ_r depends on inelasticity y, the theory curves connecting the calculated points are not smooth.
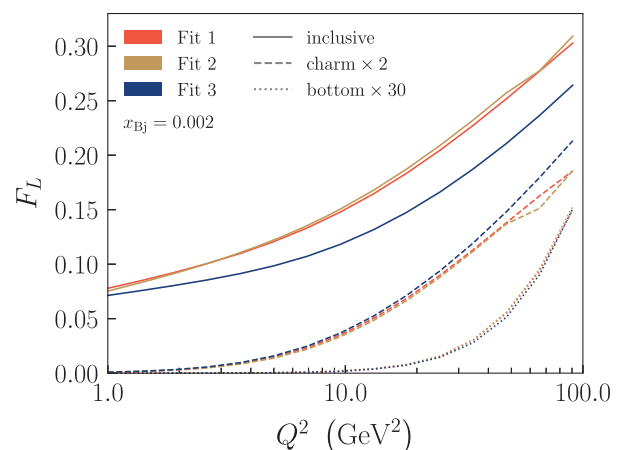
FIG. 4. Total (solid lines), charm (dashed lines), and bottom (dotted lines) longitudinal structure functions as a function of photon virtuality in the EIC kinematics calculated using the three dipole amplitude fits compatible with the heavy quark data.

provide further constraints for the initial condition of the small-x_{Bj} evolution. The currently available F_L data from HERA [48] is not able to distinguish between the different fits.

Discussion.—We have calculated heavy quark production cross sections in DIS at NLO in the CGC framework. The Bjorken-x_{Bj} dependence is obtained by solving the BK evolution equation with an initial condition extracted by fitting the total DIS cross section data in [24]. We identify a small subset of the fits reported in [24] that result in predictions for the charm and bottom structure functions which are in excellent agreement with the HERA data [25]. These three fits, constrained by both the total and heavy quark cross section data summarized in Table I, should be used in all future phenomenological applications at NLO accuracy.

This is the first time in the CGC framework with perturbative energy evolution when a simultaneous description of all small-x_{Bj} proton structure function data is obtained. A good agreement with the HERA measurements is a crucial test for the gluon saturation physics incorporated in the CGC framework and enables rigorous studies of nonlinear QCD dynamics in DIS and other scattering processes. In particular, we demonstrate that global analyses including all small-x_{Bj} structure function data are feasible at NLO and that the heavy quark production data can provide additional constraints in such analyses.

As an application, we have calculated predictions for the proton longitudinal structure function F_L, which will be measured accurately at the future Electron-Ion Collider. We reported predictions separately for the inclusive and heavy quark production cross section and showed that the remaining model uncertainty is moderate. Including the F_L data to the global analysis will further constrain the nonperturbative initial condition for the small-x_{Bj} evolution equations.

To fully explore the model uncertainties, one should perform a global analysis to the HERA inclusive and heavy quark production data, taking into account the correlated experimental uncertainties, and extract the nonperturbative model parameters with their uncertainties directly from such an analysis. Additional constraints and more detailed probes of nonlinear dynamics can be obtained by including other observables such as diffractive structure functions and exclusive cross sections. Such studies are becoming feasible thanks to the extensive progress toward NLO accuracy in the CGC framework, see, e.g., Refs. [43,44,49–58]. In the future, we plan to perform a full Bayesian analysis to determine the likelihood distribution for all the model parameters, which will also enable one to fully take into account the propagation of model uncertainties.

* henri.j.hanninen@jyu.fi
† heikki.mantysaari@jyu.fi
‡ risto.paatelainen@helsinki.fi
§ jani.j.penttala@jyu.fi

[1] R. Abdul Khalek *et al.*, Science requirements and detector concepts for the electron-ion collider: EIC Yellow Report, Nucl. Phys. **A1026**, 122447 (2022).

[2] E. C. Aschenauer, S. Fazio, J. H. Lee, H. Mäntysaari, B. S. Page, B. Schenke, T. Ullrich, R. Venugopalan, and P. Zurita, The electron-ion collider: Assessing the energy dependence of key measurements, Rep. Prog. Phys. **82**, 024301 (2019).

[3] A. Accardi *et al.*, Electron Ion Collider: The next QCD frontier: Understanding the glue that binds us all, Eur. Phys. J. A **52**, 268 (2016).

[4] H. Kowalski, T. Lappi, and R. Venugopalan, Nuclear Enhancement of Universal Dynamics of High Parton Densities, Phys. Rev. Lett. **100**, 022303 (2008).

[5] C. Marquet, M. R. Moldes, and P. Zurita, Unveiling saturation effects from nuclear structure function measurements at the EIC, Phys. Lett. B **772**, 607 (2017).

[6] H. Mäntysaari and P. Zurita, In depth analysis of the combined HERA data in the dipole models with and without saturation, Phys. Rev. D **98**, 036002 (2018).

[7] N. Armesto, T. Lappi, H. Mäntysaari, H. Paukkunen, and M. Tevio, Signatures of gluon saturation from structure-function measurements, Phys. Rev. D **105**, 114017 (2022).

[8] F. Gelis, E. Iancu, J. Jalilian-Marian, and R. Venugopalan, The color glass condensate, Annu. Rev. Nucl. Part. Sci. **60**, 463 (2010).

[9] H. Weigert, Evolution at small x_{Bj}: The color glass condensate, Prog. Part. Nucl. Phys. **55**, 461 (2005).

[10] N. N. Nikolaev and B. G. Zakharov, Color transparency and scaling properties of nuclear shadowing in deep inelastic scattering, Z. Phys. C **49**, 607 (1991).

[11] A. H. Mueller, Unitarity and the BFKL pomeron, Nucl. Phys. **B437**, 107 (1995).

[12] J. L. Albacete, N. Armesto, J. G. Milhano, P. Quiroga-Arias, and C. A. Salgado, AAMQS: A non-linear QCD analysis of new HERA data at small-x including heavy quarks, Eur. Phys. J. C **71**, 1705 (2011).

[13] T. Lappi and H. Mäntysaari, Single inclusive particle production at high energy from HERA data to proton-nucleus collisions, Phys. Rev. D **88**, 114020 (2013).

[14] B. Ducloué, E. Iancu, G. Soyez, and D. N. Triantafyllopoulos, HERA data and collinearly-improved BK dynamics, Phys. Lett. B **803**, 135305 (2020).

[15] R. D. Ball, V. Bertone, M. Bonvini, S. Marzani, J. Rojo, and L. Rottoli, Parton distributions with small-x resummation: Evidence for BFKL dynamics in HERA data, Eur. Phys. J. C **78**, 321 (2018).

[16] P. Tribedy and R. Venugopalan, QCD saturation at the LHC: Comparisons of models to $p + p$ and $A + A$ data and predictions for $p + Pb$ collisions, Phys. Lett. B **710**, 125 (2012); **718**, 1154(E) (2013).

[17] A. M. Stasto, B.-W. Xiao, and D. Zaslavsky, Towards the Test of Saturation Physics Beyond Leading Logarithm, Phys. Rev. Lett. **112**, 012302 (2014).

[18] J. L. Albacete, P. Guerrero Rodríguez, and Y. Nara, Ultra-forward particle production from color glass condensate and Lund fragmentation, Phys. Rev. D **94**, 054004 (2016).

[19] H. Mäntysaari and H. Paukkunen, Saturation and forward jets in proton-lead collisions at the LHC, Phys. Rev. D **100**, 114029 (2019).

[20] Y. Shi, L. Wang, S.-Y. Wei, and B.-W. Xiao, Pursuing the Precision Study for Color Glass Condensate in Forward Hadron Productions, Phys. Rev. Lett. **128**, 202302 (2022).

[21] B. Schenke, P. Tribedy, and R. Venugopalan, Fluctuating Glasma Initial Conditions and Flow in Heavy Ion Collisions, Phys. Rev. Lett. **108**, 252301 (2012).

[22] Y. V. Kovchegov, Small x F_2 structure function of a nucleus including multiple Pomeron exchanges, Phys. Rev. D **60**, 034008 (1999).

[23] I. Balitsky, Operator expansion for high-energy scattering, Nucl. Phys. **B463**, 99 (1996).

[24] G. Beuf, H. Hänninen, T. Lappi, and H. Mäntysaari, Color glass condensate at next-to-leading order meets HERA data, Phys. Rev. D **102**, 074028 (2020).

[25] H. Abramowicz *et al.* (H1, ZEUS Collaboration), Combination and QCD analysis of charm and beauty production cross-section measurements in deep inelastic ep scattering at HERA, Eur. Phys. J. C **78**, 473 (2018).

[26] G. Beuf, T. Lappi, and R. Paatelainen, Massive quarks in NLO dipole factorization for DIS: Transverse photon, Phys. Rev. D **106**, 034013 (2022).

[27] G. Beuf, T. Lappi, and R. Paatelainen, Massive Quarks at One Loop in the Dipole Picture of Deep Inelastic Scattering, Phys. Rev. Lett. **129**, 072001 (2022).

[28] G. Beuf, T. Lappi, and R. Paatelainen, Massive quarks in NLO dipole factorization for DIS: Longitudinal photon, Phys. Rev. D **104**, 056032 (2021).

[29] H. Hänninen, T. Lappi, and R. Paatelainen, One-loop corrections to light cone wave functions: the dipole picture DIS cross section, Ann. Phys. (Amsterdam) **393**, 358 (2018).

[30] G. Beuf, Dipole factorization for DIS at NLO: Loop correction to the $\gamma^*_{T,L} \to q\bar{q}$ light-front wave functions, Phys. Rev. D **94**, 054016 (2016).

[31] G. Beuf, Dipole factorization for DIS at NLO: Combining the $q\bar{q}$ and $q\bar{q}g$ contributions, Phys. Rev. D **96**, 074033 (2017).

[32] Y. V. Kovchegov, J. Kuokkanen, K. Rummukainen, and H. Weigert, Subleading-N_c corrections in non-linear small-x evolution, Nucl. Phys. **A823**, 47 (2009).

[33] B. Ducloué, E. Iancu, A. H. Mueller, G. Soyez, and D. N. Triantafyllopoulos, Non-linear evolution in QCD at high-energy beyond leading order, J. High Energy Phys. 04 (2019) 081.

[34] B. Ducloué, H. Hänninen, T. Lappi, and Y. Zhu, Deep inelastic scattering in the dipole picture at next-to-leading order, Phys. Rev. D **96**, 094017 (2017).

[35] I. Balitsky and G. A. Chirilli, Next-to-leading order evolution of color dipoles, Phys. Rev. D **77**, 014019 (2008).

[36] T. Lappi and H. Mäntysaari, Direct numerical solution of the coordinate space Balitsky-Kovchegov equation at next to leading order, Phys. Rev. D **91**, 074016 (2015).

[37] T. Lappi and H. Mäntysaari, Next-to-leading order Balitsky-Kovchegov equation with resummation, Phys. Rev. D **93**, 094004 (2016).

[38] E. Iancu, J. D. Madrigal, A. H. Mueller, G. Soyez, and D. N. Triantafyllopoulos, Resumming double logarithms in the QCD evolution of color dipoles, Phys. Lett. B **744**, 293 (2015).

[39] E. Iancu, J. D. Madrigal, A. H. Mueller, G. Soyez, and D. N. Triantafyllopoulos, Collinearly-improved BK evolution meets the HERA data, Phys. Lett. B **750**, 643 (2015).

[40] G. Beuf, Improving the kinematics for low-x QCD evolution equations in coordinate space, Phys. Rev. D **89**, 074039 (2014).

[41] G. Beuf, H. Hänninen, T. Lappi, and H. Mäntysaari, Color glass condensate at next-to-leading order meets HERA data, 2020, 10.5281/zenodo.4229269.

[42] F. D. Aaron *et al.* (H1, ZEUS Collaboration), Combined measurement and QCD analysis of the inclusive $e^\pm p$ scattering cross sections at HERA, J. High Energy Phys. 01 (2010) 109.

[43] H. Mäntysaari and J. Penttala, Complete calculation of exclusive heavy vector meson production at next-to-leading order in the dipole picture, J. High Energy Phys. 08 (2022) 247.

[44] H. Mäntysaari and J. Penttala, Exclusive heavy vector meson production at next-to-leading order in the dipole picture, Phys. Lett. B **823**, 136723 (2021).

[45] I. Balitsky, Quark contribution to the small-x evolution of color dipole, Phys. Rev. D **75**, 014001 (2007).

[46] H. Abramowicz *et al.* (H1, ZEUS Collaboration), Combination of measurements of inclusive deep inelastic $e^\pm p$ scattering cross sections and QCD analysis of HERA data, Eur. Phys. J. C **75**, 580 (2015).

[47] J. L. Albacete and Y. V. Kovchegov, Solving high energy evolution equation including running coupling corrections, Phys. Rev. D **75**, 125021 (2007).

[48] V. Andreev *et al.* (H1 Collaboration), Measurement of inclusive ep cross sections at high Q^2 at $\sqrt{s} = 225$ and 252 GeV and of the longitudinal proton structure function F_L at HERA, Eur. Phys. J. C **74**, 2814 (2014).

[49] R. Boussarie, A. V. Grabovsky, D. Y. Ivanov, L. Szymanowski, and S. Wallon, Next-to-Leading Order Computation of Exclusive Diffractive Light Vector Meson

Production in a Saturation Framework, Phys. Rev. Lett. **119,** 072002 (2017).

[50] P. Caucal, F. Salazar, and R. Venugopalan, Dijet impact factor in DIS at next-to-leading order in the color glass condensate, J. High Energy Phys. 11 (2021) 222.

[51] H. Mäntysaari and J. Penttala, Exclusive production of light vector mesons at next-to-leading order in the dipole picture, Phys. Rev. D **105,** 114038 (2022).

[52] G. Beuf, H. Hänninen, T. Lappi, Y. Mulian, and H. Mäntysaari, Diffractive deep inelastic scattering at NLO in the dipole picture: The $q\bar{q}g$ contribution, Phys. Rev. D **106,** 094014 (2022).

[53] F. Bergabo and J. Jalilian-Marian, One-loop corrections to dihadron production in DIS at small x, Phys. Rev. D **106,** 054035 (2022).

[54] F. Bergabo and J. Jalilian-Marian, Single inclusive hadron production in DIS at small x: Next to leading order corrections, J. High Energy Phys. 01 (2023) 095.

[55] P. Caucal, F. Salazar, B. Schenke, and R. Venugopalan, Back-to-back inclusive dijets in DIS at small x: Sudakov suppression and gluon saturation at NLO, J. High Energy Phys. 11 (2022) 169.

[56] E. Iancu and Y. Mulian, Forward dijets in proton-nucleus collisions at next-to-leading order: The real corrections, J. High Energy Phys. 03 (2021) 005.

[57] K. Roy and R. Venugopalan, NLO impact factor for inclusive photon + dijet production in $e + A$ DIS at small x, Phys. Rev. D **101,** 034028 (2020).

[58] P. Taels, T. Altinoluk, G. Beuf, and C. Marquet, Dijet photoproduction at low x at next-to-leading order and its back-to-back limit, J. High Energy Phys. 10 (2022) 184.